AD-A165 432   THE USE OF ION IMPLANTATION FOR MATERIALS PROCESSING   1/3
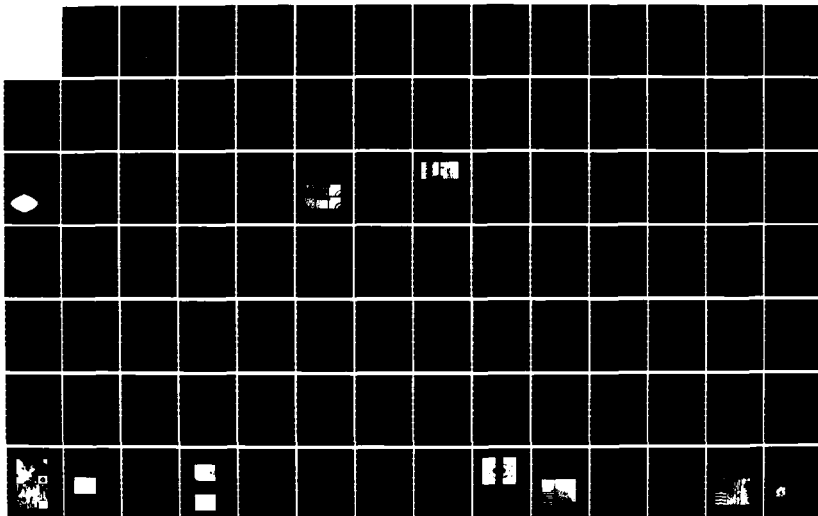   (U) NAVAL RESEARCH LAB WASHINGTON DC   F A SMIDT
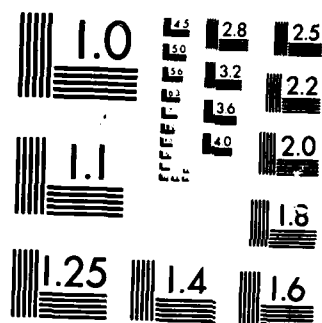   06 MAR 86 NRL-MR-5716

UNCLASSIFIED   F/G 13/8   NL

MICROCOPY RESOLUTION TEST CHART

NATIONAL BUREAU OF STANDARDS 1963 A

The Use of Ion Implantation for Materials Processing Annual Progress Report for the Period 1 October 1983 - 30 September 1984

F. A. SMIDT

Materials Modification and Analysis Branch
Condensed Matter and Radiation Sciences Division

AD-A165 432

March 6, 1986

DTIC FILE COPY

E

NAVAL RESEARCH LABORATORY
Washington, D.C.

86 3 1 030

REPORT DOCUMENTATION PAGE

1a. REPORT SECURITY CLASSIFICATION UNCLASSIFIED			1b. RESTRICTIVE MARKINGS		
2a. SECURITY CLASSIFICATION AUTHORITY			3 DISTRIBUTION/AVAILABILITY OF REPORT Approved for public release; distribution unlimited.		
2b. DECLASSIFICATION / DOWNGRADING SCHEDULE					
4. PERFORMING ORGANIZATION REPORT NUMBER(S) NRL Memorandum Report 5716			5. MONITORING ORGANIZATION REPORT NUMBER(S)		
6a. NAME OF PERFORMING ORGANIZATION Naval Research Laboratory	6b. OFFICE SYMBOL (If applicable) Code 6670		7a. NAME OF MONITORING ORGANIZATION		
6c. ADDRESS (City, State, and ZIP Code) Washington, DC 20375-5000			7b. ADDRESS (City, State, and ZIP Code)		
8a. NAME OF FUNDING / SPONSORING ORGANIZATION Office of Naval Research	8b. OFFICE SYMBOL (If applicable)		9. PROCUREMENT INSTRUMENT IDENTIFICATION NUMBER		

8c. ADDRESS (City, State, and ZIP Code) Arlington, VA 22217	10. SOURCE OF FUNDING NUMBERS			
	PROGRAM ELEMENT NO. (See page ii)	PROJECT NO.	TASK NO.	WORK UNIT ACCESSION NO.

11. TITLE (Include Security Classification)   The Use of Ion Implantation for Materials Processing
Annual Progress Report for the Period 1 October 1983 — 30 September 1984

12. PERSONAL AUTHOR(S)
Smidt, F.A.

13a. TYPE OF REPORT Progress	13b. TIME COVERED FROM 10/83 TO 9/84	14. DATE OF REPORT (Year, Month, Day) 1986 March 6	15. PAGE COUNT 235

16. SUPPLEMENTARY NOTATION

17.	COSATI CODES		18. SUBJECT TERMS (Continue on reverse if necessary and identify by block number)
FIELD	GROUP	SUB-GROUP	Auger electron spectroscopy · Ion beam enhanced deposition
			Corrosion · Rutherford backscattering (Continues)

19. ABSTRACT (Continue on reverse if necessary and identify by block number)

An interdisciplinary program on the use of ion implantation for materials processing is being conducted at NRL. This report describes the important factors in ion implantation science and technology and reports progress in the use of ion implantation to modify friction, wear, fatigue, corrosion, optical and magnetic properties of materials.

Con't'd

20. DISTRIBUTION / AVAILABILITY OF ABSTRACT ☒ UNCLASSIFIED/UNLIMITED ☐ SAME AS RPT. ☐ DTIC USERS	21. ABSTRACT SECURITY CLASSIFICATION UNCLASSIFIED	
22a. NAME OF RESPONSIBLE INDIVIDUAL F.A. Smidt	22b. TELEPHONE (Include Area Code) (202) 767-4800	22c. OFFICE SYMBOL Code 6670

DD FORM 1473, 84 MAR   83 APR edition may be used until exhausted.
All other editions are obsolete.   SECURITY CLASSIFICATION OF THIS PAGE

10. SOURCE OF FUNDING NUMBERS

	PROGRAM ELEMENT NO.	PROJECT NO.	TASK NO.	WORK UNIT ACCESSION NO.
NAVSEA	63728N	WR Z1050		66-1663-0-4
ONR	61153N	RR022-06-42		63-1020-0-4
ONR	61153N	RR022-06-42		66-0467-0-3
ONR	61153N	RR022-06-42		61-1750-0-4
ONR	61153N	RR022-06-42		66-0444-0-4
ONR	62241N	RR022-06-42		66-0447-0-4
NAPC	62241N	WF41-401-000		66-0424-A-3
ONR	61153N	RR012-01-42		66-0418-0-4
ONR	61153N	RR012-01-42		66-1790-0-4
ONR	61153N	RR022-11-41		63-1315-0-3
ONR	62761N	RF61-544-804		66-2079-0-4
SSPO	63371N	BO 951		66-2173-0-4

18. SUBJECT TERMS (Continued)

Materials processing
Wear
Sputtering
AISI 52100
Ti-6Al-4V
M50
Bearings
Friction
Oxidation
304SS
9310
Berylium
Fatigue
SIMS
Carburization
Radiation enhanced diffusion
Cascade mixing
Wear testing
316SS
Amorphous Si, Ge, GaAs
Tribology
Hardness
Anodic polarization
Ta
Surface analysis
PIXE
Hot corrosion
CoCrAlY
Ion implantation

CONTENTS

RESEARCH PROGRESS

Preface - F.A. Smidt

This report is the sixth in a series of Progress Reports on work conducted at the Naval Research Laboratory (NRL) to investigate the use of ion implantation for materials processing. The objective of the program is to develop the capabilities of ion implantation and ion beam activated deposition for new and improved surface treatment techniques of interest to Navy and DOD applications. Attainment of this objective requires both fundamental research to provide an understanding of the physical and metallurgical changes taking place in the implanted region of a material and applications oriented research to demonstrate the benefits of ion implantation.

The work reported here represents a coordinated effort in three divisions at NRL, the Condensed Matter and Radiation Sciences Division (Code 6600), the Chemistry Division (Code 6100) and the Material Science and Technology Division (Code 6300). The work includes in-house basic research conducted under the auspices of the Office of Naval Research, applied research performed for several Navy and DOD sponsors (NAVAIR, NAVSEA, SSPO) and collaborative work with scientists at other laboratories.

The purpose of this report is to make available from one source the results of all studies at NRL related to the use of ion implantation for materials processing so as to provide a more comprehensive picture of the scope and interrelationship of the research and to expedite technology transfer to the civilian industrial sector. The report consists of four sections describing the research and a cummulative bibliography of published papers and reports.

v

THE USE OF ION IMPLANTATION FOR MATERIALS PROCESSING

SUMMARY

I. ION IMPLANTATION SCIENCE AND TECHNOLOGY

Research reported in this section is directed toward a fundamental understanding of the processes and phenomena associated with ion implantation and ion beam activated deposition and the development of the necessary technology to treat surfaces in a controllable, reproduceable and economic manner.

A. Manufacturing Technology Program To Develop A Production Ion Implantation Facility For Processing Bearings And Tools

F.A. Smidt and B.D. Sartwell

A manufacturing technology project to expedite the development and transfer of ion implantation of metals to industrial practice is described. The objective of this project is to develop a prototype production facility to implant several types of aircraft and instrument bearings, and stamping and forming tools to increase their resistance to corrosion and wear and, therefore, increase their lifetimes. Research conducted in support of this project to investigate several important design issues is described including beam heating, sputtering at non-normal angles of incidence, calculation of concentration profiles and effect of residual pressure in the vacuum chamber. A major conclusion is that beam heating imposes severe constraints on the beam current density and a high throughput facility requires a diffuse beam and a batch processing mode of operation. Initial estimates of cost savings for several components are presented and are shown to be very favorable.

B. A High Throughput Metal Ion Implanter End Station

A.J. Armini and S.N. Bunker

Research in the implantation of metal ions has been shown to produce improved surface properties for a wide variety of ion species and materials. Except for the case of gaseous source materials, such as nitrogen, little attempt has been made to advance the technology to pilot production levels of implanted parts. A system is described in which a specially designed end station is combined with a commercial, mass-analyzed, high current ion implanter (10 mA beam). The goal is to produce a high throughput system optimized for ions such as chromium, which has proved valuable in providing corrosion resistance to bearings.

C. Adherent TiN Films Produced By Ion Beam Enhanced Deposition At Room Temperature

R.A. Kant, B.D. Sartwell, I.L. Singer and R.G. Vardiman

This paper describes the preliminary results of an investigation of the influence of ion implantation on the structure and mechanical properties of vapor-deposited thin films which are implanted during nucleation and growth of the films. For these studies, titanium was deposited at room temperature on M50 steel, AISI 52100 steel, and silicon substrates in a chamber backfilled with nitrogen gas to a pressure of 1×10^{-5} Torr. The films were deposited in 125 or more increments of 0.8 nm each. Between each increment, the film was implanted with 30 keV N_2^+. Auger electron spectroscopy revealed that significant reduction of carbon and oxygen occurred in the implanted films and electron microscopy showed the films to be entirely fcc with a lattice constant consistent with that of TiN. The mechanical properties of the films were investigated using scratch tests for adhesion as well as friction and wear analysis. While the unimplanted films failed to adhere, the implanted films remained adherent throughout the tests and exhibited both low friction and low wear.

D. In Situ Auger Analysis Of Surface Composition During High Fluence Ion Implantation

D.A. Baldwin, B.D. Sartwell and I.L. Singer

A multi-technique, ultrahigh vacuum (UHV) target chamber has been used to perform in situ Auger electron spectroscopy (AES) analysis during ion implantation and AES sputter depth profiling of the substrate within 1-2 min after implantation. Iron was implanted with 150 keV Ti^+ at a 45^0 angle of incidence in a target chamber with pressures ranging from 8×10^{-9} Torr. of residual gases up to 1×10^{-5} Torr. of intentionally admitted CO gas. The Ti surface concentration increased to ~15 at.% at steady-state with a curve shape that was concave downward at all fluences. The surface C concentration was found to be proportional to that of Ti for implants in CO, supporting a vacuum carburization model. Substantial O surface concentration (15-20 at.%) was detected for these runs but depth profiles showed only carburization, not oxidation of the implanted layer. The Ti/Fe surface concentration ratio is higher for implants done in CO, and this is discussed in terms of modification of the sputter yield for Ti.

E. In Situ Proton-Induced X-ray Emission And Auger Electron Spectroscopy Study Of Titanium And Niobium Implantation Of Iron Films

B.D. Sartwell and D.A. Baldwin

Implantation of 190 keV titanium and niobium ions into iron films 200 nm thick electron beam deposited onto polished Si(100) substrates has been investigated to determine changes in surface composition during implantation. Proton-induced X-ray emission was used to measure the instantaneous film thickness and the total retained dose, and Auger electron spectroscopy was used to determine the surface concentrations of the implanted species and the reactive element. Implantations were carried out both under ultrahigh vacuum conditions and with the chamber backfilled with CO to a pressure of 1×10^{-6} Torr. Elemental sputtering yields were measured for iron and the implanted element as a function of fluence. The results showed that, for titanium implantation, the addition of CO to the target chamber signficiantly reduced the sputtering yield of the substrate and increased the retained dose that could be achieved. For niobium implantation, the addition of CO to the chamber reduced the substrate sputtering yield, but not to the same degree as observed for titanium, and did not alter the total retained dose that could be achieved.

F. Sputtering And Migration During Ta Implantation Of Fe

K.S. Grabowski, F.D. Correll and F.R. Vozzo

This work evaluated the influence of sputtering and diffusion on the measured concentration profiles of Ta implanted into Fe. The samples consisted of thin Fe films deposited on sapphire or glass substrates and implanted with 150 keV Ta ions to fluences of $(1-18) \times 10^{16}$ ions/cm^2. Rutherford backscattering analysis provided measurements of the retained dose, the sputtering rate of Fe and Ta, and the evolution of the Ta depth distribution, all as a function of ion dose. These measurements indicated that preferential removal by sputtering combined with atomic migration led to a 50% increase in the saturation retained dose of Ta, when compared to the value predicted by simple theory without consideration of these two effects.

G. Carburization During Cr Self Implantation In A ^{13}CO Atmosphere

Experimental results from self implantation of Cr into Cr performed in a ^{13}C enriched CO atmosphere have shown that a significant concentration of ^{13}C was introduced into the implanted surface. A Monte Carlo calculation, with the Code EVOLVE was conducted to provide an estimate of the surface concentration introduced by collision cascade mixing processes. The calculations indicate that only a portion of the experimentally observed concentration can be accounted for by collision cascade mixing. Experimental and theoretical results are discussed.

H. Compositions Of Metals Implanted To Very High Fluences

I.L. Singer

Surface compositions and microstructures of Fe and steels implanted with Ti^+ and N^+ ions to high fluences (10^{16}-10^{18} cm^{-2}) have been examined by a variety of surface analytical techniques, including Auger electron spectroscopy, secondary ion mass spectrometry, nuclear reaction analysis, conversion electron Mossbauer spectroscopy and transmission electron microscopy. The compositions observed at very high fluences could not have been predicted by simple ion implantation (collection) models based solely on physical processes such as sputtering, lattice dilation or even atomic mixing. For example, Ti^+ implantation produced a carburized surface layer following absorption of C from gases in the vacuum chamber; implanted N and bulk C atoms were found to migrate across the implanted layer; and peak implant concentrations of interstitial atoms did not exceed the richest precipitate formed. The metallurgical state of these heavily implanted layers can, in many cases, be predicted from traditional metallurgical behaviour. An approach is suggested for calculating compositions of implanted layers that incorporates both the physical processes now included in many models and the metallurgical phases observed experimentally.

I. Surface Analysis, Ion Implantation And Tribological Processes Affecting Steels

I.L. Singer

An analytical approach is presented for investigating surface processing treatments used to improve the friction and wear (i.e., tribological) behavior of engineering alloys, with specific examples cited for ion implantation of steels. Surface composition techniques such as scanning Auger microscopy, energy dispersive X-ray analysis and secondary ion mass spectroscopy and microscopies such as transmission electron microscopy (TEM), secondary electron microscopy and interferometry have eluciated the microsctructure and chemistry of a variety of implant species (N, C, Ti and Ta) found to affect the tribological behavior of surfaces. Novel combinations of these techniques, along with metallography of ion-etched surfaces or TEM of ion-beam-etched foils, are shown to be useful methods for establishing microstructures of ion-implanted and worn surfaces. The tribological behavior of the thin implanted layer (~ 200 nm) is examined by two devices: a stickslip machine and a polishing wear apparatus, the latter having wear rate versus depth resolution of 10 to 20 nm. Tribology studies of two implanted steels, 304 stainless steel and 52100 bearing steel, are presented, and analytical investigations which have led to models for their improved wear behavior are described. A process by which implanted metal ions can react with residual gases in the vacuum chamber to "carburize" steel and produce superior tribological surfaces is also discussed.

4

II. WEAR AND FATIGUE

Research reported in this section involves the application of ion
implantation processing to the improvement of surface sensitive
mechanical properties such as wear and fatigue, and fundamental
investigations of the mechanisms which produce these changes in
properties.

A. Tribomechanical Properties Of Ion Implanted Metals

I.L. Singer

A review of tribomechanical studies supported by surface analysis
finds ion implantation capable of increasing the sliding wear resistance
of ion implanted metals in two ways. First, it can reduce friction by
modifying the surface composition (e.g., Ti^+ into steel) or by
promoting the growth of low friction oxide layers (e.g., N^+ into Ti).
Second, it can modify the subsurface composition and structure to resist
fracture and debris formation. These modifications harden the surface,
change its work-hardening behavior and/or increase residual stresses.
Microindentation hardness measurements indicate that many but not all of
the wear resistant surfaces are hardened by implantation; thus, surface
hardness is a contributing but not necessarily a controlling factor in
wear resistance. Evidence for wear reduction through the migration of N
during wear is critically reviewed. It is concluded that the principal
benefit of ion implantation is to prevent or delay the formation of wear
particles, thereby changing the wear mode during run-in and permitting
metals to reach load-carrying capacities up to their elastic limits.

B. Application Of Ion Implantation To Wear Protection Of Materials

G.K. Hubler and F.A. Smidt

Key results from the literature for the wear behavior of N- and
Ti-implanted steels are reviewed. A qualitative model which rationalizes
the mechanisms producing improvements in the sliding wear resistance of
steels is presented. In the limited regime of low sliding velocities the
model provides guidelines for choosing the experimental conditions of
applied load, composition, hardness and heat treatment of the steel under
which implantation will improve wear resistance.

5

C. Mechanical And Chemical Properties Of Tantalum-Implanted Steels

G.K. Hubler, I.L. Singer and C.R. Clayton

The surface mechanical and chemical properties of tantalum-implanted AISI 52100, AISI M50 and AISI 9310 steels and pure iron were investigated. Sputter Auger profiles of pure iron indicate significant carbon incorporation during implantation. For AISI 52100 steel the unlubricated kinetic coefficient of friction is reduced from 0.6 to 0.38, the load-carrying capacity is increased and the pitting potential in a 0.01 M NaCl solution is increased by 510 mV. The corrosion resistance of tantalum-implanted AISI M50 steel in 0.5 M H_2SO_4 is equal to that of high dose chromium implantation. The rolling contact fatigue life is significantly improved for tantalum-implanted AISI M50 steel and a 24% increase in load-carrying capacity is measured for Ryder gear scuffing tests on tantalum-implanted AISI 9310 steel. The mechanism producing the improvements in corrosion resistance is thought to be selective dissolution of iron with the formation of a tantalum-rich passive oxide film on the surface, while friction reduction is at least partly responsible for improving the wear properties.

D. Wear Behavior Of Flat And Graded Profile Boron-Implanted Beryllium

K. Kumar, H. Newborn and R. Kant

Pin-on-disk tests were performed for comparative friction and wear behavior on flat and graded profile boron implanted beryllium samples. Peak, intended boron concentrations of 10, 20, 30 and 40 atom percent were investigated. Auger Electron Spectroscopy was used to determine the boron concentration as a function of depth. Preliminary work was performed to study the effects of (1) a low temperature (450°C, 1-1/2 hours) heat treatment of the implanted specimens and (2) a change in the pin material. All of the boron implanted beryllium samples showed significant improvement versus unimplanted beryllium and an anodized beryllium surface. Graded samples showed comparable friction coefficients but inferior wear resistance with respect to the flat profile samples.

E. A Study Of The Mechanisms Of Fatigue Life Improvement In An Ion Implanted Nickel-Chromium Alloy

R.G. Vardiman and J.E. Cox

Wires of the alloy Ni20Cr with and without carbon ion implantation have been tested in tension-tension fatigue. A 17% increase in endurance limit was found with implantation. The fatigued surface was examined by SEM, and the wire was then nickel plated so that transverse sections could be made for TEM study. It was found that bulk slip was unaffected by implantation but slip in surface grains was unable to penetrate the implanted layer to a significant degree. Slip band cracking which was found in unimplanted specimens was replaced by grain boundary cracking in the implanted specimens.

III. CORROSION AND OXIDATION

Research reported in this section involves the application of ion implantation processing to modify the corrosion and oxidation behavior of surfaces, and fundamental investigations of the mechanisms which produce these changes in properties.

A. Recent Advances In The Application Of Ion Implantation To Corrosion and Wear Protection

F.A. Smidt

Substantial progress has been made in the past few years in establishing viable approaches for the use of ion implantation for corrosion and wear protection. The major appraoches, their theoretical basis and the engineering problems of scale-up to commercially acceptable rates of production and cost are examined in this paper.

B. Effect Of Cr^+ Implantation On The Thermal Oxidation of Ta

K.S. Grabowski and C.R. Gossett

Cr^+ implantation of Ta was investigated in an effort to improve the oxidation resistance of Ta at temperatures between 500 and 750°C, and for oxidation times up to 100h. Samples were implanted with 1.5×10^{17} Cr^+/cm^2 at 150 keV, and compared to samples implanted with 1×10^{16} or 1×10^{17} Ta^+/cm^2 at 145 keV to evaluate the role of physical effects from ion implantation. Following oxidation, samples were examined using helium and proton backscattering, electron and optical imaging techniques, and Auger electron spectroscopy. Improved resistance to oxidation was observed in Cr^+-implanted samples oxidized at 500°C for up to 100h, and at 600°C for about 1h. However, some local breakdown of the protective surface occurred in these samples and no protection at all was observed at 750°C. Reasons for this breakdown are discussed and alternate approaches for improving oxidation resistance using ion implantation are proposed.

C. Modification Of The Oxidation And Hot Corrosion Behavior Of CoCrAl Alloys By Ion Implantation

F.A Smidt, G.R. Johnston, J.A. Sprague, V. Provenzano, S.Y. Hwang, G.J. Meier and F.S. Pettit

The early stages of oxidation and hot corrosion at 700°C were studied in Co-22Cr-11Al and Co-22Cr-11Al-0.5Y alloys in the cast and heat-treated form. Ion implantation was used to study the effect of Y on oxidation and hot corrosion mechanisms. Analytical transmission electron microscopy, Auger electron spectroscopy, Rutherford backscattering spectroscopy and scanning electron microscopy with energy dispersive x-ray analysis were used to characterize microstructure, oxide growth rate and oxide film composition. Implantation of 2×10^{16} Y ion/cm^2 was found to increase the oxidation rate by a factor of 2, increase the hot corrosion rate and suppress void formation at the oxide-metal interface. Possible mechanisms for these observations are discussed.

IV. OTHER RESEARCH AREAS

Research reported in this section involves investigations of applications other than surface mechanical and surface chemical properties. The papers in this report deal with amorphization of semiconductor materials and modification of their optical properties.

A. Infrared Properties Of Heavily Implanted Silicon, Germanium And Gallium Arsenide

W.G. Spitzer, L. Liou, K-W. Wang, C.N. Waddell, G.K. Hubler and S-I. Kwun

A review of the techniques developed for using infrared reflection spectroscopy to study properties of heavily implanted semiconductors is presented. Several structural models are considered and calculations based on them are applied to measurements of implanted Si, Ge and GaAs. These comparisons of model calculations and measured spectra show how a number of important physical parameters can be obtained as well as reporting new information concerning implantation-induced amorphous material.

B. Amorphous Silicon Produced By Ion Implantation: Effects Of Ion Mass And Thermal Annealing

C.N. Waddell, W.G. Spitzer, J.E. Frederickson, G.K. Hubler and T.A. Kennedy

Characterization of the two optical states of amorphous Si produced by ion implantation is extended to include electron paramagnetic resonance, fundamental absorption edge, and density measurements in addition to infrared reflection. It is found that the properties of the two a-Si states are not dependent upon the mass of the incident ion (^{12}C, ^{29}Si, ^{31}P, ^{120}Sn) or upon the anneal temperature for $400° \le T_a \le 600°C$. The dangling-bond density drops about a factor of 2 when the a-Si makes a transition between the two states. The absorption coefficient also drops by more than a factor of 5, but the density of the a-Si does not change when the transition occurs. The transition between states was not completed at $T_a=300°C$, so the annealing mechanism may be temperature dependent.

C. Thermal Annealing Behavior Of Hydrogen-Free Amorphous Silicon And Germanium

G.K. Hubler, E.P. Donovan, K-W. Wang and W.G. Spitzer

Recent work has demonstrated that the infrared properties (refractive index and absorption) of amorphous silicon and germanium prepared by ion implantation depend upon the low temperature thermal annealing history ($150°C < T < 600°C$). This thermal relaxation phenomenon is the subject of this review. The data suggest the change in refractive index is caused by a structural reorganization of a continuous random network but that changes in absorption and spin density are chiefly caused by the annealing of defects within the amorphous structure.

Section I.A

MANUFACTURING TECHNOLOGY PROGRAM TO DEVELOP A PRODUCTION ION IMPLANTATION FACILITY FOR PROCESSING BEARINGS AND TOOLS

F.A. Smidt and B.D. Sartwell

Materials Modification & Analysis Branch
Condensed Matter & Radiation Sciences Division
Naval Research Laboratory

70

MANUFACTURING TECHNOLOGY PROGRAM TO DEVELOP A PRODUCTION ION IMPLANTATION FACILITY FOR PROCESSING BEARINGS AND TOOLS

F.A. SMIDT and B.D. SARTWELL

Naval Research Laboratory, Washington, DC 20375, USA

A manufacturing technology project to expedite the development and transfer of ion implantation of metals to industrial practice is described. The objective of this project is to develop a prototype production facility to implant several types of aircraft and instrument bearings, and stamping and forming tools to increase their resistance to corrosion and wear and, therefore, increase their lifetime. Research conducted in support of this project to investigate several important design issues is described including beam heating, sputtering at non-normal angles of incidence, calculation of concentration profiles and effect of residual pressure in the vacuum chamber. A major conclusion is that beam heating imposes severe constraints on the beam current density and a high throughput facility requires a diffuse beam and a batch processing mode of operation. Initial estimates of cost savings for several components are presented and are shown to be very favorable.

1. Introduction

Ion implantation has been shown to possess several distinct advantages over other techniques for the surface treatment of materials. The ability to introduce any ion into the surface region of any substrate without the constraints of thermodynamic phase equilibrium, the ability to perform the implant at a low process temperature, the ability to perform the treatment without a further need for heat treatment or refinishing, and the absence of coating adhesion problems make ion implantation a promising technique for a variety of applications. Research and development work at the Naval Research Laboratory, Harwell, Sandia National Laboratory and other university and industrial laboratories has established the effectiveness of ion implantation of metals and alloys for selected corrosion, wear and fatigue applications. There is, however, a need to address the scale-up problems of moving from an essentially laboratory technique to an industrial process. The semiconductor industry, where this transition was made several years ago, provides some guidance on potential problems and approaches. However, that industry has not had to address the problem of implanting highly complex shapes fabricated from metals and alloys.

The US Navy has established manufacturing technology programs to support projects which expedite the development and transfer of emerging technologies to industrial practice. The Naval Research Laboratory is currently conducting a manufacturing technology (ManTech) project on ion implantation for corrosion and wear resistance. This project involves (a) establishment of overall design objectives, (b) selection of a principal contractor to design and construct the

end station to process various components and to operate the entire facility, (c) selection of a commercially available implanter to be delivered to the principal contractor's plant, (d) performance of research both by NRL and the principal contractor to determine optimum implantation conditions for various components, (e) operation of the implantation facility for a ten month period to develop production techniques and establish a basis for economic projections, and (f) evaluation of the performance of selected components implanted for corrosion and wear demonstrations. The project was initiated in 1981 with the development of design objectives. A design competition was conducted in 1982 with the resultant selection in 1983 of Spire Corporation as the principal contractor. Spire is reporting on their design of the end station in another paper at this conference. Through a competitive procurement process, a contract was recently awarded to Eaton Corporation to deliver a Nova NV10-160 implanter to Spire in January 1985.

In this paper, the program objectives and design requirements for the ManTech project are reviewed. In addition, the results of research conducted at NRL in support of the project are presented. These include (a) studies of the effects of angle of incidence of the ion beam on retained dose, (b) development of a computer code to predict the effect of various mask widths on the concentration profile for implantation into a rotating cylinder, (c) development of a computer code to calculate composition profiles for any combination of implanted ion and substrate, taking into account changes in range and straggling due to changes in target composition, changes in sputtering yield with surface composition, and volume increase in the target due to the implanted ions, and (d) studies on the effect of

residual gases in the implanter chamber on surface composition and retained dose. Information in all of these areas is required to determine the optimum processing conditions for components possessing various compositions and complex geometries.

2. Program objectives and requirements

Studies performed at the Naval Research Laboratory have shown that two of the most promising applications of ion implantation are improving the corrosion resistance of aircraft gas turbine and gearbox bearings by chromium implantation [1] and the wear resistance of beryllium instrument bearings by boron implantation [2]. Relatively crude fixtures were designed and used in the NRL implanter to process the components singly. Maximum beam currents obtainable were 0.5 mA of either Cr^+ or B^+ with the processing involving a combination of electrostatic sweeping of the ion beam and workpiece manipulations. Because of the low percentage of beam utilization, throughput for the bearing components in the NRL research implanter was low and a higher throughput facility was obviously needed.

The primary consideration in the formulation of the design objective for the ManTech implantation facility was to increase the throughput to economically viable rates of production while utilizing ion implanters that are commercially available at the present time. Thus the focus of the project was intended to be on the engineering problems of implantation such as processing, heat removal, work piece manipulation, sputtering etc. rather than on the development of implanters since the latter could be expected to continue to evolve under the impetus of the demands of the semiconductor industry.

Commercial ion implanters manufactured for the semiconductor industry can produce beam currents up to 10 mA in an energy range of 25–160 kV. This level of beam current served to define certain design requirements such as the mode of surface coverage. High current ion beams require space charge neutralization in order to propagate successfully. Low energy electrons produced through the interaction of the energetic ions with residual gas molecules provide the necessary neutralization. However, if electrostatic rastering of the ion beam is attempted, the low energy electrons are removed from the beam envelope and the beam expands rapidly due to the positive space charge. The problem thus involves designing a system that provides for workpiece manipulation in front of a stationary ion beam and the end station design becomes the most important issue.

As stated above, two of the most promising applications of ion implantation for DOD applications are gearbox and gas turbine aircraft bearings and beryllium instrument bearings. Research at other laboratories has shown another major application to be implantation of various cobalt-cemented tungsten carbide tools with nitrogen to reduce wear and increase lifetime of the tools [3]. These three types of components were selected to demonstrate ion implantation technology in the ManTech project. Because of their widely variant and, in some cases, complex geometries, these components provide representative problems on which to develop the methodology for ion implantation. The geometries include spheres, cylinders, and inner and outer races for the aircraft bearings, very small cylinders and flats for the instrument bearings and disks and flats for the tools.

The ManTech project has been divided into three phases with the current schedule calling for completion of Phase I in July 1984, Phase II in January or February 1985 and Phase III in January or February 1986. The objectives in the first phase were the design of apparatus to perform the function of cooling the workpieces during implantation and manipulating the workpieces with respect to the beam, and the design of the vacuum enclosure and pumping system for the end station. Design requirements called for the capability of implanting ball bearing elements 0.25–2.5 cm in diameter, cylindrical roller bearing elements 0.2–2 cm in diameter and 0.7–7 cm long, bearing races 3–30 cm in diameter and 0.8–8 cm wide, and disks up to a *maximum* 25 cm in diameter and 6 cm thick. A maximum workpiece temperature rise of 200°C was specified for the design to enable implantation of bearing steels such as 52100 which are sensitive to annealing and overaging of the precipitate structure with attendant loss of hardness. Also in Phase I a contract will be let for the manufacture of a high-current ion implanter to be delivered at the beginning of the third phase.

The objectives in the second phase are to fabricate the apparatus designed in Phase I and to prepare the site for the implantation facility. In both Phases I and II, NRL is conducting research to determine optimum implantation conditions for the bearings and Spire Corporation is conducting research to determine optimum implantation conditions for a tungsten carbide stamping tool for chain link drives. Phase III objectives are to install and test the implanter and workpiece handling apparatus, operate and maintain the facility for ten months to demonstrate the use of ion implantation for these types of materials under prototype production line conditions, and to evaluate the implanted bearings and tungsten carbide tools and document improvements in performance.

3. Design issues – heat conduction

Among the design issues to be dealt with in a high current implantation facility, heat input from the beam and the maintenance of low substrate temperatures represent one of the most difficult problems. A typical commercial implanter with a beam current density of 3 mA/cm^2 accelerated to 100 kV produces a heat load of 300 W/cm^2 on the surface. Grabowski and Kant [4] have analyzed various methods to control target heating during ion implantation. They found radiation cooling in a vacuum to be totally inadequate for the heat inputs to be encountered in high current implantation facilities. Three regimes of conduction cooling were analyzed: (I) heat diffusion limited, (II) heat capacity limited and (III) steady state conduction to a heat sink. For most implantation doses and workpiece sizes considered, heat capacity alone is insufficient to cool the target. For example, implantation of 100 kV ions to 1 × 10^{17}/cm^2 into a carbon steel will produce a uniform temperature rise of about 460°C in targets consisting of a 1 cm thick plate or a 4 cm diameter cylinder. Thus, conduction to a heat sink is essential.

The steady state heat flux out of a plate target secured to an ideal heat sink is described by the equation

$$H_0 = k(T_w - T_s)/l, \qquad (1)$$

where H_0 is heat flux, k is the thermal conductivity (0.21 W/cm·K for M2 tool steel), T_w is workpiece temperature (assumed to be 200°C), T_s is temperature of the heat sink, and l is the workpiece thickness. For $l = 1$ cm and $T_s = 25$°C, then the maximum heat removal is 37 W/cm^2 which would require a contact area of 27 cm^2 for a 10 mA 100 keV beam incident on the workpiece. However, ideal conditions are not realized for contacts across an interface in a vacuum. The heat flux across an interface is given by

$$H_{0c} = (T_w - T_s)h_c, \qquad (2)$$

where h_c is the interface contact conductance. Using h_c equal to 0.05 W/cm^{2}K as representative of steel contacting steel in vacuum [4], then the maximum heat removal is 8.7 W/cm^2, requiring a total contact area of 115 cm^2. While this is not unreasonable for the implantation of several flat workpieces, it presents an insurmountable problem for spheres and cylinders where the contact area per component can range from 0.01 to 0.1 cm^2.

Even if one were able to overcome the thermal conductivity problem so as to maintain the workpiece temperature at 175°C, for example, there still would be the problem of the heat-diffusion-limited surface temperature rise. The magnitude of the problem is illustrated in fig. 1 for several heat flux inputs on a carbon steel target. For a 300 W/cm^2 beam and a workpiece already at 175°C, it would require only 0.03 s for the
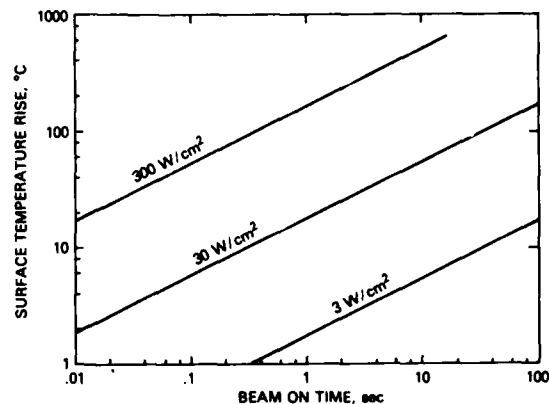

Fig. 1. Absolute surface temperature rise as a function of time an ion beam is incident on a carbon steel substrate for three input power densities.

surface temperature to rise an additional 25°C and exceed the specified 200°C maximum. This requires that the workpiece be translated at a velocity of at least 33 cm/s which implies additional design problems. Thus heat removal becomes a major constraint on the implantation facility design and leads to the fundamental insight that a high current implanter must spread the beam to reduce the power density to acceptable levels and therefore must operate in a batch mode rather than a piece by piece mode. This concept is the basis of the winning Spire Corporation design which uses a magnetic quadrupole lens to spread the beam from the implanter up to a maximum 15" diameter. The design was further optimized by using a high conductivity elastomer to increase the contact conductivity over that existing for vacuum interface conditions and to increase the contact area under load which is especially critical for curved surfaces.

4. Design issues – changes in retained dose with angle of incidence of beam

A major consideration in implantation processing is knowledge of and reproducibility of the implant concentration profile. While analytical methods such as Auger profiling and RBS are available to establish the profile experimentally it will not be feasible to analyze every implant condition and it is therefore necessary to have a theoretical understanding of the factors which influence the final concentration profile so that they can be predicted with confidence.

Grabowski et al. [5] have examined the problem of retained ions under conditions of non-normal incidence of the beam. The concentration profile at normal incidence is determined by the range (R_p) and straggling

(σ) of the implanted ions in a given substrate, the sputtering yield (S) and the total fluence (ϕ). Fig. 2 shows the evolution of an implantation profile with increasing fluence where F_{ion} is the atomic fraction of ions in the target and ω is the thickness of material sputtered off ($S\phi/N$) relative to R_p after an implantation fluence ϕ. N is the constant target atomic density. This figure was calculated for implantations with $R_p/\sigma = \sqrt{2}$ which is representative of the ranges and straggling for metal ions in steel targets.

The retained dose is dependent on the angle of incidence of the ion beam as shown by theoretical and experimental analysis of a stationary cylinder. At low fluences, where sputtering does not affect the results, the retained dose is simply related to the larger area intersected by the beam and

$$D_0 = \phi_0 \cos\theta, \tag{3}$$

where D_0 is retained dose, ϕ_0 is the fluence at normal incidence and θ is the deviation from normal incidence. In the high fluence limit the implant concentration profile follows the form of fig. 2. At steady state the atom fraction at the surface is independent of θ and approaches $1/S$. The depth of penetration below the surface is affected by the angle of incidence as $X = R_p \cos\theta$. Following Sigmund's model for the angular dependence of sputtering $S = S_0\cos^f\theta$ where S_0 is the sputtering yield at normal incidence and $f = 5/3$ for ions of nearly equal mass and in the intermediate mass range in the periodic table. The retained dose at steady state is therefore found to have the angular dependence

$$D = \frac{NR_p}{S_0}(\cos\theta)^m. \tag{4}$$

Because implant fluences for processing components for the ManTech program are expected to be in the $(1-5) \times 10^{17}/\text{cm}^2$ range, experiments were conducted in the high-fluence limit. Fig. 3 shows the retention of various ions normalized to unity at θ = 0°. All fluences were selected to produce a steady-state distribution in the target. Generally the agreement between theory and experiment is excellent. The discrepancy for Ti-implanted 304 stainless steel at 60° was believed to be due to experimental uncertainity. The discrepancy for Ta-implanted M50 is believed to be a real effect caused by preferential removal of iron combined with ion mixing. In general, the rapid decrease in retained dose at non-normal angles of incidence makes it advisable to limit the angle of incidence of the beam on the sample. The exact angle selected depends on the trade-off between inefficient use of the beam and loss of implanted ions with increased sputtering at high angles of incidence.
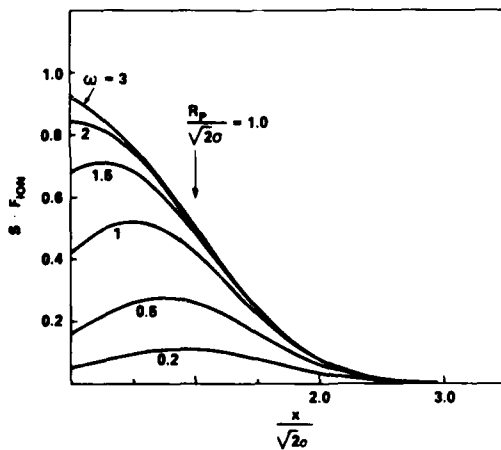

Fig. 2. Calculated values for the evolution of the implanted ion concentration profile with increasing fluence for the case of $R_p/\sigma = \sqrt{2}$. ω is the amount of material sputtered away relative to the projected range, R_p.
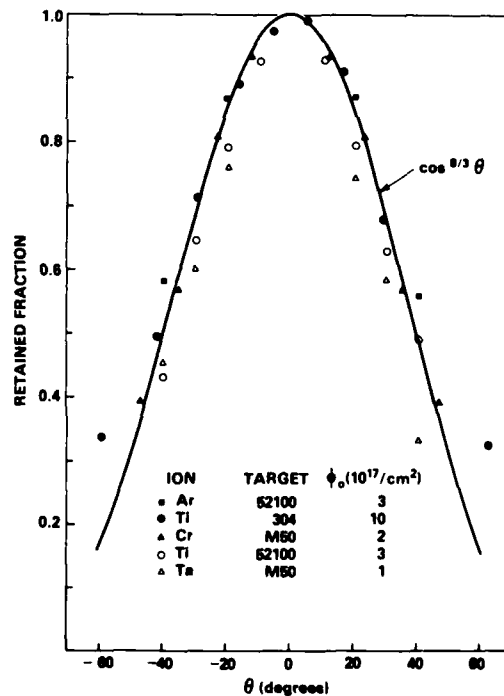

Fig. 3. Normalized retained dose in the high-dose limit (i.e., steady state distribution of implanted element in the substrate) obtained from simplified theory and from measurements on steel cylinder. Ion energy was 150 keV in all cases. Data points at normal incidence were not plotted.

I. IMPLANTATION SYSTEMS

13

5. Design issues – implantation into rotating cylinder

A computer code has been developed to predict the effect of masking a cylindrical sample for various included angles of incidence on the concentration profile of the implanted workpiece while the workpiece is being rotated [6]. Fig. 4 shows the general case in the low-fluence limit where sputtering effects are negligible. The total dose implanted into the specimen was the same for all curves. Although only four curves are shown in the figure, they were generated at 10° increments to provide a complete picture of the change in shape of the profile as a function of the included angle as determined by the beam defining aperture. The most probable depth shifted toward the surface only up to θ = 30°. Above 30°, the most probable depth remained relatively constant, with the principal change being the tail of the distribution moving toward the surface. At very high angles (75°–90°) the tail is due to an increased probability of scattering of the ion beam from the surface. The mean depth of the implanted ions decreased as cos θ. A more complex code to include the effects of sputtering is under development.

6. Design issues – prediction of composition profiles

Another factor which must be taken into account in calculating concentration depth profiles is the volume change produced by the implanted ions. A computer code called IMPLNT has been developed at NRL to calculate composition profiles for any combination of implanted ion and substrate [7]. The calculation is iterative and takes into account changes in range and

straggling due to changes in target composition, changes in sputtering yield with composition, and volume increase in the target due to the implanted ions. The effect of angle of incidence on the profile has yet to be incorporated. An example of IMPLNT calculations of 100 keV Cr implanted into Fe for several fluences is shown in fig. 5.

7. Design issues – effects of residual gases in target chamber

Another processing variable which had not been explored in adequate detail was the effect of residual gases in the implantation chamber on both surface reactions and the composition of the implanted layer. In cases such as the implantation of Ti or Ta into steels, the reaction of carbon-containing gases in the chamber with the specimen surface during ion implantation can produce a low friction wear resistant layer with beneficial properties. In other cases the formation of surface carbides on M50 steel implanted with Cr for corrosion resistance may degrade the corrosion protection [8]. Singer [9] has shown that for the case of titanium implantation into steels a carburization process takes place whereby (a) sputtering uncovers previously implanted titanium at the surface, (b) carbon containing molecules are adsorbed onto the surface, and then dissociate, (c) the carbon atoms bond to the surface titanium, and (d) the carbon is transported below the surface through a diffusion mechanism probably enhanced by the defects produced during implantation. The concentration of titanium at the surface appears to
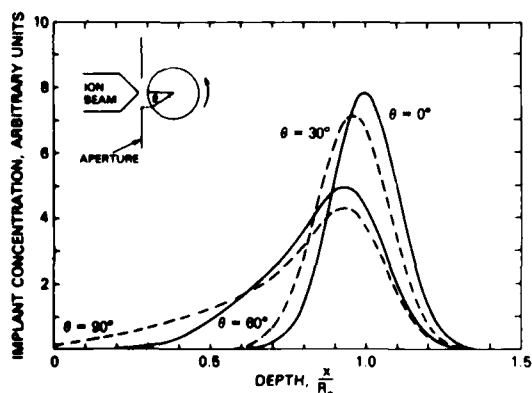
Fig. 4. Relative implant concentration as a function of depth for the case of B ion beam incident on a rotating cylinder of Be in which an aperture is used to limit the included angles of incidence. θ represents the maximum angle of incidence. R_p/σ = 7.0 for the case illustrated.
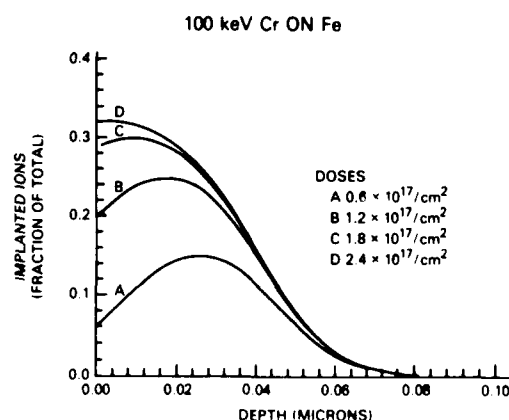
Fig. 5. Theoretical concentration vs depth profiles for 100 keV Cr⁺ on iron at normal incidence for several doses, taking into account sputtering, changes in range and straggling due to changes in target composition, and the volume increase in the target due to the implanted atoms.

14
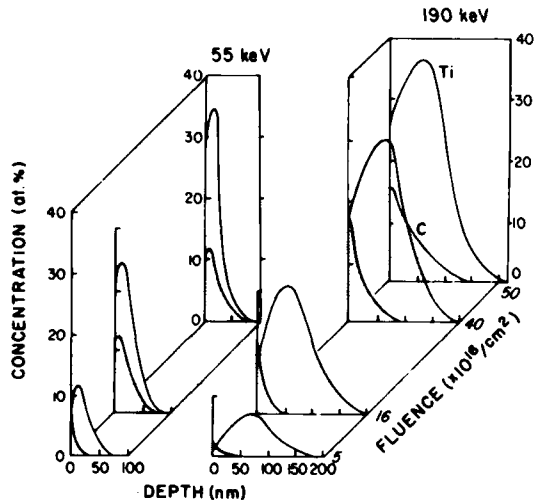
Fig. 6. Concentrations vs depth profiles for Ti and C in Ti-implanted 52100 steel at several fluences and energies; (left) 5, 16, and 40 × 10^{16} Ti$^+$/cm^2 at 55 kV; (right) 5, 16, 40, and 50 × 10^{16} Ti$^+$/cm^2 at 190 kV. Note: bulk C concentration of the steel (4 at.%) was subtracted from data.

be an important variable as shown in fig. 6 where Ti and C profiles for 55 and 190 keV implants into 52100 steel are compared as a function of fluence.

Singer and Barlak [10] proved that the carburization process was the result of interaction with the chamber atmosphere and not outdiffusion of C from the bulk by implanting at a pressure of 10^{-6} Torr of CO that was enriched with the ^{13}C isotope. SIMS analysis of the surface clearly showed the ^{13}C profile had the diffusion-like shape previously observed.

Experiments were recently conducted to further investigate this phenomenon by attaching a UHV chamber containing a CMA Auger analyzer to the ion implanter and performing in situ Auger analysis of the sample surface during implantation. Fig. 7a shows the uncorrected Auger peak heights as a function of titanium implant fluence for an implant performed in ultra-high vacuum (1 × 10^{-8} Torr) and with the target chamber backfilled to a pressure of 7 × 10^{-7} Torr of CO. Fig. 7b shows a subsequent depth profile of the implanted layer obtained by sputtering with 4.0 keV argon ions. Important observations are that the carbon and oxygen concentrations on the surface are both high in the CO atmosphere during the implantation but that only carbon diffuses below the surface. This indicates that recoil implantation is not a major contributor to the transport process. The data also indicates that it takes a higher fluence to reach a steady state titanium surface concentration for the implant in CO. Applying elemental sensitivity factors to the Auger peak heights showed that the retained dose of titanium was approx-
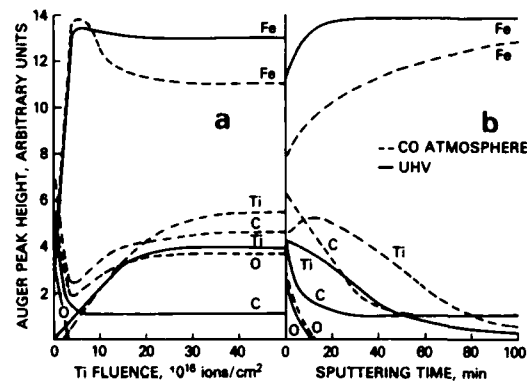

Fig. 7. (a) Auger peak height as a function of 150 keV Ti$^+$ fluence for implantation into a polished M50 substrate in ultra-high-vacuum conditions (1 × 10^{-8} Torr) and with the target chamber backfilled to 7 × 10^{-7} Torr with CO. (b) Auger depth profile of the implanted layers obtained by sputtering with 4.0 kV argon ions.

imately 30% higher for the implant performed in CO. This is believed to be caused by a reduction in the sputtering yield of the titanium due to the formation of the carburized layer. More detailed studies of these effects for pure iron substrates have recently been reported by Baldwin and Sartwell [11]. It has been concluded that control of vacuum conditions in the Man-Tech end station will be essential in order to have reproducibility among the various components to be implanted and to prevent the formation of undesired compounds (such as carbides) at the surface.

8. Throughput and operating costs of ManTech facility

Several estimates have been made of throughput for the ManTech implantation facility to project capacity and cost. The theoretical maximum throughput for an ion implanter with a 10 mA beam and a goal fluence of 2 × 10^{17} ions/cm^2 is 1125 cm^2/h. However, this cannot be achieved because of the various considerations discussed in the previous sections. An empirical expression for throughput τ is

$$\tau = (\tau_0)(F_t)(F_b)(F_v) \tag{5}$$

where τ_0 is the theoretical maximum and F_t, F_b, and F_v are factors related to thermal constraints, beam utilization, and vacuum pumpdown. If the ion beam current must be reduced to permit adequate workpiece cooling, then F_t will be less than 1. If sputtering requires that the angle of incidence of the ion beam must be restricted, then some percentage of the ion beam will be incident on masks instead of the workpieces and this is reflected in factor F_b. The factor F_v takes into account

I. IMPLANTATION SYSTEMS

how much time is spent pumping down the target chamber compared to actual processing time. For the ManTech end station designed by Spire, for spherical and flat geometry workpieces, respectively, $F_t = 1.0$ and 1.0, $F_b = 0.2$ and 0.9, and $F_v = 0.95$ and 0.95. This results in a total throughput for balls of 214 cm²/h and for flats of 951 cm²/h. Applying a similar analysis to a proposed piece-by-piece design resulted in throughputs of 43 and 95 cm²/h. These lower values were principally due to constraints imposed by the need to reduce the beam current so as to achieve adequate cooling of the workpieces.

An estimate of the operating cost for the facility has been made assuming an amortization of a $1M cost over 10 years for a capital cost of $100K per year. Total costs are shown in table 1 for 1, 2 and 3 shift operation for reasonable estimates of manpower and operating supplies. As can be seen the breakeven costs for operating the implanter range from $108/h to $136/h, and treatment costs for ball bearings range from 50–64 cents/cm² and for flat specimens from 11–14 cents/cm². These costs appear quite reasonable for expensive components like aircraft bearings which may cost as much as $1500 a piece. These costs can undoubtedly be reduced as dedicated facilities with single-purpose tooling and simplified ion optics are developed.

The cost estimate for the Navy MANTECH implantation facility can be compared with a similar estimate made for the Harwell facility [3] for implantation of components with N ions to a fluence of 1×10^{17} ions/cm². If allowance is made for the two fold increase in throughput because of the lower goal fluence and the

assumption of 100% utilization factor in the Harwell estimate, then the costs are comparable.

Estimates of cost savings for ion implantation of gas turbine bearings and a stamping die show an excellent payback from the processing. For example, a T64 #0 bearing costs $289 a piece and commonly 50% are rejected on inspection of bearings during overhauls. Occasionally a corrosion pit initiates a fatigue crack which leads to a costly overhaul ($100K). It is estimated that a bearing can be implanted in lot quantities for a cost of $52. If the elimination of corrosion increases the life expectancy by a factor of 2.5 and eliminates a 2% rate of unscheduled maintenance a cost saving of $1620/bearing can be realized. In the case of the stamping die, a die costs $5000 and lasts for about 24 h. Implantation with N at a cost of $110 should increase the life six-fold and also reduce costly down time. A cost saving per die implanted is estimated to be about $8000.

9. Conclusions

A manufacturing technology program on ion implantation is being conducted by the Naval Research Laboratory to develop a prototype production facility for various types of aircraft and instrument bearings, and stamping and forming tools. Analysis of processing parameters related to heat conduction and sputtering indicate that a diffuse-beam, batch process must be utilized and that the angle of incidence of the ion beam must be limited. Vacuum conditions must be carefully controlled to ensure reproducibility and the elimination of undesired surface contamination. Initial estimates of cost savings on several demonstration components are shown to be quite favorable.

Table 1
Estimate of the operating costs for the ManTech ion implantation facility assuming amortization of a $1M cost over 10 years

	1 shift	2 shifts	3 shifts
Capital investment[a]	$100K	$100K	$100K
Full time operator	$ 70K	$175K[d]	$280K[d]
Management	$ 30K	$ 60K	$ 90K
Utilities, consumables	$ 25K	$ 50K	$ 75K
Maintenance support	$ 20K	$ 30K	$ 40K
Total annual cost	$245K	$415K	$585K
Hourly cost[b]	$136/h	$115/h	$108/h
Throughput costs[c]			
Balls	$0.64/cm²	$0.54/cm²	$0.50/cm²
Flats	$0.14/cm²	$0.12/cm²	$0.11/cm²

[a] $1M/10 years = $100K/year.
[b] 2000 h shift year at 0.9 availability = 1800 h.
[c] 2×10^{17} ions/cm², 10 mA.
[d] Assume time and one half for shift work.

References

[1] D. Popgoshev, R. Valori and G.K. Hubler, ASME J. Lubrication Technol. 105 (1983) 534.

[2] R.A. Kant, A.R. Knudson and K. Kumar, in Metastable material formation by ion implantation, eds., S.T. Picraux and W.J. Choyke (Elsevier Science, New York, 1982) p. 253.

[3] S.J.B. Charter, L.R. Thompson and G. Dearnaley, Thin Solid Films 84 (1981) 335.

[4] K.S. Grabowski and R.A. Kant, in Ion implantation: equipment and techniques, eds., H. Ryssal and H. Glawishnig (Springer, New York, 1983) p. 364.

[5] K.S. Grabowski, N.E.W. Hartley, C.R. Gossett and I. Manning, in Ion implantation and ion beam processing of materials, eds., G.K. Hubler, O.W. Holland, C.R. Clayton and C.W. White, in press.

[6] I. Manning and R.A. Kant, Naval Research Laboratory, unpublished research (1984).

[7] C. Davisson, unpublished research (1984).

[8] W.K. Chan, C.R. Clayton and J.K. Hirvonen, in Corrosion of metals processed by directed energy beams, eds., C.R. Clayton and C.M. Preese (AIME, Warrendale, PA, 1982) p. 91.

[9] I.L. Singer, J. Vac. Sci. Technol. A1 (1983) 419.

[10] I.L. Singer and T.M. Barlak, Appl. Phys. Lett. 43 (1983) 457.

[11] D. Baldwin and B.D. Sartwell, Proc. Conf. on ion beam modification of materials, Cornell (1984), to be published in Nucl. Instr. and Meth. B.

I. IMPLANTATION SYSTEMS

Section I.B

A HIGH THROUGHPUT METAL ION IMPLANTER END STATION

A.J. Armini and S.N. Bunker

Spire Corporation
Patriots Park
Bedford, MA   01730

214

A HIGH THROUGHPUT METAL ION IMPLANTER END STATION

A.J. ARMINI and S.N. BUNKER

Spire Corporation, Patriots Park, Bedford, Massachusetts 01730, USA

Research in the implantation of metal ions has been shown to produce improved surface properties for a wide variety of ion species and materials. Except for the case of gaseous source materials, such as nitrogen, little attempt has been made to advance the technology to pilot production levels of implanted parts. A system is described in which a specially designed end station is combined with a commercial mass-analyzed, high current ion implanter (10 mA beam). The goal is to produce a high throughput system optimized for ions such as chromium, which has proved valuable in providing corrosion resistance to bearings.

1. Introduction

A considerable number of scientific papers in the past ten years have investigated the beneficial effects of ion implantation of metal tools and parts [1–3]. Most of this work was performed using implantation equipment orginally designed for the semiconductor industry.

In 1983, the Naval Research Laboratory initiated a Manufacturing Technology (MANTECH) program to build and operate a facility which will demonstrate to industry that this technology is ready for commercial utilization. The program consists of two parts. The first is performed by the Naval Research Laboratory to test and evaluate implanted military ball bearings under actual field conditions [1,2]. The second part, the design, construction and operation of a pilot production implantation facility, is being performed by Spire Corporation.

The benefits of ion implantation have been examined by numerous researchers. The materials and ion beams used vary widely and the test data is voluminous. In the MANTECH program, however, NRL has selected two specific processes which have been the subject of a sufficient number of experiments to indicate that near-term commercialization is highly probable.

The first process is the implantation of M50 ball bearings with chromium ions for improved corrosion resistance [1]. The second process is the implantation of cobalt-cemented tungsten carbide stamping or punching tools with nitrogen ions [4].

2. Facility description

The facility consist of a high-current commercial semiconductor implanter and a custom designed high throughput end station for metal parts. The implanter
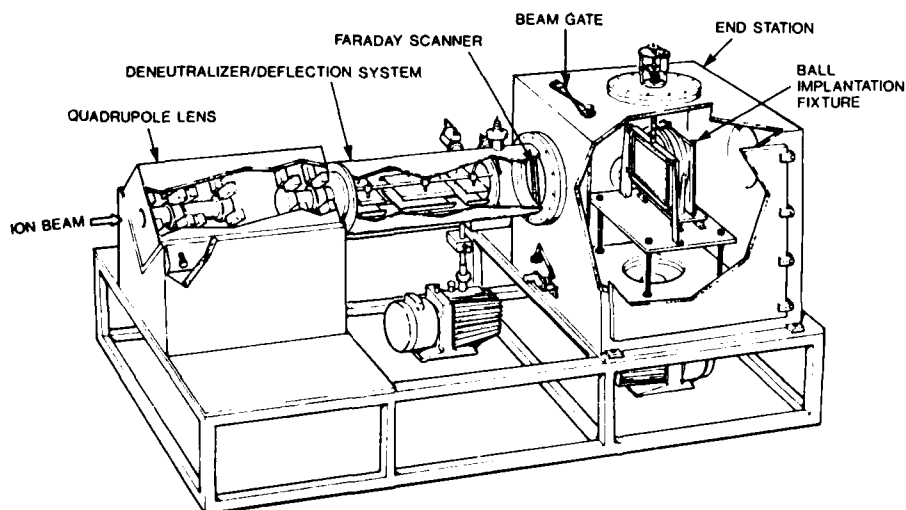

Fig. 1. Design of implanter end station used for implantation of metals into bearings.

will be capable of generating any practical ion species with particular emphasis on nitrogen (10 mA) and chromium (3 mA). This ion beam is then injected ir.) the high throughput end station as shown in fig. 1.

The beam first enters a specially designed three lens magnetic quadrupole which transforms the beam from a 0.8 cm by 2.8 cm rectangle to variously shaped broad beams up to 40 cm in diameter. The lens is thus capable of creating line beams, elliptical beams, and small spot beams on the workpiece.

The chamber following the quadrupole is an electrostatic "deneutralizer". This device intentionally destroys the space charge neutralization provided by electrons within the beam envelope, thus enabling the beam to expand due to internal charge repulsion. Local concentrations in the beam intensity will expand more than the surrounding beam, which has the effect of improving the uniformity through a cross section of the beam.

The deneutralizer plates may also be used for steering the beam spot in the conventional manner. A horizontal strip beam can be formed by the quadrupole lens and then moved perpendicularly by the plates to produce a rectangular spot or to successively dwell on individual rows of parts. The latter spreads the thermal load and improves the beam utilization efficiency. It is also possible for the beam to move on one axis to follow the motion of a moving workpiece-holding fixture.

The expansion of the local beam inhomogeneities is approximated by the expression for a strip beam [5]

$$y_f = y_i + 4.1 \times 10^6 \cdot J \cdot \sqrt{A} \cdot z^2 \cdot y_i/V^{3/2},$$

where y_i, y_f are the initial and final beam widths. J is the current density in A/cm^2, V is the beam energy in eV, A is the mass number, and z is the length of the

deneutralized zone. As an example, if one assumes that 10% of the 3 mA chromium beam is clustered in a small spot 0.5 cm square, then this spot will be expanded to a circle 55% larger in diameter than would be produced by the lens, effectively eliminating the concentration.

A first order version of the TRANSPORT program [6] has been modified to include the effects of the space charge deneutralization. This code uses successive step approximations to account for the non-linear aspects of the expansion equation. Fig. 2 shows a sample ion beam transport calculation. The upper half of the figure is the beam profile in the horizontal plane and the lower half is for the vertical plane Quadrupole lenses and the deneutralizing plates are marked. This particular profile shows the transport for a horizontal strip beam, which is a long ellipse 4 cm high by 44 cm wide. The three lenses are required to avoid trapezoidal beam profiles, as shown in fig. 2.

The end station is a large 0.68 m^3 vacuum chamber which is capable of supporting a wide variety of workpieces and their handling fixtures. Interchangeable ports are provided to simplify mounting of each fixture as shown in fig. 1. A sapphire window for pyrometer measurements is provided near the beam entrance. A rectangular, ribbed box was selected to maintain generality and ease of installing future types of fixturing that may be required during the operational phase of the program. A large area door permits easy access to the entire volume.

Vacuum is provided by a 10" cryopump, which is estimated to reach a base pressure of 1×10^{-6} Torr in about 40 min, depending on the fixturing used. Care has been taken to avoid the use of organics and high outgassing materials in the high vacuum in order to maintain a "clean" environment. Support systems
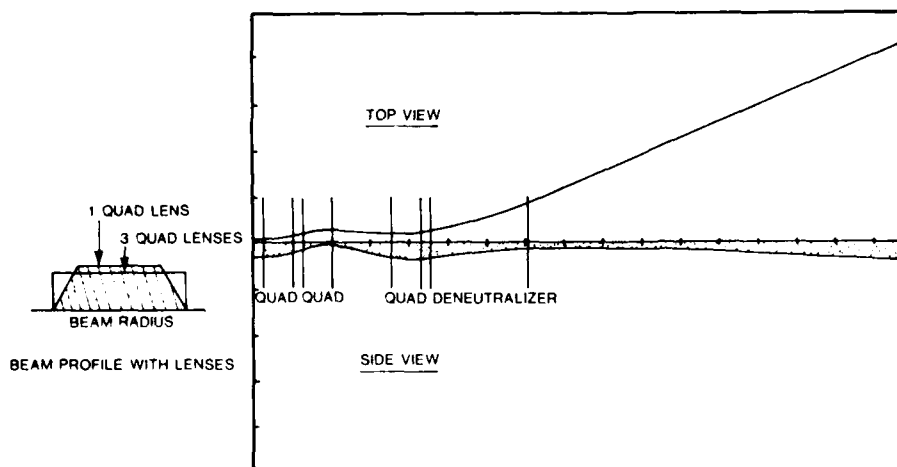

Fig. 2. Ion beam envelope through the MANTECH end station which results in a circular beam spot at the workpiece.

which could be gassy (such as motors and insulated wires) are encased in separate vacuum-tight enclosures.

3. Implantation specifications and fixtures

The primary emphasis of the MANTECH program is on the chrome implantation of special high performance bearings to reduce corrosion in marine environments. Most of the workpiece fixturing is thus specialized for this purpose and is designed to handle large numbers of small, round objects. Both roller and spherical bearings are to be implanted, each with its own unique requirements. Specifications are given in table 1.

Spherical balls are particularly difficult to adequately cool during implantation due to the low surface area in contact with a heat sink. In addition, the 15% uniformity requirement with a 30° incident angle limit affects throughput and requires novel fixturing to expose all the surface to the beam. The method adopted is to roll the balls on a cold conductive rubber surface which is covered with a nickel foil to prevent contamination. The rolling motion is achieved using uncoupled and uncorrelated X/Y linear drive mechanisms. The ball is assumed to have relatively large friction contact with the foil compared to any other surface. Attached to one drive is a "cage" holding the ball. The perpendicular drive is the cold surface.

The point on the surface of the ball that is directly under the ion beam has been mapped on a sinusoidal equal area projection of the ball's surface, which is

shown in fig. 3. A computer program generated the plot which represents hundreds of oscillations of the X/Y rolling drives. When the distribution is averaged over the circular area, which is the size of the beam spot on the sphere, a highly uniform implant distribution is produced.

Cooling is provided using the layered structure shown in fig. 4. The nickel foil, which is disposable, isolates the balls from the cooled, conductive rubber surface. The foil readily deforms to the contour of the ball pressed into the rubber, providing a large surface area of contact and acting as a grounding surface. Tests have shown considerable resistance to breakage of the foil over hundreds of rolling oscillations. The M50 steel balls are forced into the foil/rubber by an axial magnetic field. The field eliminates the need for precision tolerences between the X/Y drives, excessive forces on

Table 1
General implant specifications

1. Implant energy 120 keV
2. Ion beam is Cr^+, mass analyzed
3. Dose is typically 2×10^{17} ions/cm^2
4. Ambient vacuum better than 1×10^{-6} Torr
5. Surface temperature less than 250°C
6. Maximum angle of incidence relative to normal is 30°
7. Implant uniformity better than 15%
8. Pilot production level throughput
9. Parts handling in a laminar flow bench
10. Surface cleaning specification
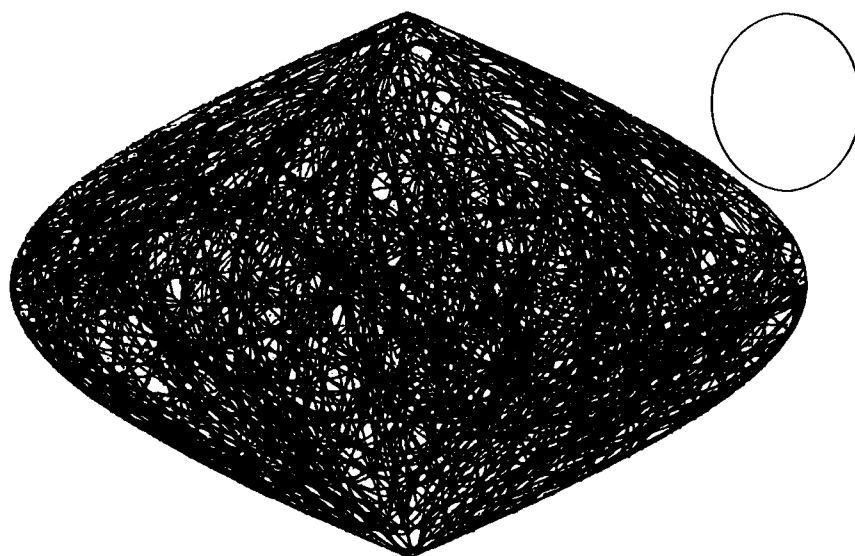11. No fixture materials that deposit contaminating films

Fig. 3. Calculation of implantation uniformity on a sphere using perpendicular rolling motions. The lines show the path of the ion beam on the surface which is drawn on an equal area sinusoidal projection. Good uniformity is produced over the entire surface.
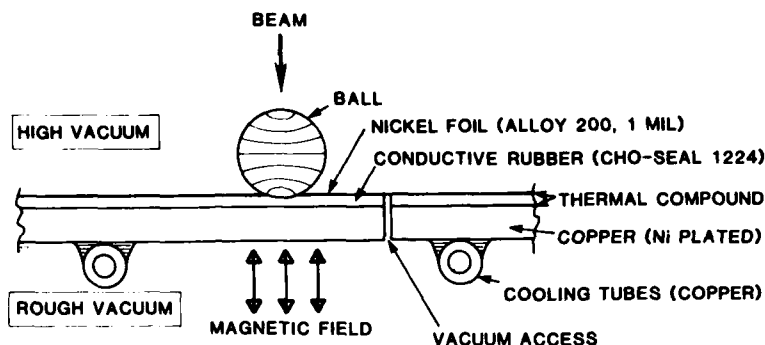
Fig. 4. Ball cooling system which uses a deformable rubber to increase surface contact area. The rubber is covered by a ductile nickel foil to preserve a clean interface to the ball.

the thin ball cages, and gravity-dependent fixturing. A residual magnetic field is naturally induced in the balls despite the constant change of axes. This is eliminated by operating the magnet with an a.c. field to degauss the balls prior to removal from vacuum. Cooling of the ball depends on the magnetic field strength and the diameter of the balls. For a large, 22.2 mm sphere, a heat load of 6 W/cm^2 can be supported and still remain within the thermal specification.

The ball cage is used to transport, mount, and roll the balls. In order to meet the 30° incident angle requirement, dual tantalum foil masks are provided for each ball. The mask is constructed in the manner shown in fig. 5. A large aperature Ta foil overlay absorbs most of the energy and shields the clamping plate from sputtering. The primary 0.1 mm thick mask is clamped for cooling. The thin foil produces minimal slit edge sputtering, has the low expansion coefficient of 6.5 × 10^{-6}/°C to prevent warping, has a low sputter coefficient, and has sputtered products that are not considered harmful to M50 steel [7]. Roller cages are very similar to the ball cage concepts with the exception that only one axis of movement is required.

The outside races are implanted using a large area, elliptical beam spot illuminating a rotating platter as shown in fig. 6. The outside races are tantalum-foil masked, and the angle of the platter with respect to the beam is typically 15–30°, depending on race dimensions. The mask produces an elliptical-shaped illuminated spot, and the rotation of the platter scans the spot around the inside circumference of the bearing surface. Cooling is provided by the cold surface of the platter, which is coupled to the workpiece through a deformable soft foil. Cooling capacity is quite high due to the large surface area of contact, low flux density, and 17% heating duty factor.

The inside races can be implanted most efficiently in a long rotating row. The beam spot is a narrow rectangle. Beam utilization is 37% for the selected roller

bearing races, but this factor will vary depending on the race geometry. The utilization factor, in this case, is approximatey the ratio of the roller length to race thickness. Tantalum masks are used to isolate the 30° zone and shield the races from the excess heat load.
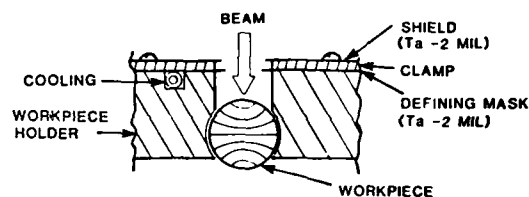
Fig. 5. Collimator mask designed to minimize edge sputtering onto workpiece with thin foils.
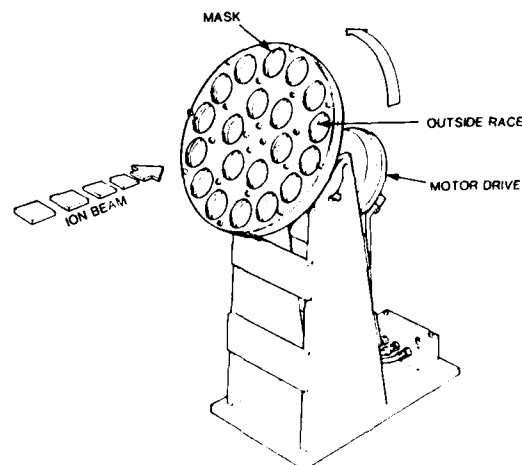
Fig. 6. Fixture designed to ion implant outside bearing races using a rotating, cooled platter.

IV. IMPLANTER COMPONENTS / END STATIONS

Table 2
Projected end station specifications

Vacuum chamber	
Size	$0.9 \times 0.9 \times 0.75 \, m^3$
Pumpdown time (to 1×10^{-6} Torr)	40 min
Vent time	0.9 min

Ion beam		
Beam current	N^+	10 mA
	Cr^+	3 mA
Beam energy		120 keV (max)
Spot size		variable shape to
		40 cm diameter
Uniformity over 30 cm diameter		± 10%

Table 3
Throughput for bearing components

Part	Dimensions	Units/ hour	Beam utiliza- tion (%)
Ball	22.2 mm diameter	4.9	24
Roller (curved (surface)	4.8 × 4.8 mm diameter	73	48
Roller flats	4.8 mm diameter	925	51
Outside race (roller)	47 mm i.d.	8.8	24
Inside race (roller)	37.4 mm o.d.	22	37

4. Projected performance summary

The production philosophy is to use large batches with long implant cycles to minimize the effect of chamber pumpdown and loading overhead. In addition, beam heating is lower, thus minimizing cooling requirements. Some parts, for example tungsten carbide punches, require no special cooling setup. The projected specifications of the system are shown in table 2. The projected throughputs for selected parts are shown in table 3.

References

[1] Y.F. Wang et al., Thin Solid Films 63 (1979) 11.
[2] G.K. Hubler et al., J. Lub. Technol. 105 (1983) 539.
[3] G. Dearnaley et al., Thin Solid Films 54 (1978) 215.
[4] Zie Zhong-Yin et al., 3rd Int. Conf. on Modification of surface properties by ion implantation, Manchester, UK (1981). p. 117
[5] T.S. Green, Rep. Progr. Phys. 37 (1974) 1257.
[6] K.L. Brown, SLAC Report #75 (1967).
[7] B. Sartwell, NRL, private communication.

Section I.C.

ADHERENT TiN FILMS PRODUCED BY ION BEAM ENHANCED DEPOSITION
AT ROOM TEMPERATURE

R.A. Kant and B.D. Sartwell[1]
I.L. Singer[2]
R.G. Vardiman[3]

[1]Materials Modification & Analysis Branch
Condensed Matter & Radiation Sciences Division
Naval Research Laboratory

[2]Surface Chemistry Branch
Chemistry Division
Naval Research Laboratory

[3]Physical Metallurgy Branch
Material Science and Technology Division
Naval Research Laboratory

25

ADHERENT TiN FILMS PRODUCED BY ION BEAM ENHANCED DEPOSITION AT ROOM TEMPERATURE

R.A. KANT, B.D. SARTWELL, I.L. SINGER and R.G. VARDIMAN

Naval Research Laboratory, Washington, D.C. 20375, USA

This paper describes the preliminary results of an investigation of the influence of ion implantation on the structure and mechanical properties of vapor-deposited thin films which are implanted during nucleation and growth. For these studies, titanium was deposited at room temperature on M50 steel, AISI 52100 steel, and silicon substrates in a chamber backfilled with nitrogen gas to a pressure of 1×10^{-5} Torr. The films were deposited in 125 or more increments of 0.8 nm each. Between each increment, the film was implanted with 30 keV N_2^+. Auger electron spectroscopy revealed that significant reduction of carbon and oxygen occurred in the implanted films and electron microscopy showed the films to be entirely fcc with a lattice constant consistent with that of TiN. The mechanical properties of the films were investigated using scratch tests for adhesion as well as friction and wear analysis. While the unimplanted films failed to adhere, the implanted films remained adherent throughout the tests and exhibited both low friction and low wear.

1. Introduction

The influence of ion implantation on the structure and properties of thin films which are implanted during deposition is being investigated using Auger electron spectroscopy, electron microscopy and mechanical testing. While it has been shown that significant improvements of film properties can be obtained if low energy (1 keV) ion bombardment is used during film nucleation and growth, the mechanisms responsible for the improvements are not fully understood. The film modifications reported for low energy ion beam assisted deposition include (1) increased adhesion and film uniformity, (2) alteration of internal stress and (3) production of phases and film morphologies at lower temperatures than would otherwise be required [1–3]. Although it is generally believed that the energy deposited by the ion beam plays a significant role in promoting these modifications, a detailed understanding requires further study. The goals of the present study are (1) to characterize the influence of higher energy ion beams on films implanted during the coating process, (2) to investigate the compositional changes, and (3) to characterize the effects on the mechanical properties. For this investigation, electron beam evaporated titanium was deposited at room temperature in a nitrogen gas environment in an attempt to form wear resistant and adherent films of TiN. Totally independent control of the titanium deposition rate and the N-implantation rate was achieved by periodically rotating the specimen away from the titanium vapor stream after a small amount of titanium had been deposited, implanting it with a correspondingly small dose of N_2^+ and then moving it back into position for further deposition. Using this technique, films approximately 100 nm thick were grown in 125 deposition/implantation steps.

2. Experimental details

For these treatments, a sample is positioned in the center of a chamber 30 cm above an electron beam evaporator and is rotated about a horizontal axis in order to expose it to either the evaporant from below or the ion beam from the side. The evaporation chamber is diffusion pumped and is isolated from the sample chamber by a pair of small apertures through which the vapor passes to impinge on the sample and a quartz crystal oscillator thickness monitor. A cryogenic pump is mounted directly opposite the sample which is itself surrounded by a cold wall held at 77 K. The mass analyzed ion beam is supplied by a Varian ion implanter.

The films which were subjected to friction, wear and adhesion testing were deposited on mechanically polished substrates of fully hardened AISI 52100 and non-hardened M50 steels. Prior to the first Ti deposition these substrates were given an initial dose of 1×10^{16} N/cm^2 using 30 keV N_2^+ ions. Substrates for films to be examined by electron microscopy were cut from silicon wafers and were given an initial deposition of approximately 100 nm of titanium. This layer served to contain the entire implanted layer within the titanium film. Each sample then received a total deposition of approximately 100 nm of Ti (assuming a density of 4.5 g/cm^3) delivered in 125 steps of 0.8 nm each. Between

XI. FINE LINE STR./DEPOSITION/ADHESION

each of these deposition steps, 30 keV N_2^+ ion were implanted to a fluence of 9.04×10^{14} N/cm^2 for the samples used for mechanical testing and to a fluence of 1.5×10^{14} N/cm^2 for the films used in Auger analysis. A portion of each sample was masked from the ion beam during ion implantation. The base pressure in the sample chamber was a 10^{-6} Torr and was increased to 10^{-5} by backfilling with N_2 gas during the implantation/deposition treatments.

In order to remove films from the Si substrates for transmission electron microscopy, one half of a folding microscope grid was glued to the coating with collodion. Since the coating–substrate interface was not implanted for these samples, the coatings remained glued to the grid when it was peeled from the substrate. The second half of the grid was then folded over the specimen which held it in place during subsequent removal of the collodion and analysis.

3. Film structure and composition

A Coates and Welter field emission scanning electron microscope was used to determine that the films were, in all cases, flat, smooth, and uniform with no visible porosity. Transmission electron microscopy and diffraction performed on both implanted and unimplanted films lifted from Si substrates showed that the structure of all the films was fcc with a lattice constant of 0.424 nm which compares favorably with 0.423 nm for TiN whereas the lattice constants for TiC and TiO are 0.432 nm and 0.429 nm respectively. The typical grain size was 10 nm for the unimplanted and 20–30 nm for the implanted films (see fig. 1).

Composition depth profiles of the films were obtained using Auger electron spectroscopy combined with argon ion sputtering. Differential Auger spectra were obtained using a single-pass cylindrical mirror analyzer with a 3.0 keV, 50 μA (70 mA/cm^2) electron beam incident on the sample. The base chamber pressure was 1.5×10^{-9} Torr. Sputtering was accomplished using a 0.5 mm-diameter, 4.0 keV Ar$^+$ beam incident at an angle of 62° with respect to the surface normal and rastered over an area of 4×4 mm^2 on the sample. The average current density over this area was 20 μA/cm^2.

Auger peak-to-peak heights for titanium, oxygen, carbon, nitrogen, and silicon were obtained as a func-
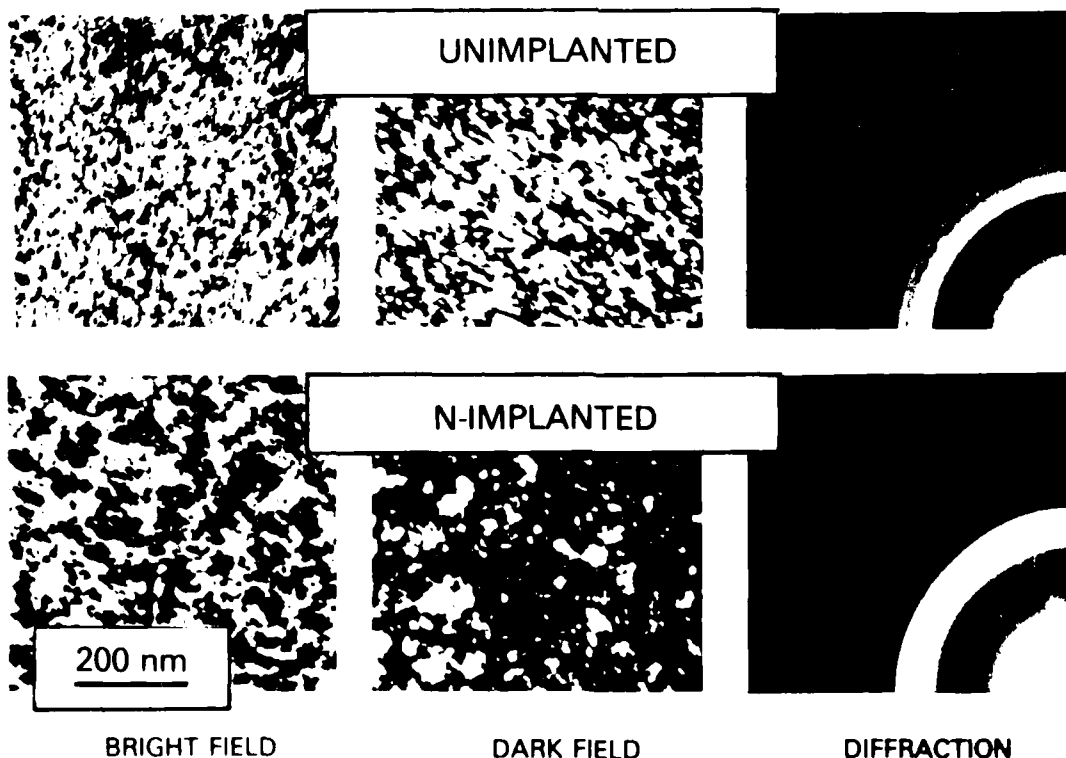

Fig. 1. Transmission electron micrographs and corresponding diffraction patterns of an as-deposited titanium film and a film that was nitrogen implanted during titanium deposition.

tion of sputtering time. Because the CMA analyzer was not able to resolve the N-KLL 379 eV peak from the Ti-LMM 387 eV peak, it was necessary to examine the ratio of the composite 379–387 eV peak to the Ti 418 eV peak. Based on an analysis of a TiN standard sample performed during ion milling, this ratio is 1.87. In addition, based on similar analyses of standard samples, the Ti 387/418 ratio is 0.75 for pure titanium, 1.2 for TiC, and 1.2 for TiO_2. Since there was a considerable amount of oxygen and carbon in the coatings, the nitrogen peak height was estimated by subtracting 1.2 times the Ti 418 peak height from the composite 379–387 peak height. All elemental peak heights were normalized using sensitivity factors obtained from the Handbook of Auger Electron Spectroscopy [4], with the exception of carbon which was measured from a TiC standard. This sensitivity factor of 0.53 was chosen because examination of the line shape indicated that the carbon was entirely carbidic, i.e., metallic carbides as distinguished from free or graphitic carbon. From the normalized intensities, the atomic fractions of each element were calculated. As a check on the procedure for calculating the nitrogen concentration, in those areas of the depth profile where the Ti and N atomic fractions were determined to be equal, the composite 379–387 peak height divided by the Ti 418 peak height was measured and it ranged from 1.85 to 1.95, in good agreement with the TiN standard.

Figs. 2a and 2b are the composition depth profiles for the unimplanted and N-implanted films on the polished silicon substrate, as determined by Auger spectroscopy. The elemental concentrations are plotted as a function of sputter time because the sputtering rate would not be expected to remain constant through a coating with such a widely varying composition. The average sputtering rate was approximately 2.1 nm per minute, assuming that the film thickness is 100 nm and that the interface occurs at a point where the titanium concentration is reduced to 50% of its steady-state value.

Observations that can be made from these depth profiles are that the titanium is highly reactive with the residual gases in the vacuum chamber, with carbon and oxygen being incorporated into the films as well as nitrogen, which constituted more than 80% of the gases present in the vacuum chamber. The average oxygen concentration was reduced by more than 50% in the implanted film, possibly due to sputter removal of the chemisorbed oxygen during each increment of implantation. Both sets of profiles have two interesting features which are not understood and are being investigated further: (1) a rapid variation in composition in the near surface region, and (2) the nitrogen and carbon concentrations followed an inverse relationship, with their sum being virtually constant throughout the thickness of the film. The implantation resulted in mixing of the film at the interface as evidenced by the decreased slope of
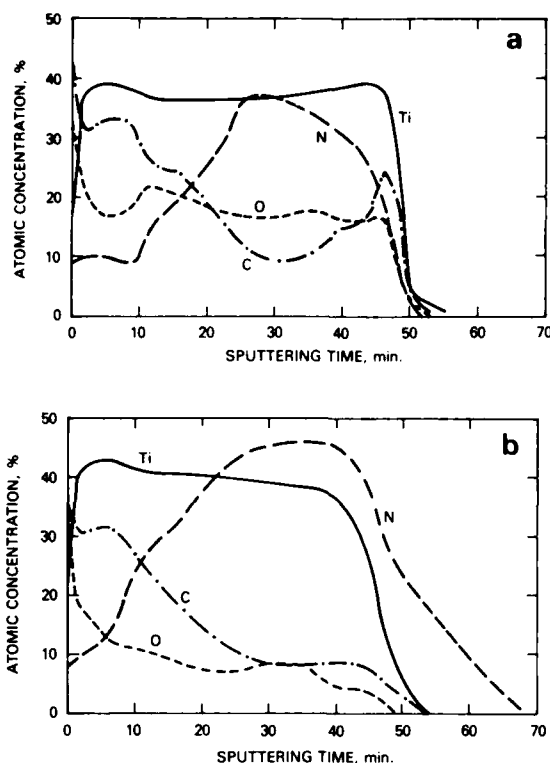
Fig. 2. Composition profiles obtained by sputter Auger electron spectroscopy of unimplanted (a) and N-implanted (b) films indicate reduced oxygen and carbon in the N-implanted regions.

the titanium concentration profile near the interface. In the as-deposited film, it required 4 min of sputtering to reduce the titanium concentration from the steady-state value to 10% of the steady-state value, whereas in the implanted film it required 9 min.

4. Mechanical tests

Scratch type adhesion testing was performed on films deposited on 52100 steel using a Rockwell C indenter with loads ranging from 10 N to 50 N. Figs. 3a and 3b are optical micrographs of the scratched regions of the unimplanted and the implanted films respectively. There is extensive cracking and peeling of the unimplanted film for all loads. No adhesion failure was observed for the N-implanted films until the depth of the depression left by the indenter exceeded 20 × the film thickness (200 nm for this sample) and then only small amounts of flaking was observed.

For the friction and wear tests a 52100 ball, 1.27 cm

UNIMPLANTED

N-IMPLANTED

100 μm
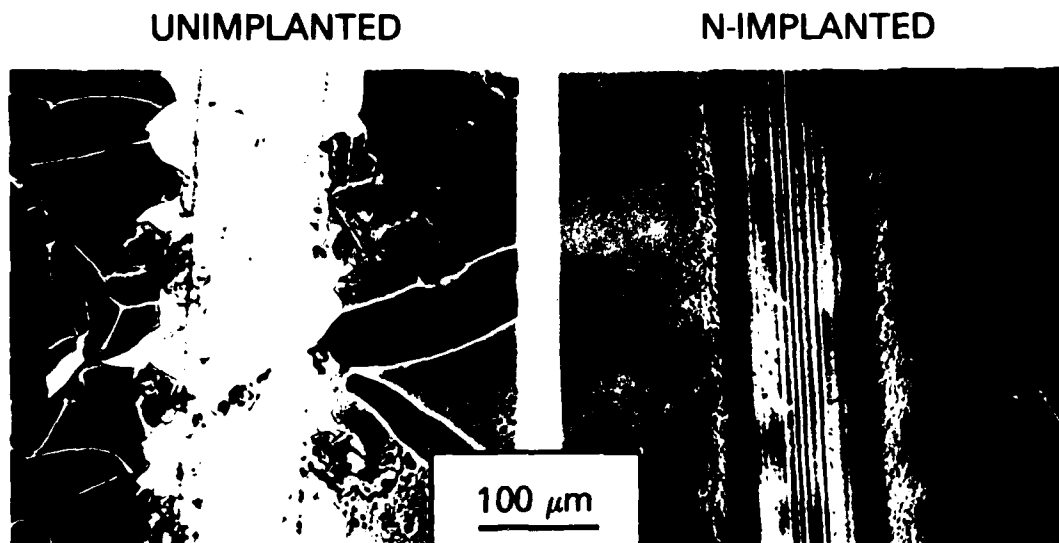
Fig. 3. Optical micrographs of deformations produced during adhesion testing. The unimplanted film (a) exhibits severe cracking, peeling, and buckling adjacent to the scratch and complete adhesion failure within the scratch. The N-implanted film (b) remains intact even within the scratch.
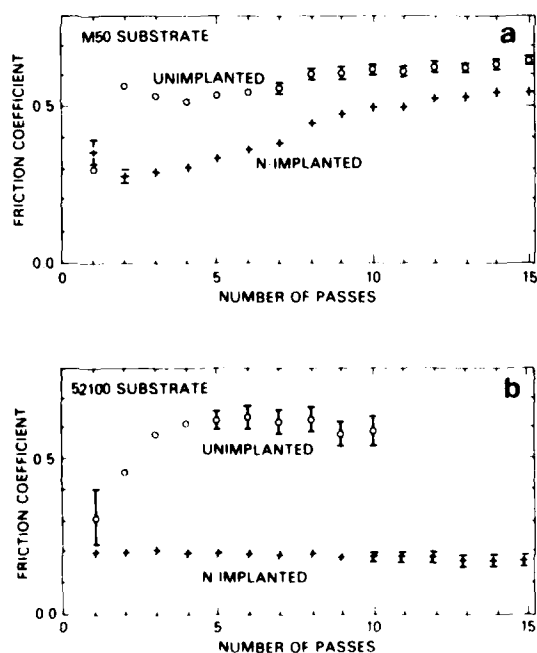
Fig 4 Friction coefficient as a function of the number of passes of a 52100 steel ball over films on a soft M50 substrate (a) and a hard 52100 substrate (b)

in diameter, was pressed against the surface with a 1 kg load. The tests were performed under dry sliding conditions and at a sliding rate of 0.1 mm/s. For both steel substrates, the unimplanted films began to flake during the first pass and the coefficient of friction increased quickly to about 0.6 (typical of steel on steel) as shown in fig. 4. The implanted films, on the other hand, remained attached even after 15 passes. Energy dispersive X-ray analysis revealed that the Ti/Fe ratios were identical inside and outside the contact zone for the film on the M50 substrate (Knoop hardness 210 kg/mm^2). The same measurements made on the film on the harder 52100 substrate (Knoop hardness 750 kg/mm^2) showed that the 13% of the Ti had been removed by the 15th pass. The friction coefficient for this case was 0.2 throughout the test (fig. 4a). For the implanted film on the M50 substrate, the coefficient asymptotically approached the value for the unimplanted case from a low of 0.3 (fig. 4b).

5. Discussion and conclusions

The experimental results are summarized as follows: (1) vapor deposition of Ti on room temperature substrates in a reactive N environment leads to the formation of a fine grained fcc phase with a lattice constant consistent with TiN; (2) all films contained significant amounts of carbon and oxygen; however, the concentration of each of these elements was reduced substantially

in the N-implanted case; (3) films deposited without N-implantation are mechanically unstable exhibiting very weak adhesion, cracking and peeling; (4) N-implantation during deposition causes a dramatic increase in the mechanical stability characterized by strong adhesion; and (5) N-implanted films exhibited low friction and wear.

A significant feature of the depth profiles is reduced C and O levels in the regions of the film which were N-implanted during film growth. Since the deposition portion of each cycle of the treatment is identical for both the implanted and the unimplanted films, the composition of a freshly deposited layer would be expected to be the same in both cases prior to each implantation phase of the treatment. It could be assumed that the reduction of the C and O concentration in this freshly deposited film is altered by the next implantation treatment by a sputter-induced desorption mechanism. This interpretation may explain the reduction of the O concentration. However, this interpretation for the behavior of C would then be in sharp contrast to the observations of Follstaedt [5] and Singer [6] who found that surface carburization of Fe and steel occurs during Ti implantation. An alternative view might be that C remains within the freshly deposited layer throughout the next implantation cycle and is buried by the subsequent depositions of Ti where it remains until its depth beneath the surface becomes comparable to the range of the N implanted during subsequent treatment cycles. Each of these subsequent implantations contributes to a wave of increasing N concentration moving toward the surface as the thickness of the film increases. In this view, it is this increase of the N content of the film that leads to the expulsion of the C. It is important to note that the reduced C levels cannot be due simply to dilution since the relative concentration of Ti remains constant throughout the film. Since the films are grown at room temperature, it is reasonable to assume that radiation-enhanced diffusion provides the mechanism for transport of C from the implanted region. The coarser grain structure observed for implanted films offers additional evidence of the presence of enhanced diffusion. Additional experiments are

under way to help provide a better understanding of the mechanisms responsible for the compositional changes observed in films implanted during nucleation and growth.

While it is tempting to ascribe the dramatic improvement in film adhesion to ion beam mixing of the interface during the early states of film growth, other factors may also contribute to the improvement. These include sputter cleaning of the substrate by the ion beam prior to the first Ti deposition and electronic excitation phenomena thought to be responsible for the so-called "stitching" observed, for example, for Au deposited on glass and irradiated by electrons [7].

The work presented here provides clear evidence that the use of ion beams at higher energies than are normally used for ion beam assisted deposition techniques offers a means of producing significant and desirable modifications of the composition and mechanical properties of vapor-deposited films.

References

[1] C. Weissmantel, Thin Solid Films 58 (1979) 101.
[2] L. Pranevicious, Thin Solid Films 63 (1979) 77.
[3] J.J. Cuomo, J.M.E. Harper, C.R. Guarnieri, D.S. Yee, L.J. Attanasio, J. Angllello and C.T. Wu, J. Vac. Sci. Technol. 20(3) (1982) 349.
[4] Handbook of Auger Electron Spectroscopy, eds., L.E. Davis, N.C. MacDonald, P.W. Palmberg, G.E. Riach and R.E. Weber (Physical Electronics Industries, Eden Prairie, Minnesota, 1976).
[5] D.M. Follstaedt, L.E. Pope, J.A. Knapp, S.T. Picraux and F.G. Yost, Thin Solid Films 107 (1983) 259.
[6] I.L. Singer, J. Vac. Sci. Technol. A1 (1983) 419.
[7] D.K. Sood, these Proceedings (IBMM '84) Nucl. Instr. and Meth. B7/8 (1985) 893.

XI. FINE LINE STR./DEPOSITION/ADHESION

Section I.D

IN SITU AUGER ANALYSIS OF SURFACE COMPOSITION DURING HIGH FLUENCE ION IMPLANTATION

D.A. Baldwin[1]*
B.D. Sartwell[2]
I.L. Singer[1]

[1]Surface Chemistry Branch
Chemistry Division
Naval Research Laboratory

[2]Materials Modification & Analysis Branch
Condensed Matter & Radiation Sciences
Naval Research Laboratory

* National Research Council Associate

IN SITU AUGER ANALYSIS OF SURFACE COMPOSITION DURING HIGH FLUENCE ION IMPLANTATION

D.A. BALDWIN *, B.D. SARTWELL and I.L. SINGER

Naval Research Laboratory, Code 6670, Washington, D.C. 20375, USA

A multi-technique ultrahigh vacuum (UHV) target chamber has been used to perform in situ Auger electron spectroscopic (AES) analysis during ion implantation and AES sputter depth profiling of the substrate within 1–2 min after implantation. Iron was implanted with 150 keV Ti^+ at a 45° angle of incidence in a target chamber with pressures ranging from 8×10^{-9} Torr of residual gases up to 1×10^{-5} Torr of intentionally admitted CO gas. A fluence of $\sim 1.0 \times 10^{16}$ cm^{-2} was needed to sputter away the C-covered air-formed oxide. The implanted Ti reached the surface at the 1 at.% level by $\sim 1.5 \times 10^{16}$ cm^{-2}. With increasing fluence, the Ti surface concentration increased to ~ 15 at.% at steady-state with a curve shape that was concave downward at all fluences. The surface C concentration was found to be proportional to that of Ti for implants in CO, supporting a vacuum carburization model. Substantial O surface concentration (15–20 at.%) was detected for these runs but depth profiles showed only carburization, not oxidation, of the implanted layer. Even in the best vacuum available (8×10^{-9} Torr), some carburization was observed and was attributed to residual gas absorption. An increase in Ti retained dose with increasing CO pressure has been observed but not yet independently confirmed. The Ti/Fe surface concentration ratio is higher for implants done in CO, and this is discussed in terms of modification of the sputter yield for Ti.

1. Introduction

The improvement of the wear and friction properties of certain steels implanted with Ti ions has been attributed to the formation of a Ti–C surface layer caused by reactions of surface Ti with C-containing gases in the vacuum system [1–3]. Vacuum carburization, according to a simple model proposed by Singer [4], occurs by a four step process: (1) sputtering uncovers implanted Ti atoms; (2) C-containing gas molecules, which constitute a significant percentage of the residual gases in the implanter chamber, adsorb preferentially onto surface Ti atoms; (3) the molecules dissociatively chemisorb to form surface carbide species; and (4) surface C atoms diffuse inward. SIMS (secondary ion mass spectrometry) analysis of metals implanted in a vacuum chamber backfilled with isotopically labeled ^{13}CO gas has shown definitively that C is incorporated into the implanted layer from gas molecules [5] and that C incorporation can be reduced by implanting in an ultrahigh vacuum (UHV) environment [6]. However, until now there have been no detailed studies of the reactions that occur between the implanted surface and the residual gases in the vacuum chamber during implantation.

This paper presents the first in situ studies of the composition of a surface during ion implantation. Auger electron spectroscopic (AES) analysis of the surface of high purity Fe samples was performed in a UHV im-

plantation chamber simultaneously with Ti^+ implantation. Surface composition as a function of ion fluence and chamber pressure, and composition–depth profiles of the implanted layer following implantation, have been obtained. These results represent a more detailed picture of the vacuum carburization process.

2. Experimental

The instrumental arrangement is shown in fig. 1. The entire UHV apparatus was mounted on a rolling platform so that it could either be positioned directly behind the permanent high vacuum (HV) implanter target chamber or detached and moved away from the implanter. The 150 keV Ti^+ beam passed through the HV target chamber into an antechamber featuring a 200 l/s ion pump, a liquid nitrogen cooled cold wall, beam-defining aperture plates and a 5 cm diameter rotating wire loop that intercepted $\sim 2\%$ of the total beam current. The ion beam entered the cryo-pumped UHV target chamber (1×10^{-9} Torr base pressure) through a UHV gate valve and was incident on the target at an angle of 45°. The Auger cylindrical mirror electron energy analyzer (CMA) probed the target face at 45° in the same plane, while a rastered 4 keV Ar^+ sputter beam was focused on the target from out-of-plane at 60° off the target normal. A precision manipulator/Faraday cup (FC) unit allowed focusing and quantification of the three beams at the desired point on each specimen.

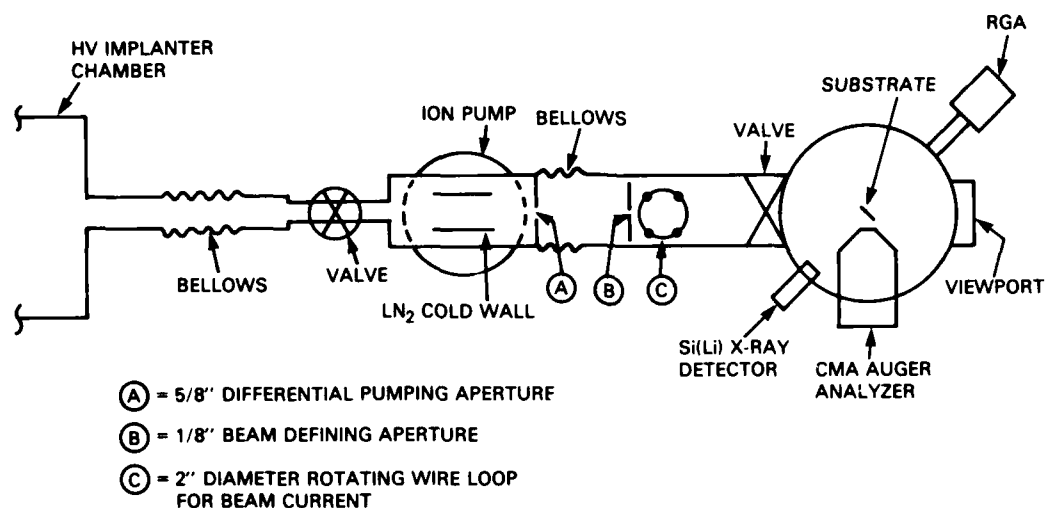I. METALS
Kinematics, Metastable phases

Fig. 1. The general purpose UHV implantation chamber shown was used in the mode allowing continuous AES surface analysis during implantation. An auxiliary leak valve (not shown) and the RGA (residual gas analyzer) allowed controlled admission of CO gas.

The FC had a 1 mm^2 entrance aperture and was used to measure the ion current density and to establish a linear correlation between the FC current density and the current measured on the rotating wire loop. Thus, by monitoring the charge incident on the wire, it was possible to determine the implant fluence. The Ti$^+$ current density during all implants was ~ 9×10^{13} ions cm^{-2} s^{-1} (15 μA cm^{-2}). The implant substrates were Marz grade polycrystalline Fe foils polished to 1 μm diamond and mounted on an Al heat sink. A calibration experiment determined that the maximum sample temperature during implantation was 80°C. Implantations were performed either in UHV or in a selected pressure of CO gas up to 1×10^{-5} Torr. The CO gas pressure was established by continuously admitting fresh CO while pumping to give a constant flow. The CO was pumped out immediately before terminating the implant, and, within 1.5 min at 3×10^{-9} Torr, the Ar$^+$ sputtering for the Auger depth profile was initiated.

Auger spectra were obtained in two different ways: (1) during Ti$^+$ implantation, with the sample at 45° to the CMA and (2) during Ar$^+$ sputter depth profiling, with the sample normal to the CMA. In both cases, a 3 keV, 50 μA (70 mA cm^{-2}) electron beam was used to excite the spectra, the CMA modulation was 3.7 eV and the spectrometer was set to repetitively scan the Auger signals of interest throughout the entire bombardment. The Auger data were quantified using sensitivity factors that were determined for the present instrument (sample normal to CMA) from the reference compounds FeTi, TiC, C-implanted Ti and air-oxidized Fe. The sensitivity factor values were 0.45, 0.18, 0.53, 0.20 and 0.32 for Ti

(419 eV) (both carbidic and metallic), Fe (651 eV), carbidic C, adventitious C, and O, respectively. The separation of the carbon Auger signal into carbidic and *adventitious components was based on the peak shape* in the dNE/dE mode spectra (see fig. 2). The sensitivity factors $S(i)$ for each element i were used to calculate atomic fractions $X(i)$ from the AES intensities $I(i)$ using the expression

$$X(i) = [I(i)/S(i)] \Big/ \Big[\sum_j I(j)/S(j) \Big]. \tag{1}$$

Eq. (1) provides concentrations, averaged over the escape depth of the Auger electrons (1 to 2 nm), which are estimated to have a relative accuracy of better than $\pm 20\%$ for Ti, Fe and C and $\pm 30\%$ for O, due to uncertainty in the composition of the oxide reference compound. Differences due to making AES measurements normal to the CMA versus at the 45° angle are within these quoted accuracies.

3. Results

Compositions of the sample surfaces are shown in fig. 2 as a function of Ti$^+$ fluence for implants performed with the UHV chamber at its best vacuum (when open to the implanter) of 8×10^{-9} Torr and with the chamber held at a CO pressure of 2×10^{-6} Torr. In both cases, the adventitious C layer, identified by the C AES lineshape, was sputter-removed by a fluence of 6×10^{15} cm^{-2} and the air formed oxide layer by 1.0×10^{16} cm^{-2}. The surface concentration of Ti, [Ti]$_s$,
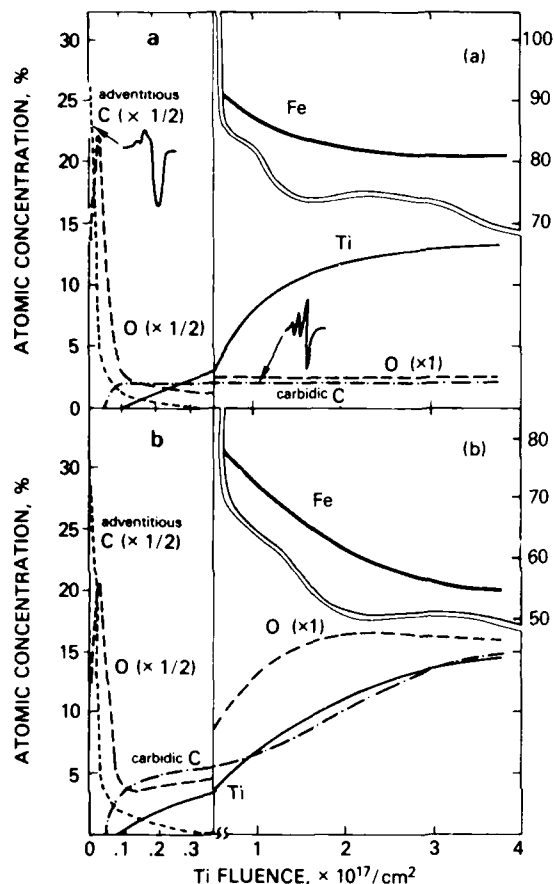
Fig. 2. Escape-depth-averaged Auger surface concentration measurements are plotted versus Ti$^+$ implant fluence. Panel (a) was recorded during implantation in 8×10^{-9} Torr residual gases while panel (b) was recorded for a CO gas pressure of 2×10^{-6} Torr. Note the scale factor changes used and the multiple scales used on the vertical axis.

showed that the C and O surface concentrations as a function of fluence behaved in the same manner described for the implantation done in 2×10^{-6} Torr.

Auger sputter depth profiles measured promptly after implantation are shown in fig. 3 for Fe implanted with 150 keV Ti$^+$ to four fluences, 0.7, 1.4, 2.3 and 3.5×10^{17} cm^{-2}, in CO at a pressure of 2×10^{-6} Torr. Implantation-induced carburization increases with Ti$^+$ fluence, though the penetration depth of the C is nearly constant. The O is confined to the outer surface region even though it is present at approximately the same surface concentration as C during the implantation. Fe comprises the balance of the atomic fractions in each profile. These in situ profiles agree with published ex situ profiles [4] except during the extremely early stages of the profile. This means that the re-growth of an air-formed oxide does not seriously distort the concentration profiles before they can be measured ex situ.

Shown in fig. 4 are Auger sputter depth profiles of Fe after implantation to steady-state with 150 keV Ti$^+$ in 7×10^{-6} Torr CO and 8×10^{-9} Torr residual gases. In the former case, steady-state was reached after a fluence of 5×10^{17} cm^{-2} and, in the latter case after 3.5×10^{17} cm^{-2}. The degree of carburization is drastically reduced, but not completely eliminated, by implanting Ti at 8×10^{-9} Torr. Comparing the areas under the Ti curves in fig. 4 and taking into account the different fluences, it appears that the retained dose of Ti increases when CO is present during the implant. A further measurement, e.g. EDX (energy dispersive X-ray analysis), would be necessary in order to confirm this.

Unlike the other profiles presented in this paper, the

reaches 1 at.% at $< 1.5 \times 10^{16}$ cm^{-2} at both pressures. With increasing fluence, [Ti]$_x$ initially increases at the same rate for the two cases, but it plateaus sooner and at a slightly lower value for the 8×10^{-9} Torr implant. At steady-state for the 2×10^{-6} Torr CO implant the Fe concentration, unlike [Ti]$_x$, is diluted by the presence of C and O. The surface carbidic carbon concentration is approximately proportional to [Ti]$_x$, though it initially rises faster and appears at lower fluence, i.e., $< 7 \times 10^{16}$ cm^{-2}. Oxygen also builds up with fluence but plateaus before either Ti or C, possibly due to electron impact stimulated desorption (ESD) of O from the surface by the AES primary electron beam. ESD is known to occur in the Ti–O system [7]. Additional implants done in CO pressures ranging from 7×10^{-7} Torr to 7×10^{-6} Torr
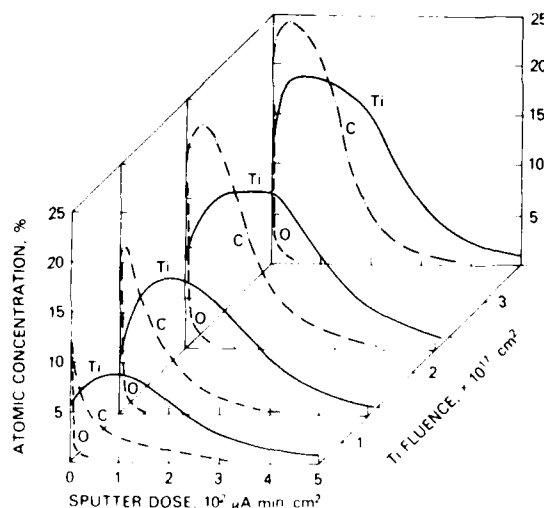

Fig. 3. AES sputter depth profiles obtained in situ within 2 min of termination of implantation are shown for four Ti$^+$ fluences, 0.7, 1.4, 2.3 and 3.5×10^{17} ions cm^{-2}.
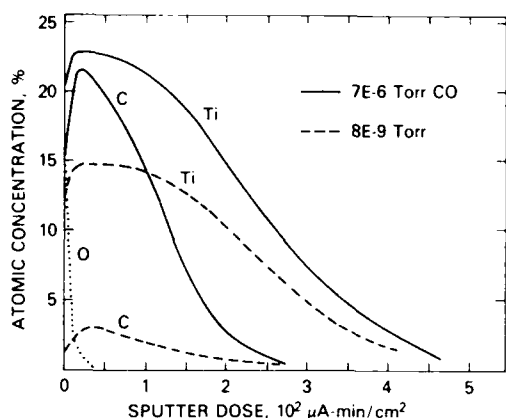
34

Fig. 4. Shown are AES sputter depth profiles obtained after implantation to steady-state fluences, 5×10^{17} cm^{-2} and 3.5×10^{17} cm^{-2}, for implants done in 7×10^{-6} Torr CO and 8×10^{-9} Torr residual gases, respectively.

one obtained for the implant in 7×10^{-6} Torr CO was performed after the implanted substrate remained undisturbed for several days in the UHV chamber. In this case, a C-covered "air-formed" oxide layer grew on the implanted substrate. This was sputtered away before the profile shown in fig. 4 was obtained.

4. Discussion

In situ Auger analysis of the Ti-implanted surface (fig. 2) verifies two of the steps of the implant-assisted vacuum carburization model [4]. First, implanted Ti atoms are uncovered at the surface after the outermost layers of the Fe substrate (the C-covered oxide layer) have been sputter-removed. Second, C-containing gas molecules can be dissociatively chemisorbed roughly in proportion to [Ti]$_s$, as was shown here for the case of CO molecules. The dissociative chemisorption is indicated by the carbidic lineshape of the AES spectra [8].

The C and O profiles in figs. 3 and 4 suggest that ballistic mixing (knock-on) is not responsible for the inward C migration. Oxygen is present at roughly the same surface concentration as C in both UHV (fig. 2a) and CO ambient (fig. 2b) implants, but it is not incorporated into the subsurface layers. Since O and C are of similar mass, ballistic mixing should produce roughly equal amounts of the two below the surface. Therefore, ballistic mixing must be ruled out unless one postulates that O out-diffuses after knock-on. Bassel et al. [6] have shown by Monte Carlo calculations that knock-on can account for only a small fraction of the carburization observed in Cr-implanted Cr substrates. Hence, it is likely that C migrates inward by a diffusion-controlled

process, as modeled by Farkas et al. [9].

Fig. 4 suggests that a larger Ti retained dose is achievable when implantation is performed in a CO atmosphere (7×10^{-6} Torr) than when implantation is performed at 8×10^{-9} Torr. The in situ surface concentration measurements during implantation shown in fig. 2 provide the possible explanation that adsorption of C and O decreases the Ti sputtering yield. One would expect that the presence of almost 35 at.%, combined, of C and O at the surface during the implant in CO (fig. 2b) would reduce the measured [Ti]$_s$, due to atomic dilution and Auger signal attenuation, compared with [Ti]$_s$ in fig. 2a. In fact, [Ti]$_s$ at steady-state for the CO case is equal to or greater than [Ti]$_s$ at steady-state for the 8×10^{-9} Torr case while [Fe]$_s$ is 58 at.% and 82 at.%, respectively, in those cases. That a reduction in Ti sputter yield may be caused by C surface contamination can be inferred from the data of Almen and Bruce [10]. They found very low self-sputtering yields for those elements that are strong carbide-formers (Ti, V, Zr, Nb, Hf, Ta) when sputtering in a non-UHV chamber, i.e., when vacuum carburization would be expected to occur. More recently, reduction of the Ti sputter yield by 11 keV Ar$^+$ due to the presence of various reactive gases has been reported by Hofer et al. [11] at gas molecule to ion arrival rate ratios greater than unity.

Other features shown by the present in situ data strongly suggest that there are chemical influences upon the results of implantation of Ti$^+$ into Fe. The profiles in figs. 3 and 4 indicate that both C and Ti concentrations rise from their surface values to maxima at some small depth (depth could not be calibrated in these experiments) beneath the surface. For Ti, this could be the result of simply not being at steady-state, but, for C, the trend is going in the opposite direction; there is greater subsurface peaking of [C] as the fluence increases (fig. 3). Preferential sputtering (affected by surface chemical bond strengths), Gibbsian segregation and radiation induced segregation (affected by chemical potential gradients) and chemical dilution by adsorbates could explain these effects. The reader is referred to recent reviews [12,13] for details on how these chemically-influenced mechanisms may affect the subsurface concentration profile.

Another chemical effect is shown in fig. 2 below 1.5×10^{16} cm^{-2} Ti$^+$ fluence. The surface carbidic C concentration rises from zero at lower fluence and climbs more steeply than [Ti]$_s$, indicating that surface Ti is not always necessary for adsorption of carbonaceous molecules. Rather, it appears that adsorption of CO onto the sputter-exposed Fe occurs; one sees in fig. 2b, compared to fig. 2a, a stronger buildup of surface carbide below 1.5×10^{16} cm^{-2}. In both figures, however, some of this low fluence carbide buildup is probably due to conversion of some of the adventitious C overlayer to carbidic

C under the influence of the Ti$^+$ beam. Lastly, consider the shape of the [Ti]$_s$ versus fluence curves in fig. 2. These curves are concave downward at all fluences in contrast to the predictions of an "s-shaped" curve (with an inflection point) by the Schulz and Wittmaack [14] model or the Davisson model [15]. These models also predict steady-state at too low a fluence. The model of Farkas et al. [9], which includes diffusion, predicts a higher fluence to reach steady-state than the other models. It appears that models considering only purely physical effects (sputtering, lattice dilation, range changes, etc.) are not able to account for the observed [Ti]$_s$ versus fluence behavior and that models that take into account chemical effects (surface compound formation, Gibbsian segregation, etc.) will be needed.

5. Conclusions

In situ AES surface analysis during implantation has been employed to test aspects of Singer's vacuum carburization model for metals implanted with carbide-forming reactive ions. Those aspects tested were supported. In addition, this first in situ study of surface concentrations versus implant fluence has yielded results both specific to the system studied and of general import. In both cases, knowledge of these surface concentrations during implantation can be considered to be essential for a full understanding of near-surface effects on the subsurface result of high fluence reactive ion implantation.

References

[1] I.L. Singer, C.A. Carosella and J.R. Reed, Nucl. Instr. and Meth. 182/183 (1981) 923.

[2] G.K. Hubler, in: Metastable Materials Formation by Ion Implantation, eds., S.T. Picraux and W.J. Choyke (Elsevier, New York, 1982) p. 341.

[3] I.L. Singer, in: Ion Implantation and Ion Beam Processing of Materials, eds., G.K. Hubler, O.W. Holland, C.R. Clayton and C.W. White (North-Holland, New York, 1984) p. 585.

[4] I.L. Singer, J. Vac. Sci. Technol. A1 (1983) 419.

[5] I.L. Singer and T.M. Barlak, Appl. Phys. Lett. 43 (1983) 457.

[6] R.H. Bassel, K.S. Grabowski, M. Rosen, M.L. Roush and F. Davarya, in press.

[7] H.J. Mathieu, J.B. Mathieu, D.E. McClure and D. Landolt, J. Vac. Sci. Technol. 14 (1977) 1023.

[8] M.P. Hooker and J.T. Grant, Surface Sci. 62 (1977) 21.

[9] D. Farkas, I.L. Singer and M. Rangaswamy, in: Ion Implantation and Ion Beam Processing of Materials, eds., G.K. Hubler, O.W. Holland, C.R. Clayton and C.W. White (North-Holland, New York, 1984) p. 609; J. Appl. Phys. (to be published).

[10] O. Almen and G. Bruce, Nucl. Instr. and Meth. 11 (1961) 279.

[11] W.O. Hofer, H.L. Bay and T.J. Martin, J. Nucl. Mater. 76/77 (1978) 156.

[12] H.H. Andersen, in: Ion Implantation and Beam Processing, eds., J. Williams and J. Poate (Academic Press, Australia, 1984) p. 127.

[13] R. Kelly, Surface and Interface Analysis, in press.

[14] F. Schulz and K. Wittmaack, Radiat. Effects 29 (1976) 31.

[15] C.M. Davisson, Naval Research Laboratory Memorandum Report 5409, to be published.

36

Section I.E

IN SITU PROTON-INDUCED X-RAY EMISSION AND AUGER ELECTRON
SPECTROSCOPY STUDY OF TITANIUM AND NIOBIUM IMPLANTATION OF IRON FILMS

B.D. Sartwell[1]
D.A. Baldwin[2]*

[1]Materials Modification & Analysis Branch
Condensed Matter & Radiation Sciences Division
Naval Research Laboratory

[2]Surface Chemistry Branch
Chemistry Division
Naval Research Laboratory

In Situ Proton-induced X-ray Emission and Auger Electron Spectroscopy Study of Titanium and Niobium Implantation of Iron Films*

B. D. SARTWELL and D. A. BALDWIN

Naval Research Laboratory, Code 6670, Washington, DC 20375 (U.S.A.)

ABSTRACT

Implantation of 190 keV titanium and niobium ions into iron films 200 nm thick electron beam deposited onto polished Si(100) substrates has been investigated. During the course of implantation of the iron films, proton-induced X-ray emission was used to measure the instantaneous film thickness and the total retained dose, whereas Auger electron spectroscopy was used to determine the surface concentrations of the implanted species and the reactive elements. Implantations were carried out both under ultrahigh vacuum conditions and with the chamber backfilled with CO to a pressure of 1×10^{-6} Torr. Elemental sputtering yields were measured for iron and the implanted element as a function of fluence. The results showed that, for titanium implantation, the addition of CO to the target chamber significantly reduced the sputtering yield of the substrate and increased the retained dose that could be achieved. For niobium implantation the addition of CO to the chamber reduced the substrate sputtering yield, but not to the same degree as observed for titanium, and did not alter the total retained dose that could be achieved.

1. INTRODUCTION

Significant reductions in both the friction and the wear of certain steels have been observed following the implantation of moderate energy titanium ions. The low friction has been attributed to the formation of an Fe-

---

Ti-C surface alloy [1, 2]. As proposed by Singer [3], titanium ions, when implanted to high fluences, assist in the carburization of the surface, causing carbon atoms to be absorbed from carbon-containing gas molecules in the vacuum chamber. In steels the Fe-Ti-C layer has been shown to be amorphous [4]. Secondary ion mass spectrometry analysis of metals implanted in a vacuum chamber backfilled with isotopically labeled ^{13}CO gas has shown that carbon is incorporated into the implanted layer from gas molecules [5] and that carbon incorporation can be reduced by implanting in an ultrahigh vacuum environment [6]. Recently, results have been presented for *in situ* studies of the composition of the surface of high purity iron foils subjected to titanium ion implantation [7]. Auger electron spectroscopy (AES) analysis was performed in an ultrahigh vacuum target chamber simultaneously with the titanium implantation. Surface compositions as a function of ion fluence for implantations performed at a chamber pressure of 8×10^{-9} Torr and with the chamber backfilled with CO to a pressure of 2×10^{-6} Torr, and composition-depth profiles of the implanted layer following implantation were obtained. The results showed that with increasing fluence the titanium surface concentration increased to approximately 15 at.% at steady state for implants performed at both pressures, with curve shapes that were concave downward at all fluences. The surface carbon concentration was found to be proportional to that of titanium for implants in CO, supporting a vacuum carburization model. Even for the implant performed at 8×10^{-9} Torr, some carburization was observed, which was attributed to residual gas absorption. An oxygen surface concentration of 15-20 at.%, higher than the carbon surface concentration, was observed

540

for the implants performed in CO but the depth profiles showed only carburization, and not oxidation, of the implanted layer. It was therefore concluded that ballistic recoil mixing does not contribute to the subsurface carburization because, since oxygen and carbon are of similar masses, ballistic mixing should produce roughly equal amounts of the two below the surface. The titanium-to-iron surface concentration ratio was observed to be significantly higher for the implants performed in CO, and it was hypothesized that this was due to a change in the sputtering yield caused by the absorption of carbon and oxygen.

In order to investigate the effects attributed to the different vacuum conditions, experiments have been conducted in which titanium ions were implanted into iron films 200 nm thick vacuum evaporated onto polished silicon substrates. Simultaneous AES analysis was performed during the implantation as in the previous study described above. In addition, proton-induced X-ray emission (PIXE) was used to determine, as a function of fluence, the thickness of the iron film and the retained dose of titanium. These measurements were made for implants performed both at 8×10^{-9} Torr and with the chamber backfilled with CO to a pressure of 1×10^{-6} Torr. Since it has been hypothesized that the implantation of other group IVB and VB elements (which are known to be strong carbide formers) might produce similar carburized surface layers that could enhance friction and wear properties [8], similar studies were performed for niobium implantation into the thin iron films under both vacuum conditions. In this paper the results of these studies are presented.

2. EXPERIMENTAL APPARATUS AND TECHNIQUES

The metallic ion beams were produced in an Extrion 200 kV ion implanter using a chlorination technique to produce the metallic chloride vapor in the hot-filament ion source. The ion beam passed through the permanently mounted high vacuum (5×10^{-7} Torr) target chamber into an antechamber featuring a 200 l s^{-1} ion pump and a liquid-nitrogen-cooled cold wall to trap gases stream-

ing from the implanter. A beam-defining aperture plate with two holes in it, 3.2 mm and 1.6 mm in diameter and spaced 2 cm apart, was mounted onto a linear motion feedthrough so that the final beam diameter entering the chamber could be either of the two sizes. Directly behind the aperture plate was a wire loop 5 cm in diameter that, when rotating, intercepted approximately 2% of the total beam current. This wire loop was used for monitoring the relative beam current entering the target chamber. The 190 keV Ti$^+$ or Nb$^+$ ion beam entered the cryo-pumped target chamber (base pressure, 1×10^{-9} Torr) shown in Fig. 1 through an ultrahigh vacuum gate valve and was incident on the substrate at an angle of 30° off the target normal. The substrates were mounted onto a target "ladder" that was attached to a heating and cooling stage on a precision x-y-z manipulator. During all implantations the samples were kept at a temperature below 20 °C. A Faraday cup with a 1 mm^2 entrance aperture was also attached to the manipulator which provided for measurement of the ion beam current density and for alignment of the ion beams with the electron beam produced by the electron gun mounted coaxially with the Auger cylindrical mirror electron energy analyzer. Also attached to the chamber was an Si(Li) X-ray detector (180 eV resolution for Mn Kα X-rays) that had a 7.62 μm beryllium entrance window. At the rear of the chamber in front of a viewport was a retractable Faraday cup with an entrance aperture 1.2 cm in diameter that was used for measuring the total ion beam current when the target ladder was translated out of the path of the beam. Also attached to the chamber was a residual gas analyzer and a precision leak valve.

The substrates for this study consisted of 1 cm^2 pieces of highly polished Si(100) onto which iron films 200 nm thick were electron beam deposited in a bell-jar system. The thickness of the films was determined using a quartz crystal oscillator. Subsequent Auger depth profiling of the films showed that they contained approximately 5 at.% O and less than 1 at.% C.

The PIXE and AES measurements for a particular set of implant parameters were performed at two different locations on the same sample. The Ti$^+$ ion current density during all implants was approximately 20 μA cm^{-2} and
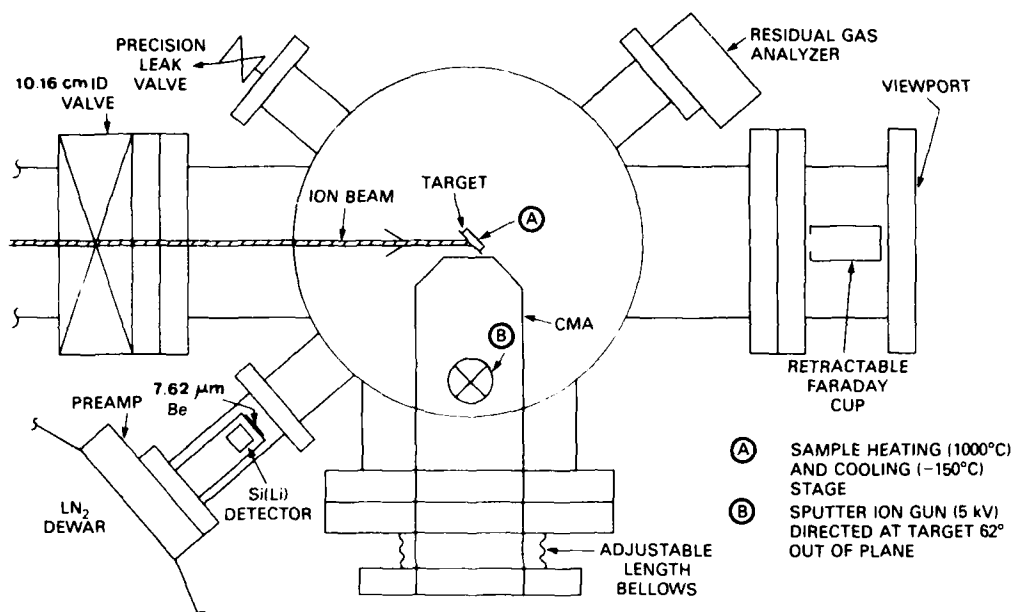
Fig. 1. Ultrahigh vacuum ion implantation target chamber containing an Auger cylindrical mirror electron analyzer CMA and an Si(Li) X-ray detector for AES and PIXE analyses respectively of target surfaces during implantation: ID, inside diameter; LN, liquid nitrogen; PREAMP, preamplifier.

the Nb^+ ion current density was approximately $10\,\mu A\,cm^{-2}$. Implantations were performed either at a pressure of 8×10^{-9} Torr, which represented the base chamber pressure when opened to the implanter, or with the chamber backfilled with CO to a pressure of 1×10^{-6} Torr. The CO gas pressure was established by continuously admitting fresh CO while pumping to give a constant flow. The CO was pumped out immediately on termination of the implant.

The procedure for the simultaneous ion implantation and AES analysis was as follows. Initially, the ion beam would be incident on the manipulator Faraday cup and the current measured on the rotating wire would be correlated with the current density measured on the Faraday cup. Then the ion beam would be turned off and the substrate placed into position so that the ion and electron beams would be incident on the sample surface at the focal point of the cylindrical mirror analyzer. Auger spectra were obtained using a 3 keV, $50\,\mu A$ electron beam (70 mA cm^{-2}), with a cylindrical mirror analyzer modulation of 3.7 V (8 V for silicon) and the spectrometer set to scan repetitively the Auger signals of interest throughout the entire implanta-

tion. The Auger data were quantified using sensitivity factors that were either obtained from the *Handbook of Auger Electron Spectroscopy* [9] or determined from reference FeTi, TiC, air-oxidized iron and silicon samples. The sensitivity factor values were 0.45 for Ti(419 eV), 0.28 for Nb(167 eV), 0.18 for Fe(651 eV), 0.32 for O(503 eV), 0.53 for carbidic C(272 eV), 0.20 for adventitious C(272 eV) and 0.06 for Si(1619 eV). The silicon sensitivity factor took into account the different modulation voltage used. The separation of the carbon Auger signal into carbidic and adventitious (organic) components was based on the peak shape in the $dN(E)/dE$ mode spectra. For all samples the carbidic carbon sensitivity factor was used except for the initial analysis prior to the start of the implantation. The sensitivity factors $S(i)$ for each element i were used to calculate atomic fractions $X(i)$ from the AES intensities $I(i)$ using the expression

$$X(i) = \left\{\frac{I(i)}{S(i)}\right\} \Big/ \left\{\sum_j \frac{I(j)}{S(j)}\right\} \tag{1}$$

Equation (1) provides concentrations, averaged over the escape depth of the Auger electrons

40

542

(1-2 nm), which are believed to have a relative accuracy of better than ±20%.

The procedure for the sequential ion implantation and PIXE was as follows. A mixture of hydrogen and chlorine gas was introduced into the ion source to provide a source for both the metal and the proton beams. To switch between the two beams required changing the implanter analyzing magnet and readjusting the quadrupole lens to provide optimum beam focus. The metal ion beams entered the target chamber through the aperture 3.2 mm in diameter whereas the proton beam entered the chamber through the aperture 1.6 mm in diameter to ensure that the PIXE analysis was conducted totally within the implanted area. During metal ion implantation the beam was rastered to ensure uniformity over the 8 mm^2 implanted area. The beams were set up using a calibration sample identical with those used in this study. The metal ion beam current density as measured on the manipulator Faraday cup was correlated with the suppressed (+100 V) ion beam current measured on the calibration sample. The total proton beam current measured on the Faraday cup in front of the viewport was correlated with the suppressed proton beam current measured on the calibration sample. Thus, during ion implantation, the total measured charge incident on the sample could be converted to fluence and, during PIXE measurements, the total measured charge could be converted to actual charge for X-ray yield calculations. During an experiment an initial PIXE measurement would be made to establish the thickness of the iron film. Then sequential Ti$^+$ or Nb$^+$ ion implants to preselected fluences and PIXE analyses would be made until the total desired fluence was attained.

For PIXE the integrated Fe L, Fe K, Ti K and Nb L X-ray peaks obtained on a multichannel analyzer were divided by the number of microcoulombs of protons incident on the sample to give an uncorrected X-ray yield. This yield could be converted to an absolute yield Y_a by taking into account the solid angle subtended by the detector and the transmission of the X-rays through the beryllium entrance window. An integral X-ray yield equation was used to relate quantitatively the experimentally measured value of Y_a to the thickness of the iron expressed in atoms per

square centimeter [10]. This integral yield equation takes into account the depth dependence of the X-ray production cross section and the X-ray attenuation. The results of these calculations are shown in Fig. 2 for both the Fe L and the Fe K lines excited by 190 keV protons. The curves are asymptotic to the thick target X-ray yields. The initial thicknesses of the iron films as measured by PIXE agreed to within 10% of the 200 nm thickness measured by the quartz crystal oscillator. In each instance the PIXE yield was normalized to coincide exactly with that for a film 200 nm (1.7×10^{18} atoms cm^{-2}) thick. The curves in Fig. 2 were then used to determine the iron film thickness during the course of the ion implantation. Because of the better counting statistics, data are only presented for measurements of the Fe L line.

The retained dose ϕ_r of titanium or niobium was obtained using the equation [10]

$$\phi_r = \frac{Y_a \cos \theta}{\sigma_X(E_0)} \qquad (2)$$

where $\theta = 30°$ and $\sigma_X(E_0)$ is the Ti K or Nb L X-ray production cross section at $E_0 = 190$ keV. Values of σ_X were obtained directly or by interpolation of available data [11]. This equation neglects the energy loss of the protons in traversing the implanted layer and the attenuation of the X-rays exiting the sample. Computer calculations of the projected range R_p and straggling ΔR_p of 190 keV Ti$^+$ and Nb$^+$ ions in iron are as follows: for titanium, $R_p = 59$ nm and $\Delta R_p = 29$ nm; for niobium,
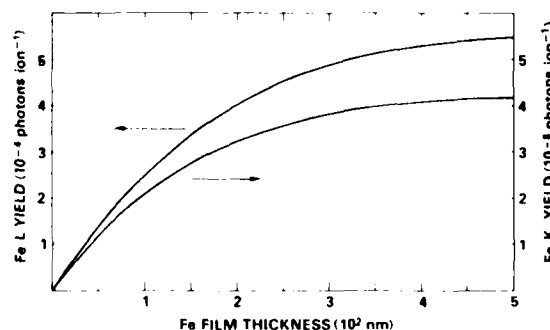

Fig. 2. Fe L and Fe K absolute X-ray yields as a function of iron film thickness for excitation by 190 keV protons. The curves were generated by an integral approximation to the theoretical X-ray yield equation.

R_p = 35 nm and ΔR_p = 15 nm. The transmission of Ti K and Nb L through layers of thicknesses equivalent to the projected ranges is virtually 100%. With respect to proton energy loss, it is estimated that the maximum systematic error associated with using eqn. (2) to measure the retained dose is 12%.

3. RESULTS AND DISCUSSION

Figures 3(a) and 3(b) show the iron film thickness (expressed in atoms cm^{-2}) and the retained titanium as a function of Ti^+ ion fluence for implantations performed at 8×10^{-9} Torr (hereinafter referred to as ultrahigh vacuum) and in CO at a pressure of 1×10^{-6}
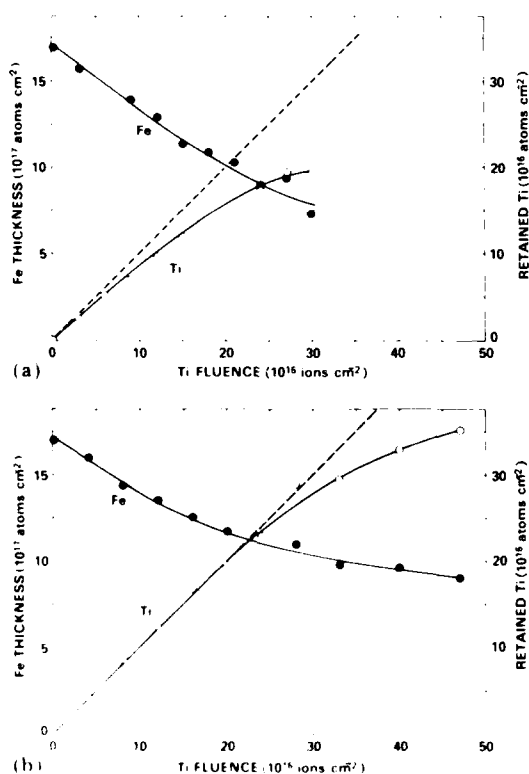
Torr respectively. Each data point represents a point where the implantation was interrupted and a PIXE measurement was taken. The broken line in each figure represents the retained dose of titanium at the zero-sputtering limit. Lines were hand fitted to the data points using a French curve. Figure 4 shows the composition of the sample surfaces as determined by AES as a function of Ti^+ ion fluence for implants performed at both pressures. These measurements were done at a different location of the same sample on which the PIXE measurements were conducted.

From Fig. 3 it is evident that, for the ultrahigh vacuum implant, the retained titanium deviates from the zero-sputtering limit early in the implant and that it is approaching a

Fig. 3. Iron thickness and retained dose of titanium as a function of fluence for the implantation of 190 keV Ti^+ ions into an iron film 200 nm thick electron beam deposited onto an Si(100) substrate (a) for an implantation performed at a pressure of 8×10^{-9} Torr and (b) for an implantation performed with the chamber backfilled with CO to a pressure of 1×10^{-6} Torr: ·····, expected retained dose in the zero-sputtering limit.

Fig. 4. Atomic concentrations as determined by AES for iron, titanium, carbon, oxygen and silicon as a function of fluence for the implantation of 190 keV Ti^+ ions into an iron film 200 nm thick electron beam deposited onto an Si(100) substrate (a) for an implantation performed at a pressure of 8×10^{-9} Torr and (b) for an implantation performed with the chamber backfilled with CO to a pressure of 1×10^{-6} Torr: ○, retained dose of titanium as determined by PIXE.

544

steady state value after 3×10^{17} Ti$^+$ ions cm^{-2}. For the implant in CO, however, the retained titanium follows the zero-sputtering limit curve up to a fluence of 2×10^{17} Ti$^+$ ions cm^{-2} and is continuing to increase at a fluence of almost 5×10^{17} Ti$^+$ ions cm^{-2}. At 3×10^{17} Ti$^+$ ions cm^{-2} the retained titanium is 40% higher for the implant in CO. From the iron data, it is evident that the sputtering rate for iron is reduced for the implant in CO. It is possible to estimate elemental sputtering yields S from Fig. 3 by measuring the slope of the iron curve at any fluence. This gives the number of iron atoms removed per incident titanium ion. It is also possible to estimate the titanium elemental sputtering yield at any fluence by taking the difference between the slopes of the zero-sputtering limit curve and the experimentally determined retained dose curve. If the retained dose curve is flat, then $S_{Ti} = 1$. The calculated iron sputtering yields S_{Fe} are 3.5 atoms ion^{-1} and 1.8 atoms ion^{-1} and the calculated titanium sputtering yields S_{Ti} are 0 atoms ion^{-1} and 0.7 atoms ion^{-1} at the zero-fluence limit and 3×10^{17} Ti$^+$ ions cm^{-2} respectively for the implant in ultrahigh vacuum. For the implant in CO the S_{Fe} values are 3.0 atoms ion^{-1} and 1.0 atoms ion^{-1} and the S_{Ti} values are 0 atoms ion^{-1} and 0.3 atoms ion^{-1} at the zero-fluence limit and 3×10^{17} Ti$^+$ ions cm^{-2} respectively. Thus, although the initial iron sputtering yields were similar for the implants at both pressures, after a fluence of 3×10^{17} Ti$^+$ ions cm^{-2} the total sputtering yield for iron and titanium was a factor of 2 less for the implant in CO.

For the AES measurements, it was intended that the implantation be allowed to proceed until the silicon substrate started to be uncovered. For the implant in ultrahigh vacuum, this occurred at a fluence of approximately 5.5×10^{17} Ti$^+$ ions cm^{-2} as shown in Fig. 4(a). However, for the implant in CO, no silicon was observed even after a fluence of almost 1.5×10^{18} Ti$^+$ ions cm^{-2} (at which time the filament in the electron gun burned out, terminating the experiment involuntarily). A subsequent PIXE analysis of the implanted area indicated that the retained dose had increased substantially above what it was at 5×10^{17} Ti$^+$ ions cm^{-2}. Combining these data with those from Fig. 3(a) produced the curves shown in Fig. 5. From the slopes of the lines connecting the last two data points in Fig. 5
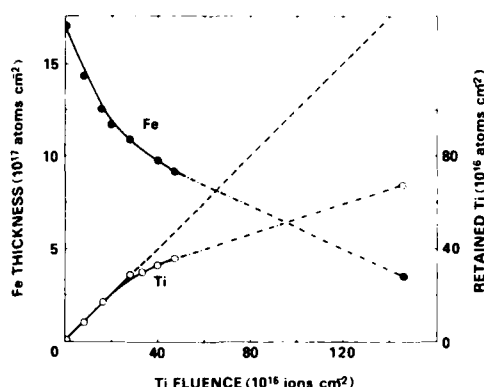
Fig. 5. Iron thickness and retained dose of titanium as a function of fluence for 190 keV Ti$^+$ ion implantation with the chamber backfilled with CO to a pressure of 1×10^{-6} Torr, showing the final two data points obtained at a fluence of 1.46×10^{18} Ti$^+$ ions cm^{-2}.

(shown as chain lines because the exact shape is unknown), it was possible to calculate an iron sputtering yield S_{Fe} of 0.6 atoms ion^{-1} and a titanium sputtering yield S_{Ti} of 0.6 atoms ion^{-1}. The total sputtering yield of the metal species was thus the same at this very high fluence as it was at 3×10^{17} Ti$^+$ ions cm^{-2}.

From the AES data, it was determined that the adventitious carbon layer and the air-formed oxide layer were sputter removed after a fluence of $(1-2) \times 10^{16}$ Ti$^+$ ions cm^{-2}. With increasing fluence the titanium surface concentration increased at a faster rate for the implant in ultrahigh vacuum, with a steady state surface concentration not being reached until a fluence of more than 5×10^{17} Ti$^+$ ions cm^{-2}, at which time the silicon substrate started to be exposed. For the implant in CO, the carbon and oxygen surface concentrations continued to increase up to the very high fluences, with steady state values not being achieved for titanium, carbon or oxygen at 1.5×10^{18} Ti$^+$ ions cm^{-2}. The iron surface concentration was significantly reduced for the implant in CO, presumably as a result of atomic dilution and Auger electron attenuation caused by the presence of the carbon and oxygen. However, the titanium-to-iron concentration ratio was the same for the implants in ultrahigh vacuum and CO up to a fluence of 5×10^{17} Ti$^+$ ions cm^{-2}. Also shown in Fig. 4 are the data points for the retained dose of

43

titanium as determined by PIXE. For the implant in CO, the retained dose parallels the titanium surface concentration whereas, for the implant in ultrahigh vacuum, the retained dose increases at a much faster rate than the surface concentration does.

Since niobium is also a very reactive metal, it was expected that Nb^+ ion implantation into the iron films would produce results similar to the titanium implantation, *i.e.* lower sputtering yields and higher retained doses for the implantation in CO, with the effect being even more pronounced because of the increased mass and higher sputtering yield of niobium. However, the results as presented in Figs. 6 and 7 showed that the effects were considerably less pronounced than for the titanium. The PIXE results

shown in Fig. 6 indicate that, although the shapes of the retained dose curves were different, the retained dose did achieve a steady state value of virtually the same level and at similar fluences for both cases. The AES analyses were carried out to higher niobium fluences as shown in Fig. 7. A final PIXE analysis was performed on these samples after an implant fluence of 3.6×10^{17} Ti^+ ions cm^{-2} for the ultrahigh vacuum implant and 4.3×10^{17} Ti^+ ions cm^{-2} for the implant in CO. As shown in Fig. 7, the retained dose of niobium remained at a constant value, indicating that steady state had been achieved at a fluence between 1.8 and 2.0×10^{17} Ti^+ ions cm^{-2} for implants at both pressures. The AES data show substantial incorporation of carbon and oxygen into the near-surface region for the
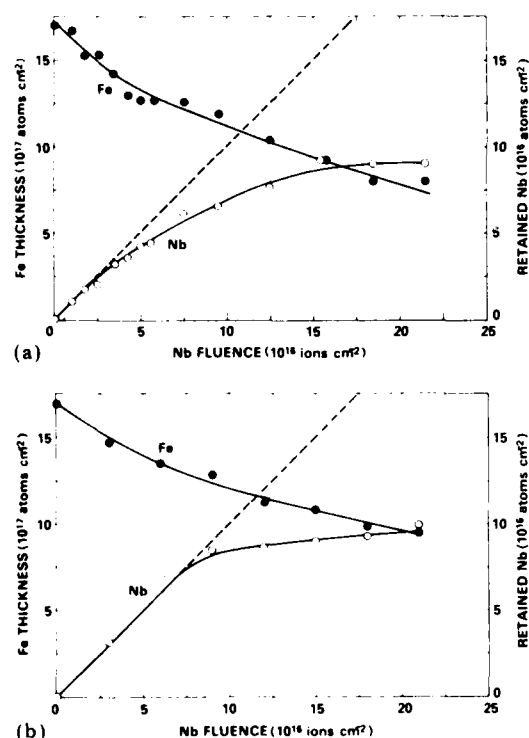
Fig. 6. Iron thickness and retained dose of niobium as a function of fluence for the implantation of 190 keV Nb^+ ions into an iron film 200 nm thick electron beam deposited onto an Si(100) substrate (a) for an implantation performed at a pressure of 8×10^{-9} Torr and (b) for an implantation performed with the chamber backfilled with CO to a pressure of 1×10^{-6} Torr; -----, expected retained dose in the zero-sputtering limit.
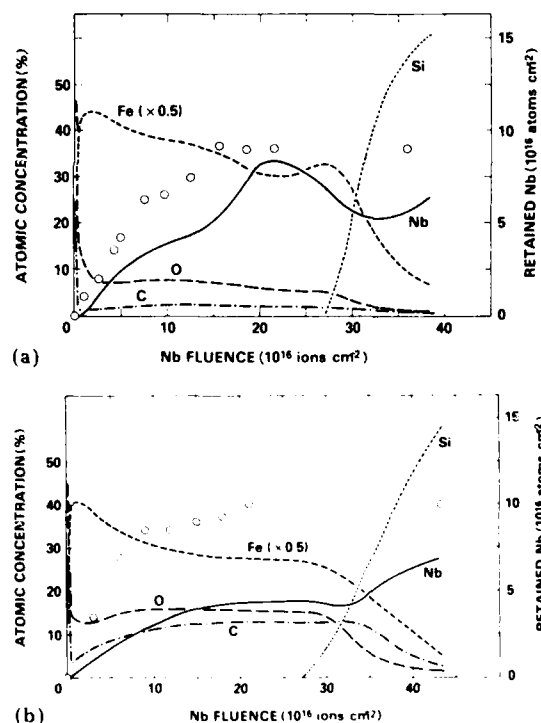
Fig. 7. Atomic concentrations as determined by AES for iron, niobium, carbon, oxygen and silicon as a function of fluence for the implantation of 190 keV Nb^+ ions into an iron film 200 nm thick electron beam deposited onto an Si(100) substrate (a) for an implantation performed at a pressure of 8×10^{-9} Torr and (b) for an implantation performed with the chamber backfilled with CO to a pressure of $\times 10^{-6}$ Torr: O, retained dose of niobium as determined by PIXE.

546

implant in CO. The apparent higher niobium concentration for the ultrahigh vacuum implant may be an artifact of the method for calculating atomic per cent concentrations from the Auger data. If, in the CO implant, the niobium is present mainly as a carbide or oxide, the niobium sensitivity factor could be changed significantly. No NbC calibration sample was available to verify this.

Tables 1 and 2 summarize the elemental sputtering yields calculated for the iron and implanted elements at different fluences for the two implant pressures. For both the titanium and the niobium implantation in CO, there is a significant reduction in the total sputtering yield compared with the implantation in ultrahigh vacuum. Also, even for the ultrahigh vacuum implants, the total sputtering yield for the metal species decreases by 30% for titanium and almost 50% for niobium after implantation to 3×10^{17} ions cm^{-2} and 2×10^{17} ions cm^{-2} respectively. This could possibly be explained by an increase in surface roughness during the implantation. It has been observed in other studies conducted at this laboratory that, for tantalum implantation into high purity iron

samples, the generation of surface roughness was substantially greater for an implant done in ultrahigh vacuum than for an implant done with the chamber backfilled with CO.

It is clear that the addition of CO to the target chamber to pressures consistent with those used in many implantation systems can drastically alter the sputtering yields and, for titanium, can result in significantly increased retained doses. The equation derived by Sigmund [12] for the backward sputtering yield of kiloelectronvolt ions is

$$S = \text{constant} \times \frac{S_n(E) \, \alpha(M_2/M_1)}{U_0} \qquad (3)$$

where $S_n(E)$ is the nuclear stopping power of the incoming ion of initial energy E, U_0 is the surface binding energy and $\alpha(M_2/M_1)$ is a function essentially of the ratio of the target mass M_2 to projectile mass M_1. The nuclear stopping power is relatively insensitive to additions of light elements such as carbon. For example, the calculated nuclear stopping power for 190 keV Ti^+ ions on iron is 1.28×10^3 keV μm^{-1} whereas it is 1.32×10^3 keV μm^{-1} for 190 keV Ti^+ ions on Fe_3C. Therefore the large changes in the values of S for im-

TABLE 1

Summary of the sputtering yields S, expressed in atoms per ion, calculated from the slopes of the iron thickness and retained dose curves obtained by proton-induced X-ray emission for 190 keV Ti^+ ion implantation

	S for implants in ultrahigh vacuum at the following fluences		S for implants in CO at 1×10^{-6} Torr at the following fluences		
	0 Ti^+ ions cm^{-2}	3×10^{17} Ti^+ ions cm^{-2}	0 Ti^+ ions cm^{-2}	3×10^{17} Ti^+ ions cm^{-2}	1.4×10^{18} Ti^+ ions cm^{-2}
Fe	3.5	1.8	3.0	1.0	0.6
Ti	0	0.7	0	0.3	0.6

TABLE 2

Summary of the sputtering yields S, expressed in atoms per ion, calculated from the slopes of the iron thickness and retained dose curves obtained by proton-induced X-ray emission for 190 keV Nb^+ ion implantation

	S for implants in ultrahigh vacuum at the following fluences		S for implants in CO at 1×10^{-6} Torr at the following fluences	
	0 Nb^+ ions cm^{-2}	2×10^{17} Nb^+ ions cm^{-2}	0 Nb^+ ions cm^{-2}	2×10^{17} Nb^+ ions cm^{-2}
Fe	9.2	4.0	6.4	2.4
Nb	0	1	0	0.9

plantation in a CO environment must be related to changes in the surface binding energy. Additional experiments are planned to investigate these effects more fully and to correlate them with theoretical predictions.

4. CONCLUSIONS

For titanium implantation into iron, the addition of CO to the target chamber can significantly alter the sputtering yield of the substrate and the retained dose that can be achieved. For the production of wear-resistant surface layers, this effect could be taken advantage of, with deliberate introduction of a reactive gas such as CO into the implantation chamber possibly to increase the thickness of the amorphous carburized layer and to increase the concentration of the implanted element for a given fluence. For corrosion applications, this effect must also be considered in that the formation of carbides in the near-surface region could have a deleterious effect on corrosion resistance.

The assumption that a similar effect will occur for implantation of other group IVB and VB elements is not true, at least for niobium. Although the sputtering yield of the substrate is changed, the total retained dose is not affected by the addition of CO to the implantation chamber.

Predictive models of the surface concentration of implanted atoms as a function of fluence and the fluence required to achieve steady state must be modified to take into account the changes in surface binding energy and surface compound formation resulting from interactions with reactive gases present in the target chamber.

REFERENCES

1 G. K. Hubler, in S. T. Picraux and W. J. Choyke (eds.), *Metastable Materials Formation by Ion Implantation, Materials Research Society Symp. Proc.*, Vol. 7, Elsevier, New York, 1982, p. 341.
2 I. L. Singer, in G. K. Hubler, C. W. White, O. W. Holland and C. R. Clayton (eds.), *Ion Implantation and Ion Beam Processing of Materials, Materials Research Society Symp. Proc.*, Vol. 27, Elsevier, New York, 1984, p. 585.
3 I. L. Singer, *J. Vac. Sci. Technol. A, 1* (1983) 419.
4 I. L. Singer, C. A. Carosella and J. R. Reed, in R. E. Benenson, E. H. Kaufmann, G. L. Miller and W. W. Scholz (eds.), *Proc. 2nd Int. Conf. on Ion Beam Modification of Materials, Albany, NY, 1980*, in *Nucl. Instrum. Methods, 182-183* (1981) 934.
5 I. L. Singer and T. M. Barlak, *Appl. Phys. Lett., 43* (1983) 457.
6 R. H. Bassel, K. S. Grabowski, M. Rosen, M. L. Roush and F. Davarya, to be published.
7 D. A. Baldwin, B. D. Sartwell and I. L. Singer, in J. W. Mayer (ed.), *Proc. 4th Int. Conf. on Ion Beam Modification of Materials, Ithaca, NY, July 16-20, 1984*, in *Nucl. Instrum. Methods*, to be published.
8 G. K. Hubler, I. L. Singer and C. R. Clayton, *Proc. Int. Conf. on Surface Modification of Metals by Ion Beams, Heidelberg, September 17-21, 1984*, in *Mater. Sci. Eng., 69* (1985) 203.
9 L. E. Davis (ed.), *Handbook of Auger Electron Spectroscopy*, Physical Electronics Industries, Eden Prairie, MN, 1976.
10 A. B. Campbell and B. D. Sartwell, *Thin Solid Films, 64* (1979) 445.
11 J. W. Mayer and E. Rimini (eds.), *Ion Beam Handbook for Material Analysis*, Academic Press, New York, 1977.
12 P. Sigmund, *Phys. Rev., 184* (1969) 383.

Section I.F

SPUTTERING AND MIGRATION DURING Ta IMPLANTATION OF Fe

K.S. Grabowski[1]
F.D. Correll[2]
F.R. Vozzo[1]*

[1]Materials Modification & Analysis Branch
Condensed Matter & Radiation Sciences Division
Naval Research Laboratory

[2]Physics Department
U.S. Naval Academy
Annapolis, MD 21402

* NRC Research Associate

SPUTTERING AND MIGRATION DURING Ta IMPLANTATION OF Fe

K.S. GRABOWSKI, F.D. CORRELL * and F.R. VOZZO

Naval Research Laboratory, Washington, DC 20375, USA

This work evaluates the importance of sputtering and diffusion to the measured concentration profiles of Ta implanted into Fe. The samples consisted of thin Fe films deposited on sapphire or glass substrates and implanted with 150 keV Ta ions to fluences of $(1-18) \times 10^{16}$ ions/cm^2. Rutherford backscattering analysis provided measurements of the retained dose, the sputtering rate of Fe and Ta, and the evolution of the Ta depth distribution, all as a function of ion dose. These measurements indicated that preferential removal by sputtering combined with atomic migration led to a 50% increase in the saturation retained dose of Ta, when compared to the value predicted by simple theory without these two effects.

1. Introduction

Ta implantation of steels is currently of practical interest because of its ability to improve resistance to corrosion [1] and wear [2]. However, insufficient knowledge of sputtering during Ta implantation has prevented satisfactory prediction of Ta retention versus ion dose [3], and hence of optimum conditions for processing. In this work the sputter coefficient, S, mean projected range, R_p, range straggling, σ, and depth profiles of Ta were experimentally determined following Ta implantations into Fe films. These results are compared to different model calculations.

Both phenomenological and physical models can be used to describe the ion implantation process. The phenomenological model for ion retention by Liau and Mayer produces satisfactory agreement with experimental results [4] but provides little information on the operant physical mechanisms. A number of important physical mechanisms which influence the implantation process have recently been reviewed by Andersen [5], and many of them have been included in various implantation models. Models based on computer simulation [6] and solutions to the diffusion equation ([7] and references therein) have both been described. For this work both approaches were utilized.

2. Experiment

Thin films of Fe were prepared by e-beam evaporation onto substrates of either sapphire ($0.5 \times 6 \times 12.5$ mm) or glass ($1 \times 7 \times 25$ mm). Films on sapphire substrates were about 200 nm thick and the one film on

---

* Physics Department, US Naval Academy, Annapolis, MD 21402, USA.

glass was about 400 nm thick. Their impurity content was determined by Auger electron spectroscopy (AES) with Ar sputtering, and also by nuclear reaction analysis (NRA) using 2.42 MeV ^{3}He as the probe [8]. The 200 nm films were found to have an O composition gradient from about 8 at.% near the surface to about 4 at.% at 125 nm, and a uniform C content of about 1.5 at.%. The 400 nm film had about 7 at.% O and 0.5 at.% C throughout.

All samples were secured by Ag paint to a water-cooled support to maintain their temperature below 50°C during implantation. Only the central one-third of each sapphire-supported sample was implanted. Both ends were masked by razor blades to provide a sharp edge for sputter-erosion measurements and to allow determination of the original Fe film thickness. Only the last 2 mm from one end of the 400 nm thick film were so masked.

Six samples were implanted to doses of $(1-18) \times 10^{16}$ Ta/cm^2 with 150 keV Ta$^+$ ions. The 400 nm thick film was used for the highest-dose implantation. Ion fluxes were within about 50% of 4.9 μA/cm^2 during all the implantations, and the target chamber pressure was typically 1.5×10^{-4} Pa. This produced an impingement ratio of Ta ions to gas molecules of about 0.07 at the sample surface.

Following Ta implantation all the films were analyzed by Rutherford backscattering spectroscopy (RBS). These measurements were performed using a 2.0 MeV He beam, a scattering angle of 135°, and both normal incidence and 15° grazing exit geometries. The ion beam, detector, and target normal all lay in the same plane. A modified version of Niiler's spectrum fitting program, PROFILE [9], was used to determine the depth distribution of Ta in the implanted specimens. Both energy-loss straggling and detector resolution were taken into account. The retained dose of Ta and the

quantity of Fe sputtered away were evaluated from the integrated intensity of the backscattered signal from Ta and Fe in the film. The impurity content of implanted films was also analyzed by AES and NRA. The RBS measurements of initial film thickness and material removed by sputter erosion were complemented by step-height measurements using both a stylus and a double-pass interferometer.

3. Theory

The implantation of Fe by various doses of Ta was modelled by two different computer programs. Initially, Davisson's IMPLNT code [10] was used. This code is based on the approach of Kräutle [6], but additionally can include preferential sputtering. IMPLNT does not include diffusion. To consider diffusion (actually ion mixing in this case), the program of Farkas et al. [11] was used, which does not explicitly include changes in the ion range or straggling. To make the two calculations comparable, a constant ion range and straggling were used in both programs. The diffusion coefficient, when used, was considered constant for all depths.

4. Results and discussion

4.1. Range, straggling, and sputtering

Three primary parameters for modelling of Ta implantation of Fe were measured in this work. The projected range, R_p, and straggling, σ, were measured to be 20.6 nm and 12.2 nm, respectively, from RBS of the 1×10^{16} Ta/cm^2 sample. These numbers include corrections for finite target sputtering and the presence of oxide on the sample surface at the start of implantation. They should be compared with an R_p of 20.2 nm and a σ of 7.0 nm predicted by EDEP1 [12] calculations.

A summary of sputter coefficient measurements is shown in fig. 1. The solid line represents $S = 6$, the number used in all modelling for this work. RBS directly measured S since it measures in at./cm^2 units. The statistical accuracy of the RBS measurements for Ta, Fe, and the total was better than 1%. The other measurements of S were based on sputter-erosion step heights, which require knowledge of the target density. The density of pure Fe was assumed. The stylus measurements were reproducible within about 5 nm, while the interferometer measurements were accurate within about 10 nm. A constant total sputtering coefficient of 6 appears somewhat low but in acceptable agreement with all but the highest fluence data. The larger disagreement there is not completely understood, but may be associated with the uniqueness of the 400 nm thick sample. It alone was on a glass substrate and was evaporated separately.
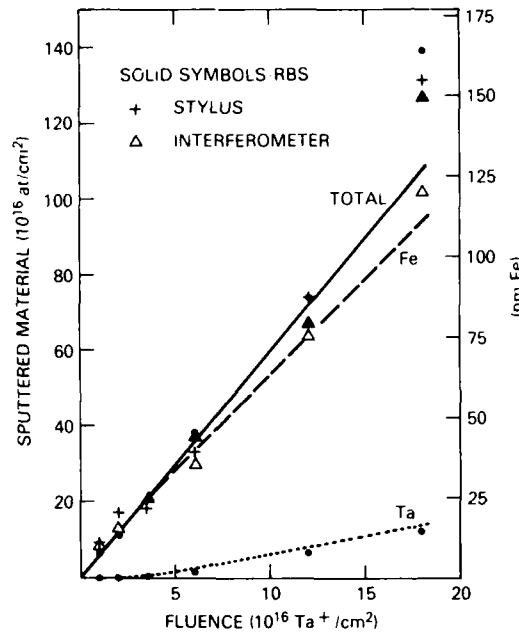
Fig. 1. Sputtering from Ta implantation of Fe. Solid line represents $S = 6$. Values for Ta, Fe and the total (Ta + Fe) provided by RBS. Step height measurements were converted to total quantity of material removed using the density of bulk Fe. Dashed and dotted lines show predictions of IMPLNT code for $S = 6$, $R_p = 20.6$ nm, and $\sigma = 12.2$ nm. These values used in all subsequent IMPLNT calculations.

The possibility of preferential sputter removal during Ta implantation was evaluated by comparing IMPLNT calculations using constant $S = 6$ (and measured R_p and σ) against RBS measurements of Ta and Fe removal as a function of Ta dose. The IMPLNT calculations are shown by dotted and dashed lines in fig. 1. There is a tendency for Ta to be sputtered less and Fe more than predicted by IMPLNT. This suggests that preferential sputtering of Fe may have occurred.

4.2. Ta retention

Fig. 2 illustrates the disagreement between experiment and IMPLNT calculations of Ta retention as a function of fluence. These experimental results are similar to those previously reported for Ta implantation of AISI-52100 and AISI-M50 [3], two martensitic bearing steels. The IMPLNT calculation used measured values for R_p, σ, and S. Including preferential sputtering of Fe while maintaining an S of 6 in the model could not significantly improve the agreement. Clearly the measured 50% enhancement in saturation retained dose indicates something is lacking from the IMPLNT model.

IX. SPUTTERING/SIMS

49

Fig. 2. Retention of implanted Ta in Fe. Symbols represent RBS measurements of retained Ta. Curve shows prediction of IMPLNT code.

4.3. Ta depth distribution

To evaluate the shortcomings of IMPLNT, Ta depth distributions were investigated as a function of ion dose. The profiles calculated by IMPLNT using measured R_p, σ, and S are shown in fig. 3. Steady state is obtained at a dose of about 12×10^{16} Ta/cm^2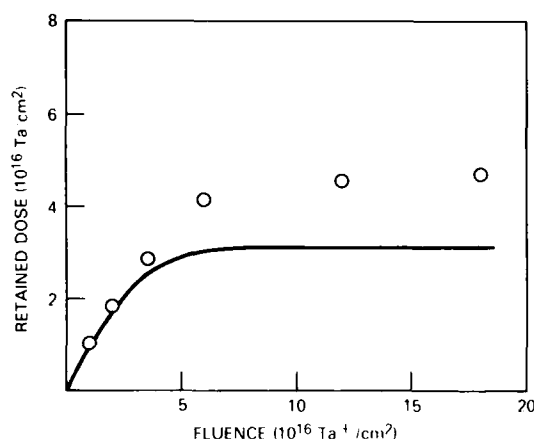. The maximum Ta concentration of 15.9% occurs at the surface, and is less than the normally expected value of $1/S$ (16.7 at.%) because of the large value of σ relative to R_p. This ratio is large enough that approximately 5% of the low-fluence Gaussian distribution resides outside the sample surface.

The experimental Ta distributions were obtained by
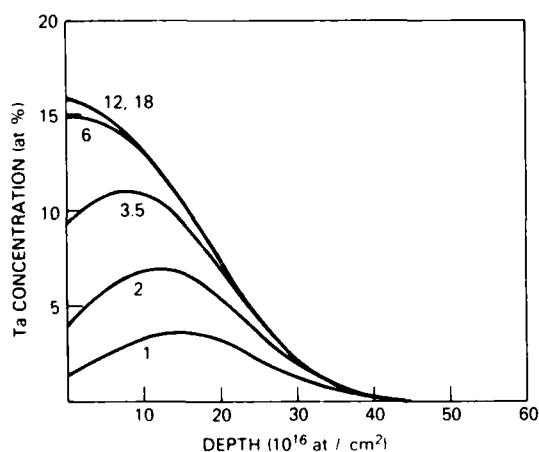
Fig. 3. Ta depth profiles calculated with IMPLNT code for fluences of $(1-18) \times 10^{16}$ Ta/cm^2.
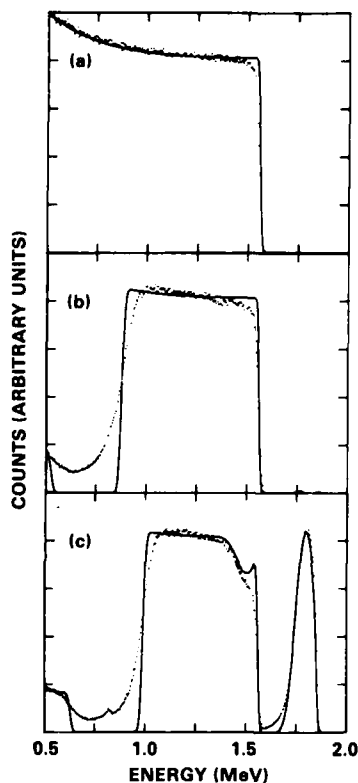
Fig. 4. RBS spectra for pure and Ta-implanted Fe. Points represent measured spectra, lines show calculated spectra for: (a) pure, bulk Fe; (b) 200 nm thick Fe film on sapphire; (c) same film after implantation of 6×10^{16} Ta/cm^2.

successively guessing the Ta distribution until satisfactory agreement between measured and calculated RBS spectra was obtained. Fig. 4 shows some examples of the quality of this fitting procedure. All three spectra are for the 15° grazing exit sample geometry. Surface signals from Ta, Fe and O would appear at 1.85, 1.56, and 0.83 MeV, respectively.

As can be seen in fig. 4a for a polished, pure, bulk Fe standard, the fits obtained were not perfect. The rounded corner experimentally seen at the surface is not completely understood, but is believed to be partially due to native oxide on the sample and partially to surface roughness effects [13].

In fig. 4b, additional discrepancies between measured and fit spectra are found for the as-deposited pure Fe film. Besides the rounding of the corner at the surface, there is a larger slope to the experimental Fe yield throughout the film. This disagreement can be eliminated by adding an O gradient to the film, at levels consistent with those measured by AES and NRA. The much more diffuse back edge to Fe in the experimental
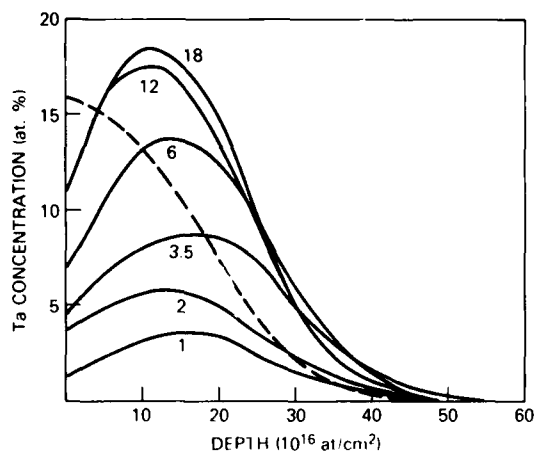
Fig. 5. Ta depth profiles deduced from RBS measurements using PROFILE code. Solid lines show profiles for Ta fluences of $(1-18) \times 10^{16}$ Ta/cm^2. Apparent depletion near surface of high fluence samples probably due to surface roughness, contamination, and C incorporation. Eliminating these might double surface Ta concentration. Dashed line shows IMPLNT prediction for 18×10^{16} Ta/cm^2.

Fig. 6. Ta depth profiles calculated with code of Farkas et al., for 18×10^{16} Ta/cm^2. Solid lines include diffusion, with indicated values for D and $\sigma = 7.0$ nm. Dashed line represents $D = 0$ and $\sigma = 12.2$ nm. Dotted line shows RBS determined profile. $J = 2.7 \times 10^{13}$ Ta cm^{-2} s^{-1} for all curves.

spectra is believed to be caused by a Fe-film thickness variation. A random variation in film thickness, with a standard deviation of about 9 nm, would explain this observed discrepancy.

A representative fit from the 6×10^{16} Ta/cm^2 implanted sample is shown in fig. 4c. This fit only considered Ta and Fe atoms to be present in the sample. Besides the discrepancies described in fig. 4b, there appears to be an additional decrease in the experimental Fe yield between the surface and the peak in the Ta distribution. AES analysis indicated that considerable carbon enrichment occurred in just this region of all the samples implanted with Ta to doses in excess of about 2×10^{16}/cm^2. This result is consistent with previous work by Singer on Ta-implanted AISI-52100 bearing steel [14].

The results of this fitting procedure, considering only Ta and Fe to be present in each sample, is shown by the solid lines in fig. 5. If the Ta signal dilution effects from surface roughness, and C and O in the samples were to be included in the fitting procedure it is expected that the surface concentration of Ta for the three highest doses would increase by nearly a factor of 2 and the profiles would move about 10% closer to the surface. Also shown in fig. 5 is the steady state distribution expected from IMPLNT.

Examination of fig. 5 and further comparisons with fig. 3 indicates that implanted Ta penetrates more deeply into the sample than predicted by IMPLNT, for Ta doses in excess of 2×10^{16}/cm^2. Furthermore, the maxi-

mum Ta concentration at steady state exceeds $1/S$, using the measured value for S of 6.

To obtain the observed peak Ta concentrations at steady state without preferential sputtering or migration would require an S of about 5.6. This value produces even larger disagreement with the RBS measurements of fig. 1, especially for the case of the highest-dose implanted sample, and is therefore unlikely to be correct. Instead, preferential sputter removal of Fe during implantation resulting in a larger Ta concentration is more likely to have occurred. Such a process would only slightly decrease the total sputter coefficient, S, but would significantly delay Ta removal, thereby improving agreement with the Ta sputtering data in fig. 1 and improving agreement in fig. 5. Such preferential removal of Fe may have been influenced by the observed presence of carbon near the surface, considering that Ta is more reactive with C then is Fe. Unfortunately, we are not yet able to determine the degree of preferential Fe removal which may have occurred.

The greater penetration of Ta at high doses than that predicted by IMPLNT suggests that enhanced migration by ion mixing occurred in these samples. Additional modelling of Ta concentration profiles was performed using the code of Farkas et al., including the effect of diffusion coefficients of $(1-6) \times 10^{-15}$ cm^2/s and experimental beam fluxes. In this modelling, a σ of 7.0 nm for the Ta distribution (as calculated by EDEP1) was typically used, since ion mixing may have contributed to the straggling value measured for Ta.

IX. SPUTTERING/SIMS

51

The solid lines in fig. 6 show the calculated Ta distributions for the highest dose case and three different diffusion coefficients. The dashed line shows the predicted profile without diffusion and with the measured straggling of 12.2. nm. The dotted line shows the measured profile from RBS. Qualitatively, it appears that a D of about 3×10^{-15} cm^2/s would be necessary in this case, at least within the damage region, to allow sufficient penetration of Ta to occur and provide agreement with the RBS result. This indicates that a D/J ratio of about 11×10^{-29} cm^4 would be necessary, for the flux. J, of 2.7×10^{13} Ta cm^{-2}s^{-1} appropriate to this sample.

This value of D/J (or Dt/ϕ) should be compared to the value which can be obtained from the work of Bøttiger et al. [15], on ion mixing of a Pt marker layer in Fe by 150 keV Ar ions. They measured the increase in variance of the Pt marker distribution as a function of dose. Since a variance increase is equivalent to $2Dt$, their variance data can produce a Dt/ϕ value. One obtains a maximum value of 2.5×10^{-29} cm^4 for room temperature implantation and low doses, but a value about 3 times lower for higher fluences. By scaling these values upward by a factor of about 5 for the increased efficiency of damage deposition by Ta ions (at the surface), we find our estimated value for Dt/ϕ reasonable although slightly larger when compared to the results of Bøttiger et al.

5. Conclusions

The measured depth profiles of Ta indicate that ion mixing and probably preferential removal of Fe occur during Ta implantation of Fe. This leads to about a 50% increase in the maximum retained dose of Ta. Significant C incorporation near the surface also occurs for doses approaching the steady-state condition. Such incorporation may have influenced the sputtering process. Further modelling which includes preferential removal and depth-dependent diffusion is necessary before ade-quate predictions will be available for the retention of Ta ions as a function of dose.

References

[1] V. Ashworth, D. Baxter, W.A. Grant and R.P.M. Procter, Corr. Sci. 17 (1977) 947.
[2] N.E.W. Hartley and J.K. Hirvonen, Nucl. Instr. and Meth. 209/210 (1983) 933 (Proc. 3rd Int. Conf. Ion Beam Modification of Materials).
[3] K.S. Grabowski, N.E.W. Hartley, C.R. Gossett and I. Manning, Mat. Res. Soc. Symp. Proc. 27 (1984) 615.
[4] Z.L. Liau and J.W. Mayer, in: Treatise on Materials Science and Technology, vol. 18, Ion Implantation. ed., J.K. Hirvonen (Academic Press, New York, 1980) p. 17.
[5] H.H. Andersen, in: Ion Implantation and Beam Processing, eds., J.S. Williams and J.M. Poate (Academic Press, Sydney, 1984) p. 127.
[6] H. Kräutle, Nucl. Inst. and Meth. 134 (1976) 167.
[7] R. Collins, Nucl. Instr. and Meth. B2 (1984) 809 (Proc. 10th Int. Conf. Atomic Collisions in Solids).
[8] C.R. Gossett, Nucl. Instr. and Meth. 218 (1983) 149. (Proc. 6th Int. Conf. Ion Beam Analysis).
[9] A. Niiler, R. Birkmire and J. Gerrits, Ballistics Research Lab. Technical Report, ARBRL-TR-02233 (1980).
[10] C.M. Davisson, Naval Research Lab. Memorandum Report 5409, to be published.
[11] D. Farkas, I.L. Singer and M. Rangaswamy, J. Appl. Phys., to be published.
[12] I. Manning and G.P. Mueller, Comp. Phys. Commun. 7 (1974) 85.
[13] R.D. Edge and U. Bill, Nucl. Instr. and Meth. 168 (1980) 157. (Proc. 4th Int. Conf. Ion Beam Analysis).
[14] I.L. Singer, Appl. Surface Sci. 18 (1984) 28.
[15] J. Bøttiger, S.K. Nielsen, H.J. Whitlow and P. Wriedt, Nucl. Instr. and Meth. 218 (1983) 684. (Proc. 6th Int. Conf. Ion Beam Analysis).

Section I.G

CARBURIZATION DURING Cr SELF IMPLANTATION IN A ^{13}CO ATMOSPHERE

R.H. Bassel and K.S. Grabowski[1]
M. Rosen[2]
M.L. Roush and F. Davarya[3]

[1]Materials Modification & Analysis Branch
Condensed Matter & Radiation Sciences Division
Naval Research Laboratory

[2]Radiation Matter Interaction Branch
Condensed Matter & Radiation Sciences Division
Naval Research Laboratory

[3]Chemical and Nuclear Engineering Department
University of Maryland
College Park, MD 20745

CARBURIZATION DURING Cr SELF IMPLANTATION IN A ^{13}CO ATMOSPHERE

R.H. BASSEL, K.S. GRABOWSKI and M. ROSEN

Naval Research Laboratory, Washington, DC 20375, USA

M.L. ROUSH and F. DAVARYA

Chemical and Nuclear Engineering Department, University of Maryland, College Park, Maryland 20745, USA

Self implantation of Cr into Cr has been performed in a ^{13}C enriched CO atmosphere and a significant concentration of ^{13}C was found in the implanted surface. A Monte Carlo calculation, with the Code EVOLVE, indicates that only a portion of this concentration can be accounted for by collision cascade mixing. Experimental and theoretical results are discussed.

1. Introduction

A number of experiments have been performed showing high concentrations of carbon in surfaces implanted with carbide forming metal ions [1–5]. The most recent of these experiments [5], in which Ti implantations were performed in vacuum back filled isotopic ^{13}CO gas, gave direct evidence that C can be absorbed from residual gases in a vacuum chamber during implantation. The mechanism by which the C is incorporated, whether by diffusion or by collisional processes, is not clear.

In the present experiment and analysis, we delineate the role played by collisional processes by considering the self-implantation of Cr ions into Cr in a ^{13}C enriched atmosphere. This has two advantages. The first is that experimentally we avoid chemical effects due to disparate beam and target ions. The second advantage is that the theoretical model we can employ is somewhat simpler than that proposed [4] to explain the results of Singer.

2. Experimental procedure

Substrates of quenched AISI-MSO bearing steel were polished to a 1 μm diamond finish, cleaned and coated with 80 nm of Cr by e-beam evaporation. The samples were implanted with 150 keV Cr$^+$ to a fluence of 2×10^{17} cm^{-2} in an UHV chamber (base pressure of 4×10^{-6} Pa) back filled with ^{13}CO to a partial pressure of 1.5×10^{-4} Pa. The relative impingement rate of CO molecules to Cr$^+$ was about 14. Secure clamping maintained the target temperature below 100°C throughout the implantation.

Following implantation, depth profiles of Cr, C and O were obtained by Auger electron spectroscopy (AES) in conjunction with Ar$^+$ sputtering. Derivative spectra were taken in the multiplex mode using 2-keV primary electrons and a 3-eV modulation. Sensitivity factors, accurate to 10%–20%, were obtained from chromium carbide powders. (The reference powders were sputtered under identical conditions to the samples.) Sputtering was provided by a 2-keV, 20 μA/cm^2 Ar$^+$ beam that was produced by backfilling the UHV chamber (base pressure of 1×10^{-7} Pa) with 7×10^{-3} Pa Ar. Depth scales were obtained by measuring the crater depth using an interferometer, and assuming a constant sputtering rate.

The relative contribution of ^{13}C to the AES carbon signal was determined by secondary-ion mass spectroscopy (SIMS). A 5.5-keV primary beam of Ar$^+$ was used at a current density of 40 μA/cm^2 to produce the secondary ions. Again, the depth scale was determined by measuring the crater depth with an interferometer.

3. Experimental results

The AES results indicate that a peak of some 32 atomic percent of carbon, (AES does not distinguish between ^{13}C and ^{12}C), and about 60 atomic percent Cr occurs near the surface. The atomic percentage of carbon goes through a minimum of 4% at a depth of about 30 nm. We take this to be the bulk value.

The ability to differentiate between ^{12}C and ^{13}C allowed SIMS to verify that the C signal seen near the surface in AES resulted mostly from ^{13}C incorporated from the ^{13}CO present in the vacuum. Although the shaded region in fig. 1, which shows the ^{13}C enrichment
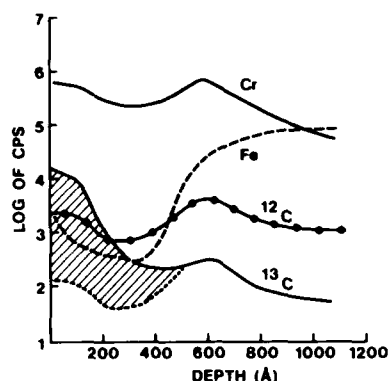
Fig. 1. Positive secondary ion spectra, in units of counts per second (CPS), from a Cr sample implanted with Cr in a ^{13}CO atmosphere. The shaded region shows the ^{13}C enrichment produced by the implantation. The ^{12}C profile is the same as that for the implantation in UHV.

produced by the implantation, indicates that the near surface enrichment measured by SIMS is some five times larger than that of ^{12}C, uncertainties due to matrix effects in the sample allow us to say only that the near surface ^{13}C concentration is greater than that of ^{12}C. The residual ^{13}C background (seen from examination of UHV implanted samples and shown in fig. 1) was consistently found to be about 10% of the ^{12}C signal and is believe to be caused by ^{12}CH molecules formed during profiling. The bumps seen in the ^{12}C, Cr and Fe signals at the surface and at 60 nm are largely artifacts caused by an increase in ionization probability induced by the presence of O. The oxygen resides in the native oxides present on the original surface of the substrate and the sample's own surface.

4. Calculation model

It is known that CO preferentially breaks up to form Ti C and Ti O complexes when CO impinges on titanium [6]. Further, it is known that oxygen desorbs under electron bombardment [7] and that only Ti-C survives. Since only C and not O enrichment was observed by AES, it is assumed that Cr behaves similar to Ti in the presence of CO and ionizing radiation. $Cr_{23}C_6$, Cr_7C_3, and Cr_3C_2 are the known stable compounds of Cr and C. The amount of C required to form these compounds upon coverage of pure Cr corresponds to a C:Cr ratio between 0.26 and 0.67. An average value of 0.5 during the implantation is not an unrealistic one. Our calculations were performed using carbon surface coverages equal to 30%, 60% and 120% of a Cr monolayer. As the simulated bombardment progressed, the

^{13}C fraction on the surface was assumed to remain constant.

Calculations were carried out using the University of Maryland time dependent Monte Carlo code EVOLVE [8] using the Molière potential. Details of this code can be found in ref. [8] and will not be discussed here. We assume that a 2.5 nm layer of Cr_2O_3 originally is present on the target surface and that a fluence of 3×10^{16} cm^{-2} is required to sputter away this layer before carburization can begin [9]. We carried out the calculations, therefore, to a maximum fluence of 1.7×10^{17} cm^{-2}. The code EVOLVE can consider systems made up of at most three types of atoms. Since AES does not distinguish between ^{13}C and ^{12}C, we performed two calculations. For the first we chose the three species to be O, Cr, and ^{13}C. For the second, we represented the O and C initially resident in the target by ^{12}C.

5. Results of the calculation

Fig. 2 shows C depth profiles as a function of carbon surface coverage for a 150 keV Cr beam implanted to a
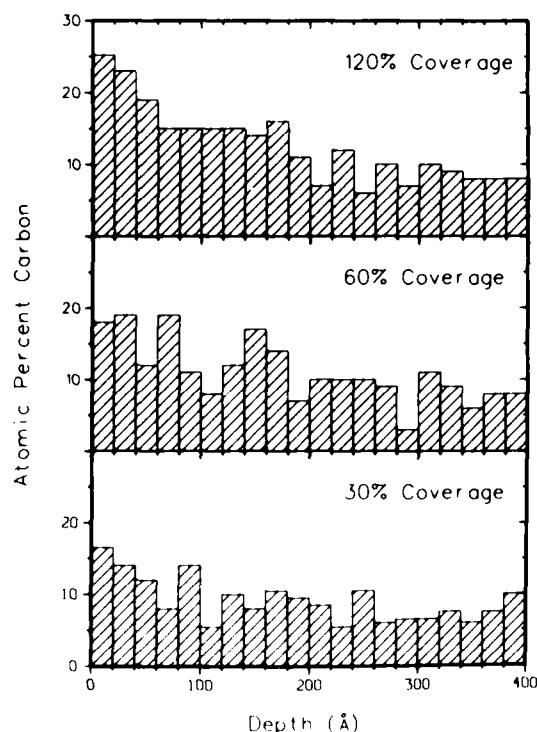

Fig. 2. Calculated concentration profiles of carbon from 150 keV Cr implantation of Cr in a ^{13}CO atmosphere as a function of carbon surface coverage. Initial O and C sample concentrations of 5% and 10% are assumed. All carbon atoms are taken to be ^{12}C.

fluence of 1.7×10^{17} cm^{-2}. For these calculation, no distinction is made between ^{12}C and ^{13}C: 5% O and 10% C bulk target concentrations are assumed, as these were the values indicated by an early AES analysis. Significant amounts of carbon are found at the surface; 17%, 18% and 25% for the 30%, 60% and 120% carbon coverages, respectively, Fig. 3 shows the results of the calculation (for 120% surface ^{13}C coverage) in which ^{12}C is distinguished from ^{13}C and also the atomic percent of excess carbon (i.e. above bulk value) obtained from the AES analysis. Since we represent both the oxygen and the carbon in the sample as ^{12}C, we took 2/3 of the calculated ^{12}C concentration to represent the actual ^{12}C profile. For this calculation a peak surface C concentration of 22.5% is found, of which 12.5% is ^{13}C. Although the experimental AES peak carbon concentration has an uncertainty of approximately ± 15%, the calculated value, even given its uncertainty, is below the measured one. The calculated and experimental fall off rates are about equal, and therefore the experimental fall-off-to-bulk-value distance (~ 28 nm) is significantly greater than that calculated. Preferential sputtering does not affect the comparison of the calculated and experimental results as it occurs in both. Furthermore, a calculation using incident 5 keV Ar atoms indicated no significant contribution during the Auger analysis.

6. Summary and conclusions

It has been demonstrated experimentally that Cr implanted into Cr in the presence of a ^{13}CO atmosphere produces high ^{13}C buildup in the surface. In contrast implantations under UHV conditions showed no significant C enrichment.

Our model predicts the occurrence of considerable surface carbon build up by collision cascade mixing. A comparison of the theoretical and experimental areas under the depth profiles shows that the theoretical area for the 120% surface coverage case is of the order of one third of that measured by AES. In order for collision mixing to enrich the subsurface C to the extent measured, the surface would need to be covered by approximately 3 monolayers of C throughout the implantation process. The calculated profile, however, falls off at the same rate as the measured profile. These calculations indicate that collision mixing cannot by itself account for all of the observed C enrichment profile. At the temperatures of this experiment, and those of Singer, it is quite reasonable to expect diffusion processes to occur.

Fig. 3. Calculated concentration profiles of ^{13}C and total carbon for 150 keV Cr implantation of Cr in a ^{13}CO atmosphere, for the case of 120% ^{13}C surface coverage. Also shown is the depth profile of excess carbon (i.e. above bulk value) as determined by AES analysis of the sample.

References

[1] C.A. Carosella, I.L. Singer, I.L. Singer, R.C. Bowers and C.R. Gossett, Ion Implantation Metallurgy, eds., C.M. Preece and J.K. Hirvonen (Metallurgical Society of AIME Warrendale, PA, 1980) p. 103.
[2] J.A. Knapp and S.T. Picraux, Appl. Phys. Lett. 37 (1980) 330. See also Ion Implantation Metallurgy, eds., C.M. Preece and J.K. Hirvonen (Metallurgical Society of AIME, Warrendale, PA, 1980) p. 182.
[3] I.L. Singer, C.A. Carosella and J.R. Reed, Nucl. Instr. and Meth. 182/183 (1981) 923.
[4] I.L. Singer, J. Vac. Sci. Technol. A1 (1983) 419.
[5] I.L. Singer and T.M. Barlak, Appl. Phys. Lett. 43 (1983) 457.
[6] M.P. Hooker and J. Grant, Surface Sci. 62 (1977) 21.
[7] H.J. Mathieu, J.B. Mathieu, D.E. McClure and D. Landholt, J. Vac. Sci. Technol. 14 (1977) 1023.
[8] M.L. Roush, T.D. Andreadis and O.F. Goktepe, Radiat. Effects 55 (1981) 119.
[9] I.L. Singer, private communication.

Section I.H

COMPOSITIONS OF METALS IMPLANTED TO VERY HIGH FLUENCES

I.L. Singer

Surface Chemistry Branch
Chemistry Division
Naval Research Laboratory

57

Compositions of metals implanted to very high fluences

I L Singer, *Chemistry Division, Code 6170, US Naval Research Laboratory, Washington, DC 20375 USA*

Surface compositions and microstructures of Fe and steels implanted with Ti⁺ and N⁺ ions to high fluences (10¹⁶–10¹⁸ cm⁻²) have been examined by a variety of surface analytical techniques, including Auger electron spectroscopy, secondary ion mass spectrometry, nuclear reaction analysis, conversion electron Mossbauer spectroscopy and transmission electron microscopy. The compositions observed at very high fluences could not have been predicted by simple ion implantation (collection) models based solely on physical processes such as sputtering, lattice dilation or even atomic mixing. For example, Ti⁺ implantation produced a carburized surface layer following absorption of C from gases in the vacuum chamber; implanted N and bulk C atoms were found to migrate across the implanted layer; and peak implant concentrations of interstitial atoms did not exceed the richest precipitate formed. The metallurgical state of these heavily implanted layers can, in many cases, be predicted from traditional metallurgical behaviour. An approach is suggested for calculating compositions of implanted layers that incorporates both the physical processes now included in many models and the metallurgical phases observed experimentally.

1. Introduction

Unique surface alloys can be produced by injecting atoms, as high energy ions, into substrates held at room temperature[1-4]. Ion implantation has been used for many years in the electronics industry to introduce small but precise quantities of dopant impurities into semiconductors[1-3]. More recently, ion implantation has been shown capable of benefiting the chemical and mechanical properties of metals[3,4]. However, unlike their semiconductor counterparts, metal substrates generally do not need to be annealed after implantation, but do require implantations to very high fluences, i.e. to concentrations of implant species in excess of 10 to 20 atomic%.

What compositions and microstructures are produced by very high fluence implantations into metals held at room temperature? One would like to be able to predict the metallurgical state of metals implanted to high fluences. Unfortunately, in most of the ion implantation (also known as ion collection) models, the compositions attainable are described solely in terms of physical processes, such as stopping power (i.e., projected range and straggling), lattice dilation and sputtering[5,6]. Some models also include atomic mixing[7] and radiation-enhanced diffusion[8] to account for the enhanced kinetics observed during irradiation. But none to date describes the chemical processes in enough detail to predict the metastable or stable phases (described in this paper and elsewhere[9,10]) observed for implantations into metals held at room temperatures. In the absence of a complete theoretical model to account for the observations, one can systematize the results of detailed surface analytical studies of implanted surfaces. This paper takes the latter approach but attempts to point out

ways in which present day models may be modified to reliably predict compositions of metals implanted to very high fluences.

The compositions and microstructures of Ti⁺- and N⁺-implanted steels are presented here as examples of the metallurgical state of metals implanted to very high fluences, and a metallurgical basis for the compositions obtained at very high fluences will be given. Among other effects, it will be shown that phase formation can limit the implant concentrations attainable, that chemical bonds between the implanted species and the substrate atoms can hinder solute redistribution, and that novel surface compounds form as a result of chemical reactions between the sputter-eroded surface and residual gases in the vacuum chamber.

Investigations of Ti⁺- and N⁺-implanted steels have been motivated by tribological studies showing that these two implantation treatments greatly improved the friction and wear properties[11-13]. In order to establish a chemical and microstructural basis for the benefits, extensive surface analytical investigations have been carried out. Compositions have been obtained by AES (Auger electron spectroscopy) and SIMS (secondary ion mass spectrometry) sputter depth profiling and by nondestructive Rutherford backscattering and nuclear reaction analyses. Microstructures have been studied by conversion electron Mossbauer spectroscopy (CEMS), which detects phases of Fe within 100 nm of an Fe alloy surface, and by transmission electron microscopy of thin foils stripped from implanted surfaces. Applications of most of these techniques (excluding CEMS) for studying ion implantation and tribology are discussed in detail elsewhere[14]

All implantations reported in this paper were performed under vacuum conditions no better than 10^{-6} torr, and with substrate temperatures kept near room temperature (i.e. below 310 K).

2. Vacuum carburized layers by implantation of strong carbide forming ions

Composition. Implantation of metal ions that are strong carbide formers (see Figure 1) produces unexpected surface compositions. In addition to the implanted metal atoms, the surface contains C atoms absorbed from gas molecules in the vacuum chamber[14,19]. The Ti-implanted Fe surface exemplifies the compositions obtained at very high fluences. As seen in Figure 2, Ti profiles evolve from Gaussian-like curves at low fluences to near sputter-limited profiles at highest fluences. Diffusion-like profiles of C are also observed at higher fluences. However, as a comparison of the 55 keV and 190 keV profiles in Figure 2 shows, the C buildup does not scale directly with fluence, but rather with the surface concentration of Ti[17,18]. The evolution of the Ti and C profiles and the implant-assisted vacuum carburization process will be discussed in more detail later.

Ti implantation has been shown to produce carburized layers in substrates other than Fe-based alloys, among which are Ni[19], a Co-based alloy[20]. Ti alloys[21], even Cr carbides[20] and Ti

Figure 1. heats of formation for selected transition metal carbides and nitrides (from ref 27)

carbides[21]. Implantations of other metal ions known to be strong carbide formers have also produced carburized layers in a variety of metals, these systems include Cr^{+} into steel[22] and Cr[23]; Nb[+] into steels[24], Hf[+] into steel and Al[24]; and Ta[+] into Fe[25], steel[14], and Cu[26]. V[+] and Zr[+] implants are also expected to form carburized layers, based on their carbide forming ability[27] (see Figure 1). On the other hand, implantation of Mo[+] or Ni^{+} ions, neither of which are strong carbide formers (see Figure 1), did not produce carburized steel surfaces[24].

Implant-assisted carburized layers have also been formed by implanting inert ions into metals alloyed with strong carbide-formers. Two examples found at NRL are Ar^{+}-implanted ($5 \cdot 10^{17}$ cm^{-2} at 100 keV) into an FeTi intermetallic and into type-304 steel[26].

Microstructure. The microstructures of vacuum carburized layers have been investigated by ion channeling into implanted single crystals of Fe[16] and by transmission electron microscopy and diffraction of implanted layers. Ti^{+}-ion implantation has produced amorphous layers in Fe[16] and a steel[17]. The amorphous layer grows from the surface inwards, commensurate with the buildup of the carburized layer[16]. Ta[+]-ion implantation also amorphizes steels[28], and both Ti and Ta implants amorphitize the second phase Cr carbides in steels[17,28]. Finally, dual implants of C[+] and Ti^{+} ions can produce amorphous layers in both the Fe and carbide phases of steels[29,31]. Moreover, the experiments of Knapp *et al*[31] have tentatively identified the (C, Ti) concentration boundary of the Fe-Ti-C ternary phase diagram that separates the crystalline from amorphous phases.

Metallurgy. the C profiles obtained during high fluence implantation of Ti^{+} ions can be accounted for by an implant-assisted carburization process[18]. The four steps that make up this process are illustrated schematically in Figure 3 for the case of Ti-implanted Fe. The first step is sputtering. During implantation,
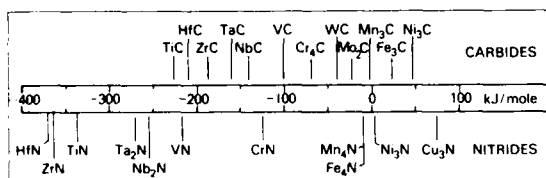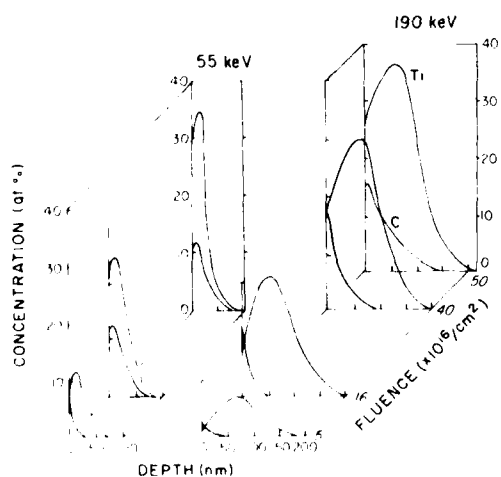
Figure 2. Concentration vs depth profiles for Ti and excess C in Ti-implanted steel at several fluences and energies (left) 5, 16 and 40 $\cdot 10^{16}$ Ti cm^{-2} at 55 keV, (right) 5, 16, 40 and 50 $\cdot 10^{16}$ cm^{-2} at 190 keV (from ref 18)
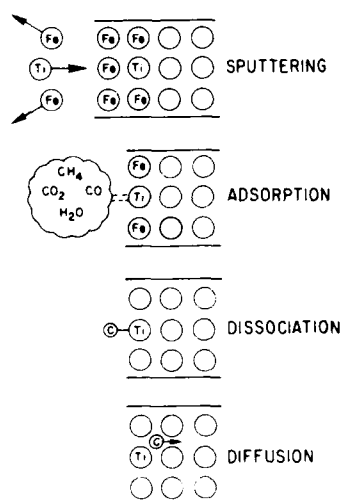
Figure 3. Schematic illustration of four steps required for vacuum carburization of Fe during Ti-implantation

854

the bombarding ions sputter-erode the surface, first removing the carbon-covered oxide film that overlays the metallic substrate, then the Fe atoms themselves. Eventually the implanted Ti atoms are uncovered, exposing them to the vacuum-solid interface.

The second step is adsorption. At chamber pressures of $p = 10^{-6}$ torr, typical of present day implantation chambers, residual gas molecules strike each surface atom once each second. Ti atoms, among the strongest carbide formers (see Figure 1), are known to have a high affinity for carbonaceous residual gas molecules such as CO, the sticking probability at low surface coverages can be as high as one[32]. Therefore, so long as the impingement rate of carbonaceous gas molecules is greater than the sputter erosion rate, an adsorbed gas layer should build up in proportion to the Ti surface concentration. *In situ* AES analysis of Fe surfaces during Ti-implantation has recently verified this buildup[1]

The third step is dissociation. Adsorbed carbonaceous gas molecules cannot themselves carburize the surface, they must first dissociate to form surface carbide species. This process of dissociative adsorption is favoured over molecular adsorption at or above room temperature (300 K) for Ti and several other strong carbide formers (e.g. Hf, Zr, La, Nb and V) exposed to CO[27]

The fourth step is diffusion. Surface carbide species are the sources of free carbon atoms that migrate inward and carburize the implanted layer.

The processes described in this model have recently been investigated, and steps two, three and four have been verified. The absorption of C from residual gas molecules was verified by implanting Ti into Fe and Ni substrates situated in a vacuum chamber that was backfilled with isotopic ^{13}CO gas. Composition vs depth profiles of the implanted surfaces by secondary ion mass spectrometry showed a ^{13}C carburized layer[1]

The question of whether the C diffuses in or is 'knocked in' has recently been clarified by the aforementioned *in situ* analysis of the implanted surface composition[1] Although nearly equal concentrations of surface carbide and oxide species collected on the surface during implantation, only the C atoms penetrated the implanted layer. Since O and C are nearly equal in mass, nearly equal concentrations of O and C would have been found below the surface if 'knock-on' were responsible for carburization. Therefore, it is likely that C enters substrate by a diffusion process.

Returning to the first step in the model, sputtering, one can see that it can qualitatively account for the observed energy and fluence dependences seen in the composition profiles of Figure 2. The higher energy 190 keV implants penetrate deeper than the 55 keV implants (projected ranges of 28 nm vs 59 nm respectively[14]) and therefore require higher fluences to bring the Ti atoms to the surface by sputter erosion (approximately energy independent[15]) The lower energy 55 keV implants are uncovered at a lower fluence and develop a carburized layer sooner than the 190 keV implants

By similar arguments, higher mass ('heavier') ions require lower fluences to carburize substrates. In general, heavier ions penetrate substrates less deeply and sputter them more rapidly than do lighter ions. The tradeoff, however, is a thinner, less concentrated carburized layer. These considerations also apply to implantation at angles off normal incidence[16,17] and are particularly important when considering the processing parameters needed for improving mechanical or chemical properties by vacuum carburization

These qualitative considerations of the physical and chemical processes that bring about vacuum carburization have been incorporated by Farkas *et al*[18] into a computational model for

calculating Ti and C profiles in Ti-implanted steel. The computed profiles were obtained by solving simple diffusion equations (Fick's law) for Ti and C subject to the following boundary conditions: incremental Gaussian distributions of Ti ions were collected; the lattice was dilated in proportion to the concentration of Ti ions; the surface was sputter-eroded at a constant rate; the buildup of C on the surface was taken to be proportional to the surface Ti concentration (which coupled the two diffusion equations); and the Ti and C atoms were allowed to diffuse inward. A good fit to all seven profiles in Figure 2 was achieved using a physically reasonable sputtering yield of 2 and diffusivities of 6×10^{-15} cm^2 sec^{-1} for both Ti and C.

The computed profiles also indicated how diffusion, or perhaps more accurately atomic mixing, of Ti can influence the overall composition of the implanted layer. The effects of mixing, as a function of fluence, can be inferred from the plots of the 55 keV implant profiles with and without diffusion (Figure 4). At low fluences, mixing accelerates the buildup of Ti on the surface, thereby promoting earlier carburization. At higher fluences, mixing decelerates the surface buildup of Ti by lowering the concentration of subsurface Ti that arrives at the eroding surface. Higher fluences are therefore needed to achieve steady state in an atomically mixed layer, but in exchange more Ti will be retained. Experiments are in progress to verify these effects and to discover the effects of C on the diffusivity and sputtering rate of Ti.

3. Solute redistribution and phase formation in N-implanted steels compositions

The alloy constituents in steels can greatly influence the concentration depth profiles of implanted N. In steels containing high concentrations (> 10 atomic%) of strong nitride formers (see Figure 1) such as Cr, the N profiles assume the expected Gaussian-like distributions up to very high fluences. This behaviour is illustrated in Fig. 5, which presents a family of N depth profiles for 40 keV N implants into the high Cr (20 atomic%) steel, type-304[19]. Up to a fluence of 2×10^{17} cm, the profiles are nearly Gaussian, with a slight bulge on the near-surface side. Presumably, the strong bonds formed between the implanted N atoms and the substrate's Cr atoms prevent most of the N from diffusing away from the region of high N concentration. For fluences greater than 4×10^{17} cm^{-2}, reliable profiles could not be obtained over the entire implant depth because the surfaces blistered due to implantation. The oxygen profiles at 4
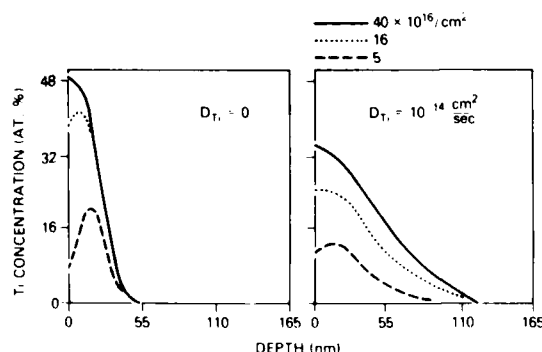

Figure 4. Computed concentration vs depth profiles of Ti implanted into Fe at 55 keV with (right) and without (left) Ti diffusion (from ref 38)
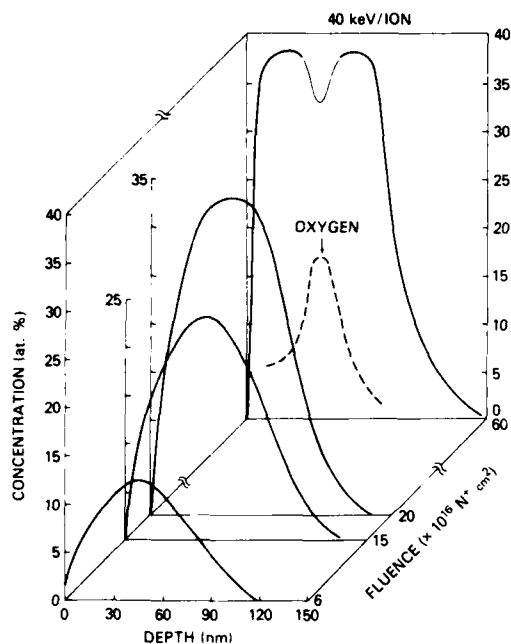
Figure 5. Concentration vs depth profiles of N implanted into type-304 steel at 40 keV N⁺ Profiles were obtained by Auger sputter depth profiling. N concentrations were quantified by ¹⁴N(α, γ)¹⁸F resonant reaction analysis

Figure 6. Concentration vs depth profiles of N implanted into Fe at 40 keV N⁺ Profiles were obtained by Auger sputter depth profiling. N concentrations were quantified by ¹⁴N(α, γ)¹⁸F resonant reaction analysis.

(not shown) and 6×10^{17} cm⁻², obtained by Auger sputter depth profiles, suggest that the blisters nucleated at the depth of the N peak concentration (about 38 atomic% in this steel), then had their cavity walls oxidized on exposure to air.

By contrast, N profiles in Fe and low alloy steels implanted to high fluences show distinctly non-Gaussian behaviour[14,39,44]. Figure 6 illustrates a family of N depth profiles in Fe (99.99 atomic%, pure) samples implanted at the same time as those reported in Figure 5. At fluences as low as 4×10^{16} cm⁻², a small excess N concentration builds up at the surface. At higher fluences, between 2 and 4×10^{17} cm⁻², the concentration of N at its peak depth begins to saturate (approximately 33 atomic%), and the N which continues to be retained in the implanted layer redistributes in a trapezoid-like profile. This redistribution of N away from the peak depth has been monitored by Barnavon *et al*[40] in an elegant ¹⁵N marker experiment. The initially Gaussian-like portion of a ¹⁵N profile (obtained at 1×10^{17} cm⁻² 40 keV N⁺) flattened out and broadened after two successive implants of ¹⁴N at fluences of 1×10^{17} cm⁻² each.

The migration of N atoms to the surface is revealed even more dramatically in Figure 7a. In this Auger sputter depth profile of a low carbon (1 atomic%) steel (type-1018) implanted with N to high fluences at high energy (4×10^{17} cm⁻² at 180 keV N⁺), the near surface N peak is clearly separated from the deeper Gaussian-like distribution of N atoms. Figure 7a also shows a large buildup of C near the surface, with a peak concentration more than 10 times the bulk C concentration and more than 1000 times greater than the concentration of soluble C in the ferrite matrix. Similar C and N profiles have also been observed in two high carbon (5 atomic%) tool steels, type-52100[45] and type-M2[46]
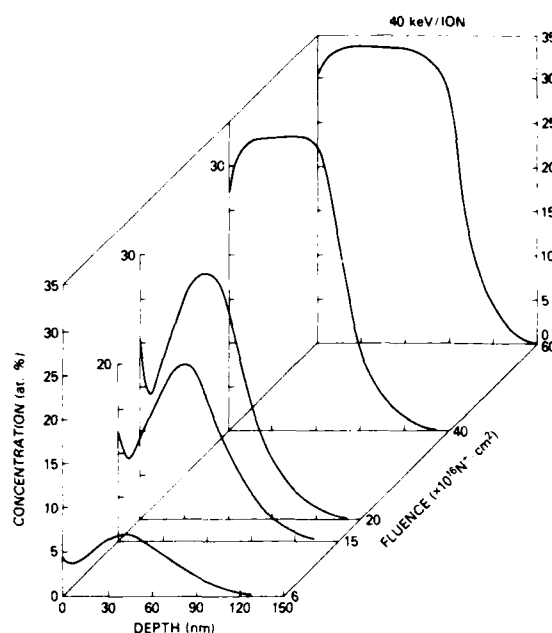
By contrast, no surface N peak and only a small surface C profile is seen in the high Cr type-304 steel (<0.2 atomic% C) (see Figure 7b), implanted at the same time and conditions as the carbon (type-1018) steel (Figure 7a). The surface C profile is believed to arise from the vacuum carburization process (discussed in the previous section) and not from out-migration of C from the substrate. These results suggest, again, that interstitial solute atoms can be hindered from migrating away from the highly concentrated regions of the implanted layer if they can bond strongly to solute atoms in the substrate, as C and N can bond to Cr in high Cr steels.

Microstructures. The microstructures formed by high fluence N-implantation into Fe-based alloys have been examined principally by the technique of conversion electron Mossbauer spectroscopy (CEMS) and, to a lesser extent, by transmission electron microscopy (TEM). Results of these studies are summarized below and in Table 1.

N implantation into Fe or low alloy steels produces second phase nitrides including $\alpha''\text{-Fe}_{16}\text{N}_2$, $\gamma'\text{-Fe}_4\text{N}$ and $\epsilon\text{-Fe}_2\text{N}$, with Fe_2N phase predominating at the highest fluences[47,48]. In carbon steels, N implantation can dissolve pre-existing phases (e.g. Fe_3C carbides[49] and α-martensite[50]), convert the α phase to γ-austenite[51] and form second phases. The second phases have been identified as α-Fe₄(1, γ- and ε-Fe₃(1, again with a Fe₂I phase predominating at highest fluences, where I = C, N or a mixture of C and N[49,50,51]. Several studies[49,50,51] have suggested that carbonitrides may form in preference to nitrides, depending on implant fluence and bulk C concentration. However, the exact compositions, be they carbides, nitrides or carbonitrides, cannot be determined by CEMS because the technique is sensitive only to structure and not to composition.
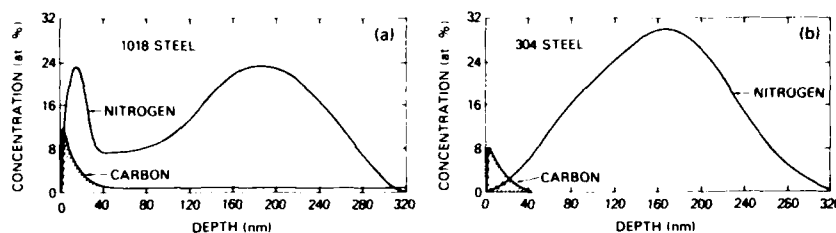
Figure 7. Concentration vs depth profiles of N and C in N-implanted (a) type-1018 steel and (b) type-304 steel for a fluence of 4×10^{17} N$^+$ cm^{-2} at 180 keV N$^+$. Profiles were obtained by Auger sputter depth profiling, the N concentrations were quantified by ^{14}N(α,γ)^{15}F resonant reaction analysis and the C, by Auger analysis of known reference carbides

Table 1. Metallurgical processes observed in N-implanted steels (See text for details)

Steel	Solute redistribution	Phases dissolved	Phases formed
Low alloy	N outdiffuses	γ-Fe	Austenite, nitrides
Carbon	N and C outdiffuse	Carbides, carbon-martensite	Austenite, nitrides, carbonitrides
High Cr	N immobilized		Cr and Fe nitrides
Austenitic (Cr Ni)	N immobilized	α'-martensite	Cr and Fe nitrides; austenite

In Cr steels, one finds CrN^{56}, (Cr, Fe)$_2$N$_{1-x}$^{57}, and, at highest fluences, Fe$_2$N^{53}. One exception to this is heavily deformed austenitic steel, where the substrate before implantation is predominantly α'-martensite. N implantation into deformed type-304 steel did not produce Cr nitrides^{58}; rather, it reverted the α'-martensite to austenite, with the majority of N remaining in solution^{59}.

Metallurgy. A coherent picture of the metallurgy of N implanted steels emerges from the compositional and microstructural studies presented here and summarized in Table 1. In Fe and low alloy steels with or without C, the implanted N atoms are mobile and move away from regions (depths) of high N concentrations. Many of the atoms leave the substrate via the surface, while some get trapped at the metal oxide metal interface; others may even migrate into the bulk substrate^{53}. Those atoms retained in the implanted layer can be expected to occupy interstitial lattice sites which are conducive to the formation of the increasingly N-rich precipitates. These phases precipitate out, presumably with increasing stresses built up by the implantation process^{60}. The maximum N concentration reported for N-implanted Fe is about 33 atomic%,^{19,42}, a limit consistent with the implanted layer being transformed into the richest nitride phase of Fe, i.e. Fe$_2$N.

In carbon steels, two additional processes take place. First, N implantation frees bound C atoms by dissolving small carbide precipitates (e.g. M$_3$C) and removing C from the α'-martensite. Second, some of these C atoms migrate to the surface, along with implanted N atoms, producing a C and N enriched near-surface layer as depicted in Figure 7a. Thus, it is likely that distinct phases of carbides, nitrides and carbonitrides exist at different depths in the implanted layer.

Preliminary evidence for layering of phases has been obtained by Carbucicchio *et al*^{51} by monitoring conversion electrons representing three different sampling depths in N-implanted steels. One could obtain a more accurate depth-dependence of the various phases by combining the CEMS technique

with Auger sputtering depth profiling: Auger analysis would record the composition of successive layers removed by ion etching, while CEMS would determine the phases in the remaining implanted layer at each step.

In steels containing high solute concentrations of strong nitride formers such as Cr, the Cr-N bond^{61} renders implanted N relatively immobile despite the concentration gradients, the stresses, and the defect fluxes, all of which could drive the N atoms to the surface^{62}. In the case of an austenitic Cr steel, ion channeling investigations have shown that at low concentrations ($\leq 10^{16}$ cm^{-2}) the implanted N atoms occupy the same lattice site (octahedral) found in splat quenched, N-containing austenitic steel^{63}. The bonding at this site insures the preferential formation of Cr or (Cr, Fe) nitride precipitates over Fe precipitates. The absence of CrN precipitates in heavily deformed austenitic steels, after N-implantation, may be due to the absence (or distortion) of octahedral sites in the α'-martensite structure.

The immobility of N results in higher retained doses for the Cr steels^{39,43,44} (as well as an increased likelihood of blistering). One can account roughly for the higher concentration of N in type-304 steel (38 atomic% N) than in Fe (33 atomic% N) as follows: Diluted by 38% N, the composition of the steel surface is given by 44% Fe, 13% Cr, 5% Ni and 38% N. When second phase nitrides are considered, the composition becomes 26% CrN, 66% Fe$_2$N plus 5% Ni and 3% N. The Fe$_2$N concentration (66%) is in good agreement with the value of 55% measured by dos Santos *et al*^{55} for type-304 steel implanted with N ions to 6×10^{17} cm^{-2}.

4. Discussion

Through the use of advanced surface analytical techniques, the ion implantation community is becoming more aware of the metallurgical complexity of surfaces implanted to very high fluences at room temperature. Twenty years ago, in their pioneering studies of sputtering during ion bombardment to high fluences, Almen and Bruce could only speculate that contaminant

857

gases in the vacuum chamber may have affected the sputtering yields of the more reactive implant ions[34]. Today we recognize at least one of the processes by which residual gas molecules interact with bombarded surfaces to alter the composition, i.e. the example of implant-assisted vacuum carburization. This chemical process, as we have seen, may influence many of the physical processes occuring in the bombarded surface. For example, Almen and Bruce observed a periodicity in the self-sputtering yield of metals, with minima grouped about strong carbide formers like Ti, Nb and Ta, and noted that the periodicity correlated with the binding energy of the metals. As an alternative explanation, one might suggest that the sputtering rate of the carbide formers (metals) is lowered by the presence of C, which is replenished from the gas phase as fast as it is sputter removed from the surface (see, for example, ref 65). A more detailed explanation, however, would have to treat the effect of carbide formation on the surface segregation and preferential sputtering during ion bombardment.

Vacuum carburization is a rather exotic metallurgical process affecting metals implanted to high fluences. Less exotic and less well understood are the mechanisms controlling the redistribution of interstitial N and C atoms that migrate to the surface of low alloy steels as a result of N implantation. Zomorrodian *et al*[66] have reported a similar surface N buildup in Cu and Ag implanted with low-energy (< 5 keV) N_2^+ ions, which they attribute to radiation-enhanced diffusion. An alternative mechanism might be radiation-induced-segregation[67], where interstitial solutes are carried by defect fluxes moving towards the surface.

It is clear that interstitial solute migration can be affected by the formation and dissolution of phases. Strong bonds formed between metallic solute atoms in the lattice and interstitial solutes have been shown to hinder N redistribution in the high Cr type-304 steel[12,19], in metallic Cr^{43} and in a Ti alloy[68]. Yet during Ti implantation, C diffuses inward without forming TiC micro-precipitates as would happen during high-temperature carburiz-ation of high-alloy steels[69], presumably there is competition here between phase formation and phase dissolution during implantation.

Although the kinetic processes are not well understood, the compositions and microstructures formed by implantation of interstitials to very high fluences appear to be predictable from equilibrium phase diagrams. For example, the maximum concentration of N in Fe saturates at about 33 atomic%, a value corresponding to the richest equilibrium nitride phase, Fe_2N. We have also observed that C implanted into Ti saturates at a composition of about 50 atomic%, and forms a continuous TiC layer in the surface.[13] Furthermore, in Fe-Cr alloys, N implantation forms Cr or CrFe nitrides before forming Fe nitride, in accordance with the ternary Fe-Cr-N diagram.[1] Another example is the transformation of the martensitic phase of type-304 steel to the austenitic phase by high-influence N implantation[55]. Interstitial N atoms are known to stabilize the austenitic phase in metastable type 304 steels. Moreover, the lattice dilations produced by the implanted N atoms[5] agreed with the values predicted for N dilation of bulk austenitic steels.[1] These results suggest that equilibrium phase diagrams are a reasonable guide to the principal phases and compositions achievable by implantation of interstitial atoms to very high fluences. Myers[13] has successfully applied this approach to describe the phases formed by low fluence implantation into metals subjected to post-implantation annealing.

Once the metallurgical process is recognized, realistic models for the composition of metals implanted to high fluences can be

constructed. These models must include well known physical processes such as sputtering, lattice dilation, atomic mixing, radiation enhanced diffusion and/or other radiation-assisted transport processes. They should also include chemical processes such as surface compound formation (e.g. from gas surface reactions or solute outmigration), phase formation and phase dissolution. One way of incorporating chemical processes is to let the richest phase predicted from phase diagrams serve as a boundary condition and require that all atoms in excess of its concentration diffuse away. A specific example of this integrated approach is the computational method of Farkas *et al*[38] described earlier, with adjustable parameters to obtain best fits for physical constants (e.g. sputtering yields, diffusivities) and with boundary conditions to describe the physical and metallurgical processes (e.g. lattice dilation, surface compound formation).

In conclusion, high fluence implantation into metals produces compositions which cannot be predicted solely on the basis of physical processes. Metallurgical processes, not unlike those found in traditional metallurgy, appear to dictate the compositions and microstructures achievable. Calculation of composition profiles from first principles may not be possible at present because the kinetics of solute redistribution and the mechanisms of phase formation and dissolution during irradiation are not well understood. However, realistic profiles should be calculable by combining physical and metallurgical processes into existing ion implantation models.

References

[1] J W Mayer, L Eriksson and J A Davies, *Ion Implantation in Semiconductor, Silicon and Germanium* Academic Press, New York (1970).
[2] G Dearnaley, J H Freeman, R S Nelson and J Stephen, *Ion Implantation*. North-Holland, Amsterdam (1973).
[3] P Townsend, J C Kelly and N E W Hartley, *Ion Implantation, Sputtering, and their Applications* Academic Press, New York (1976).
[4] *Ion Implantation* (Edited by J K Hirvonen) Academic Press, New York (1980).
[5] F Schulz and K Wittmaak, *Rad Effects*, 29, 31 (1976).
[6] H Krautle, *Nucl Instrum Meth*, 134, 167 (1976).
[7] Z L Liau and J W Mayer, in *Ion Implantation*, (Edited by J K Hirvonen), p 17, Academic Press, New York (1980).
[8] G Carter, R Webb and R Collins, *Rad Effects Letts*, 43, 125 (1979).
[9] W A Grant, *J Vac Sci Technol*, 15, 1644 (1978).
[10] J M Poate and A G Cullis, in *Ion Implantation* (Edited by J K Hirvonen), pp 85-113, Academic Press, New York (1980)
[11] N E W Hartley, in *Ion Implantation* (Edited by J K Hirvonen), p 321, Academic Press, New York (1980)
[12] G K Hubler, in *Metastable Materials Formation by Ion Implantation* (Edited by S T Picraux and W J Choyke), p 341, Elsevier, New York (1982).
[13] I L Singer, in *Ion Implantation and Ion Beam Processing of Materials* (Edited by G K Hubler, O W Holland, C R Clayton and C W White), p 585, North-Holland, New York (1984).
[14] I L Singer, *Appl Surface Sci*, 18, 28 (1984).
[15] C A Carosella, I L Singer, R C Bowers and C R Gossett, in *Ion Implantation Metallurgy*, p 103, Metallurgical Society of AIME, Warrendale, PA (1980)

[16] D M Follstaedt, J A Knapp and S T Picraux, *Appl Phys Lett*, 37, 330 (1980).

[17] I L Singer, C A Carosella and J R Reed, *Nucl Instrum Meth*, 182 183, 923 (1981).

[18] I L Singer, *J Vac Sci Technol*, A1, 419 (1983).

[19] I L Singer and T M Barlak, *Appl Phys Lett*, 43, 457 (1983).

[20] S A Dillich and I L Singer, *Thin Solid Films*, 108, 219 (1983).

[21] I L Singer and S A Dillich, unpublished.

[22] W K Chan, C R Clayton and J K Hirvonen, in *Corrosion of Metals Processed by Directed Energy Beams* (Edited by C R Clayton and C M Preece, p 91, AIME, NY (1982).

[23] R H Bassel, K S Grabowski, M Rosen, M L Roush and F Davarya, *Nucl Instrum Meth B*, in press.

[24] R A Jeffries and I L Singer, unpublished.

[25] K S Grabowski, F D Correll and F R Vozzo, presented at the *Ion Beam Modification of Materials Conference*, Cornell, New York, July (1984), to be published.

[26] D A Baldwin and I L Singer, unpublished.

[27] J B Benziger, *Appl Surface Sci*, 6, 105 (1980).

[28] C R Clayton, W K Chan, J K Hirvonen, G K Hubler and J R Reed, *Fundamental Aspects of Corrosion Protection by Surface Modification, The Electrochemical Society Proceedings* (Edited by E McCafferty, C R Clayton and J Oudar), Vol 84 3, p 17 (1984).

[29] D M Follstaedt, F G Yost and L E Pope, in *Ion Implantation and Ion Beam Processing of Materials* (Edited by G K Hubler, O W Holland, C R Clayton and C W White), p 655, North-Holland, New York (1984).

[30] J A Sprague, I L Singer and R A Jeffries, in *Scanning Electron Microscopy 1984* (Edited by O Johari), SEM Inc, Chicago (1984).

[31] J A Knapp, D M Follstaedt and B L Doyle, presented at the *Ion Beam Modification of Materials Conference*, Cornell, New York (July 1984) to be published.

[32] Y Fukada, G M Lancaster, F Honda and J W Rabalais, *J Chem Phys*, 15, (1978).

[33] D A Baldwin, B Sartwell and I L Singer, presented at the *Ion Beam Modification of Materials Conf*, Cornell, New York (July 1984) to be published.

[34] I Manning and G P Mueller, *Comp Phys Communs*, 7, 84 (1974).

[35] H H Andersen and H L Bay, in *Sputtering by Particle Bombardment* 1, (Edited by R Behrisch), p 173, Springer, Berlin (1981).

[36] I L Singer and R A Jeffries, in *Ion Implantation and Ion Beam Processing of Materials* (Edited by G K Hubler, O W Holland, C R Clayton and C W White), p 673, North-Holland, New York (1984).

[37] K S Grabowski, N E W Hartley, C R Gossett and I Manning, in *Ion Implantation and Ion Beam Processing of Materials* (Edited by G K Hubler, O W Holland, C R Clayton and C W White), p 615, North-Holland, New York (1984).

[38] D Farkas, I L Singer and M Rangaswamy, in *Ion Implantation and Ion Beam Processing of Materials* (Edited by G K Hubler, O W Holland, C R Clayton and C W White), p 609, North-Holland, New York (1984).

[39] W M Bone, R J Colton, I L Singer and C R Gossett, *J Vac Sci Technol*, A2, 788 (1984). (Summary abstract only.)

[40] T Barnavon, J Tousset, S Fayeulle, P Guiraldenq, D Treheux and M Robelet, *Rad Effects*, 77, 249 (1983).

[41] J B Pethica, R Hutchings and W C Oliver, *Nucl Instrum Meth*, 209 210, 995 (1983).

[42] J T A Pollock, M J Kenny and P J K Patterson, in *Ion Implantation and Ion Beam Processing of Materials* (Edited by G K Hubler, O W Holland,

C R Clayton and C W White), p 691, North-Holland, New York (1984).

[43] N Moncoffre, T Barnavon, J Tousset, S Fayeulle, P Guiraldenq, D Treheux and M Robelet, *N 410- ASI Surface Engineering Conference*, Les Arcs, France, (Edited by R Kossowski and S C Singhal), Martinus-Nijhoff, The Hague (1984).

[44] P D Goode and I J R Baumvol, *Nucl Instrum Meth*, 189, 161 (1981).

[45] T E Fischer, M J Luton, J M Williams, C M White and B R Appleton, *ASLE Trans*, 26, 31 (1983).

[46] I L Singer and R A Jeffries, in *Ion Implantation and Ion Beam Processing of Materials*, (Edited by G K Hubler, O W Holland, C R Clayton and C W White), p 667, North-Holland, New York (1984).

[47] G Longworth and N E W Hartley, *Thin Solid Films*, 48, 95 (1978).

[48] K Hohmuth, B Rauschenbach, A Kolitsch and E Richter, *Nucl Instrum Meth*, 209 210, 249 (1983).

[49] R Frattini, L Giordano, S Lo Russo, G Principi and C Tosello, *Proc Int Conf on Applications of the Mossbauer Effect*, Jaipur, December 1981, Indian National Science Academy (1982).

[50] R Frattini, G Principi, S Lo Russo, B Tiveron and C Tosello, *J Mat Sci*, 17, 1683 (1982).

[51] M Carbucicchio, L Bardani and S Tosti, *J Appl Phys*, 52, 4589 (1981).

[52] G Principi, P Matteazzi, E Ramous and G Longworth, *J Mat Sci*, 15, 2665 (1980).

[53] C A dos Santos, M Behar, J P de Souza and I J R Baumvol, *Nucl Instrum Meth*, 209 210, 907 (1983).

[54] G Marest, C Skoutarides, Th Barnavon, J Tousset, S Fayeulle and M Robelet, *Nucl Instrum Meth*, 209 210, 259 (1983).

[55] E Ramons, G Principi, L Giordano, S Lo Russo and C Tosello, *Thin Solid Films*, 102, 97 (1983).

[56] M Baron, A L Chang, J Schreurs and R Kossowsky, *Nucl Instrum Meth*, 182/183, 531 (1981).

[57] F G Yost, S T Picraux, D M Follstaedt, L E Pope and J A Knapp, *Thin Solid Films*, 107, 287 (1983).

[58] R G Vardiman, R N Bolster and I L Singer, in *Metastable Materials Formation by Ion Implantation* (Edited by S T Picraux and W J Choyke), p 269, North Holland, New York (1982).

[59] R G Vardiman and I L Singer, *Materials Letts*, 2, 150 (1983).

[60] N E W Hartley, *J Vac Sci Technol*, 12, 485 (1975).

[61] I L Singer and J S Murday, *J Vac Sci Technol*, 17, 327 (1980).

[62] G Dearnley, *Appl Phys Letts*, 28, 244 (1976).

[63] J L Whitton, M M Ferguson, G T Ewan, I V Mitchell and H H Plattner, *Appl Phys Letts*, 41, 150 (1982).

[64] O Almen and G Bruce, *Nucl Instrum Meth*, 11, 279 (1961).

[65] P Varga and E Taglauer, *J Nucl Mat*, 111/112, 726 (1981).

[66] A Zomorrodian, S Tougaard and A Ignatiev, *Physica Scripta*, T6, 76 (1983); *J Vac Sci Technol*, A1, 339 (1983).

[67] A D Marwick, in *Surface Modification and Alloying by Laser, Ion and Electron Beams* (Edited by J M Poate, G Foti and D C Jacobson), Chapter 8, Plenum Press, New York (1983).

[68] R Hutchings and W C Oliver, *Wear*, 92, 143 (1983).

[69] *Handbook of Stainless Steels* (Edited by D Peckner and I M Bernstein), Chapter 17, p 25, McGraw-Hill, New York (1977).

[70] I L Singer and R G Vardiman, unpublished.

[71] *Metals Handbook*, Vol 8, p 422, ASM, Metals Park, OH (1973).

[72] See ref 69, Chapter 4, p 27.

[73] S M Myers in *Ion Implantation* (Edited by J K Hirvonen), pp 50 84, Academic Press, New York (1980).

855

Section I.I

SURFACE ANALYSIS, ION IMPLANTATION AND TRIBOLOGICAL PROCESSES AFFECTING STEEL

I.L. Singer

Surface Chemistry Branch
Chemistry Division
Naval Research Laboratory

SURFACE ANALYSIS, ION IMPLANTATION AND TRIBOLOGICAL PROCESSES AFFECTING STEELS

Irwin L. SINGER

Surface Chemistry Branch, 6170, Naval Research Laboratory, Washington, DC 20375, USA

An analytical approach is presented for investigating surface processing treatments used to improve the friction and wear (i.e., tribological) behavior of engineering alloys, with specific examples cited for ion implantation of steels. Surface composition techniques such as scanning Auger microscopy, energy dispersive X-ray analysis and secondary ion mass spectroscopy and microscopies such as transmission electron microscopy (TEM), secondary electron microscopy and interferometry have eluciated the microstructure and chemistry of a variety of implant species (N, C, Ti and Ta) found to affect the tribological behavior of surfaces. Novel combinations of these techniques, along with metallography of ion-etched surfaces or TEM of ion-beam-etched foils, are shown to be useful methods for establishing microstructures of ion-implanted and worn surfaces. The tribological behavior of the thin implanted layer (~ 200 nm) is examined by two devices: a stickslip machine and a polishing wear apparatus, the latter having wear rate versus depth resolution of 10 to 20 nm. Tribology studies of two implanted steels, 304 stainless steel and 52100 bearing steel, are presented, and analytical investigations which have led to models for their improved wear behavior are described. A process by which implanted metal ions can react with residual gases in the vacuum chamber to "carburize" steel and produce superior tribological surfaces is also discussed.

1. Introduction

Advances in ultra high vacuum (UHV) technology and solid state electronics over the past two decades have led to developments of electron, ion and photon beam technologies for analyzing compositions and microstructures of surfaces as well as for modifying them. The semiconducting industry has exploited these developments to gain an understanding of electronic materials (especially the surfaces) and to build improved devices [1-4]. Engineering alloys pose a challenge in the 1980s similar to semiconducting materials in the 1960s. Metallurgical processes are capable of producing alloys with exceptionally good bulk properties. However, components often fail because of a weakness at the surface. Advances in surface treatments of alloys are being sought to improve components as well as to provide a better understanding of surface sensitive mechanical properties.

Film deposition is one technology capable of tailoring surface properties independent of bulk properties [5]. An alternative technology is ion implantation, a process which modifies surfaces directly by injecting atoms into them. Although developed primarily for the semiconducting electronics industry, ion implantation has the capabilities for modifying surface mechanical properties of engineering alloys [1,3]. This paper focuses on one such property, tribological behavior, and presents an approach taken by me and my colleagues at the US Naval Research Laboratory for investigating ion implantation as a means of improving the tribological properties of engineering components.

Tribology is the study of the behavior of materials in rubbing contact. Tribologists have long known that three of the most obvious tribological processes – adhesion, friction and wear – are surface sensitive [6–8]. For example, air-formed oxides (usually less than 3 nm thick) on metals permit metals to contact other metals without adhering, while as little as a monolayer of a fatty acid can reduce the friction coefficient (tangential force divided by normal force) to less than 0.1 and reduce wear by a factor of 10^5 or more. However, only recently, with the advent of UHV chambers and advanced analytical spectroscopies, have tribologists been able to investigate the chemi-

Table 1

Analytical techniques and microscopies used to analyze ion-implanted steels and worn surfaces; composition can be elemental (E) and/or chemical (C); microstructure can be crystallographic (X) or textural (T)

Technique	Acronym	Information	Wear scar analysis (lateral resolution, nm)
Composition			
Auger electron spectroscopy	AES		
Scanning Auger microscopy	SAM	E, C	100
X-ray photoelectron spectroscopy	XPS	E, C	No
Secondary ion mass spectrometry	SIMS	E, C	1000
Energy dispersive X-ray analysis by electrons	EDX	E	2000
X-ray fluorescence	XRF	E	No
Ion (proton)-induced X-ray analysis	IIXE (PIXE)	E	No
Rutherford backscattering spectrometry	RBS	E	No
Nuclear reaction analysis	NRA	E	No
Electron energy loss spectroscopy	EELS	E	100
Microstructure			
Transmission electron microscopy	TEM	T	1
Selected are-diffraction	SAD	X	20
Scanning electron microscopy	SEM	T	10
Ion channeling	IC	X	No
Differential interference contrast	DIC	T	5; 2000 [a]
Michelson interferometry	MI	T	5; 2000 [a]

[a] Height; width.

cal and microstructural basis of surface-sensitive tribological processes [9]. In the present study, surface analytical techniques have played a major role. Those found most suitable for analyzing ion implanted alloys and wear scars are listed in table 1 and are described in sections 2.1 and 2.2.

Dearnaley and Hartley at AERE Harwell in the early 1970s were the first to report that significant reductions in friction and wear could be achieved by injecting high concentrations (1 to 20 at%) of selected atoms into engineering materials [10,11]. Early results were obtained with simple friction and wear devices such as pins sliding against flats. Later, the beneficial effects were demonstrated more convincingly by lifetime tests of implanted engineering components (e.g. knives, dies, etc.) [12]. Many of these effects were confirmed and new effects discovered by Hirvonen and co-workers at the Naval Research Laboratory (NRL) in the late 1970s [13–15]. Ion implantation processing for improving tribological properties has since become a world wide endeavor [16].

Results of two such investigations performed with simple pin-against-flat and pin-against-cylinder geometries are presented in fig. 1. The two graphs on the left depict the wear behavior of a fully-hardened bearing steel (AISI-52100) implanted with Ti ions ($4.6 \times 10^{17}/cm^2$ at 190 keV) under poor lubrication (left) and good lubrication (center) conditions [15], and the graph on the right, an N-implanted austenitic stainless steel (AISI-304) under good lubrication conditions [13,14]. For Ti-implanted 52100 steel worn under poor lubrication conditions, the onset of catastrophic wear was delayed; under good lubrication conditions, the "run-in" wear was reduced by a factor of ten. For N-implanted 304 steel worn under good lubrication conditions, the wear mode was changed from severe to mild. While these experiments demonstrated the efficacy of ion implantation, they were unsuitable for understanding the effect of ion implantation on wear processes. For example, the initiation period for severe wear varied greatly from one run to the next, as indicated by the horizontal arrows
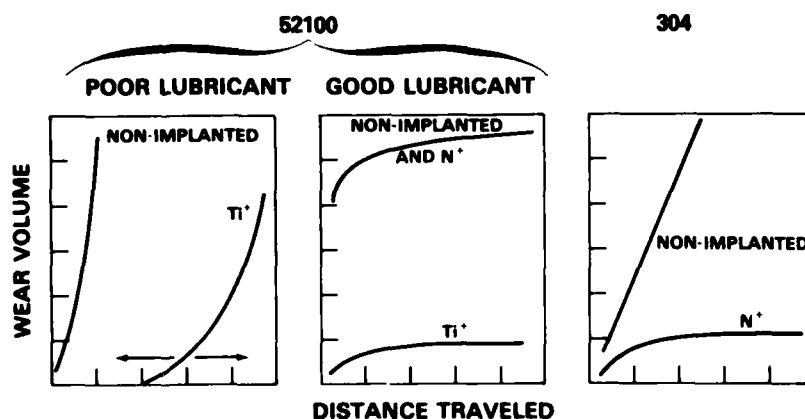

Fig. 1. Wear volume versus distance traveled for 52100 and 304 steels under indicated conditions. From Carosella et al. [15] and Hirvonen et al. [14].

in fig. 1 (left). Moreover, the severe wear scars produced by these tests were very difficult to analyze even with microprobe techniques.

These and other shortcomings of conventional wear experiments led to the development at NRL of several specialized methods for investigating ion implanted surfaces. The methods summarized in sections 2.3.1 and 2.3.2 enabled the chemistry and microstructure of an implanted surface to be followed as the implanted layer (less than 200 nm thick) was worn through. One of these methods, a polishing wear technique, gives wear resistance versus depth information with a depth resolution of about 20 nm. Section 3 presents applications of these methods to the aforementioned cases of N-implanted 304 steel and Ti-implanted 52100 bearing steel, as well as two related case studies. Explanation for the effects of N and Ti implantation are given. Finally, procedures are recommended in section 4 for the efficient use of surface analytical techniques to evaluate tribological applications.

2. Investigative methods

2.1. Techniques to identify chemical constituents

2.1.1. Surface spectroscopies

This section illustrates the use of analytical tools which probe only 1–2 nm of the surface. Of these Auger electron spectroscopy, AES, is probably the most powerful technique presently available for chemical analysis of ion implanted and worn surfaces. It is used in conjunction with ion milling to obtain composition versus depth profiles (hereafter called sputter depth profiles) of implanted layers (typically 50 to 200 mm thick) with excellent lateral (100 to 1000 nm) and depth (1 to 3 nm) resolution. Depth scales are established to an accuracy of ± 5 nm by measuring the depths of ion milled craters (see example in fig. 11). AES is especially sensitive (0.1 at%) to many of the low mass elements (C, N, B, O) which, as interstitial elements or metallide formers, affect the mechanical behavior of metals. Auger, therefore, has the sensitivity required to analyze tribological components which are routinely implanted to fluences from 10^{16} to 10^{18} ions/cm^2 in order to achieve peak implant concentrations up to 50 at%. In addition, Auger spectroscopy can provide detailed chemical bond information on these and many transition metal elements.

An example of the depth profiling capabilities of Auger is given in fig. 2, an analysis of N implanted steels [17–19]. Gaussian-like profiles of N were obtained for fluences from 1 to 20×10^{16}/cm^2 (at 40 keV/ion) in high Cr alloy steels, as illustrated by the "nitrogen in 304" steel profile. However, in low Cr alloy steels, the N profiles for a fluence of 2×10^{17}/cm^2 became heavily skewed towards the surface, as exemplified by the "nitrogen in 52100" steel

I.L. Singer / Processes affecting steels
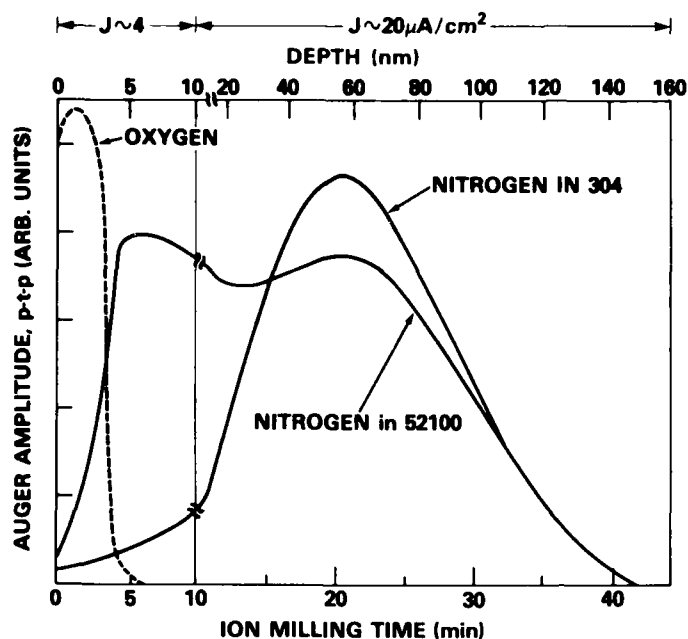
Fig. 2. Auger sputter depth profiles for N implanted to a fluence of $2 \times 10^{17}/cm^2$ at 40 keV/ion into 52100 and 304 steels. Note slower sputtering rates for profiles at surface. Depth scale obtained by measuring depths of sputtered craters.

profile. This skewed profile is not the implant sputter-limited profile which one obtains at fluences of $10^{18}/cm^2$; rather, it is a profile suggestive of outdiffusion during the implantation process.

Chemical bond information obtained from Auger spectra helps account for the differences in the two profiles. AES and X-ray photoelectron spectroscopy (XPS) studies on N-implanted 304 steel (Fe–18Cr–8Ni, by weight) indicated that N bonded selectively to Cr in the fluence range of 5 to 20 × $10^{16}/cm^2$ [20]. The Cr–N bond might have reduced the mobility of N in high Cr steels, where under stresses generated by ion implantation [21] the less tightly bound interstitial N in low alloy steel could have migrated outward.

Auger sputter depth profiling has also proven extremely valuable for studying metal ion implants. Transition metal ions such as the carbide formers V, Ti, Nb, Zr, Hf and Ta have great potential for reducing wear and friction of steel components [15,18,22,23]. An Auger sputter profile of Ti-implanted 52100 steel, reproduced in fig. 3, illustrates the wealth of detail obtainable. Ignoring for the moment the oxide layer, which actually forms after implantation is halted, we see there are not one but two foreign atoms incorporated in the steel surface: Ti and C. The Ti has nearly reached the implant sputter-limited profile at this high fluence, $4.6 \times 10^{17}/cm^2$ (at 190 keV). The C, whose presence above bulk level (4 at%) was unexpected, has a high surface concentration which falls off with a diffusion-like tail into the bulk.
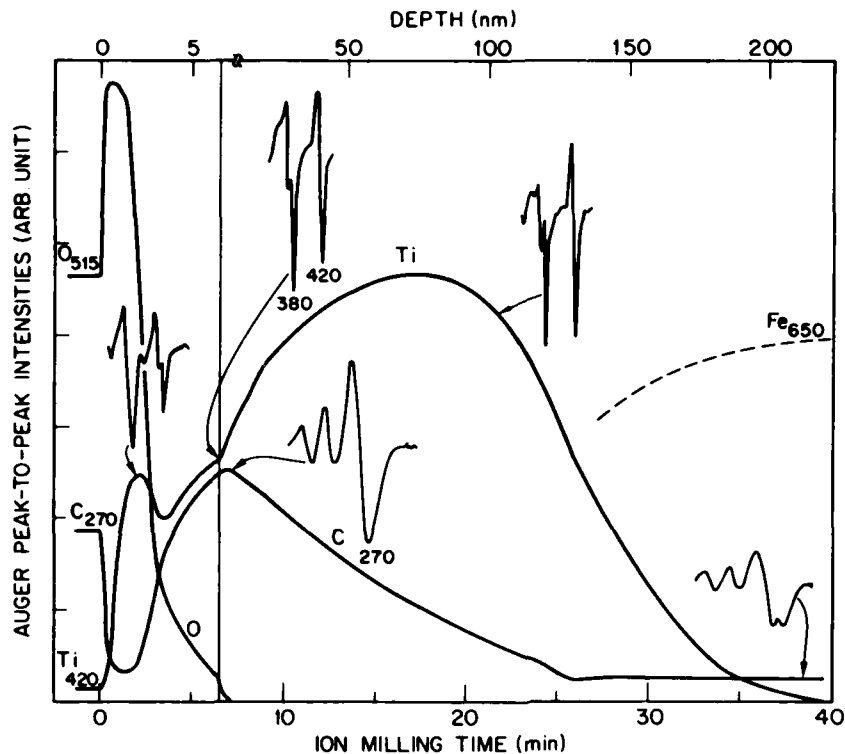
Fig. 3. Auger sputter depth profile of Ti-implanted 52100 steel (50×10^{16} Ti/cm^2 at 190 keV). Oxide layer, shown with expanded depth scale on left, was profiled at a low ion milling rate ($J \sim 3$–5 μA/cm^2). Implant region, on right, was profiled at $J \sim 25$ μA/cm^2. Portions of Ti(LMM) spectra (360–430 eV) were obtained with modulation amplitude of 3 eV; and those of the C(KLL) spectra (250–280 eV) with 1 eV. From Singer et al. [22].
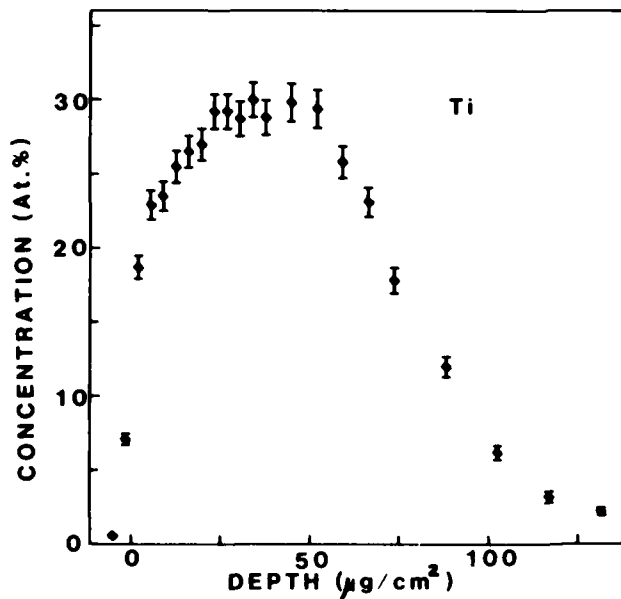
Fig. 4. Nuclear reaction analysis profile of Ti implanted (4.6×10^{17} Ti/cm^2, 190 keV) into 52100 steel by menas of the ^{48}Ti(p, γ)^{49}V resonance reaction. From Carosella et al. [15].
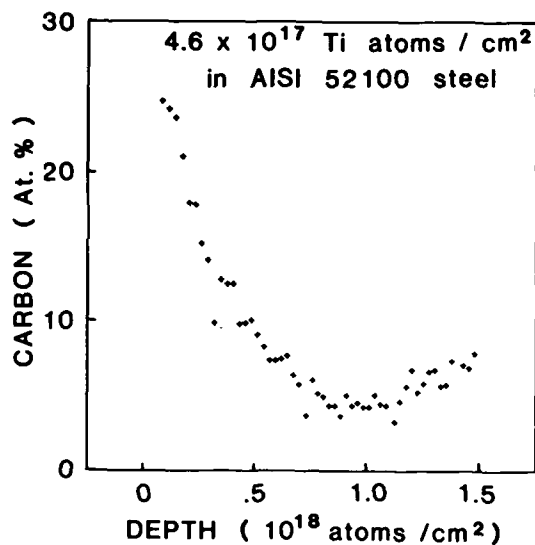
Fig. 5. Nuclear reaction profile of carbon in Ti implanted AISI 52100 steel by means of $^{12}C(^{3}He, ^{4}He)^{11}C$ reaction showing that a substantial amount of carbon enters the steel during implantation. From Hubler [41].

Both the Ti and C Auger sputter profiles have been verified by nondestructive nuclear reaction analysis (NRA) techniques developed by Gossett at NRL [24,25]. The Ti profile, obtained by a $^{48}Ti(p, \gamma)^{49}V$ reaction, is shown in fig. 4. The C profile, obtained by a $^{12}C(^{3}He, ^{4}He)^{11}C$ reaction is shown in fig. 5. The C profile confirmed that the Auger sputter profile of C (in fig. 3) was not produced by the sputter profiling process itself.
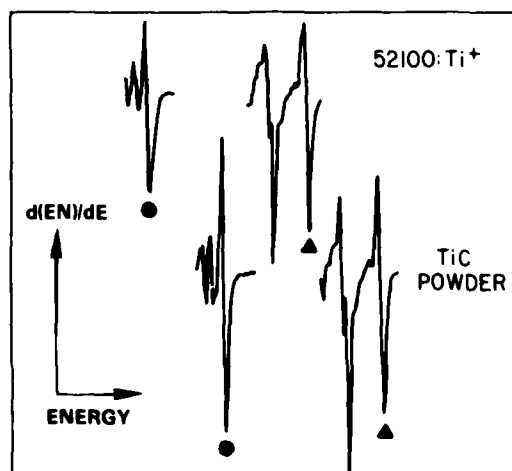
Fig. 6. Auger derivative spectra of C(KLL) and Ti(LMM) energy regions of (upper) Ti-implanted 52100 steel below oxide/metal interface and (lower) ion-milled TiC powder; (●) 272 eV C peak; (▲) 420 eV Ti peak. From Singer [27].

72

Auger spectra have also been used to identify the chemical states of Ti and C in the Fe–Ti–C layer [22]. The LMM spectrum of Ti, depicted in fig. 3, shows TiC-like bonding at the metal/oxide interface. Likewise, the KLL spectrum of C indicates bonding to Ti. These two spectra are reproduced in fig. 6 along with spectra from a TiC crystallite to illustrate their similarities. Towards the bulk, the LMM spectrum of Ti becomes metal-like and the KLL spectrum of C evolves into that of a (FeCr)-carbide. Similar Ti and C spectra have been obtained for high fluence Ti implants into pure Fe, alloy steels, Co, Al and even carbides.

The chemistry of the oxide layer can also be studied in detail by Auger analysis. The oxide, as seen in fig. 3, consists of an outer Fe_2O_3 layer (determined by MVV spectra of Fe (not shown)), followed by a TiO_2 layer (identified by the LMM spectra of Ti depicted in fig. 3). This oxide and the adventitious C layer which covers it formed on the implanted surface *after* implantation was terminated. Nonetheless the oxide must not be overlooked since oxides can play a major role in the friction (via adhesion) and wear (via debris formation) of steels [26].

Finally, Auger sputter profiles have been obtained for steels implanted with Ti over a range of energies and fluences used for processing engineering component. Fig. 7 depicts two families of composition versus depth profiles for implantation energies of 55 and 190 keV [27]. These profiles of Ti and excess C not only helped to establish the source of excess C, but also provided a chemical basis for the friction and wear behavior of Ti-implanted steels [28] as will be described in section 3.2.

There are several well documented problems associated with interpreting Auger sputter profiles [29,30]. I would like to address two of these. The first concerns the reliability of chemical information obtainable from ion milled surfaces. In general, an ion beam can cause chemical reactions to occur (e.g. by forming or breaking bonds), which may render Auger or XPS analysis suspect. However, a surface suffers considerably greater damage during ion implantation (at 40–200 keV) than during ion milling (at 2 keV) [31], and whatever chemistry is obtained from ion milled surfaces was probably established by the implanted ions themselves.

The second concerns quantitative compositions vs. sputter depth profiles. In our work, depth scales are determined directly by interferometry of craters produced by ion milling during sputter depth profiling (see section 2.2 below). Auger spectra taken in the derivative mode are quantified by the usual normalizing procedure, using sensitivity factors obtained from reference compounds (e.g. alloys and carbide powders of known composition) and from reference spectra (e.g., NRA spectra). Our values generally agree with most of the sensitivity factors for metallic elements from the PHI handbook [32]. However, sensitivity factors for oxidized metals can be a factor of two different from those of the pure metal species (e.g., the 385 eV spectrum of Ti). The
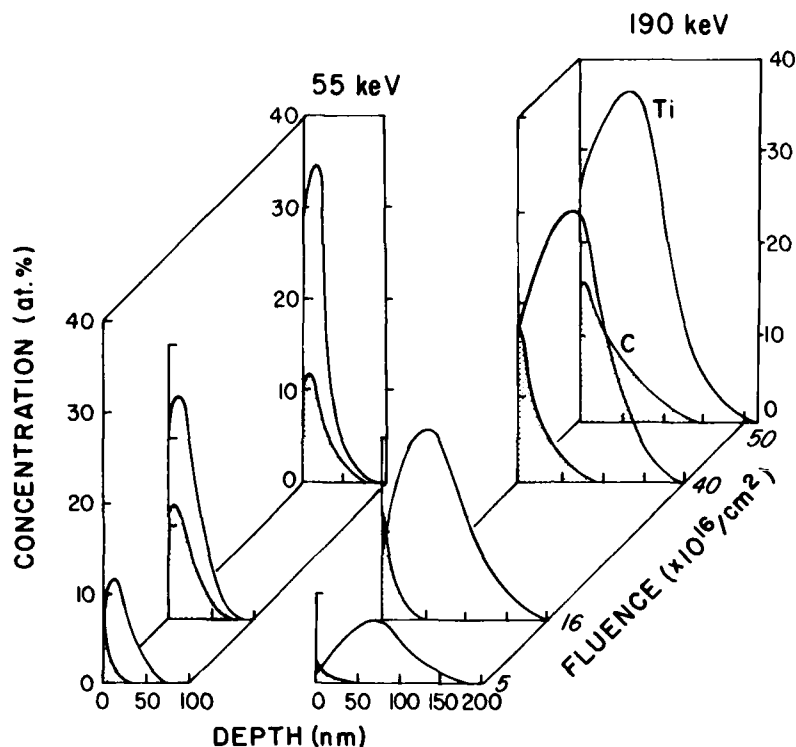
Fig. 7. Auger sputter depth profiles for Ti and C in Ti-implanted 52100 at several fluences and energies; (left) 5, 16, and 40×10^{16} Ti$^+$/cm^2 at 55 keV; (right) 5, 16, 40, and 50×10^{16} Ti$^+$/cm^2 at 190 keV. Note: bulk C concentration of the steel (4 at%) was subtracted from data. From Singer [27].

most abused sensitivity factor found in the literature is that of C. The value given in the PHI handbook is for a graphitic carbon yet it is often applied indiscriminately for carbides. Carbides can have sensitivity factors up to 3 × or more greater than graphite. Misuse of this sensitivity factor, made all too easy by computer-automated composition analysis, can lead to gross over-estimates in carbide concentrations [33]. This error can generally be avoided by use of appropriate reference compounds as calibration standards.

X-ray photoelectron spectroscopy, XPS, can be used in an identical manner as AES for composition versus sputter depth profiles, chemical analysis, etc. XPS presently has limited spatial resolution and requires longer data acquisition times than Auger, both due to limitations imposed by the X-ray source.

Secondary ion mass spectrometry, SIMS, because of its great atomic sensitivity (ppm for many elements), has played a dominant role in the elemental analysis of implanted semiconductors [34]. It also can provide some limited chemical information through fragmentation patterns and has microprobe capabilities with 1 μm resolution. SIMS, however, is more difficult to quantify
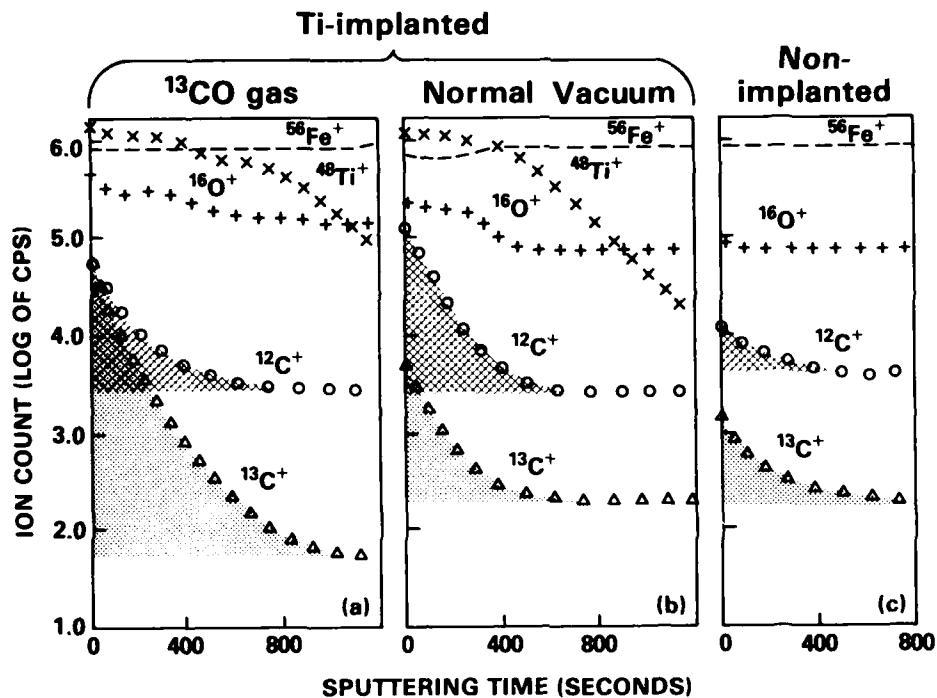
Ti-implanted

Fig. 8. SIMS sputter depth profiles of 304 steel substrates obtained with 5.5 keV O_2^+ beam at current density J: (a) Ti-implanted in partial pressure of ^{13}CO gas ($J = 200$ $\mu A/cm^2$); (b) Ti-implanted in normal vacuum ($J = 90$ $\mu A/cm^2$); (c) non-implanted ($J = 90$ $\mu A/cm^2$). From Singer and Barlak [35].

than AES or XPS, especially for high fluence implants, where matrix effects can control the ionization yield of sputtered particles.

SIMS, by virtue of its isotope sensitivity, has made a unique contribution to *the understanding of the origin of C in Ti-implanted steel. Several years ago we* speculated that, during implantation, C is absorbed from residual gas molecules impinging on the sputter-eroded surface [22]. Highly reactive Ti ions at the surface becomes sites for dissociative chemisorption of gases, producing a source of free C atoms to migrate into the surface. This hypothesis was recently verified by SIMS [35]. In the experiment, Ti was implanted into steel surfaces with normal vacuum conditions (10^{-6} Torr) and with the vacuum chamber backfilled with ^{13}CO gas. SIMS profiles of the implanted layers, shown in fig. 8, indicated a nearly 30-fold increase in the ^{13}C-to-^{12}C ratio for the sample implanted in the presence of ^{13}CO gas.

2.1.2. Thin film spectroscopies

This section illustrates the use of spectroscopies which probe depths of 1 μm or more non-destructively. X-ray emission spectroscopy, XES, can be very useful for identifying implanted species (at fluences $> 10^{16}/cm^2$) rapidly and

I.L. Singer / Processes affecting steels

non-destructively. Energetic ions [36,37], X-rays [38] or electrons [39] can be used to induce X-ray emission from atoms to depths much greater than the implanted layer. One consequence of the greater sampling depth of these spectroscopies is that the dose of the implant retained by the substrate can be measured from the ratio of the implant-to-substrate X-ray intensity. An example of energy dispersive X-ray analysis, EDX, of the retained dose of Ti implanted into steel is given in fig. 9 [40]. The vertical scale on the left gives the ratio of the peak intensities of Ti($K\alpha$) to Fe($K\beta$) spectra. The retained dose scale on the right was calibrated by assuming full retention at a fluence of 5×10^{16}/cm, i.e., Ti($K\alpha$)/Fe($K\beta$) = 0.20; at this low fluence, Auger analysis (fig. 7) showed no evidence of sputter removal of implanted Ti. The retention efficiency (retained dose/fluence) fell below 1 at higher fluences as sputtering removed implanted Ti. This effect was more pronounced for the lower energy (more shallow) implants, consistent with the Auger data in fig. 7. The scatter in the data of fig. 9 is not due to errors in EDX measurements; ratio data recorded on the same samples over a two year period agreed to better than 4%. Rather, the scatter arises from errors in the fluence measurements. Similar retention curves have been obtained by X-ray fluorescence analysis, XRF. EDX, however, has the advantage of being incorporated in a scanning electron microscope and, thus, becomes a very powerful microprobe tool for wear scar analysis.
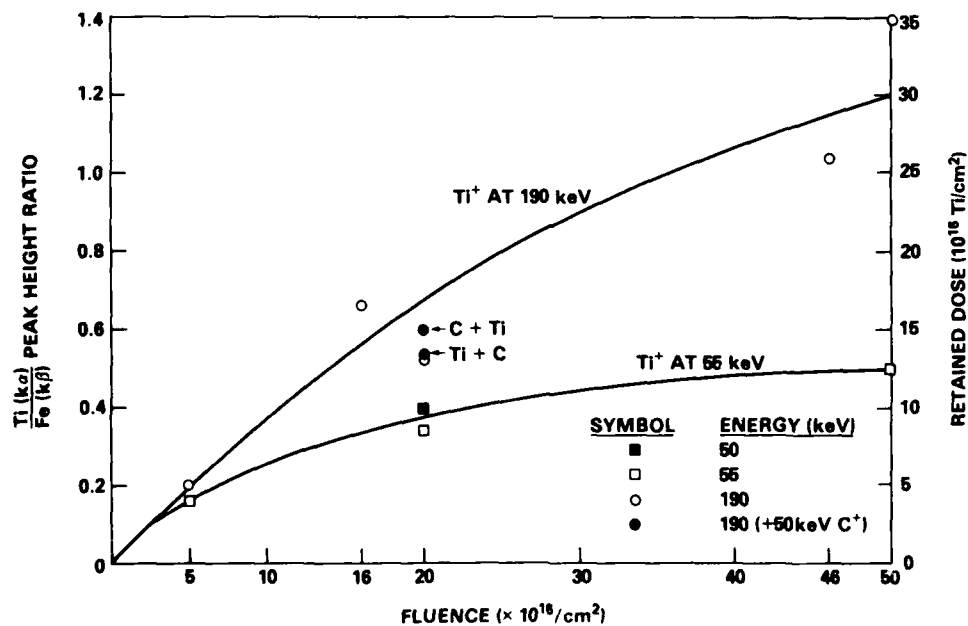
Fig. 9. EDX intensity ratios (Ti to Fe) versus fluence for Ti-implanted 52100 steels at several energies. The electron beam energy was 20 keV; the angle of incidence was 45°. The solid lines are best guess curves for 55 and 190 keV implants.

Rutherford backscattering spectrometry, RBS, and nuclear reaction analysis, NRA, are the classic spectroscopies in the field of ion implantation [1-4]. Both use high energy (MeV) beams of protons or alpha particles to obtain non-destructive and quantitative composition versus depth analysis with a depth resolution typically 10 to 20 nm. RBS detects elastically backscattered particles, usually protons or alpha particles, and therefore is sensitive to all atoms at or below the surface. It is applied most efficiently to study implants of heavy atoms into lighter substrates; examples of its application to ion implantation are found in many books and articles [1-3,41].

NRA detects (in principle) only particles emitted by a selected nuclear reaction and, therefore, is sensitive to a particular atom. It is most useful for analyzing implants having masses similar to or lighter than the substrate atoms, as in the cases of Ti implanted in steel (fig. 4) and C absorbed in steel (fig. 5). Atomic sensitivity and depth resolution vary considerably, depending on the nuclear reaction employed. However, new techniques for high sensitivity, high resolution (1-3 nm) NRA are being developed to keep pace with the demand for improved analytical capabilities [41,42].

Electron energy loss spectrometry, EELS, is a technique for detecting low mass elements (e.g., C, N, O) in thin foil samples [43]. EELS and XES can be performed on thin foils of implanted substrates, along with scanning transmission electron microscopy, STEM, in order to correlate implant concentrations with microstructural changes.

2.2. Techniques to identify microstructures

Transmission electron microscopy, TEM, has provided the most detailed microstructural analysis of ion implanted materials [44]. Thin foil specimens are usually prepared by cutting a thin disk of the implanted (or worn) surface, then etching to perforation from the backside. An example of a TEM microstructural analysis is presented in fig. 10, which depicts TEM images and selected are diffraction (SAD) patterns of a 52100 steel, before and after implantation of Ti (4.6×10^{17}/cm^2 at 190 keV) [45]. The steel in its hardened state had a lath-like matrix with small carbide precipitates; the SAD pattern indicated a body-centered tetragonal (martensite) matrix. TEM images of the Ti-implanted steel were quite featureless, except for the contrast differences from grain to grain and from carbide to matrix. SAD patterns of each of these contrast features were indexed to amorphous Fe [22]. Thus, high fluence Ti implantation rendered both the carbide and the matrix of 52100 steel amorphous. TEM studies by Knapp et al. [46] have shown that Fe is also driven amorphous by high fluence Ti implantation. Vacuum carburization of Fe or steel appears responsible for causing the surface to go amorphous for reasons not yet understood.

Fig. 10. TEM images and SAD patterns from thin foil specimens of hardened 52100 steel. (a) Non-implanted; (b) Ti-implanted. 5×10^{17} Ti$^+$/cm^2. Courtesy of J.A. Sprague.

TEM generally examines the most prominent microstructural features over a depth of 50 to 200 nm, depending on the mean free path of the high energy electrons. In order to obtain microstructure versus depth analysis by TEM, Vardiman and Singer [47] have prepared thin foils of implanted substrates whose implanted layers have been ion milled to selected depths using Auger sputter profile analysis. Results of TEM analysis of these front-surface milled foils will be presented in section 3.1.

Ion channeling, IC, is a backscattering technique performed on single crystals to obtain disorder versus depth profiles [48]. Because IC detects atoms located *off* an atomic lattice site, the degree of disorder in an implanted layer can be determined by measuring the backscattering yield on-axis relative to the yield off-axis. This powerful technique can be used in conjunction with RBS or NRA to correlate microstructural changes with composition changes of implanted surfaces. For example, using IC, NRA and RBS, Knapp et al. [46] were able to correlate the disorder depth of a Ti-implanted Fe surface with
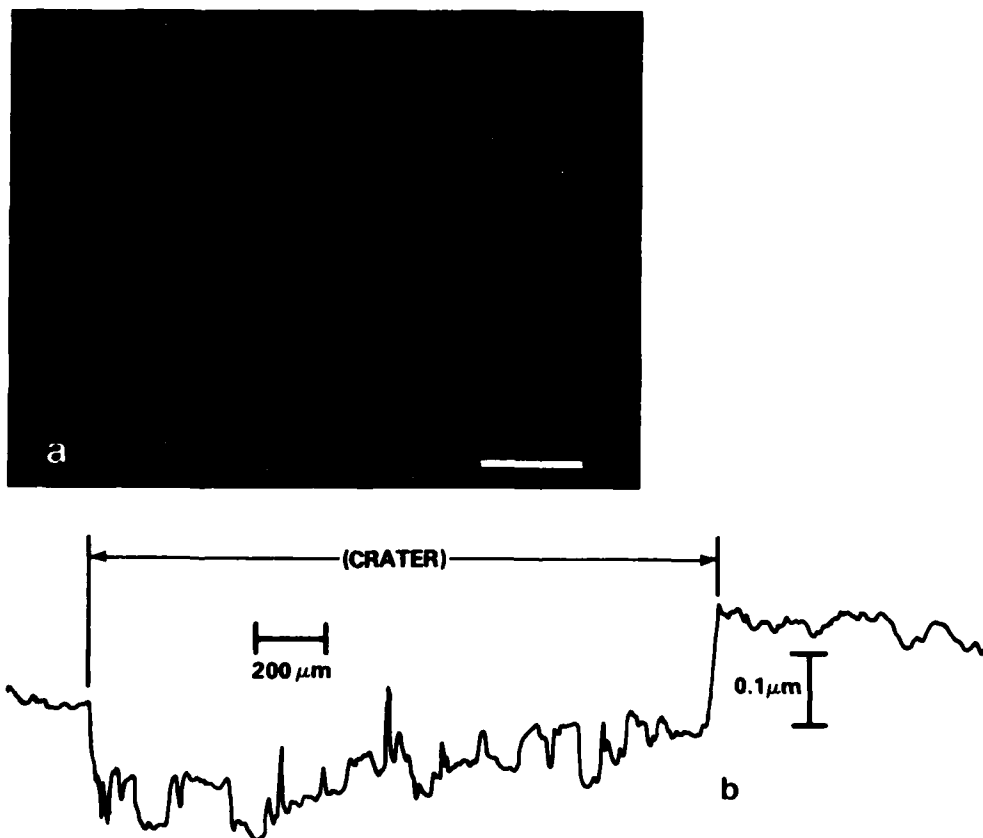
Fig. 11. 2 keV Ar ion-milled crater in 304 steel. (a) Optical interferogram showing Michelson interference lines (fringe spacing = 294 nm); scale mark represents 200 μm. (b) Stylus trace across crater. From Singer [49].

79

the growth of an Fe–Ti–C layer. TEM studies, as mentioned earlier, showed the disorder layer to be amorphous.

Microstructural studies of ion implanted surfaces can also be performed by metallographic analysis of etched surfaces. For metallographic analysis, surfaces must be carefully polished before implantation then etched to accurately determined depths. Both conditions can be met for AES or SIMS sputter profiles, and craters left by in milling are usually suitable for metallographic analysis. As illustrated in fig. 11, ion milling on polycrystalline 304 steel produced a textured surface because each grain etched at a different rate depending on its orientation relative to the ion beam. Ion milling to approximately the same depth in Ti-implanted 304 steel produced no texture, from which it was inferred that Ti implantation destroyed the crystallinity by rendering the surface amorphous [49]. A recent TEM analysis confirmed that the Ti-implanted 304 steel surface is, indeed, amorphous [50].

Metallographic analysis can also be performed on substrates with finer microstructural features than found in 304 steel. Differential interference contrast (DIC) micrographs of craters milled in Ti-implanted 52100 steel showed distinctly different textures, depending on implant fluence [51]. At $5 \times 10^{16}/cm^2$ the crater surface (fig. 12, right) was roughened, like that of non-implanted 52100 steel. At $50 \times 10^{16}/cm^2$, however, the crater (fig. 12, left) etched smoothly as would be expected of an amorphous layer. Surface features shown in figs. 11 and 12 were found during metallographic analysis, routinely performed in our lab to ascertain textures of substrates before and after implantation, wear or sputter profiling. Routine metallographic analysis is highly recommended to complement and give direction to further microprobe analyses.

2.3. Tribology

Two rather simple devices are used in our laboratory for examining the response of implanted surfaces to wear. One is a "stickslip" machine, so called because many material couples tend to stick, then slip, instead of sliding smoothly during rubbing contact. The stickslip machine replicates a fairly severe adhesive wear situation when metal is slide against metal. The entire history of the run-in process can occasionally be found in a track 5 mm long produced after only 2 unidirectional passes. The second device is a polishing machine which subjects the implanted surface to the cutting action of very fine abrasive particles. Abrasive wear rates have been correlated with hardness so that the relative polishing rates of implanted layers can, in many cases, be considered a measure of the relative hardness of the implanted layer [52]. Both devices have been found to be very sensitive, and reproducibly so, to implanted surfaces; in addition, worn surfaces produced by these machines are particularly amenable to chemical and microstructural analysis.

Fig. 12. DIC (Nomarski) photos of 52100 steel. (a) Implanted with 5×10^{16} Ti/cm^2 at 190 keV and ion milled to a depth of 150 nm. (b) Implanted with 5×10^{17} 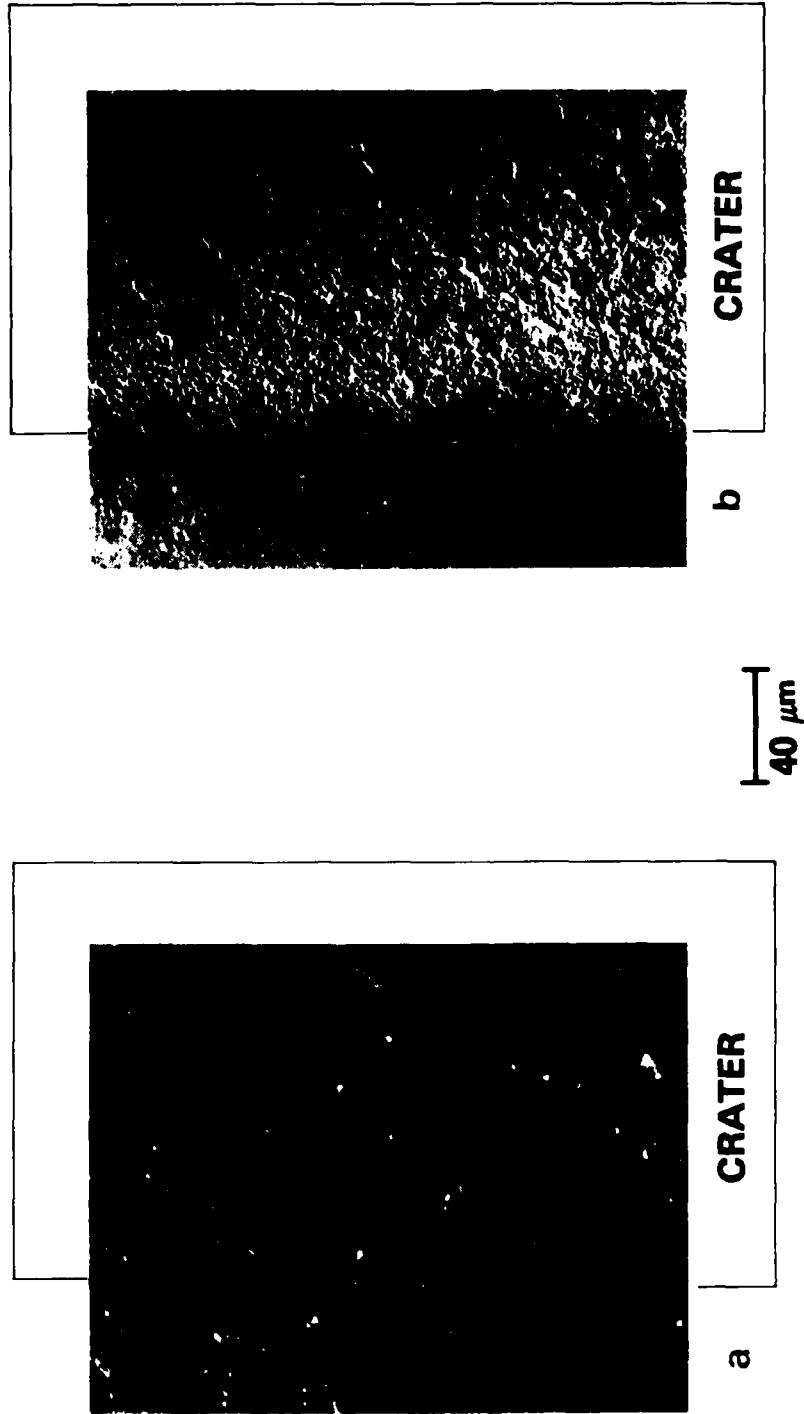Ti/cm^2 at 190 keV and ion milled to a depth of 150 nm. The left hand portion of each micrograph is as-implanted material that was masked to prevent ion milling. From Hubler et al. [51].

2.3.1. Stickslip machine

The stickslip machine utilizes a sphere-against-flat geometry to obtain friction coefficients and wear tracks for subsequent analysis. A 1.27 cm diameter AISI-52100 steel ball is attached to an arm which applies the load against a flat disk. The disk, attached to a piston-driven platform, slides beneath the stationary ball. Two pairs of strain gauges, bonded to the arm, measure the normal and tangential forces of the ball sliding against the disk. Disks and balls are thoroughly solvent cleaned before implantation.

Friction measurements are performed in laboratory air (40–60% RH at ~ 22°C) at a sliding speed of 0.1 mm/s. A normal force of 9.8 N (1 kgf) is used (in most runs) producing a peak Hertzian pressure of 0.85 GPa (123 kpsi). The first pass on each track is 5 mm in length; subsequent unidirectional passes over the same track are 3 mm each, leaving a track with one pass and multipass scars. At least two tracks are run for each implant treatment, sometimes four: two for unlubricated (dry) and two for lubricated sliding conditions. Once sliding commences the kinetic coefficient of friction, μ_k, typically varies no more than ±0.05 along a given traverse and is often reproducible to ±10% from one track to another on a given pass. When stickslip occurs, however, μ_k jumps between a high and low value.

Wear tracks are examined optically by DIC microscopy to determine the surface texture and by interferometry to measure the depth of the wear or plastic deformation. SEM/EDX and SAM are then used to obtain more detailed chemical analysis of the identifiable features in the wear track such as the wear debris.

2.3.2. Polishing machine

A vibratory polisher, charged with 1–5 μm diamond paste on a synthetic textile cloth, abrades steel surfaces at a fairly slow rate (2–6 nm/min) [53]. The relative wear rates of implanted to non-implanted surfaces can be obtained with a depth resolution of 10–20 nm by abrading implanted and reference disks simultaneously for periods of 5 to 10 min. To ensure reproducible results, nine disks, three each in three equally weighted holders, are polished simultaneously until wear rates reach a constant value [17,52–54]. Three of the disks are then implanted, reweighed, then polished and weighed at 5 or 10 min intervals along with the remaining six reference disks. The relative wear resistance, RWR, of each implanted disk is calculated from mass losses of the implanted (ΔM_I) and reference (ΔM_R) disk as the inverse of their ratio, i.e., RWR = $(\Delta M_R / \Delta M_I)$. The thickness of the worn layer is given by $\Delta M / \delta A$, in which δ is the density of the worn material (accounting for the implanted species as well as the host) and A is the area of the disk. Weight loss measurements are usually reproducible to better than 5 μg, which corresponds to depths of about 5 nm for a 1.3 cm diameter steel disks. Therefore, RWR values at wear depth increments as low as 10 nm can be resolved.

In addition to providing RWR versus depth data, abraded surfaces can be analyzed at selected wear depths by optical microscopy to examine surface textures (e.g. scratch sizes), by EDX or AES to determine compositions at wear depths, and by TEM to obtain microstructures of implanted, worn surfaces. The TEM studies, though tedious, have proven most valuable as will be discussed in section 3.1.

3. Case studies

The approach we have taken to understand tribomechanial effects imparted by ion implantation is to correlate chemical and microstructural changes with tribological behavior of the worn surfaces. The beneficial effects of. N-implanted into 304 steel and Ti-implanted into 52100 steel (see fig. 1) will now be explained. In 304 steel, N implants will be shown to control the microstructure of worn surfaces. In 52100 steel, the fluence at which Ti is implanted will be shown to control the composition of the surface, and the composition shown to determine the friction and wear behavior. The chemistry of an implanted 304 steel surface which has been deformed during sliding is reported in a third case study. Finally, the effect of implantation angle on the friction behavior and chemistry is discussed.

3.1. N-implanted 304 steel

Fig. 1 shows that N implantation dramatically altered the lubricated sliding wear behavior of 304 steel. In fact, a more detailed analysis of the wear track on the N-implanted cylinder showed virtually no wear and almost no (< 50 nm) plastic deformation. Auger sputter profiles of the track in the implanted portion indicated that nearly all of the N in the track was retained as initially implanted (i.e. as shown in fig. 2). By contrast, tracks nearly 10 μm deep were formed on the nonimplanted portion of the same cylinder. SEM photos of scratches found in the two tracks showed clearly that the two surfaces responded much differently to wear [14]: fine scratches in the non-implanted region showed considerable plastic flow at the edges, whereas scratches in the N-implant track had the shape of a sharp "V" groove. One explanation given for this behavior was that N hardened the 304 steel surface [13].

However, polishing wear studies of the N-implanted surface suggested that something more subtle may have happened: that N implantation, in fact might have prevented the unwanted hardening which occurred during wear of the 304 surface [17,52,54]. Fig. 13 presents the relative wear resistance (RWR) versus depth measurements (top) combined with Auger sputter profiles (bottom) of the implanted N distribution before and at several stages of wear. The RWR is lower at depths where implanted N atoms were found. Further investigations

83
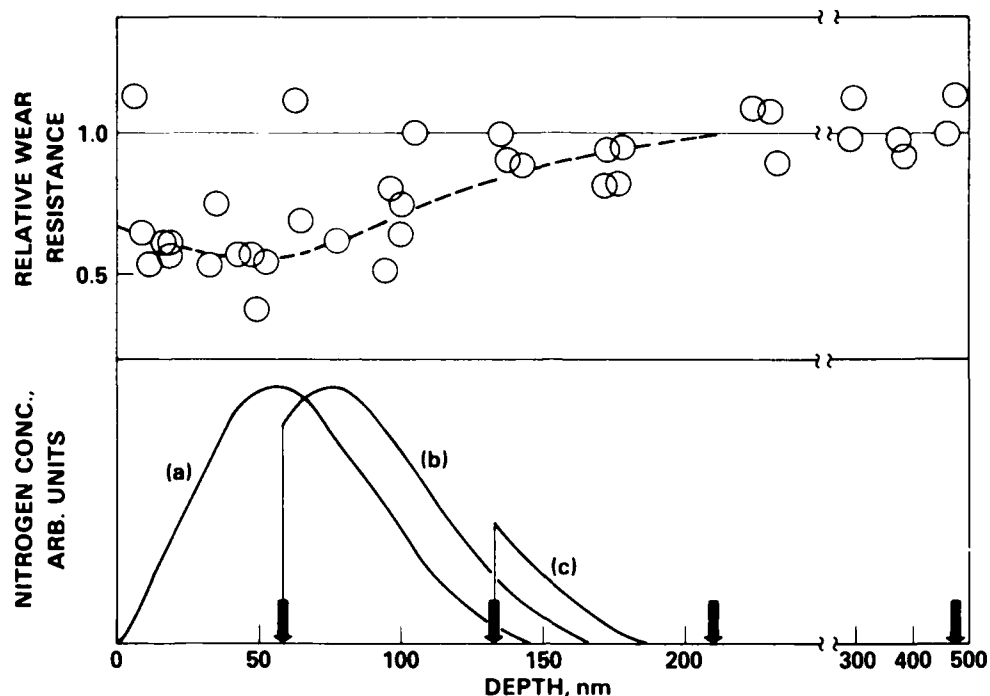
Fig. 13. Upper: Relative wear resistance of nitrogen-implanted to nonimplanted 304 steel versus depth. Lower: Nitrogen concentration versus depth profiles of surfaces exposed to (a) no wear and (large arrows) various stages of wear. Note depth scale change at 250 nm. From Bolster and Singer [17].

showed that the RWR of austenitic 304 steel was much higher than that of a ferritic steel of the same hardness. A comparison of RWR to bulk hardness values for carbon steels (quenched-tempered and nitrided) and 304 steel is presented in fig. 14. The enhanced abrasion resistance of 304 steel was
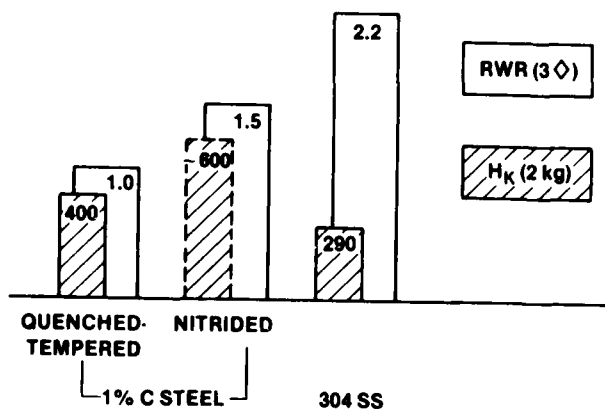
Fig. 14. Comparison of abrasion resistance (RWR) and Knoop hardness of three steels. From Bolster and Singer [17].

attributed to strain hardening of the surface during polishing [52]. This effect was known to occur in austenitic steels subjected to abrasion or "trepanning" (smooth rubbing) [55].

It then became apparent that the surface of 304 steel might not be as ductile or soft as the bulk hardness values would indicate. Hsu et al. [56] had recently investigated the sliding wear behavior of 304 steel. They observed that severe wear occurred by delamination of thin, brittle layers from the intrinsically softer 304 substrate. The brittle layers were identified by TEM to contain a martensitic phase which resulted from a stress induced transformation of the austenite. Bolster and Singer therefore speculated that N, a known austenite stabilizer, might have prevented the 304 steel surface from transforming and becoming brittle martensite, thereby preventing the deleterious hard-skin-on-soft-substrate wear condition [52].

TEM investigations were next carried out by Vardiman et al. [57] on polished 304 surfaces to determine the microstructure responsible for abrasion hardening and N-implantation softening. The non-implanted polished surface showed a mixture of deformed austenite (γ-phase) and martensite (α'-phase). After implantation, nearly all the martensite was converted to austenite. Even after polishing the implanted surface to a depth near its peak concentration, austenite still remained the predominant phase [58]. Selected area diffraction (SAD) patterns of the non-implanted an N-implanted surfaces which identified these two phases are shown in fig. 15. The N-transformed austenite showed two rings for each reflection, with the inner ring corresponding to a dilated 304 steel lattice. Vardiman and Singer found that the inner ring was commensurate with a lattice dilated by N at its peak concentration [47]. This dilation suggests that all the implanted N atoms (up to 24 at%) remained in solid solution. Thus, implanted N was retained in this heavily worked surface in a supersaturated solid solution, and stabilized the austenite against transforming to martensite during subsequent wear.

Microstructural changes in abraded and implanted 304 steel surfaces were expected to be confined to depths less than 1 μm. The traditional metallographic approach of analyzing tapered sections could not be relied on for such thin layers. However, a new approach combining ion milling with TEM, proved very successful. Briefly, 3 mm disks of abraded surfaces were ion milled to selecte depths, then thinned from behind for TEM examination. Results [47,58] of two such examinations are presented in table 2. In the first, the martensite layer produced by 3 μm diamond polishing was found to be confined to the outermost 50 nm of a 304 steel disk. In the second, the N-converted austenite was found to extend no deeper than the implanted layer ($\sim$ 200 nm).

In summary, detailed microstructural analysis supported the hypothesis that N implantation stabilized the austenitic phase in 304 steel and thereby inhibited the formation of the deleterious strain-induced martensite.
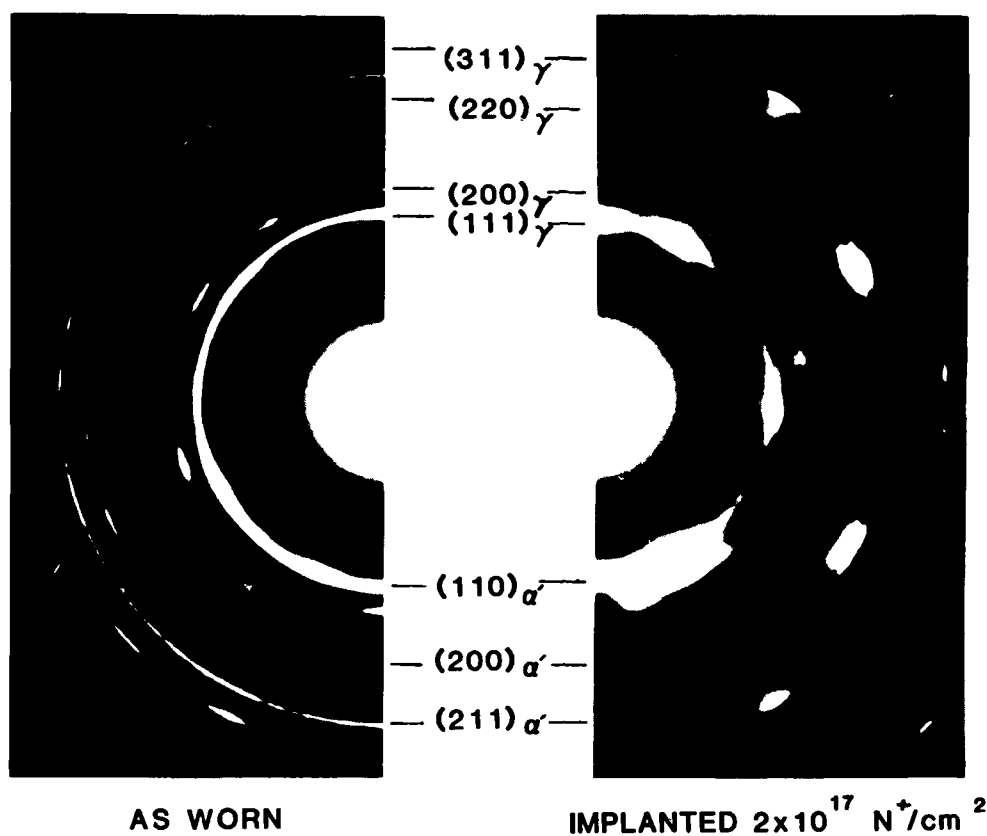
Fig. 15. SAD patterns from abraded 304 steel surfaces; 11.6 μm selected area. From Vardiman et al. [57].

3.2. Ti-implanted 52100 steel

Ti was found unique among a variety of implant species in its ability to reduce wear of hardened 52100 bearing steel under severe sliding conditions

Table 2
Phases observed by selected area diffraction on stress-transformed 304 steel before and after ion milling (α' – bcc; γ – fcc; γ^N – fcc with N in solution)

Specimen preparation	Before	After	Ion milling depth (nm)
Abraded (3 μm diamond)	$\alpha' + \gamma$	Mostly γ	50
Rolled (97% reduction), N-implanted ($2 \times 10^{17}/cm^2$ at 75 keV)	$\alpha' + \gamma^N$	Mostly α'	200

[15]. The pin-on-disk and ball-on-cylinder results, illustrated schematically in fig. 1, led to more detailed stickslip tests of the high fluence ($5 \times 10^{17}/cm^2$ at 190 keV) Ti-implanted surface. Friction measurements showed that the kinetic coefficient of friction in dry sliding was reduced from $\mu_k = 0.6$ (steel-against-steel) to $\mu_k = 0.3$ and that lubricated (hexadecane) sliding proceeded without stickslip [15]. Tracks produced during dry sliding showed essentially none of the wear, surface texturing or debris formation found with steel-against-steel [22,28]. An interferogram and DIC micrograph of a 10 pass track, shown in fig. 16, illustrate the scuffing wear resistance of Ti-implanted to high fluences into 52100 steel [28]. In polishing wear tests, the Ti-implanted 52100 steel was up to 6 times more abrasion resistant than non-implanted 52100 steel, with an RWR versus depth profile similar to the Ti concentration versus depth profile [18]. The RWR profile is reproduced in fig. 17.

This remarkable friction and wear behavior has been attributed to an amorphous Fe–Ti–C layer which forms during implantation of Ti to highest fluences [22] (see fig. 10). High fluences are necessary to produce the vacuum carburized surface layers discussed in section 2.1. The fluence needed to obtain

Fig. 16. Optical micrographs of wear track on Ti-implanted 52100 steel (5×10^{17} Ti/cm^2 at 190 keV). DIC photo with interferogram inset (fringe spacing = 273 nm). 15th pass track for which $\mu_k = 0.3$. From Singer and Jeffries [28].
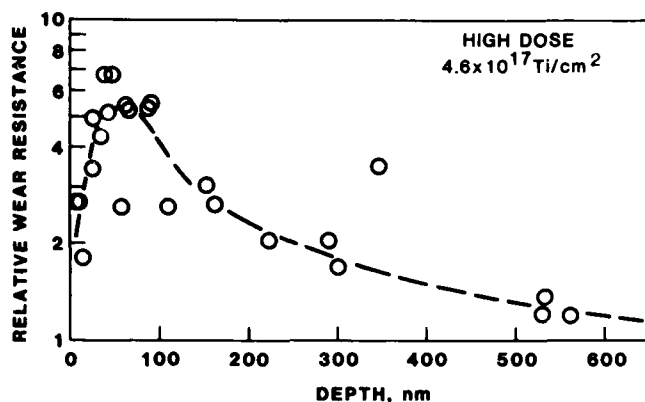
Fig. 17. RWR of Ti-implanted 52100 steel versus depth; $4.6 \times 10^{17} Ti/cm^2$ at 190 keV. From Singer et al. [18].

a carburized layer sufficient for imparting wear resistance depends on the energy of implantation. A fluence of $2 \times 10^{17}/cm^2$ is sufficient for shallow implants at an energy of 50 keV, but $5 \times 10^{17}/cm^2$ is needed for deeper implants at 190 keV to produce a fully carburized layer (see fig. 7). C implantation does not give the low friction, wear resistant surface obtained by vacuum carburization [59]. It is an open question, however, whether the tribological behavior of the surface is a consequence of the microstructure, e.g., of an amorphous layer or of the chemistry, e.g., a less adherent, shear resistant oxide layer which grows on top the vacuum carburized surface after implantation.

The role of surface chemistry in the friction and wear behavior of Ti-implanted into steel at lower fluences was investigated by Singer and Jeffries [28].
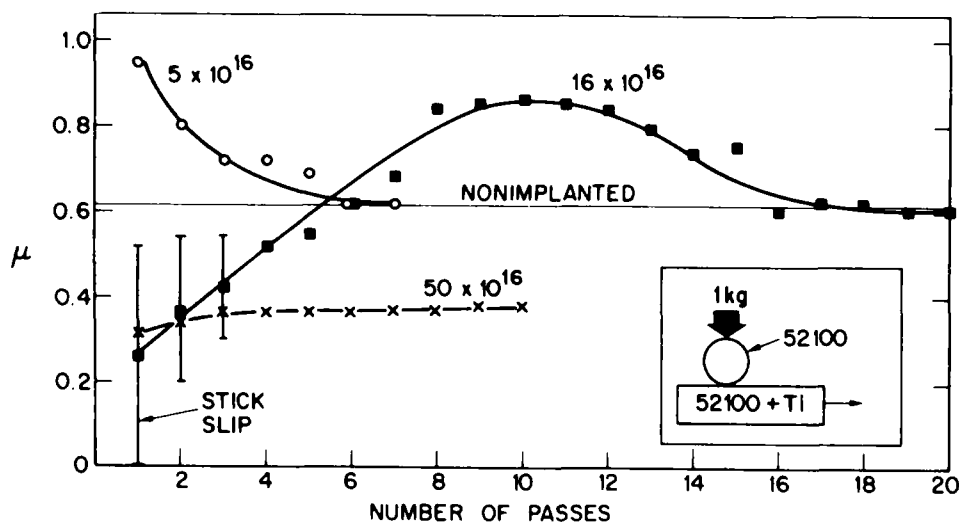
Fig. 18. Coefficient of dry sliding friction versus number passes for 52100 steels implanted with Ti at indicated fluence. Schematic of friction test shown in inset. From Singer et al. [22].

The study was prompted by the unexpectedly high friction coefficients obtained on 52100 steel implanted with Ti to low (5×10^{16}/cm^2) and medium (16 to 20×10^{16}/cm^2) fluences [22]. Plots of μ_k values as a function of pass number, presented in fig. 18, gave high friction values ($\mu_k \sim 0.8$) on first pass against surfaces implanted to a low fluence, and after 8 passes against surfaces implanted to medium fluences. Auger analysis showed that the first and tenth pass tracks of the two implanted surfaces respectively had, in common, an Fe–Ti composition devoid of the friction-reducing carburized layer; they also lacked the heavily oxidized layer which, as will be shown later, controls the steady state friction. An Fe–Ti composition elicits a higher frictional force than Fe sliding against Fe because the more reactive Ti promotes greater adhesion [60].

The low fluence sample came by its Fe–Ti surface composition naturally, since a fluence of 5×10^{16} Ti/cm^2 at 190 keV was too low to form a vacuum carburized layer (see Auger depth profiles for 190 keV implants in fig. 7). The medium fluence sample, however, developed an Fe–Ti surface composition only after some wear had occurred. Before wear, the as-implanted surface, shown in fig. 19, had a "partially" carburized surface layer, 40–50 nm thick. Ten successive passes of the steel slider over the same track sheared off this partially carburized layer, exposing the underlying Fe–Ti alloy. The depth of the sheared layer, 45 nm, was measured directly by interferometry as shown in the micrograph inset in fig. 20.
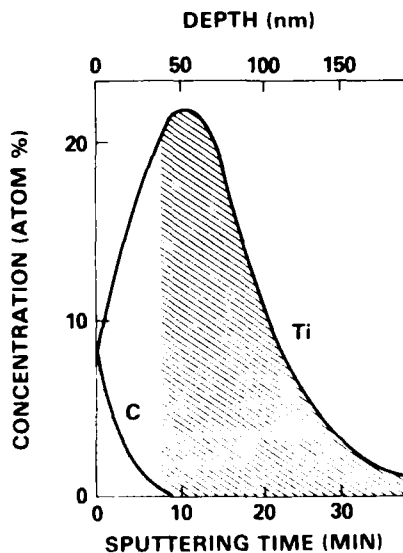
Fig. 19. Auger sputter depth profiles of Ti and excess C (above bulk 4 at%) in 52100 steel implanted 1.6×10^{17}Ti/cm^2 at 190 keV. See text for significance of cross-hatched area. From Singer and Jeffries [28].

To prove that wear, not just deformation, had occurred, an SEM/EDX analysis of the wear track was performed. The track, as seen in the DIC micrograph in fig. 20, contained large debris-free regions as well as debris particles. Debris-free regions inside the track had two-thirds the Ti concentration as the as-implanted surface, according to the $Ti(K\alpha)/Fe(K\beta)$ ratios. This ratio is identical to the fraction of Ti contained below the partially carburized layer of the as-implanted surface (cross-hatched area in fig. 19). Debris in the track gave larger $Ti(K\alpha)/Fe(K\beta)$ ratios than the as-implanted surface, as would be expected of debris originating from wear of the implanted layer.

Debris flakes found on sliders consisted of compacted surface layers that had worn off the track during sliding. A SEM micrograph of the debris flake generated during the 10 passes of sliding just described is shown in fig. 21. The surface of the flake was sufficiently featureless and smooth that reliable sputter depth profiles could be obtained with a conventional Auger microprobe (5 μm spot size). Auger sputter depth profiles for Fe. Ti, O and C leveled out within minutes of sputtering (at 20 μA/cm^2). Spectra taken 10 min after steady state was reached are also shown in fig. 21. Lineshapes of Ti(LMM) spectra
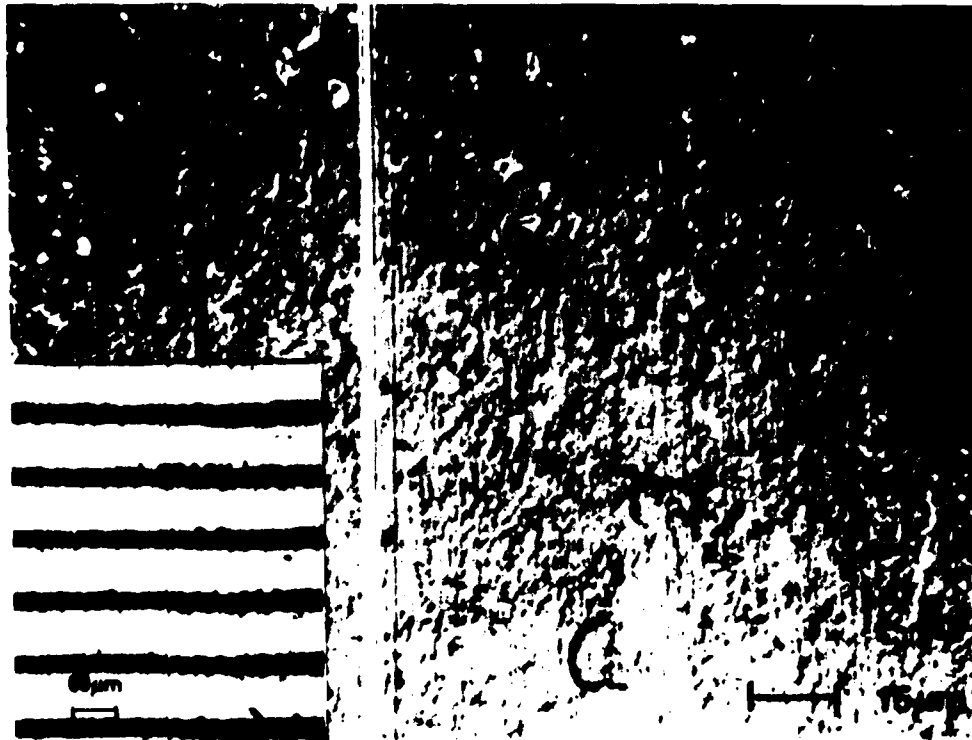

Fig. 20. Optical micrographs of a wear track on Ti-implanted 52100 steel (1.6×10^{17}/cm^2 at 190 keV). DIC photo which interferogram inset (fringe spacing = 273 nm). 10th pass track for which $\mu_k = 0.8$. From Singer and Jeffries [28].

indicated TiO_2, and those of Fe(LMM) and Fe(MVV) indicated Fe oxide; almost no C (< 1%) was detected. Semiquantitative analysis using sensitivity factors obtained from reference compounds [28] gave a composition of $Fe_{32}Ti_{13}O_{55}$ or, roughly 40% TiO_2, 60% Fe/Fe_2O_3. The debris contained almost 50% more Ti than was expected from the near surface composition (fig. 19), i.e. Ti/Fe ~ 0.25. Moreover, the Ti was fully oxidized, and the Fe almost fully oxidized. These studies suggest that, even during low speed sliding (0.1 mm/s), debris flakes can become heavily oxidized and Ti may segregate to the flake's surface.

Oxidation also appears responsible for reducing the high friction coefficient obtained from steel against the Fe–Ti layer. In both the low ($5 \times 10^{16}/cm^2$) fluence and the medium ($16 \times 10^{16}/cm^2$) fluence cases (see fig. 18), μ_k dropped from 0.8 to a steady state value of 0.6 after several passes. In steady state, all surfaces in sliding contact – debris on the slider, debris in the track, and the debris-free regions of the track – showed considerable oxidation [28]. Moreover, Ti in the near surface region (first 20 nm) was oxidized. This chemistry is revealed in the detailed Auger microprobe analysis presented in fig. 22. Three regions of a 14 pass track in a $16 \times 10^{16} Ti/cm^2$ fluence surface were sputter depth profiled simultaneously: the as-implanted surface, a debris-free region of the wear track, and a debris spot on the track. The wear track, besides having lost its partially carburized layer, was oxidized much deeper than the as-implanted layer. The debris was also oxidized. In both cases, the metallic Ti was
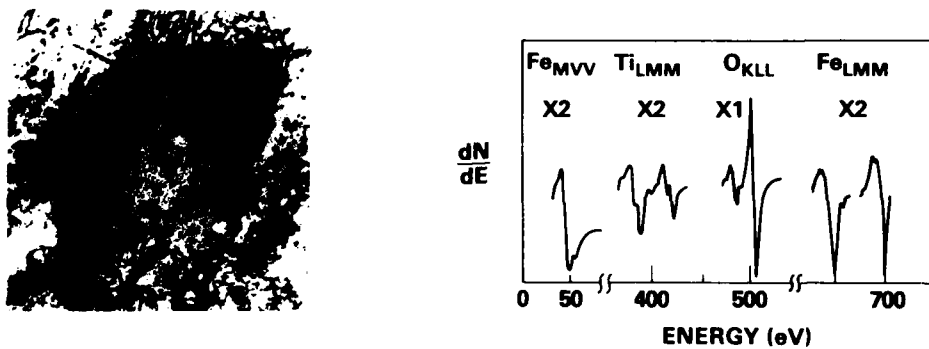
Fig. 21. (a) Scanning electron micrograph and (b) steady-state Auger spectrum of debris flake on slider, after 10 passes against 52100 steel implanted to $1.6 \times 10^{17} Ti/cm^2$ at 190 keV, where $\mu_k = 0.8$. (a) Scale mark represents 20 μm.

AD-A165 432   THE USE OF ION IMPLANTATION FOR MATERIALS PROCESSING   2/3
              (U) NAVAL RESEARCH LAB WASHINGTON DC   F A SMIDT
              86 MAR 86 NRL-MR-5716

UNCLASSIFIED   F/G 13/8   NL
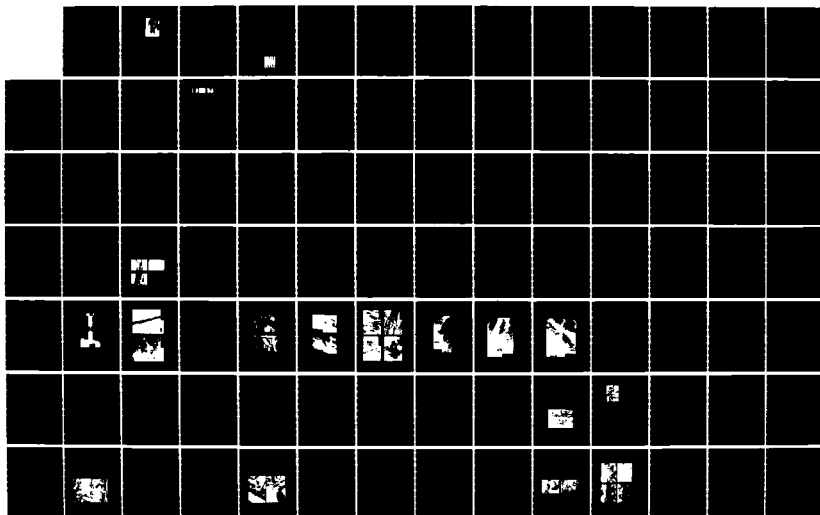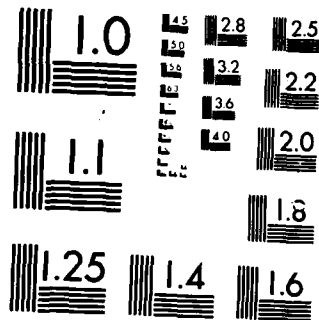
MICROCOPY RESOLUTION TEST CHART

NATIONAL BUREAU OF STANDARDS 1963 A
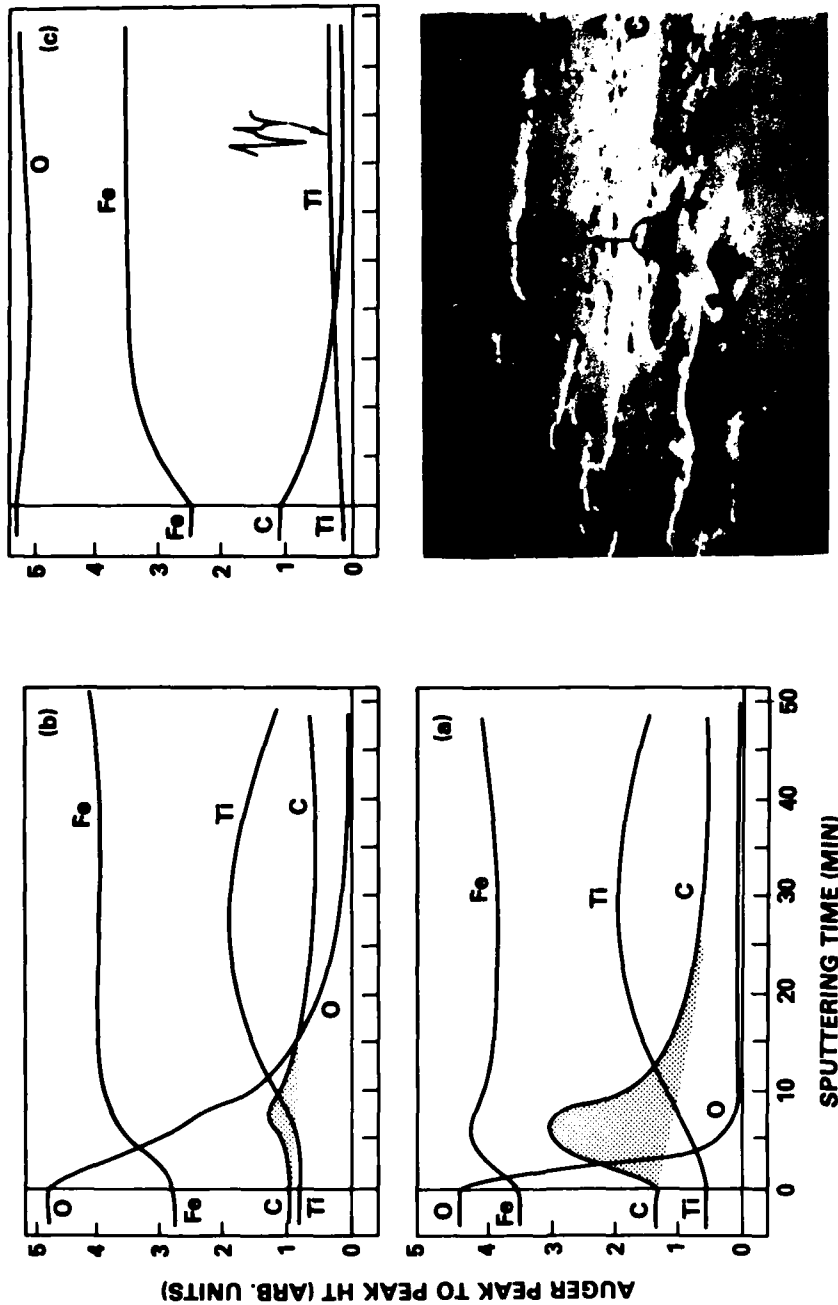
Fig. 22. Auger microprobe analysis of wear track. SEM photo of track area in medium fluence disk worn to steady state. Auger microprobe spectra (a) out of track, (b) debris-free region in track, (c) debris flake in track. Auger conditions: $V_e = 5$ keV; $V_{mod} = 3$ eV for Ti_{420} and O_{515}; $V_{mod} = 6$ eV for C_{270} and Fe_{650}. From Singer and Jeffries [28].

converted to oxidized Ti, diminishing its chemical reactivity, and thereby decreasing the adhesion and frictional coupling.

In summary, detailed surface chemical analysis has elucidated the carburization process responsible for the beneficial effects of Ti implantation. It has also provided evidence for correlating friction coupling of Fe-alloys with the chemical state of the contacting surfaces.

3.3. (Ti + C)-implanted 304 steel

The third case addresses the analysis of plastically deformed wear tracks. The objective of this study was to determine the effectiveness of ion implantation on the wear behavior of steels subjected to plastic deformation during sliding. Briefly, it is well known that tracks on a metal substrate will begin to deform plastically if the contact stress produced during sliding exceeds the elastic limit of the substrate. Plastic deformation causes a smooth surface to roughen, thereby accelerating wear by repeated plowing and fracture. Type-304 steel was the substrate of interest because of its previously described pathological behavior during plastic deformation.

The effect of implanting both Ti and C were investigated. Ti was chosen to reduce adhesion during dry sliding contact and C, which behaves like N in steel, to stabilize the austenite matrix during deformation. Ti was implanted near the surface and formed the Fe–Ti–C layer discussed earlier. C was implanted deeper ($\sim$ 300 nm peak deep) to affect the plastically deforming subsurface layers. The plastically deformed track, shown in fig. 23, was generated on the stickslip machine after 20 sliding phases of a hardened 52100 steel ball against the implanted 304 steel substrate. Deformation of the track was anticipated [61] since the Hertzian stress (0.85 GPa) produced by the hard ball on the softer 304 steel exceeded the yield strength (0.54 GPa) of 304 steel. The Michelson interferogram of the track showed a plowed (and grooved) center portion $\sim$ 600 nm deep with ridges $\sim$ 600 nm high along the side walls of the track. Nomarski micrographs of the scar (not shown) showed little if any debris in the implanted track.

Auger sputter depth profiles were obtained on spots in and out of the track using a conventional SAM system (PHI model 545). The electron beam (10 μm diameter) was repositioned manually from a featureless spot deep in the track to one outside the track, then back in, etc. during the ion milling operation. Profile data were later separated into the two profiles shown in fig. 23, in which dashed lines connect the actual profile data given by solid lines. The composition of the track was nearly identical to that of the original surface albeit depressed 600 nm below the original surface by plastic deformation. Some wear (10–20 nm) of the surface was suggested by the slight shift to the left of the Ti peak inside the track. The slight decrease ($\sim$ 10%) in the Ti, Fe and C Auger intensities inside the track relative to outside the track was
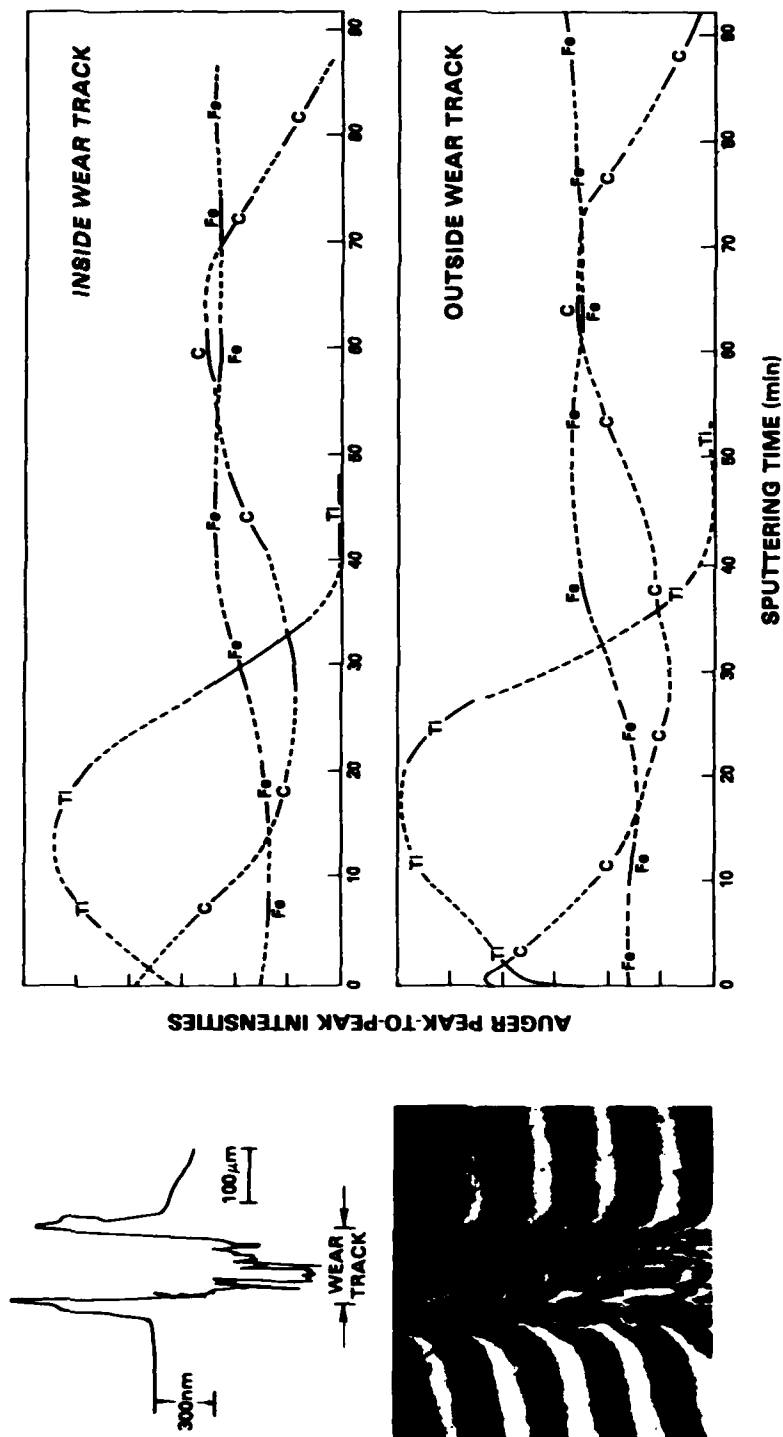
Fig. 23. Left: Michelson interferogram of a wear scar on (Ti + C)-implanted 304 steel. Right: Auger sputter profiles inside (top) and outside (bottom) the wear track.

attributed to effects of roughness on the collected Auger intensity. Finally, the depth of the C with respect to the surface inside the track did not shift despite the heavy plastic deformation, indicating that C did not migrate under the applied load and sliding induced stresses. EDX confirmed that the Ti layer was retained in the depressed track.

This study, as well as the one on wear of partially carburized Ti-implanted steel surfaces, should indicate the care one must take in using analytical tools to evaluate the wear behavior of ion implanted surfaces. Plastic deformation must not be confused with wear, as pointed out by Fischer et al. [62]; otherwise, one might have concluded incorrectly from fig. 23 that Ti and C had migrated below the surface during 600 nm of wear. Also, many wear tracks have more rugged terrains than that shown in fig. 23. Yet, despite the wear, tracks may contain much of the original surface on ridges, and valleys or in debris particles. Analytical studies of such such tracks must be performed with microprobes having the appropriate lateral and depth resolution in order to properly interpret the results.

As an example, Lo Russo et al. [63] used a broad beam NRA technique to measure the concentration of N retained in a fretted wear scar whose depth was ascertained to be 5 μm by weight loss measurements. They reported detecting 20% of the N dose found in the as-implanted surface. This result has been cited [11,12] as evidence for N migration into the bulk during wear, when in fact N could have been retained in plastically deformed valleys of the original surface or in debris generated from the original surface. Future reports of analytical studies on ion implanted wear surfaces should be reviewed more critically.

3.4. Ta-implanted 52100 steel

The final case examines the effect of implantation angle on the friction coefficient of Ta-implanted 52100 steel. Ta, like Ti, is one of several strong carbide formers (e.g. Ti, Ta, Hf, V, Zr, Nb) expected to produce a vacuum carburized layer on steel when implanted to high fluences. Ta, however, should require lower fluences than Ti to achieve a fully carburized layer because it does not penetrate as deep as the lighter Ti atom and sputters Fe faster (i.e. with a higher sputtering yield). Dry sliding studies of 52100 steel sliders against Ta-implanted (1.8×10^{17}/cm^2 at 150 keV) 52100 steel gave a low friction ($\mu_k = 0.4$), wear resistant surface for implantation at normal incidence to the substrate, but a high friction ($\mu_k = 0.6$), scarred surface for implantation at an angle of 40° to the surface. If implantation cannot be performed effectively at angles off the normal, then curved surfaces (e.g. bearing rolles, races and cutting tools) will pose special processing problems.

Auger sputter depth profiles, shown in fig. 24, indicated that the composition of the implanted layer was changed drastically by Ta implantation off
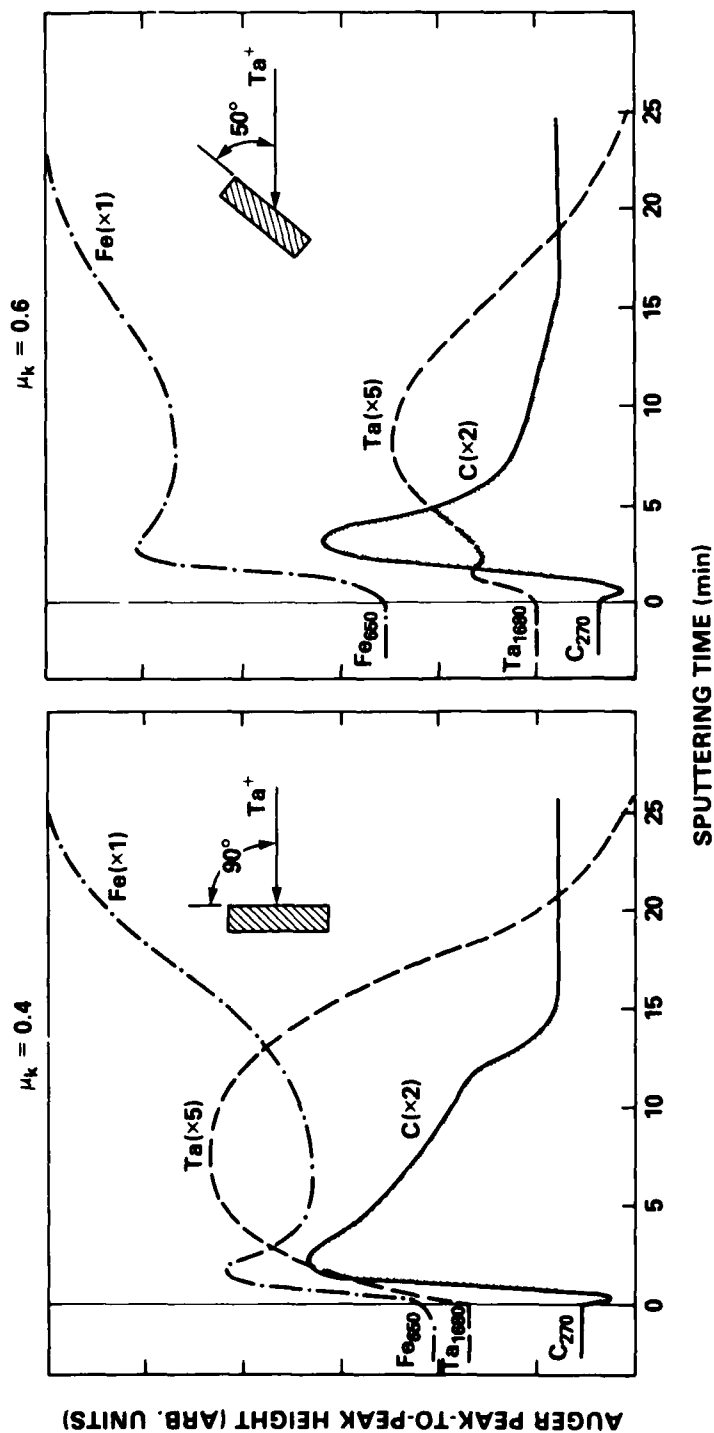
Fig. 24. Auger sputter depth profiles of Ta-implanted 52100 steel $91.8 \times 10^{17}/cm^2$ at 150 keV). Ta beam was directed at normal (left) and oblique (right) incidences to substrate.

normal. The surface Ta concentration at a 50° implantation angle was approximately 1/3 that of Ta implanted at normal incidence; the carburized layer was also reduced considerably. Hence, implantation at 50° did not produce a sufficiently high surface concentration of a vacuum carburized Fe–Ta–C to reduce friction.

At present, there is no detailed model which can predict the composition profile of carbide-forming ions implanted at a given angle versus fluence. Such a model must take into account both well understood phenomena, e.g. the angular dependence of fluence, ion range and sputtering yield, and poorly understood phenomena, e.g., carburization during implantation and sputtering yields of carburized alloy layers. Only recently, with the advent of high current implanters and surface analytical techniques, has the issue of vacuum/surface interactions received so much attention, even though the classic studies in 1961 by Almen and Bruce [64] indicated anomalous sputtering yields of carbide-forming metals. Detailed analytical studies (RBS, NBA, AES, PIXE, EDX) of high fluence implants are presently being performed at NRL to assist in the development of models for predicting compositions of alloys implanted to high fluences [65–67].

4. Summary and recommendations

A surface analytical approach has been presented for investigating the effects of ion implantation on friction and wear behavior of steels. Surface analytical techniques such as SAM, EDX, and SIMS, and microscopies such as TEM, SEM, and interferometry have elucidated the microstructure and chemistry of a variety of implants (N, C, Ti and Ta) found to affect the tribological behavior of surfaces. Novel combinations of these techniques, such as metallography of ion-etched surfaces or ion beam etching of TEM foils, have been shown to be useful alternative methods for establishing microstructures of implanted and/or worn surfaces. Detailed Auger studies of Ti-implanted steels have led to an understanding of the vacuum carburization process, which produces low friction, wear resistant surfaces on steels.

The following recommendations are offered for using surface analytical tools in conjunction with studies of modified surfaces for tribological applications. The recommendations refer specifically to ion implantation but they may also be applied to other surface processing technologies:

(a) Establish retained dose versus fluence curves for the implant species/ substrate combinations under investigation. For species heavier than $Z = 11$, XES techniques (XRF, EDX, PIXE) give non-destructive and rapid analyses. For lighter mass elements, wavelength dispersive XES or NRA (or RBS, if feasible) are necessary for non-destructive analysis. NRA and RBS, unlike the XES techniques, provide composition versus depth profiles.

97

(b) Obtain a surface chemical analysis (AES, XPS, or SIMS sputter depth profile) on one sample from each implantation batch. This should provide positive identification of substrate composition and implant species as well as verify intended fluence. (Mistakes in each of these three categories are not unheard of!)

(c) Examine the chemistry of the implanted surface. In particular, pay attention to oxide thickness, implant distribution profiles, redistribution of alloy constituents (e.g. surface segregation) and presence of unexpected species (e.g. carbon from the vacuum system). This task is handled most easily by Auger analysis, with support from the other analytical tools as discussed in section 2.1.

(d) Examine the microstructure of the implanted surface. Look for phase transformation presence of new phases and lattice location of implanted species. TEM and IC provide the most detailed information. Metallography of etched surfaces, though less specific, can also be useful.

(e) Examine wear scars. Look for wear mode (e.g. abrasive, adhesive), plastic deformation and nature of wear debris. Optical techniques such as DIC and interferometry are easier to use and often more sensitive to topographical changes than SEM.

(f) Identify chemical and microstructural features of the wear scar. Microprobe analysis by SAM, SIMS or STEM should be performed only after the topographical features of the wear scar have been examined.

Acknowledgments

References

[1] G. Dearnaley, J.H. Freeman, R.S. Nelson and J. Stephen, Ion Implantation (North-Holland, Amsterdam, 1973).
[2] J.W. Mayer, L. Ericksson and J.A. Davies, Ion Implantation in Semiconductors, Silicon and Germanium (Academic Press, New York, 1970).
[3] P. Townsend, J.C. Kelly and N.E.W. Hartley, Ion Implantation, Sputtering, and their Applications (Academic Press, New York, 1976).
[4] W.-K. Chu, J.W. Mayer and M.-A. Nicolet, Backscattering Spectrometry (Academic Press, New York, 1978).
[5] R.F. Bunshah, Ed., Deposition Technologies for Films and Coatings (Noyes, Park Ridge, NJ, 1982).

[6] F.P. Bowden and D. Tabor, The Friction and Lubrication of Solids (Oxford University Press, London, 1950).

[7] I.V. Kragelskii, Friction and Wear (Butterworths, London, 1965).

[8] E. Rabinowicz, Friction and Wear of Materials (Wiley, New York, 1966).

[9] D.H. Buckley, Surface Effects on Adhesion, Friction, Wear and Lubrication (Elsevier, Amsterdam, 1981).

[10] N.E.W. Hartley, Tribology 8 (1975) 65; Wear 34 (1975) 427.

[11] N.E.W. Hartley, in: Ion Implantation, Ed. J.K. Hirvonen (Academic Press, New York, 1980) p. 321.

[12] G. Dearnaley, in: Ion Implantation Metallurgy, Eds. C.M. Preece and J.K. Hirvonen (Metallurgical Soc. of AIME, Warrendale, PA, 1980) p. 1.

[13] J.K. Hirvonen, J. Vacuum Sci. Technol. 15 (1978) 1662.

[14] J.K. Hirvonen, C.A. Carosella, R.A. Kant, I.L. Singer, R. Vardiman and B.B. Rath, Thin Solid Films 63 (1979) 5.

[15] C.A. Carosella, I.L. Singer, R.C. Bowers and C.R. Gossett, in: Ion Implantation Metallurgy, Eds. C.M. Preece and J.K. Hirvonen (Metallurgical Soc. of AIME, Warrendale, PA, 1980) p. 103.

[16] Much of the literature in this field is published in conference proceedings cited in refs. [15,22,23–25,51,66,67].

[17] R.N. Bolster and I.L. Singer, ASLE Trans. 24 (1981) 526.

[18] I.L. Singer, R.N. Bolster and C.A. Carosella, Thin Solid Films 73 (1980) 283.

[19] W.M. Bone, R.J. Colton, I.L. Singer and C.R. Gossett, J. Vacuum Sci. Technol. A2 (1984).

[20] I.L. Singer and J.S. Murday, J. Vacuum Sci. Technol. 17 (1980) 327.

[21] N.E.W. Hartley, J. Vacuum Sci. Technol. 12 (1975) 485.

[22] I.L. Singer, C.A. Carosella and J.R. Reed, Nucl. Instr. Methods 182/183 (1981) 923.

[23] F.G. Yost, L.E. Pope, D.M. Follstaedt, J.A. Knapp and S.T. Picraux, in: Metastable Materials Formation by Ion Implantation, Eds. S.T. Picraux and W.J. Choyke (North-Holland, New York, 1982) p. 261.

[24] C.R. Gossett, Nucl. Instr. Methods 168 (1980) 217.

[25] C.R. Gossett, Nucl. Instr. Methods 191 (1981) 335.

[26] See ref. [9], chs. 5 and 6.

[27] I.L. Singer, J. Vacuum. Sci. Technol. A1 (1983) 419.

[28] I.L. Singer and R.A. Jeffries, J. Vacuum Sci. Technol. A1 (1983) 317.

[29] R. Holm and S. Storp, Appl. Phys. 12 (1977) 101.

[30] E. Taglauer, Appl. Surface Sci. 13 (1982) 80.

[31] See ref. [1], ch. 3, or ref. [3], ch. 4.

[32] L.E. Davis, Ed., Handbook of Auger Electron Spectroscopy (Physical Electronics Industries, Eden Prairie, MN, 1976).

[33] I.L. Singer, ASLE Trans. 26 (1983) 473.

[34] J.M. Morabito and R.K. Lewis, in: Methods of Surface Analysis, Ed. A.W. Czanderna (Elsevier, Amsterdam, 1975) p. 279.

[35] I.L. Singer and T.M. Barlak, Appl. Phys. Letters 43 (1983) 457.

[36] I.V. Mitchell and J.F. Ziegler, in: Ion Beam Handbook for Material Analysis, Eds. J.W. Mayer and E. Rimini (Academic Press, New York, 1977) ch. 5.

[37] F. Folkmann, J. Phys. E8 (1975) 429.

[38] L.S. Birks, X-Ray Spectrochemical Analysis (Interscience, New York, 1969).

[39] J.I. Goldstein, D.E. Newbury, P. Echlin, D.C. Joy, C. Fiori and E. Lifshin, Scanning Electron Microscopy and X-Ray Micro Analysis (Plenum, New York, 1981).

[40] I.L. Singer and R.A. Jeffries, unpublished data, 1982.

[41] G.K. Hubler, Nucl. Instr. Methods 191 (1981) 101.

[42] C.R. Gossett, in: Industrial Applications of Surface Analysis, Eds. L.A. Casper and C.J. Powell (American Chemical Society, Washington, DC, 1982) p. 49.

[43] D.C. Joy, in: Introduction to Analytical Electron Microscopy, Eds. J.J. Hren, J.I. Goldstein and D.C. Joy (Plenum Press, New York, 1979) ch. 7;
also D.M. Maker, ibid., ch. 9.

[44] See ref. [1], ch. 3, or conferences cited in ref. [16].

[45] J.A. Sprague, unpublished, 1980.

[46] J.A. Knapp, D.M. Follstaedt and S.T. Picraux, in: Ion Implantation Metallurgy, Eds. C.M. Preece and J.K. Hirvonen (Metallurgical Soc. of AIME, Warrendale, PA, 1980) p. 152.

[47] R.G. Vardiman and I.L. Singer, Mater. Letters 2 (1983) 150.

[48] See ref. [4], ch. 8.

[49] I.L. Singer, J. Vacuum Sci. Technol. 12 (1981) 175.

[50] D.M. Follstaedt, F.G. Yost, L.E. Pope, S.T. Picraux and J.A. Knapp, Appl. Phys. Letters 43 (1983) 357.

[51] G.K. Hubler, P. Trzaskoma, E. McCafferty and I.L. Singer, in: Ion Implantation into Metals, Eds. V. Ashworth, W.A. Grant and R.P. Procter (Pergamon, Oxford, 1982) p. 24.

[52] R.N. Bolster and I.L. Singer, Appl. Phys. Letters 17 (1980) 327.

[53] R.N. Bolster and I.L. Singer, Symp. on Mechanical Properties, Performance, and Failure Modes of Coatings at National Bureau of Standards, Gaithersburg, MD, May 1983.

[54] I.L. Singer and R.N. Bolster, in: Ion Implantation Metallurgy, Eds. C.M. Preece and J.K. Hirvonen (Metallurgical Soc. of AIME, Warrendale, PA, 1980) p. 116.

[55] R.C.D. Richardson, Wear 10 (1967) 353.

[56] K.-L. Hsu, T.M. Ahn and D.A. Rigney, in: Wear of Materials – 1979, Eds. K.C. Ludema, W.A. Glasser and S.K. Rhee (ASME, New York, 1979) p. 12;
K.-L. Hsu, T.M. Ahn and D.A. Rigney, Wear 60 (1980) 13.

[57] R.G. Vardiman, R.N. Bolster and I.L. Singer, in: Metastable Materials Formation by Ion Implantation, Eds. S.T. Picraux and W.J. Choyke (North-Holland, New York, 1982) p. 269.

[58] R.G. Vardiman, R.N. Bolster and I.L. Singer, to be published.

[59] I.L. Singer and R.A. Jeffries, Appl. Phys. Letters 43 (1983) 925.

[60] K. Miyoshi and D.H. Buckley, ASLE Trans. 23 (1981) 460.

[61] See, for example, ref. [6], pp. 12–17.

[62] T.E. Fischer, M.J. Luton, J.M. Williams, C.W. White and B.R. Appleton, ASLE Trans. 26 (1983) 466.

[63] S. Lo Russo, P. Mazzoldi, I. Scotoni, C. Tosello and S. Tosto, Appl. Phys. Letters 34 (1979) 627.

[64] O. Almen and G. Bruce, Nucl. Instr. Methods 11 (1961) 257.

[65] R.H. Bassel, K.S. Grabowski, M. Rosen, M.L. Roush and F. Davarya, 10th Intern. Conf. on Atomic Collisions in Solids, Bad Iburg, Red. Rep. of Germany, July 1983.

[66] P.R. Malmberg, R.G. Allas, J.M. Lambert, P.A. Treado and G.W. Reynolds, 10th Intern. Conf. on Atomic Collisions in Solids, Bad Iburg, Fed. Rep. of Germany, July 1983.

[67] D. Farkas, M. Rangaswami and I.L. Singer, Materials Research Society Symp. on Ion Implantation, Boston, MA, 1983.

Section II.A

TRIBOMECHANICAL PROPERTIES OF ION IMPLANTED METALS

I.L. Singer

Surface Chemistry Branch
Chemistry Division
Naval Research Laboratory

101

TRIBOMECHANICAL PROPERTIES OF ION IMPLANTED METALS

IRWIN L. SINGER, Naval Research Laboratory, Chemistry Division,
Code 6170, Washington, D.C. 20375

ABSTRACT

A review of tribomechanical studies supported by surface
analysis finds ion implantation capable of increasing the
sliding wear resistance of ion implanted metals in two ways.
First, it can reduce friction by modifying the surface
composition (e.g. Ti^+ into steel) or by promoting the growth of
low friction oxide layers (e.g. N^+ into Ti). Second, it can
modify the subsurface composition and structure to resist
fracture and debris formation. These modifications harden the
surface, change its work-hardening behavior and/or increase
residual stresses. Microindentation hardness measurements
indicate that many but not all of the wear resistant surfaces
are hardened by implantation; thus, surface hardness is a
contributing but not necessarily a controlling factor in wear
resistance. These mechanisms of wear reduction and the chemical
and microstructural modifications responsible for them are
discussed. Evidence for wear reduction through the migration of
N during wear is critically reviewed. It is concluded that the
principal benefit of ion implantation is to prevent or delay the
formation of wear particles, thereby changing the wear mode
during run-in and permitting metals to reach load-carrying
capacities up to their elastic limits.

INTRODUCTION

Ion implantation has been highly touted by the material research
community as a surface processing treatment for protecting metals against
wear. So far, however, it has been regarded with healthy skepticism by many
tribologists who are waiting for experimentally verifiable explanations of
how a thin (100 nm) surface alloy can increase the wear resistance of
metals. These explanations have been coming, slowly but steadily, from
simple friction and wear tests supported by microscopic analyses of wear
scars, and from surface analytical studies aimed at identifying the
compositions and microstructures responsible for wear resistance. While
these tests adequately describe the response of implanted layers to sliding
contact, they are too crude to examine the tribomechanical properties of the
thin (~100nm) implanted layer. More direct measures of these properties
have been obtained from two very surface sensitive techniques,
microindentation hardness and polishing wear studies. This paper reviews
many of these studies and provides evidence for four mechanisms by which ion
implantation improves the sliding wear resistance of metals.

The second section describes two ways that ion implantation can affect
sliding wear processes: it can alter the deformation behavior of a metal
surface under stresses transmitted during sliding, and it can reduce the
stresses transmitted. The third section examines the tribomechanical
effects of Ti- and N-implantation on the friction and sliding wear behavior
of selected metals. Studies involving high speed sliding have been excluded
because of the uncertainties associated with heating effects. Surface
hardness and abrasion resistance studies are also presented in the context
of identifying mechanisms of sliding wear resistance. Evidence for N
migration during the wear process is also discussed. The fourth section

then considers a variety of ion implantation treatments and the chemical and microstructural changes which reduce friction and delay or prevent wear during sliding contact.

Sliding and Wear Processes Affected by Ion Implantation

Detailed description of the wear processes occurring when two metals are placed in sliding contact can be found in references [1-6]. Briefly, wear is a complex interplay between adhesion, deformation and friction. Although relatively independent processes before sliding, adhesion and deformation become coupled during sliding by friction, which transmits high shear stresses to the uppermost surface layers and causes them to deform. Is this an adhesive wear mode or a deformation wear mode?

Two of the three processes, adhesion and friction, are very sensitive to the surface composition. For example, it is well known that oxide films can eliminate severe adhesion and reduce the coefficient of friction [1,3]. Steels sliding in a vacuum lose their oxides and experience severe and rapid adhesive wear, whereas the same steels sliding in a good lubricant have their oxides replenished and wear more slowly by deformation-controlled processes [3]. Therefore, it is easy to understand how ion implantation can affect adhesion and friction. By modifying the composition of the uppermost layers of metals, ion implantation can reduce the chemical affinity of surfaces in contact, promote oxide growth and/or strengthen the metal oxide/metal interface. We will see, later, how reducing friction also decreases the deformation mode of wear.

However, to understand how implantation can affect the deformation mode of wear directly, it is necessary to examine how a metal surface deforms. Initially, deformation is elastic, but goes plastic when the shear stress exceeds the yield stress of the metal or when it encounters stress concentrators such as inclusions or microcracks. Plastic deformation, the accumulation of plastic strain, may be accompanied by a variety of effects including work hardening, buildup of residual stresses [7], development of texture [5,6] and phase transformation [8]. When plastic deformation processes are exhausted, cold working ends and fracture begins [4-6]. In ductile metals, flow-induced cracks nucleate and grow in the subsurface; when they reach the surface, plate-like particles are formed. In hardened metals or coatings, fatigue cracks nucleate and grow; then fine debris particles are produced by brittle fracture at the edges of surface cracks. In addition, oxide particles can form by repetitive shear and regrowth of thin oxide films.

Ion implantation can affect the deformation mode of wear by modifying the composition and microstructure of the near-surface layer. The flow strength (hardness) of the surface can be increased by solid-solution strengthening or precipitate formation. The work-hardening behavior can be altered by stabilizing the microstructure, possibly by changing the stacking fault energy [5]. In addition, a more homogeneous defect structure can be produced.

Implantation may also protect against wear by introducing residual compressive stresses into the surface. Compressive stresses can blunt crack propagation and resist the lifting off of plate-like particles by opposing sliding-induced tensile stresses. Residual stress produced by treatments such as shot peening have been used for years to increase resistance against rolling contact fatigue. Recently, Ho et al. [9] have demonstrated that residual stresses can also increase sliding wear resistance so long as they exceed the stresses induced during sliding.

Finally, implantation can reduce the deformation wear rate indirectly by reducing the coefficient of friction. Lowering the coefficient of friction reduces the intensity of the stresses transmitted to the surface. Moreover, it relocates the maximum shear stress component from the uppermost layer for $\mu > 0.4$ to a depth well below (10-20% of the contact diameter) the surface for $\mu < 0.2$ [7].

The load carrying capacity, as might be anticipated, also depends on friction. The load at which the elastic limit is reached can be calculated from P and τ, where P is the peak Hertzian pressure and τ is the yield stress in pure shear. For ideal elasto-plastic materials in the important ball-on-flat geometry, P is given by [7]

$$P = 3L/2\pi a^2 \tag{1}$$

$$\text{and } a = \left(\tfrac{3}{4} RL\right)^{\frac{1}{3}} \left[\frac{(1-\nu_1)^2}{E_1} + \frac{(1-\nu_2)^2}{E_2}\right]^{\frac{1}{3}} \tag{2}$$

where a is the radius of contact under normal load L, R is the radius of curvature of the ball, $E_{1,2}$ and $\nu_{1,2}$ are the elastic modulus and Poisson's ratio of the ball and flat, respectively. If we apply Tresca's yield criterion $\tau = Y/2$, where Y is the yield strength, then the pressure-to-yield ratio at the load limit, L_{max}, may be approximated by

$$P/Y)_{max} \approx 2.3 \ (1 - \mu) \tag{3}$$

for $\mu < 0.8$ [7]. The dependence of L_{max} on μ follows by substituting eqs. 1 and 2 into 3, giving

$$L_{max} \propto (1 - \mu)^3 \tag{4}$$

Eq. 4 shows that reducing μ can greatly increase the load carrying capacity. Eq. 3 will be used to predict the pressure-yield-ratio during sliding contact with friction; it will then be compared with observed P/Y values. Two caveats, however, should be mentioned. First, Eq. 3 underestimates $P/Y)_{max}$ when a lubricant is present; a lubricant tends to distribute the load over a larger area than would be calculated from Eq. 2. Second, when calculating observed P/Y values, it should be realized that the yield strength of a worn surface layer can be much higher (2-7 times) than the bulk yield strength [10]. Therefore, predictions made using Eq. (3) should be considered semiquantitative.

TRIBOMECHANICAL PROPERTIES OF ION IMPLANTED METALS

This section reviews the tribomechanical properties of a variety of ion implanted metals and alloys. Compositions, microstructures and bulk hardness for many of these alloys are given in Table I. All of the investigations reviewed in this paper employed one or more surface analytical tools to ascertain composition and/or microstructures of the implanted surfaces. In several cases the compositions or microstructures responsible for wear resistance have been identified.

TABLE I. Composition, microstructure and bulk hardness of selected metals

Metal Designation	Composition (wt %)	Microstructure	Hardness (GPa)
Steels			
52100	Fe 1.5Cr-1C	Martensite	8.0 }
Fe1C	Fe-1C	Tempered Martensite	1.7-4.0
1018	Fe-0.2C	Ferrite + Fe Carbide	2.8
440C	Fe-18Cr-1C	Martensite + Cr Carbides	7.8
304	Fe-18Cr-8Ni	Austenite	2.9
Ti-6Al-4V	Ti-6Al-4V	α and β Ti	6.0
Stoody 3	Co-31Cr-13W-2.2C	Co(Cr)+Cr_7C_3+W_6C	6.6

Sliding wear studies permit several tribomechanical properties of ion implanted layers to be measured. These include friction coefficients and load-carrying capacities. In addition, the wear mode can be determined by analyzing the topography of the wear track and the debris generated. In the investigations reviewed, experiments were performed in a ball-against-flat geometry, with (initially) smooth surfaces, and at low speeds (<0.1 m/sec).

The hardness of implanted surface layers has been measured by Pethica [11] using a specially designed microindentation hardness (MIH) apparatus. Hardness numbers were obtained with a diamond pyramid indentor penetrating to depths as shallow as 50 nm.

Polishing wear measurements have been obtained by Bolster and Singer [12,13] with depth resolutions of 20 nm. Relative wear resistance (RWR) vs. depth profiles for implanted vs. non-implanted flats, shown in Fig. 1, illustrate the depth resolution. They also show that the steady state RWR values for two (304 and Stoody 3) of the four metals are higher than might be predicted from their bulk hardness values. RWR values, initially believed to measure surface hardness [12], are now thought to be related to the work-hardening rates of metals.
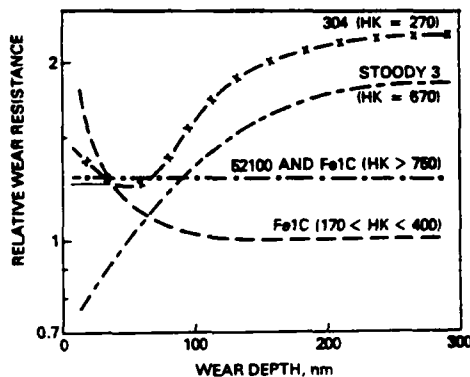
FIG. 1 RWR vs. depth profile for three steels and Stoody implanted with N. Bulk Knoop hardness, HK, is given in kgf/mm².

Implantation of Ti

Implantation of Ti into steels and Stoody 3 to high fluences has produced dramatic reductions in both friction and wear. In a hardened bearing steel, type 52100, it reduced the dry sliding friction coefficient from $\mu = 0.6$ (steel-vs-steel) to $\mu = 0.3$ and prevented the formation of oxide debris normally generated during dry sliding contact [14-16]. In soft (annealed) steels it again reduced friction and thereby delayed the onset of ductile fracture and plate-like debris formation [17,18]. Similar effects were achieved in a carbide strengthened Co-based alloy, Stoody 3 [19,20]. In that study equally low friction, wear resistant surfaces were obtained by covering nonimplanted Stoody 3 with a monolayer of a lubricious fatty acid, thereby confirming that low friction alone could produce the observed wear resistance [19].

A unique surface alloy, composed of Fe+Ti+C, has been found responsible for the low friction on steels [15,16]. When implanted to high fluences, Ti ions assist in the ''vacuum carburization'' of the surface, causing C atoms to be absorbed from gas molecules in the vacuum chamber [21]. In steels the Fe+Ti+C layer, and those produced by the intentional implantation of C, have been shown to be amorphous [15,22]. Analytical studies have found that low friction and wear resistance continues so long as the Fe+Ti+C layer is retained. This layer has remained intact even after being depressed to 1 μm below the non-worn surface [17,18,23]. In Stoody 3, a ''vacuum carburized'' layer was found in the Co matrix and the carbide phases [19].

The load-carrying capacity of dual implants of Ti and C into a variety of stainless steels (soft and hard) and Fe has been investigated by Pope, et

al. [24,25] under the rather severe conditions of dry sliding contact at low speed (15mm/sec). This treatment reduced friction by approximately a factor of two and prevented wear at loads up to the maximum load-carrying capacity of the steels. For example, in a hardened 440C steel whose yield strength was Y = 1.8 GPa, the low friction (μ = 0.30) surface resisted wear up to a Hertzian pressure of P = 2.9 GPa [25]. The observed pressure to yield ratio P/Y = 1.6 is identical to that predicted from eq. 3.

MIB studies of these wear resistance Ti and Ti + C layers found no increase in surface hardness [26,27]. Polishing wear studies, however, showed dramatic increases (from x3 to x10) for Ti-implanted hard and soft steels [13,28] and Stoody 3 [20]. These increases have not been explained.

Implantation of N

N into steel is the implantation treatment most commonly used to improve its wear resistance. Four important conclusions about its tribological behavior can be drawn from studies on simple friction and wear apparatus. First, the friction coefficient does not decrease significantly in any of the steels, even those showing increased wear resistance [14,17,18,25,29,30]. In fact, one low speed sliding study of steel against N-implanted steel [17] showed increased wear resistance despite a slight increase in the friction coefficient. Therefore, the improved wear resistance cannot be attributed to a reduction in friction, as is the case for Ti-implanted steel. Second, large increases in wear resistance are obtained in ductile steels, but essentially no changes have been found in the four hardened (martensitic) steels examined. Third, the wear resistance has been attributed to changes in the wear mode and not simply to a "slowing down" of the wear rate [18,25,29]. Fourth, wear resistance has persisted up to loads that reach the load-carrying capacity of the steels. I have calculated pressure-to-yield ratios from wear data for 304 steel from two different investigations [29,30] and find values from 1.2 to 2.5 times larger than predicted from eq. 3 (see Table II). Therefore since friction isn't reduced, implantation must affect the way steel surfaces respond to deformations induced by the stresses transmitted during sliding.

TABLE II. Load carrying capacity of selected ion-implanted metals.

Implanted Species	Ref.	Metal Substrate	Slider	Y (GPa)	Frict. Coef.	P/Y Observed	P/Y Predicted
Ti + C	22	440C	440C	1.8	0.3	1.6	1.6
N	30	304	304	0.6*	0.7	1.8	0.7
N	29	304	Al_2O_3	0.6*	0.15	2.5	2.0
N	41	Ti6Al4V	Al_2O_3	0.83	0.17	2.9	1.9
N	41	Ti	Al_2O_3	0.28	0.17	3.1	1.9

*Estimated as Y=H/3 where H is the hardness [10].

The SEM photos of wear tracks in Fig. 2 show clearly that N-implantation altered the flow behavior of 304 and 1018 surfaces of steels during sliding. In the early "run-in" stage of wear, tracks in non-implanted steels show more ductile fracture than those in N-implanted surfaces [17, 18]. Ductile fracture in these steels produces shear marks transverse to sliding direction, plates uplifted from the tracks, and plate-like debris smeared along the track. This mode of wear was delayed in the N-implanted tracks, despite having the same friction history as the non-implanted track [18]. Profilometry has shown that surfaces of tracks formed during sliding at high load can be depressed from 0.1 to 1 μm below the nonworn surface. Auger analysis of these tracks found no change in composition of worn and non-worn surfaces, indicating that only the underlying metal was deformed during sliding [17,18,23].
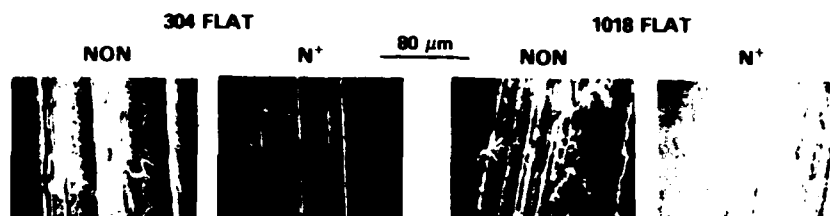
FIG. 2 SEM micrograph of wear tracks formed during dry sliding. (Left) after 3 passes on 304 steel; (right) after 7 passes on 1018 steel.

Microindentation hardness and polishing wear studies showed no changes in the surface hardness or abrasion resistance (see Fig. 1) of N-implanted hardened steels which, to repeat, showed no increased sliding wear resistance. In contrast, N-implantation was able to increase the MIH value of Fe by 50-100% [29] and the RWR value of a ductile steel (tempered Fe1C) by about that amount (see Fig. 1). Presumably N strengthens ferritic Fe by forming nitrides, solution strengthening and pinning dislocations [31]. Another strengthening mechanism for steels recently proposed by Fischer, et al. [17] is that microprecipitates of carbides form from C atoms that segregate to steel surfaces during high fluence implantation [17,18]. Since surface segregation of solute C has been observed for Ar and Fe implants as well as N implants, this mechanism should be independent of implant species. Microindentation hardness results for the austenitic 304 steel have been much less definitive [27]. N-implantation clearly hardened electropolished 304. But in polished 304, already hardened by abrasion, N-implantation did not substantially increase the hardness and may have softened it. Polishing wear studies showed that the RWR values of 304 steel were lowered by N-implantation [12,13].

Austenitic 304 is known to have a high work-hardening rate when it undergoes a phase transformation during abrasion [32]. N-implantation is believed to interfere with this phase transformation, thereby lowering its capacity to work-harden. Vardiman, et al. [33] have identified the microstructures associated with polishing then N-implanting 304 steel. Polishing strain-hardened γ(fcc)-austenite phase transformed it to an α'(bcc)-martensite phase. N-implantation reverted the martensite back to a N-dilated austenite [34]; in addition, the austenite was stabilized against transforming to martensite during further polishing.

Stabilization of the austenite by N-implantation can increase the wear resistance of 304 steel during sliding. In its unstable condition, the near surface layer work-hardens and becomes a hard, brittle layer attached to a softer, ductile substrate [8]. With a N-implanted layer, the near surface remains austenitic, work-hardens less and thereby resists the deleterious sliding condition of a hard layer on a soft substrate. TEM studies have confirmed that martensite forms in wear tracks of 304 steel [8,35], but so far the microstructure of a wear track on N-implanted 304 steel has not been identified.

Finally, it appears that steels containing nitride formers (e.g., Cr,V,Al) are benefited more by N-implantation than low alloy steels. This may be due the chemical pinning of implanted N to these atoms [36] and its effect on maintaining implantation induced residual stresses. It has been shown that implanted N redistributes in metals without nitride formers but maintains a Gaussian profile in the presence of these alloys [13,23] up to fluences causing the surface to blister [37].

Implantation of N into Ti Alloys. Ti and Ti alloys have notoriously poor resistance to delamination in sliding wear. Several studies have shown that N implantation into Ti can impart wear resistance and lower friction [38,39]. (C implants have provided similar benefits but required post-implantation heat treatments [40]). The delay in severe wear of Ti-6Al 4V as

a function of N fluence has been demonstrated convincingly by Hutchings and Oliver [39]. Their results were obtained with a stationary ruby ball (d = 5mm) against a Ti-6Al-4V disk (speed = 3mm/sec) sliding in alcohol. Severe wear occurred immediately in a non-implanted disk, but was delayed from 1 to 10^4 cycles as implant fluences increased from 0.5 to $4x10^{17}$ N/cm^2. Before wear, the tracks remained smooth and the coefficient of friction stayed low, μ = 0.17. Surface analysis showed that a thin $Ti(O_{1-x}N_x)$ layer formed during sliding and that low friction persisted so long as this layer remained intact. After removal of the layer, the tracks resembled non-implanted wear tracks, the wear rate increased a hundred-fold and the friction coefficient jumped to μ = 0.4. This is a clear case of N-implantation delaying wear by changing the wear mode.

Surface hardness studies were performed on the same specimens. At fluences from 0.5 to $4x10^{17}$ N/cm^2 MIH values increased from 60% to 180%, leveling off at fluences greater than $1x10^{17}$ N/cm^2. Since no TiN precipitates were observed at $1x10^{17}$ N/cm^2, solid solution hardening was indicated. Moreover, since most of the hardening had occurred at lower fluences, it could not account for the nearly logarithmic increase in wear resistance with higher fluence. Hutchings and Oliver postulated that N promotes the growth of a wear resistant, low friction oxide layer. Alternatively, N-implantation may be changing the work-hardening behavior of Ti. Although no measurements have been performed on N-implanted Ti, RWR measurements on C-implanted Ti show increases up to a factor of 6.

Oliver, et al. [41] have reported the load-carrying capacities of both pure Ti and Ti-6Al-4V implanted with N. Using their data, I have calculated pressure-to-yield ratios ~ 50% greater than the ratios predicted by eq. 3 (see Table II). The calculated ratios, however, should be regarded as upper limit values since it is likely that the alcohol contributed to the load-carrying capacity and the actual yield strength of the surface was probably much higher than the bulk value [10].

N-implantation into Electroplated Cr has also changed the wear behavior of this hard metallic coating. Oliver et al. [26,29] showed that wear of the non-implanted Cr began when sliding induced transverse cracks. Next, fine debris generated at the edges of these cracks got trapped between the track and the slider and abraded the Cr surface. This mode of wear was prevented by N-implantation, and without changing the friction coefficient, resulting in a reduced wear rate (by a factor of 20-50 in the particular test) of the Cr plate. Surface hardness measurements showed N-implantation increased MIH values up to 30% [26].

N-implantation into Stoody 3. Low speed, dry sliding studies on N-implanted Stoody 3 showed the same friction and similar plastic deformation as on non-implanted Stoody 3 [20]. However, Co-debris particles were found in non-implanted wear tracks but only slider debris (steel, Stoody, Ni alloys) could be found in N-implanted tracks. Polishing wear measurements showed N-implantation reduced the RWR of Stoody 3. N-implantation appears to interfere with the work-hardening of Stoody 3, the mechanism responsible for giving it high abrasion resistance and suspected of reducing the sliding wear resistance.

N Migration and Wear

So far, no mention has been made of the mobile interstitial model which depicts N migrating below the wearing surface [42]. As intriguing and plausible as the idea may be, to date there is no irrefutable evidence for it in the literature. The often referred to results of Lo Russo, et. al. [43] should not be cited as evidence for N migration because no microprobe analysis of the wear scar was provided. A broad-beam nuclear reaction technique was used which detected 20% of the original N content in a region worn under reciprocating sliding. A likely source of N is debris that was

108

worn from the implanted surface then entrapped in the scar. Cui Fu-Zhai, et. al. [44] provided a more detailed wear scar analysis, by secondary ion mass spectroscopy and profilometry, to support their finding that approximately 10% of the implanted N was detected in a track nearly 2μm below the original surface. However, their analyzing beam was also wider than 2 of the 3 tracks analyzed. In addition, all tests were performed at loads high enough to depress the track by plastic deformation. To date, the more detailed microprobe analyses of wear tracks on implanted surfaces have shown that implanted ions do not migrate below the worn surface [17,18,22, 23,24,25,29,35,39].

COMPOSITIONS AND MICROSTRUCTURES THAT INCREASE SLIDING WEAR RESISTANCE

Surface Compositions that Reduce Friction

Ti-implantation to high fluences ''carburizes'' the surface, thereby producing a low friction surface on metals; too low a fluence creates a highly adhering, high friction surface [16]. The fluences and energies needed to produce this surface have been described by Singer and Jeffries [45]. This implantation treatment is particularly beneficial for the harder, more wear resistant alloys such as 52100 [14] and 440C [25] steels, for which N-implantation does not appear to be very effective. For more ductile steels, dual implants of Ti + N or Ti + C are recommended. Singer and Jeffries [18] have shown that the two act synergistically: Ti reduces friction and N increases resistance to deformation-induced wear. Other strong carbide forming implants such as Ta [23], Hf, Nb, and probably Zr and V, should provide similar friction and wear benefits as Ti, with the possibility of increased corrosion resistance as well [46].

Ion implantation can also promote the formation of lubricious (i.e. low friction) oxides on metals. As indicated earlier, Hutchings and Oliver [39] have suggested that implanted N atoms in Ti may have stimulated the growth of a wear resistant Ti oxynitride layer. Moreover, thick oxynitride layers which can form during N-implantation might decrease friction during run-in. The wear resistant, low friction films that Shephard and Suh [38] observed on N-implanted annealed Fe and Ti were probably oxynitrides, not metal nitrides.

Microstructures that Increase Fracture Resistance

In order to resist wear, the implanted layer must be able to withstand the stresses induced during sliding without fracturing. One way ion implantation has been able to accomplish this is by hardening the surface. The implant species can harden the surface directly by forming second phases, solution strengthening and pinning dislocations [31]. It can also contribute, indirectly, by dissolving phases already present, causing solutes in the lattice to redistribute and by creating defects. However, as indicated by the hardness and wear studies of Ti-6Al-4V, hardening of the surface alone cannot account for the wear improvements [39]. Moreover, Shephard and Suh [38] have concluded from theoretical studies that a hardened implanted layer cannot increase the load carrying capacity during sliding unless it also reduces friction, which is not the case for most N-implanted metals.

A second way in which implantation can protect against wear is to produce microstructures that resist excessive work hardening. Results from polishing wear studies demonstrate that ion implantation can modify the work hardening behavior of metals [12,13]. The N stabilized austenitic phase of type-304 steel is one example of a microstructure less prone to sliding wear failure [33]. Other examples considered in the literature are the stabilization of the fcc phase of Co in Stoody 3 (against the fcc to hcp transition) by N-implantation [20], the amorphization of steel surfaces by

Ti-implantation [14,22], and the hexagonal lattice expansion (i.e. c/a ratio increase) of Ti to modify its operating slip system by N-implantation [38].

There has recently been a proliferation of studies on microstructures formed in ion-implanted metals. The number of phases identified in steels, alone, by conversion electron Mossbauer spectroscopy [47,48] is overwhelming. Deciding which microstructures are responsible for any tribomechanical effect is a challenging task.

A third, more general way in which implantation may protect against wear is by introducing residual stresses in the surface. Residual compressive stresses introduced by high fluence implantations (of virtually any atom) have been shown to be extremely high, possibly in excess of the bulk yield strength of the metal itself [49]. In ductile metals, these stresses may counter those produced during sliding and may prevent cracks from growing and plate-like particles from lifting off the track. The photomicrographs of Fig. 2 show clearly that N-implantation into the two softer steels has delayed incipient plate formation. In harder, more brittle metals such as electroplated Cr [29] or nitrided steel [50], a net compressive stress at the surface may prevent cracks from opening and the surface from fracturing.

CONCLUSIONS AND RECOMMENDATIONS

A survey of the tribomechanical properties of ion implanted metals has suggested four mechanisms by which an ion implantation treatment can reduce sliding wear in metals. It can 1) produce a low friction surface by altering the surface chemistry; 2) modify the microstructure to harden the surface; 3) stabilize microstructures against deleterious work-hardening effects; and 4) introduce residual stresses to combat fracture. A summary of the effects on selected ion-metal substrates is given in Table III. By preventing or delaying the formation of wear particles, implantation alters the wear mode during the early ''run-in'' stage of wear. The change in wear mode has permitted several of the ion-implanted metals to withstand Hertzian pressures that reach the elastic-deformation limit of the metal (see Table II). Most implantation treatments have not yet been optimized, so it is likely that future treatments (e.g. dual implants, high emperature implants, ion beam enhanced deposition), will provide long r lasting, higher load carrying capacities for a wide variety of metals.

Table III. Tribomechanical properties affected by ion implantation
            (0) no change; (I) increase; (D) decrease; (N.D.) no data

Implanted Species	Substrate	Friction Coef.	Wear Scar Analysis	Surface Hardness	Polishing Resistance
Ti	52100	D	No oxide debris	0	I
N	Ti-6A1-4V	D	Submicron oxide debris; delayed plates	I	N.D.
N	ferritic steels	0	Delayed plates	I	I
N	austenitic steel	0	Delayed plates	I/D	D
N	martensitic steel	0	No change	0	0

This review has been limited to investigations of polished surfaces, implanted at or near room temperatures then subjected to low speed sliding. In practice, engineering surfaces have rougher finishes due to machining, grinding or lapping; ion beams can easily heat a substrate above 500°C at typical beam power densities of $2W/cm^2$ or greater; and components may be run at high speeds or in high temperature environments. Future investigations must address these issues and tackle the difficult but important task of characterizing the surface.

To illustrate the second point, there are several ion beam/surface interactions, besides implantation alloying, that can affect the tribological behavior of surfaces. Poor vacuum conditions during implantation can contaminate surfaces with carbon, which may be lubricious [26]. Excessive target heating during implantation in a poor vacuum can lead to the growth of extremely thick oxide layers. In alloys, heating can also promote decarburization and surface segregation of impurities (e.g. Si, S, B). Sputtering, especially common with heavy atoms implanted to high fluences, can remove native oxide layers, may alter the near surface composition [15] and can produce unexpected surface textures [19]. Each of the above implantation effects may change the tribological behavior of implanted metals, but not by the expected mechanism. Surface analytical studies should be carried out in conjunction with wear studies so that unanticipated surface films are not overlooked.

REFERENCES

1. F.P. Bowden and D. Tabor, Friction and Lubrication of Solids (Oxford Press, Oxford). Part I (1950); Part II (1964).
2. H. Czichos, Tribology (Elsevier, Amsterdam, 1978).
3. D.H. Buckley, Surface Effects in Adhesion, Friction, Wear and Lubrication (Elsevier, Amsterdam, 1981).
4. N.P. Suh, The Delamination Theory of Wear, Wear 44 (1977).
5. Fundamentals of Friction and Wear of Materials, D.A. Rigney, ed. (ASM, Metals Park, OH, 1981).
6. R. Glardon and I. Finnie, ASME Trans 103, 333-340 (1981).
7. D.A. Hills and D.W. Ashelby, Wear, 75, 221-240 (1982).
8. K.L. Hsu, T.M. Ahn and D.A. Rigney, Wear 60, 13 (1980).
9. J.W. Ho, C. Noyan, J.B. Cohen, V.D. Khanna and Z. Eliezer, Wear 84, 183 202 (1983).
10. R.C.D. Richardson, Wear 10, 353-382 (1967).
11. J.B. Pethica: in Ion Implantation into Metals, V. Ashworth, ed. (Pergamon Press, Oxford, 1982) pp 147-156.
12. R.N. Bolster and I.L. Singer Appl. Phys. Letts. 17, 327 (1980).
13. R.N. Bolster and I.L. Singer ASLE Trans. 24, 526 (1981).
14. C.A. Carosella, I.L. Singer, R.C. Bowers and C.R. Gossett, in: Ion Implantation Metallurgy, C.M. Preece and J.K. Hirvonen, eds. (AIME, Warrendale, PA 1980) p. 103.
15. I.L. Singer, C.A. Carosella and J.R. Reed, Nucl. Instrum. Methods 182/183, 923 (1981).
16. I.L. Singer and R.A. Jeffries, J. Vac. Sci. Technol. A1, 317 (1983).
17. T.E. Fischer, M.J. Luton, J.M. Williams, C.W. White and B.R. Appleton, ASLE Trans. 26, 466 (1983).
18. I.L. Singer and R.A. Jeffries, ''Friction, Wear and Deformation...'', these proceedings.
19. S.A. Dillich and I.L. Singer, Thin Solid Films 108, 219-227 (1983).
20. S.A. Dillich, R.N. Bolster and I.L. Singer, these proceedings.
21. I.L. Singer and T.M. Barlak, Appl. Phys. Lett. 43, 457-459 (1983).
22. D.M. Follstaedt, F.G. Yost and L.E. Pope, these proceedings.
23. I.L. Singer, Appl. Surface Sci. 18, (1984).
24. L.E. Pope, F.G. Yost, D.M. Follstaedt, J.A. Knapp and S.T. Picraux, in: Wear of Materials - 1983, K.C. Ludema, ed. (ASME, New York, NY 1983), 280.
25. L.E. Pope, F.G. Yost, D.M. Follstaedt, S.T. Picraux and J.A. Knapp, these proceedings.

26. J.B. Pethica, R. Hutchings and W.C. Oliver, Nucl. Instrum. Methods., 209/210, 995-1000 (1983).
27. W.C. Oliver, R. Hutchings, J.B. Pethica, I.L. Singer and G.K. Hubler, these proceedings.
28. I.L. Singer, R.N. Bolster and C.A. Carosella, Thin Solid Films, 73, 283 (1980).
29. W.C. Oliver, R. Hutchings and J.B. Pethica, Metall. Trans, A (to be published).
30. F.G. Yost, S.T. Picraux, D.M Follstaedt, L.E. Pope, and J.A. Knapp, Thin Solid Films, 107 287-295 (1983).
31. H. Herman, Nucl. Instrum. Methods, 182/183, 887-898 (1981).
32. C. Allen, A. Ball and B.E. Protheroe Wear, 74, 287-305 (1981).
33. R.G. Vardiman, R.N. Bolster and I.L. Singer, MRS Symp. 7, 269 (1982).
34. R.G. Vardiman and I.L. Singer, Material Letts. 2, 150-154 (1983).
35. D.M. Follstaedt, F.G. Yost, L.E. Pope, S.T. Picraux and J.A. Knapp, Appl. Phys. Lett. 43, 358-360 (1983).
36. I.L. Singer and J.S. Murday, J. Vac. Sci. Technol. 17, 327-329 (1980).
37. W.M. Bone, R.J. Colton, I.L. Singer and C.R. Gossett, J. Vac. Sci. Technol. A2 (1984).
38. S.R. Shephard and N.P. Suh, J. Lub. Technol., 104, 29-38 (1982).
39. R. Hutchings and W.C. Oliver, Wear 92, 143-153 (1983).
40. R.G. Vardiman, these proceedings.
41. W.C. Oliver, R. Hutchings, J.B. Pethica, E.L. Paradis and A.J. Shuskas, these proceedings.
42. N.E.W. Hartley, in: Ion Implantation, J.K. Hirvonen, ed. (Academic Press, NY, 1980) p. 321.
43. S. Lo Russo, P. Mazzoldi, I. Scotoni, C. Tosello and S. Tosto, Appl. Phys. Letts. 34, 627 (1979).
44. F.Z. Cui, H-D. Li, X-Z. Zhong, Nucl. Instrum. Methods 209/210, 881-887 (1983).
45. I.L. Singer and R.A. Jeffries, ''Processing Steels by Ti-implantation'', these proceedings.
46. G.K. Hubler, P. Trzaskoma, E. McCafferty and I.L. Singer, in: Ion Implantation into Metals, V. Ashworth, ed. (Pergamon Press, Oxford, 1982), 24-34.
47. G. Marest, C. Skoutarides, Th. Barnavon, J. Tousset, S. Fayeulle and M. Robelet, Nucl. Instrum. Methods 209/210, 259-265 (1983).
48. E. Ramons, G. Principi, L. Giordano, S. Lo Russo, and C. Tosello, Thin Solid Films, 102, 97-106 (1983).
49. N.E.W. Hartley, J. Vac. Sci. Technol. 12, 485 (1975).
50. G.M. Ecer, S. Wood, D. Boes and J. Schreurs, Wear 89, 201-214 (1983).

Section II.B

APPLICATION OF ION IMPLANTATION TO WEAR PROTECTION OF MATERIALS

G.K. Hubler and F.A. Smidt

Materials Modification & Analysis Branch
Condensed Matter & Radiation Sciences Division
Naval Research Laboratory

113

Section IV. Metals: Applications and Steels

APPLICATION OF ION IMPLANTATION TO WEAR PROTECTION OF MATERIALS

G.K. HUBLER and F.A. SMIDT

US Naval Research Laboratory, Washington, D.C. 20375, USA

Key results from the literature for the wear behavior of N- and Ti-implanted steels are reviewed. A qualitative model which rationalizes the mechanisms producing improvements in the sliding wear resistance of steels is presented. In the limited regime of low sliding velocities the model provides guidelines for choosing the experimental conditions of applied load, composition, hardness and heat treatment of the steel under which implantation will improve wear resistance.

1. Introduction

Ion implantation has many conceptual features that recommend it for use in wear protection applications. The nearly unlimited choice of elemental species which can be implanted, the freedom from thermodynamic constraints, and the ability to perform the implant at low temperatures provide a flexibility in choice of treatment, processing variables and substrate material which cannot be matched by conventional diffusion or coating methods. Tribological applications were among the first applications considered for ion implantation in non-semiconductor materials and several reports of success appeared in the literature [1-3]. As the number of investigations increased, cases also began to appear where marginal improvements in performance and lack of reproducibility were also observed [4]. This problem of inconsistent results is due in part to the complexity of the wear process itself where factors such as the chemical and mechanical properties of the material in the wear couple, load, configuration, relative sliding velocity, lubrication, and temperature are all first order experimental parameters. Results of laboratory wear tests tend to reflect the almost infinite combination of the above parameters so that data from different testing procedures is often difficult to compare. The greatest problem, however, is the lack of a working model which explains or at least rationalizes why ion implantation improves wear resistance. If such a model could be established and quantified, then the task of defining the boundary conditions for when ion implantation will produce improvements would be greatly simplified.

The aim of this paper is to establish a framework within which one may begin to understand why ion implantation reduces wear and what material and experimental conditions can be expected to produce positive wear results. We can at best expect to produce only a qualitative rationale because present wear theories are only qualitative in nature.

2. Background

Our approach is threefold. Firstly, only the wear of N- and Ti-implanted non-austenitic steels are considered. Austenitic steels constitute a special case because of their high strain hardening coefficients. The wear behaviour of these steel is reviewed elsewhere [5,6]. Secondly, we choose at the outset to emphasize the changes in macroscopic properties produced by ion implantation and ignore as much as possible the microstructural basis for the property changes. This facilitates comparison with theories of wear which to a large extent are formulated using macroscopic quantities [7]. Microstructure will be addressed later in connection with the types of steels and heat treatments. Thirdly, the experimental conditions are restricted to sliding wear situations under boundary lubrication or unlubricated conditions. Generally, laboratory wear apparatus operates at low sliding velocities (up to 10 cm/s) and medium to high maximum Hertzian stresses, P_0 (kg/mm^2), to achieve boundary lubrication (e.g. $0.1 \leq P_0 \leq Y$, where Y is compressive strength). The slow sliding velocities imply that the surface temperature is low which minimizes the oxidative and adhesive wear components of the wear rate [8,9].

One might object that limiting the discussion to the sliding wear of non-austenitic steels at low velocities considerably narrows the scope and usefulness of a model of wear. However, it has the advantage of channeling the discussion into the area where the majority of literature results have been generated. Moreover, it is expected that the concepts developed in the discussion on sliding wear will be applicable to other wear situations and materials, albeit with some modification required. Most machinery operates with some form of lubrication yet a significant fraction of results in the literature are generated for the unlubricated condition. In this discussion lubrication is not emphasized because we feel that the unlubricated condition is a useful

experimental means to study surface asperities in contact and that unlubricated wear simulates the less frequent asperity contact events through the lubricating film in the lubricated case [10,11].

3. Survey of wear behavior

Fig. 1 is a collection of data from the literature (subject to the constraints mentioned above) which represents all of the observed effects which any wear model
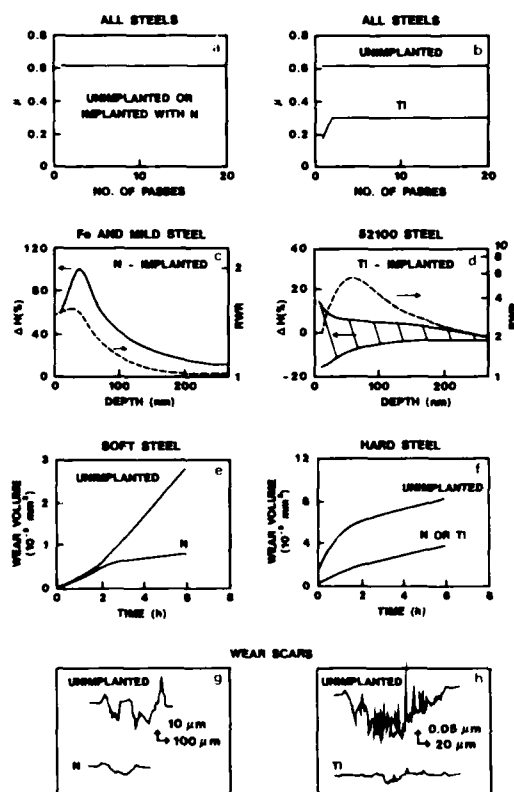

Fig. 1. Representative summary of wear data from the literature. a) Friction behavior for dry sliding versus the number of passes that a ball is slid on a polished flat for N-implanted or unimplanted steels [14]. b) Same as a) but for Ti implantation [13,14]. c) Hardness versus depth for N-implanted Fe [15] and relative abrasive wear resistance (RWR) versus depth for N-implanted mild steel [6,16]. d) Same as c) but for Ti-implanted 52100 steel [17,18]. e) Typical lubricated wear behavior versus sliding distance for unimplanted an N-implanted soft steel [19]. f) Typical lubricated wear behavior versus sliding distance for unimplanted and N-implanted hard steel [20]. g) Surface profiles of wear scars for lightly loaded unimplanted and N-implanted 0.2C steel after lubricated wear test [20]. h) surface profiles of wear scars for heavily loaded unimplanted and Ti-implanted 440C steel after unlubricated wear test [21].

must be able to rationalize for N (2 to 5×10^{17}/cm^2, 50 to 150 keV) and Ti (5×10^{17}/cm^2, 190 keV or 2×10^{17} Ti/cm^2, 90 to 190 keV + 2×10^{17} C$^+$/cm^2, 50 keV) [12] implantation. Fig. 1 is an attempt to reduce the data to a least common denominator for the purpose of simplifying the task of constructing a model. There will be variations in these data from different experimenters which will be taken as a second order effect for present purposes.

In figs. 1a and b note that the friction coefficient in unlubricated sliding for N-implanted hard or soft steels is unchanged and for Ti-implanted steels is reduced by a factor of two [13,14]. In figs. 1c and d it is observed that the microhardness and abrasive wear resistance of N-implanted steels are well correlated [6,15,16]. For Ti-implanted steels, however, there is no increase in hardness [17] to correspond with the large increase in abrasive wear resistance [18]. Figs. 1e and f illustrate the wear improvements expressed as wear volume versus sliding distance for lubricated wear couples [19]. The trend for the same data for unlubricated couples is generally similar but with different absolute values for wear volume and sliding distance. For N implanted into soft steels, fig. 1e, a true absolute difference in wear rate after similar run-in periods is observed. The case of hard steels, fig. 1f, is characterized by the majority of the wear occurring during run-in, and steady-state wear rates that are quite similar. This shows that sliding distance is a first order parameter because the wear depends upon the sliding distance at which it is measured. In general, reduction in wear is ~ 10 × for both N and Ti implantation. figs. 1g and h illustrate the typical surface profiles after conclusion of a wear experiment. The profile for N-implanted steel [20] characterizes the surface condition for lubricated sliding at maximum Hertzian pressures (MHP), P_0, much less than the yield strength, Y, of the material. The profile for Ti-implanted steel [21,22] is indicative of lubricated or unlubricated sliding when $P_0 \sim Y$. Note that the grooving of the surface is greatly reduced in the implanted samples.

Several interesting conclusions can be drawn from these data:

1) The mechanisms producing the same magnitude of wear resistance for Ti and N implantation are fundamentally different as demonstrated by the different friction and hardness behaviors as shown in figs. 1a–d.

2) Wear reduction for Ti-implantation is not caused by an increase in hardness [17] because the improvement in wear is a factor of ~ 10 and the increase in hardness is ~ 0.

3) The improvement in wear is intimately related to plastic deformation of the surface, especially during the run-in period (figs. 1e–h).

4. Wear mechanisms

Substantial progress has been made in recent years in understanding the elasto-plastic response of materials subject to pressure under sliding contacts. Results from this work provide a useful framework to evaluate ion implantation results. Typically it is thought that the actual asperity contact area is a factor of 10^{-2} to 10^{-4} smaller than the apparent contact area [23]. By modeling both the asperity tips and the contact patch by a ball-on-flat geometry, calculations of the elasto-plastic response may be applied to either the asperities or the contact patch by simply changing the value of the ball radius (estimates of asperity radii vary between 50 nm and 5 μm).

Hills and Ashelby [24] and Hamilton and Goodman [25] have calculated the behavior of ductile metals for a ball sliding on a flat surface. For $\mu = 0$, the instantaneous stress at the surface and along the center line of contact is symmetric and mostly compressive. For $\mu = 0.5$ the compressive stress maximum shifts to the leading edge of the contact, is greater than for the static case, is tensile at the rear edge of the contact and nearly as high in magnitude as the compressive stress at the leading edge (e.g., the stress is cyclic for one pass of the ball). Calculations of the volume of the plastically deformed zone beneath the contact show the following dependence versus μ. As μ increases, the volume of the plastically deformed zone increases, the magnitude of the maximum stress increases, and the depth of the maximum stress decreases and comes to the surface near the contact edges at a value of $\mu \cong 0.33$. In these calculations it is assumed that plastic yielding occurs when P_0 exceeds three times the yield stress in shear, τ_0.

The elastic limit and shakedown limit expressed as P_0/τ_0 are plotted versus μ in fig. 2 [24]. The shakedown refers to the accumulation of residual stress caused by plastic deformation which exists as a result of the cyclic stress history and is a distinct process from that of strain hardening which produces a change in the yield strength as a result of cyclic loading. Non-austenitic steels have low strain hardening coefficients and inclusion of strain hardening effects would not greatly alter conclusions based on these calculations. The shakedown limit is greater than the elastic limit because the residual stresses counter-balance a portion of the applied stress. If the stresses are such that P_0/τ_0 is beneath the elastic limit then the load will be supported with no permanent deformation. Above the elastic limit, plastic deformation will occur until the contact area increases to support the load without further permanent deformation. For $\mu \le 0.3$ this will happen for a higher specific load as a result of shakedown. For μ values above the vertical dashed line the point of maximum stress is at the surface and for μ less than the dashed line position, the point of maximum stress is subsurface.

Let us examine the run-in from the standpoint of the above calculations and fig. 2. Figs. 1e-h indicate that much of the benefit of ion implantation for soft or hard steels derives from its effect during the run-in period. Run-in phenomena are poorly understood because the stresses on asperities exceed the shear strength of the steel. Wear particles are generated which become trapped and are themselves deformed and contribute to wear by abrasive action. With knowledge of the effects of implantation on run-in in figs. 2e-h, some general observations on the run-in process can be made.

Hard steel – unimplanted: P_0^b (MHP on contact patch) $\le \tau_0$ so that there is no bulk deformation, but P_0^a (MHP on asperities) $\gg \tau_0$ so that asperities deform. The contact area increases through asperity deformation, fracture, and shearing until $P_0^a \le \tau_0$ (for $\mu \cong 0.6$; see fig. 2). Deep grooves (fig. 2g) cannot be caused by plastic yielding of the bulk and therefore must be caused by transport of material from low points to high points. Wear during this period is the result of particles generated by microshear and fracture.

Hard steel – N-implanted: The physical manifestation of N implantation is to increase the Y and τ_0 of the surface ($\tau_0 \approx Y/2$). Very direct evidence of this surface strengthening exists from three different experiments on N-implanted ferrous alloys, two of which are shown in fig. 1c where increases in the hardness and abrasive wear resistance were measured [13-16]. The third is a measurement of low-cycle strain controlled fatigue of 4140 steel (0.4C) by Jata et al. [26] which showed that the cyclic stress amplitude needed to produce the same strain as for unimplanted samples increases by 15%. As a result of strengthening, $P_0^a \ge \tau_0$ so that less asperity deformation, microshear and fracture are necessary be-
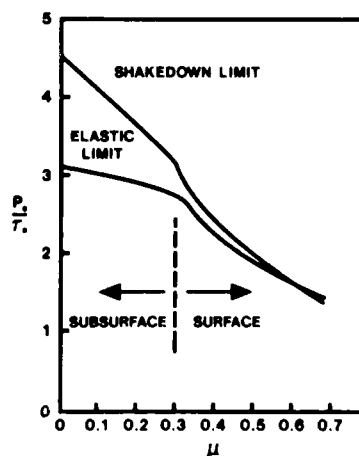

Fig. 2 Calculations of the elastic and shakedown load limits in ideal elasto-plastic solids expressed as P_0/τ_0 versus the coefficient of friction [24].

fore the area increases sufficiently to support the load. The increased strength causes the load to be supported over a smaller contact patch. This qualitative picture for hard and soft steels is supported by the observation from fig. 1f that the surface behaves as if it has already been run in (implying the shakedown limit for asperities has been reached) and by the fact that 20 μm deep grooves in fig. 1g cannot be produced by bulk deformation because $P_0^b < \tau_0$.

Soft steel - N-implanted: $P_0^b > \tau_0$, $P_0^a \gg \tau_0$. Here the argument is similar to the above for unimplanted hard steels except that subsurface deformation will also occur which will have the effect of worsening both material transport and wear. The wear scar would be expected to be depressed beneath the original surface by bulk deformation and the wear surface will be severly grooved. Wear-in of implanted soft steels shown in fig. 1e shows that run-in proceeds similarly to unimplanted steels. This is caused by the fact that chief deformation at this stage is in the unimplanted bulk material, which is not effected by the implanted layer. In addition, Kuhlmann-Wilsdorf suggests that asperities can be generated at the surface during wear-in when dislocations emerge as a result of stress relief during bulk deformation [27], further enhancing the wear rate. If the shakedown limit of the bulk and asperities is reached prior to the total removal of the N-implanted surface by microshear and fracture, then an improved wear rate in steady state can be achieved as in fig. 1e.

Hard steel - Ti-implanted: As already discussed, the friction reduction from 0.6 to 0.3 reduces the shear forces transmitted to the surface, and increases the load limit, P_0/τ_0, as shown in fig. 2. The increase in contact area necessary to reduce P_0 for asperities to a value below the shakedown limit ($P_0 \leq 3\tau_0$) occurs rapidly so that the implanted surface behaves as if it already was in the run-in condition.

Soft steel - Ti-implanted: Singer and Jeffries have shown that reduced friction by Ti implantation of a soft steel does not provide long lasting wear resistance [14]. The subsurface deformation during shakedown in this case disrupts the surface layer (50 nm for Ti versus 150 nm for N) such that microshear and fracture remove the low friction layer before completion of shakedown during run-in. Singer has also shown that for mild steels, implantation of N followed by Ti gives greater wear resistance than either N or Ti alone [14]. In this case, the subsurface is strengthened and the low friction surface layer is supported such that the run-in resembles that of Ti-implanted hard steels.

As mentioned previously, fig. 1d indicates that hardness plays no role in improving the sliding wear resistance of Ti-implanted steel shown in fig. 1f. This point is more difficult to rationalize. It is possible that the amorphous surface layer is more ductile [17] than the unimplanted steel so that easy plastic deformation of

asperity tips could further speed the run-in by rapidly increasing the actual area of contact. An increase in ductility would also be consistent with the lack of a correlation between abrasive wear resistance and hardness in fig. 1d. In this case, most of the energy imparted to the surface by abrasion is dissipated by deformation and ploughing rather than by cutting.

Steady state wear: A number of theories have been proposed to explain the wear rate in the steady state regime and many involve a fatigue and fracture mechanism. In fatigue theories of wear, cyclic stresses in elastically deformed zones beneath asperity contacts nucleate and propagate subsurface cracks [28] which grow to a critical length and then delaminate to generate plate-like wear particles [9]. For N-implantation, where $\mu = 0.6$ for asperity contacts, the maximum stress is at the surface where the strengthening of the steel will have its greatest effect. The strengthened surface resists strain at imperfections (e.g. inclusions, second phase particles, etc.) which are the nucleation centers for cracks. Compressive stresses generated as a result of implantation may also play a role in counterbalancing the tension component of the cyclic stress which will reduce crack propagation [29]. For Ti implantation, where $\mu = 0.3$ for the asperity contacts, the volume of the plastically deformed zone is reduced. This has the effect of decreasing the number of possible nucleation centers and decreasing the number of cracks experiencing cyclic stress intensity values higher than the threshold for crack propagation. Therefore, crack nucleation and crack propagation are suppressed. Thus, without considering fatigue mechanisms in detail it is possible to rationalize improvements in steady state wear for both N- and Ti-implanted steels, though again the mechanism for each ion is fundamentally different. It is noteworthy that significant fatigue life improvement has been measured for N-implanted 1018 [30] and 4140 [26] steels in stress controlled high cycle fatigue experiments where the stresses were cyclic between compression and tension and were a maximum in the implanted surfaces. These experiments support an earlier suggestion [5] that there may be a correlation between improved fatigue behavior and improved wear behavior for N-implanted mild steels. We are unaware of any fatigue measurements on Ti-implanted steels which would help to confirm this correlation.

5. Experimental conditions for wear improvement

The use of the terminology of "hard" or "soft" steels in the previous discussion is obviously an oversimplification and was used for convenience in order to develop a rationale to explain wear results. Clearly whether a material is hard or soft depends upon the relative values of the hardness of the steel and the applied load. A

model to predict the qualitative wear behavior of N-implanted steels has been proposed by Hubler [5] and is repeated here. Briefly, the assumption is made that nitrogen implantation strengthens the ferrite phase of the steel, but does not strengthen the martensitic phase. Then the increase in strength of any given steel would depend upon the carbon content and the previous heat treatment of the steel. Nitrogen implantation will have the greatest effect on low carbon steels and high carbon steels tempered to low hardness, and will have the least effect on high carbon steels in the quenched state. This simple picture, coupled with consideration of the relative magnitude of hardness and load, agrees with the general trends over a wide range of results in the literature.

The most extensive study to date is that of Yu et al. [19] which characterized lubricated-sliding behavior of N-implanted steels in different tempering conditions for the configuration of a stationary cylinder sliding on a rotating cylinder. The experiments of Yu et al. are unique because of the variety of steels which were tested under identical experimental conditions. These results are extremely useful for studying systematic trends. Fig. 3 shows a portion of their data for a mild steel and a hard steel where the steady state wear rate of the rotating cylinder versus load is plotted. For the implanted 0.2C mild steel a large wear improvement was observed at low loads, but at higher loads the improvement was quite small. This is consistent with the arguments for mild steels mentioned previously where at high loads, the N-implanted surface is removed during the run-in and that at the proper load, mild steel shows a large improvement in wear. For the 1.0C steel in the hardened condition, there is little improvement of the

wear rate at low loads, and modest improvements in the wear rate at high loads. From the same study, a measurement was made of the wear rate of 1.0 C bearing steel versus hardness. The relative improvement in wear was greatest for the lowest hardness ($\times 50$) and least for the highest hardness ($\times 1.3$) which demonstrates the dependence on the pretest heat treatment of the steel. Also, Bolster et al. [16] have shown that the relative abrasive wear resistance of tempered high carbon steel can be restored to that of the as-quenched condition by nitrogen implantation at that N implantation does not improve the wear resistance of hard 1.0C steel.

The data of Yu et al. also show that large wear improvements may be expected for a nitriding steel. Dearnaley reported this effect and attributed it to the strong chemical affinity of the nitride forming elements in the steel for the implanted nitrogen which gives added strength over just chemical nitriding alone [31].

The rules for applying Ti-implantation to improve wear appear to be more straight-forward than for N-implantation. Titanium implantation has improved all steels implanted to date, provided that the MHP applied to the apparent contact area does not exceed the yield strength of the steel. An unusual feature of Ti-implanted specimens has been demonstrated by Pope et al. [21]. They measured wear improvements for an unlubricated pin-on-disk configuration at loads up to and exceeding the yield stress of 440C stainless steel whereas N did not improve wear resistance at the loads tested. The typical MHP in the experiments of Yu et al. for lubricated conditions and N-implanted steels were only $P_0 = 0.1Y$. These results suggest that as far as ion implantation is concerned, lowering the coefficient of friction is a more potent means of improving wear resistance than strengthening the surface. Singer has argued that this empirical fact can be rationalized with the aid of fig. 2 [29]. For Ti implantation, reducing the friction coefficient from 0.6 to 0.3 can increase the maximum Hertzian pressure necessary to exceed the shakedown limit by a factor of more than 2 [32]. For N-implantation where $\mu = 0.6$, an upper limit for the amount of strengthening may be taken as a factor of 2 for the hardness increase of pure Fe (fig. 2c) and for harder steels the increase in strength is probably considerably less (15% for 4140 steel). Furthermore, the calculations in fig. 2 assume that τ_0 is constant in the region in which the stress is distributed. Since much of the stress is distributed beneath the strengthened implanted layer, calculating the increase in P_0 as being proportional to τ_0 gives only an upper limit. Because of this upper limit and the fact that steels are hardened less than a factor of two, the increase in the maximum Hertzian pressure by N implantation to remain below the elastic limit is certainly less than a factor of two. This argument can rationalize the greater load carrying capacity for Ti- over N-implanted steels, but requires
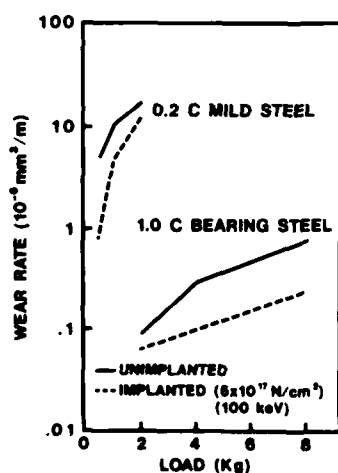

Fig. 3 Wear rate with lubrication versus load for N-implanted and unimplanted 0.2C steel and 1.0C steel [19].

improved calculations of the effects of surface strengthening on elastic properties to be developed further.

N migration: Two examples from the literature are useful to review here regarding N migration during wear. Cui Fu-Zhai et al. weighed the disks of 0.2C steel in pin-on-disk wear from which one can compute the volume of material (averaged over the entire wear scar) removed from the disks shown in fig. 1g resulting in values of 1.0 μm and 0.2 μm removed for unimplanted and implanted, respectively [20]. The profile for the unimplanted disk shows grooves as deep as 20 μm and that a large fraction of the material missing from the groove has been relocated to ridges which lie above the height of the original surface. The wear depth in the implanted sample is $> 5 \mu$m which is much greater than the implantation depth, and 13% of the original N dose was measured in the scar. The weight loss however, indicates that only 0.2 μm of material was removed from the surface which is consistent with 13% of the as-implanted N remaining at that depth when compared to the as-implanted N profile. Therefore, we conclude that there is no evidence here that N migrates during wear and that the depression must be caused by a plastic deformation mechanism during run-in. The latter conclusion is surprising because P_0 was $\ll Y$ in this experiment. Fig. 1h shows the wear grooves for unimplanted or Ti-implanted 440C stainless steel after unlubricated wear. The depression could be construed as being caused by removal of material. Since most of the implanted Ti was found to be retained in the wear groove the conclusion could also be reached that Ti migrated during wear. The authors point out, however, that the depression is primarily caused by plastic deformation of the subsurface induced by the high P_0 used in this experiment [22]. These two examples demonstrate some of the caveats to claims of impurity migration beneath a wear scar. To date we are not aware of any conclusive evidence that N migrates during wear.

6. Conclusions

In this paper we have emphasized general concepts from which a rationale for why ion implantation reduces wear has emerged. The model is capable of qualitatively explaining most of the typical wear phenomena summarized in fig. 1, and provides a framework from which one is able to predict the experimental conditions necessary to achieve improved sliding-wear results. This conditions include the composition, hardness, and heat treatment of steel, and the specific load.

The model requires only three simple assumptions: 1) Nitrogen implantation strengthens the surface of low carbon steels or tempered high carbon steels; 2) Ti implantation reduces the friction coefficient; and 3) the

description of an elasto-plastic solid under sliding contacts with friction by Hills et al. and Hamilton et al. describes the behavior of a surface asperity. Experimental evidence supports the first two assumptions but the latter assumption fails in the initial run-in period when the shear forces on asperities exceed the fracture strength of the material. The latter failure is generic to theories of wear and is an important obstacle to the development of a quantitative wear model. Nevertheless, these calculations provide a physical basis for why assumptions 1 and 2 can improve wear, and why reducing friction is more effective than strengthening the surface.

Several additional general statements may be made regarding the results reviewed here.

– Most of the benefit of ion implantation in soft, ductile materials occurs by means of altering the run-in behavior.
– For hard steels, the measured wear improvement occurs during run-in and steady state wear rates are not appreciably altered.
– To assess the benefit of ion implantation, wear measurements as a function of both sliding distance and load are necessary. The range of loads experienced by the wear couple should be stated and expressed in terms of the reduced unit P_0/Y.
– It is important to define failure criteria (it is likely to be entirely different for $P_0 = 0.1Y$ and $1.5Y$).
– Deep grooving of surfaces where $P_0 < Y$ are caused by an accumulation of microscopic deformation (ploughing), shear and fracture events.
– Ti improves wear resistance of all steels for loads $P_0 \leq Y$, and hard steels for $P_0 \leq 1.5Y$.
– N improves mild steels or tempered high carbon steels for loads $P_0 \leq KY$, where the constant K is an unknown fraction. Results reviewed here suggest $K \sim 0.2$.
– There is no conclusive evidence in the literature that nitrogen migrates during wear.

References

[1] N.E.W. Hartley, Wear 34 (1975) 427.
[2] J.K. Hirvonen, J. Vac. Sci. Tech. 15 (1978) 1662.
[3] G. Dearnaley and N.E.W. Hartley, Thin Solid Films 54 (1978) 215.
[4] A.K. Suri, R. Nimmagadda and R.F. Bunshah, Thin Solid Films 64 (1979) 191.
[5] G.K. Hubler, in: Metastable Materials Formation by Ion Implanted, eds., S.T. Picraux and W.J. Choyke (Elsevier, New York, 1982) p. 341.

[6] R.N. Bolster and I.L. Singer, Appl. Phys. Lett. 17 (1980) 327.

[7] L.E. Samuels, E.D. Doyle and D.M. Turley, in: Fundamentals of Friction and Wear of Materials, ed., D.A. Rigney (ASM, 1981) p. 13.

[8] A.Z. Szeri, in: Tribology, ed., A.Z. Szeri (McGraw-Hill, New York, 1980) p. 1.

[9] N.P. Suh, in: Tribological Technology, ed., P.B. Senholzi (Martinus Nijhoff Publishers, The Hague, 1982) p. 37.

[10] D.A. Rigney, Fundamentals of Friction and Wear of Materials (ASM, 1981) p. 1.

[11] A.W.J. de Gee, in: Tribological Technology, ed., P.B. Senholzi (Martinus Nijhoff Publishers, The Hague, 1982) p. 209.

[12] Either treatment results in an amorphous Fe–Ti–C surface; see refs. [13,22].

[13] I.L. Singer, C.A. Carosella and J.R. Reed, Nucl. Instr. and Meth. 182/183 (1981) 923.

[14] I.L. Singer and R.A. Jeffries, Ion Implantation and Ion Beam processing of Materials, eds., G.K. Hubler, O.W. Holland, C.R. Clayton and C.W. White (Elsevier, New York, 1984) p. 667.

[15] J.B. Pethica and W.C. Oliver, in: Metastable Materials Formation by Ion Implantation, eds., S.T. Picraux and J. Choyko (Elsevier, New York, 1982) p. 373.

[16] R.N. Bolster and I.L. Singer, in press.

[17] W.C. Oliver, R. Hutchings, J.B. Pethica, I.L. Singer and G.K. Hubler, in: Ion Implantation and Ion Beam Processing of Materials eds., G.K. Hubler, O.W. Holland, C.R. Clayton and C.W. White (Elsevier, New York, 1984) p. 603.

[18] I.L. Singer, R.N. Bolster and C.A. Carosella, Thin Solid Films 73 (1980) 283.

[19] Yu Kun, Li Heng-De, Zhang Xiao-Zhong and Tian Jia-He, Nucl. Instr. and Meth. 209/210 (1983) 1063.

[20] Cui Fu-Zhai, Li Heng-De and Zhang Xiao-Zhong, Nucl. Instr. and Meth. 209/210 (1983) 881.

[21] L.E. Pope, F.G. Yost, D.M. Follstaedt, J.A. Knapp and S.T. Picraux, in: Wear of Metals (ASME, 1983) p. 280.

[22] D.M. Follstaedt, F.G. Yost and L.E. Pope, in: Ion Implantation and Ion Beam Processing of Materials, eds., G.K. Hubler, O.W. Holland, C.R. Clayton and C.W. White (Elsevier, New York, 1984) p. 655.

[23] F.T. Barwell, in: Treatise on Materials Science and Technology, ed., D. Scott (Academic Press, New York, 1979) vol. 13, p. 2.

[24] D.A. Hills and D.W. Ashelby, Wear 75 (1982) 221.

[25] G.M. Hamilton and L.E. Goodman, J. Appl. Mech. 33 (1966) 371.

[26] K.V. Jata and E.A. Starke, Jr., J. Metals 35 (1983) 23.

[27] D. Kuhlmann-Wilsdorf, in: Fundamentals of Friction and Wear of Materials, ed., D.A. Rigney, (ASM, 1981) p. 119.

[28] D.K. Benson, in: Achievement of High Fatigue Resistance in Metals and Alloys, ASTM publication no. 467 (1969) p. 188.

[29] I.L. Singer, in: Ion Implantation and Ion Beam Processing of Materials, eds., G.K. Hubler, O.W. Holland, C.R. Clayton and C.W. White (Elsevier, New York, 1984) p. 585.

[30] W.W. Hu, C.R. Clayton, H. Herman and J.K. Hirvonen, Scripta Met. 12 (1978) 697.

[31] G. Dearnaley, in: Ion Implantation Metallurgy, eds., C.M. Preece and J.K. Hirvonen (AIME, 1980) p. 1.

[32] A more detailed treatment may be found in ref. [29] where the load carrying capacity increases by a factor of 5.4 for $\mu = 0.6 \rightarrow 0.3$.

IV. METALS
Applications, Steels

Section II.C

MECHANICAL AND CHEMICAL PROPERTIES OF TANTALUM-IMPLANTED STEELS

G.K. Hubler[1]
I.L. Singer[2]
C.R. Clayton[3]

[1]Materials Modification & Analysis Branch
Condensed Matter & Radiation Sciences Division
Naval Research Laboratory

[2]Surface Chemistry Branch
Chemistry Division
Naval Research Laboratory

[3]Materials Science Department
State University of New York
Stony Brook, NY 11794

Mechanical and Chemical Properties of Tantalum-implanted Steels*

G. K. HUBLER and I. L. SINGER

U.S. Naval Research Laboratory, Washington, DC 20375 (U.S.A.)

C. R. CLAYTON

Materials Science Department, State University of New York, Stony Brook, NY 11794 (U.S.A.)

(Received September 17, 1984)

ABSTRACT

The surface mechanical and chemical properties of tantalum-implanted AISI 52100, AISI M50 and AISI 9310 steels and pure iron were investigated. Sputter Auger profiles of pure iron indicate significant carbon incorporation during implantation. For AISI 52100 steel the unlubricated kinetic coefficient of friction is reduced from 0.6 to 0.38, the load-carrying capacity is increased and the pitting potential in a 0.01 M NaCl solution is increased by 510 mV. The corrosion resistance of tantalum-implanted AISI M50 steel in 0.5 M H$_2$SO$_4$ is equal to that of high dose chromium implantation. The rolling contact fatigue life is significantly improved for tantalum-implanted AISI M50 steel and a 24% increase in load-carrying capacity is measured for Ryder gear scuffing tests on tantalum-implanted AISI 9310 steel. The mechanism producing the improvements in corrosion resistance is thought to be selective dissolution of iron with the formation of a tantalum-rich passive oxide film on the surface, while friction reduction is at least partly responsible for improving the wear properties.

1. INTRODUCTION

The practical value of ion implantation would be significantly enhanced if a single ion implantation treatment could improve both the wear and the corrosion resistance of steels. One candidate treatment for bearing steels is

titanium implantation which has been shown to produce a surface with improved resistance to lubricated and unlubricated sliding wear [1-3]. The titanium-rich surface alloys are amorphous, have a low coefficient of friction and contain 10-20 at.% C. The carbon is introduced during implantation by means of irradiation-enhanced diffusion of carbon originating from surface-adsorbed carbonaceous molecules (ion-beam-induced carburization). Unfortunately, only marginal improvements in the corrosion resistance were measured for titanium-implanted steel in either acid solutions or chloride-ion-containing pitting solutions [4]. Systematic considerations suggested that the mechanism of forming an amorphous layer by vacuum carburization should apply to other carbide-forming elements from groups IVB and VB of the periodic table [5]. From these, niobium and tantalum have the highest thermodynamic stability in aqueous solutions and might be expected to produce surfaces which are more corrosion resistant than those produced with titanium. Therefore the investigation of corrosion and wear properties of steels was continued and extended to other ion species.

In this paper the corrosion, wear and surface chemistry of tantalum-implanted pure iron, AISI 52100 steel and AISI M50 steel are reported. As in titanium implantation, the tantalum-implanted surfaces are found to be partially vacuum carburized and to have superior wear resistance. However, the corrosion resistance is markedly better for tantalum implantation and is therefore a treatment which can produce resistance to both corrosion and wear. Beneficial effects produced by tantalum implantation on rolling contact fatigue of AISI M50 steel and on scuffing of

AISI 9310 steel are also presented which serve to demonstrate the viability of this treatment in realistic engineering situations.

2. EXPERIMENTAL DETAILS

2.1. Material

The compositions of AISI 52100, AISI M50 and AISI 9310 steels are given in Table 1. Both AISI 52100 and AISI M50 were tempered to a Knoop hardness of close to 800 HK. AISI 9310 is a case-carburized steel with 0.1 wt.% C in the bulk and 0.85 wt.% C in the case. The hardness of the case was also 800 HK. All samples were obtained from the Naval Air Propulsion Center (D. Popgoshev), Trenton, NJ. AISI M50 and AISI 52100 are relatively free of non-metallic inclusions because the material was fabricated using the vacuum-induction-melted vacuum-arc-remelted process. Samples for sputter Auger profiling consisted of iron films 200–400 nm thick electron beam evaporated onto sapphire or glass substrates. Corrosion and wear samples were cut from rods 0.95 cm in diameter and polished to a mirror finish using 1.0 μm diamond paste in the final step.

2.2. Chemical analysis

Auger sputter depth profiles were obtained with a cylindrical mirror analyzer (PHI model 545 system) under the following conditions: electron energy, 5 keV; modulation energy, 3 eV peak to peak; argon ion energy, 2 keV; current density, 10 μA cm^{-2}. Depth scales for the profiles were determined by optical interferometry from the step heights of ion-milled craters. Semiquantitative analysis was achieved by normalizing the Auger peak-to-

peak intensities of the C(270 eV), Fe(650 eV) and Ta(1680 eV) lines with the following normalization constants: $N^C = 0.21$, $N^{Fe} = 0.19$ and $N^{Ta} = 0.08$. The values for iron and tantalum are the elemental sensitivity factors from the PHI handbook [6], and the value for carbon was determined from a TaC reference standard. The normalized peak height data are considered to be semiquantitative since it is likely that some preferential sputtering of carbon, if not iron, occurs during argon ion milling.

2.3. Corrosion

Potentiodynamic scans were performed in either deaerated 0.5 M H_2SO_4 solution or deaerated 0.01 M NaCl (pH 6 acetate buffered). Both solutions were at room temperature and the potential was scanned at a rate of 1 mV s^{-1} in the positive direction. The potential scan began directly on immersion into the acid solution. For the NaCl solution the samples were first polarized in the cathodic direction for 30 min at a negative potential which produced a current of 5 mA cm^{-2} in order to reduce the air-formed oxide film. All potentials were measured versus a saturated calomel electrode (SCE).

2.4. Friction

Kinetic coefficient μ_k of friction measurements were carried out using an AISI 52100 steel ball 1.27 cm in diameter sliding on implanted AISE 52100 flats with no lubrication (dry sliding). Friction measurements were performed in laboratory air (a relative humidity of 40%–60% at about 22 °C) at a sliding speed of 0.1 mm s^{-1}. A normal force of 9.8 N (1 kgf) was used, producing a peak hertzian pressure of 0.85 GPa (123 klbf in^{-2}). A detailed description of the experimental method has been given elsewhere [2].

2.5. Mechanical tests

Rolling contact fatigue tests were carried out at the Naval Air Propulsion Center. In this accelerated fatigue test a maximum hertzian stress of 4.83 GPa (700 klbf in^{-2}) is applied by pressing two hardened steel disks against a rod 0.95 cm in diameter of the material to be tested. The rod is rotated at a speed of 12 500 rev min^{-1} until the surface fails by generation of fatigue spalls. Data are plotted on the Weibull probability scale of

TABLE 1

Steel compositions

Steel	Amount (wt.%) of the following elements in the steel					
	C	Cr	Mn	Si	Mo	Other
AISI 52100	1.05	1.45	0.35	0.22		
AISI M50	0.85	4.0	0.27	0.17	4.25	1.0 V
AISI 9310^a	0.10	1.2	0.55	0.22	0.12	3.25 Ni

^{a}Case carburized to a hardness of 800 HK.

percentage of failures *versus* the number of cycles. 11-15 tests are run for each condition to obtain statistics. The number of cycles for 10% and 50% failure ᵣes (denoted L_{10} and L_{50} respectively) and the slope of the failure rate are the standard means of quoting rolling contact fatigue data. The relative sliding velocity in this test is 0 cm s^{-1} (no slip), the lubricant is Hercolube A and the control test is run on an unimplanted portion of each rod to ensure that there are no differences between the bulk properties of the implanted and those of the unimplanted conditions. All samples were ion implanted with the angle of incidence to the surface normal confined to $\pm 30°$ and the implantation conditions are listed in Table 2.

The test procedure and data evaluation methods for Ryder gear scuffing tests have been described in *ASTM Standard D 1947* [7]. The Ryder gear tests were performed at the Naval Air Propulsion Center. High precision 28-tooth test gears with a 8.89 cm pitch diameter are machined from AISI 9310 steel, are case hardened and are then ground. The test is run using Hercolube A as the lubricant and the rotation speed is 10 000 rev min^{-1}. The sliding velocity on the gear tooth varied from 0 cm s^{-1} at the pitch diameter to a maximum of 1470 cm s^{-1} at the gear tip. A load is applied hydraulically to the gears and a test

of 10 min duration is conducted. All 28 gear teeth are then measured for area of scuffing, the load is increased and the test sequence is repeated. The test gear is wider than the drive gears so that it can be reversed and a second set of data can be obtained on the same gear. The load at which 22.5% of the tooth area is scuffed is the figure of merit. The implantation conditions were 1×10^{17} Ta^{+} ions cm^{-2} at an energy of 150 keV. During implantation an aperture restricted the tantalum ion beam to angles of incidence to the normal of the gear teeth of between $0°$ and $30°$. The maximum hertzian pressure applied to the implanted gears was 1.42 GPa (206 klbf in^{-2}).

2.6. Implantation

Implantations were performed in a cryo-pumped vacuum chamber at a pressure of 3×10^{-6} Torr or less. Samples were mounted on a water-cooled aluminum block by means of clamps for cylindrical samples and by means of a heat sink grease for thin flat specimens. Rolling contact fatigue rods and the Ryder gears were actively cooled during implantation by means of a water-cooled feed-through rotating at a rate of 2 rev min^{-1}. A total beam current of 100 μA Ta^{+} ions was raster scanned to ensure uniformity of the implanted region and the maximum flux was 10 μA cm^{-2}. The temperature of the rotating samples was con-

TABLE 2

Rolling contact fatigue lifetimes for AISI M50 steel

Test	Ion	Dose ($\times 10^{17}$ ions cm^{-2})	Energy (keV)	L_{10} ($\times 10^6$ cycles)	L_{50} ($\times 10^6$ cycles)	Slope
1			Control	3.0	20.8	0.97
	Cr^{+}	1.0	100	5.9	32.6	1.1
2			Control	6.5	16.6	2.0
	Cr^{+}	1.0	100	5.8	14.2	2.1
3			Control	3.6	12.9	1.5
	Cr^{+}	1.0	100	3.7	10.3	1.9
4			Control	8.5	15.9	3.0
	Cr^{+}	2.0	150	6.6	20.6	1.7
5			Control	6.3	14.7	2.2
	Cr^{+} + Mo^{+}	2.0-0.35	150-100	3.9	15.3	1.4
6			Control	1.6	15.1	1.6
	Ta^{+}	0.5-1.5	85-170	15.1	26.7	3.3
Average of control tests 2-6				5.9	15.0	2.1

11 failures for test 6, 15 failures for tests 1-5.

tinuously monitored by means of an optical pyrometer. The temperature of the AISI M50 rolling contact fatigue rod was maintained below 180 °C and the AISI 9310 Ryder gear below 125 °C during implantation. All other samples were kept at a temperature of less than 40 °C.

3. RESULTS

3.1. Auger analysis

Sputter Auger profiles of tantalum and carbon were measured on thin iron films implanted with tantalum to fluences of 0.1×10^{17}, 0.2×10^{17}, 0.35×10^{17}, 0.6×10^{17}, 1.2×10^{17} and 1.8×10^{17} ions cm^{-2} at 150 keV. The profiles for fluences of 0.2×10^{17}, 0.6×10^{17} and 1.8×10^{17} Ta$^+$ ions cm^{-2} are shown in Fig. 1. At the lowest dose the tantalum distribution peaks at a depth of about 25 nm and has a low surface concentration. Carburization has already begun since the carbon surface concentration is twice that for the 0.1×10^{17} Ta$^+$ ions cm^{-2} dose. For doses between 0.2×10^{17} and 0.6×10^{17} Ta$^+$ ions cm^{-2}, the carbon concentration grows very rapidly and appears to saturate at the latter dose. The tantalum surface and peak concentrations also grow very rapidly for doses between 0.2×10^{17} and 0.6×10^{17} Ta$^+$ ions cm^{-2} but are not saturated until the dose of 1.2×10^{17} Ta$^+$ ions cm^{-2} is reached. The profiles of carbon and tantalum for the highest dose of 1.8×10^{17} Ta$^+$ ions cm^{-2} shown in Fig. 1 are essentially the same as the profiles for the dose of 1.2×10^{17} Ta$^+$ ions cm^{-2} and the same as the profiles for AISI 52100 steel implanted under the same conditions [8]. Therefore the high dose profiles in Fig. 1 can be taken as a representative characterization of steels implanted at normal incidence with 150 keV tantalum ions to a fluence of about 10^{17} ions cm^{-2} or more.

3.2. Corrosion

Figure 2 presents potentiodynamic polarization scans in 0.5 M H$_2$SO$_4$ for unimplanted AISI M50 steel and for AISI M50 implanted with tantalum, chromium or titanium. The results for chromium and titanium are reproduced here for comparison purposes from ref. 9. The energies and fluences for tantalum (1×10^{17} ions cm^{-2}; 150 keV) and titanium (2×10^{17} ions cm^{-2}; 55 keV) were chosen to
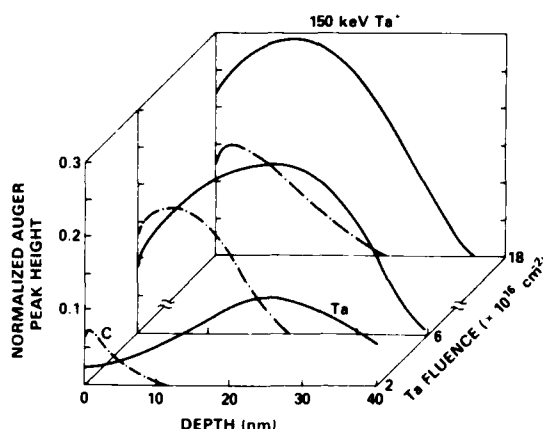
Fig. 1. Auger sputter depth profiles of tantalum and carbon for pure iron films implanted with three different doses of 150 keV tantalum ions.
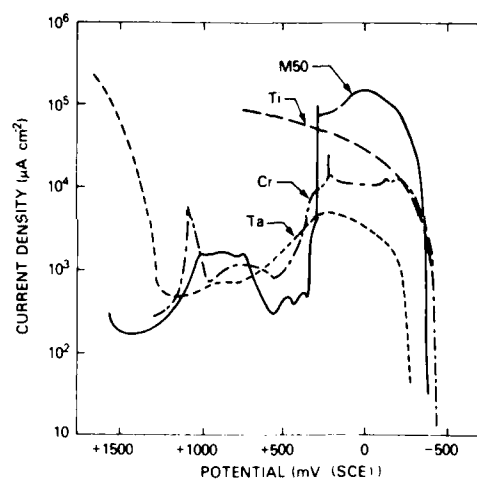
Fig. 2. Potentiodynamic polarization data produced in 0.5 M H$_2$SO$_4$ for AISI M50 steel, and for AISI M50 implanted with titanium, chromium and tantalum.

yield similar implant profiles and depths of the carburized surface layer. From the reduction in the critical current density for passivation shown in Fig. 2, it is apparent that tantalum implantation gives a corrosion resistance equal to or better than that of chromium implantation (2×10^{17} ions cm^{-2}; 150 keV; 20 at.% surface concentration) whose corrosion behavior is typical for stainless steel. It should be noted also that titanium implantation does not passivate the surface. This clearly demon-
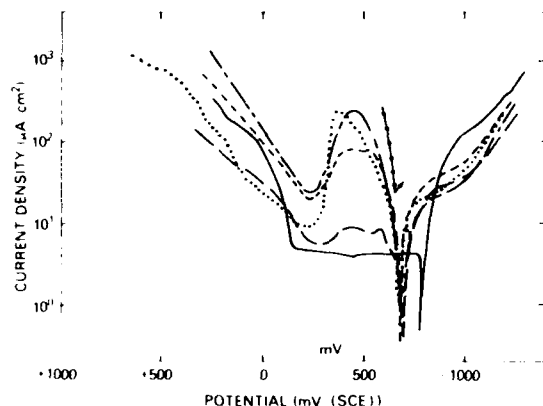
Fig. 3. Potentiodynamic polarization data produced in a buffer solution of pH 6 containing 0.01 M NaCl for AISI 52100 steel, and for AISI 52100 implanted with 150 keV tantalum ions to several different fluences: ●, 0 ions cm^{-2}; ····, 0.10×10^{17} ions cm^{-2}; - -, 0.20×10^{17} ions cm^{-2}; -----, 0.35×10^{17} ions cm^{-2}; , 0.60×10^{17} ions cm^{-2}; ——, 1.80×10^{17} ions cm^{-2}.

strates that tantalum is more effective than titanium for corrosion inhibition.

The effect of the tantalum ion dose on the passivation of AISI 52100 steel in a 0.01 M NaCl solution is shown in Fig. 3. Unimplanted AISI 52100 pits almost immediately (pitting potential $E_b = 650$ mV). Passivity is greatly improved by tantalum implantation even at the lowest tantalum dose. At successively higher doses the critical current density is reduced in a regular fashion, indicating increasing passivity with increasing dose. At the highest dose the passive current density is very low (about $5 \mu A$ cm^{-2}) and the pitting potential E_b is 140 mV, which corresponds to an increase ΔE_b in the pitting potential of +510 mV compared with unimplanted material.

3.3. Friction

The kinetic coefficients μ_k of friction in dry sliding for AISI 52100 steel implanted with tantalum to doses of 1.2×10^{17} ions cm^{-2} and 1.8×10^{17} ions cm^{-2} were 0.38 and 0.37 respectively. μ_k for unimplanted steel was measured to be 0.6. Optical micrographs and interference step height measurements of friction tracks indicated virtually no wear scar or wear debris on the implanted surface

whereas the unimplanted sample showed a wear scar which contained wear oxide debris.

3.4. Mechanical tests

Rolling contact fatigue tests are required to qualify a new surface treatment for an aircraft bearing steel. The results of the tests for AISI M50 implanted with tantalum are compared in Table 2 with data for six other tests where chromium or chromium plus molybdenum ions were implanted into AISI M50. The work on chromium-implanted rods was performed in support of an aircraft bearing corrosion investigation [10] and is reported here for the first time. Table 2 shows that for chromium implantation the results are very mixed with improvement indicated in test 1 and essentially no change or degradation in the other tests. The average result is that there is no significant change in the rolling contact fatigue using chromium or chromium plus molybdenum ions. The result for test 6 for tantalum ions is interesting for two reasons: (1) the magnitude of the improvement in L_{10} and L_{50} is large and (2) the L_{10} and L_{50} lifetimes of the unimplanted control agree with the average lifetimes of untreated AISI M50 steel for tests 2-6. Therefore the result is not suspect because of an artificially low lifetime of the base material as was the case for test 1 where an improvement was seen but which was not reproducible when the life of the base material was greater than 4×10^6 cycles.

The first experiment in which implanted tantalum was shown to improve wear resistance was that of Hartley and Hirvonen [11] for Falex scuffing tests on several steels. Of particular note was the large improvement in scuffing resistance for tantalum-implanted AISI 9310 steel. To verify this result under more realistic conditions, a set of AISI 9310 steel Ryder gears was implanted and tested. Figure 4 shows the test results plotted as the average area of gear teeth scuffed versus applied load. As a result of ion implantation, the load-carrying capacity of the gear set increased 31%. The load-carrying capacity of 37.8 kN m^{-1} (2160 lbf in^{-1}) for the control gear, which was run immediately before the implanted gear, agrees with the average of a large number of accumulated control tests to within 5%. Using the accumulated average value as the baseline, the load-carrying
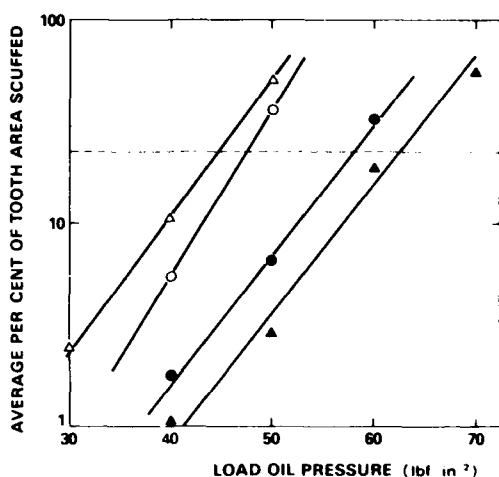
208

Fig. 4. Results of Ryder gear scuffing tests on AISI 9310 steel plotted as the average percentage of tooth area scuffed vs. hydraulic oil pressure which applies the load to the gears: ●, ▲, gear implanted with 1 × 10^{17} Ta$^+$ ions cm^{-2} at 150 keV; ·, measured at the 22.5% scuffed level, tantalum implantation increases the load-carrying capacity by 31%.

Symbol	Side	Unimplanted or implanted	Load-carrying capacity (kN m^{-1})
··	A	Unimplanted	37.8
·	B	Unimplanted	37.8
●	A	Implanted	49.5
▲	B	Implanted	49.5

capacity of the implanted gears is still 24% higher than for unimplanted gears.

4. DISCUSSION

The Auger measurements in Fig. 1 are consistent with the picture that tantalum ion implantation is analogous with the extensively studied case of titanium implantation into steels. In brief, during implantation, carbonaceous molecules are adsorbed on the surface by previously implanted tantalum that is uncovered by sputtering. The molecules dissociate and the freed carbon atoms diffuse into the surface by an ion-beam-enhanced diffusion mechanism [2, 5]. At some point in the build-up of the Fe–Ti–C or Fe–Ta–C alloy, a crystalline-to-amorphous transition occurs. For titanium implantation this amorphous alloy formation has occurred in every steel studied to date, requires that the carbon be present and is independent of whether the carbon is introduced by the vacuum carbu-

rization process outlined above or is subsequently ion implanted [3]. For tantalum implantation, we have direct evidence from transmission electron microscopy that tantalum-implanted AISI 52100 steel is amorphous [12] and it can reasonably be assumed that an amorphous layer is formed by tantalum implantation into AISI M50 and AISI 9310 steels as well.

While the tantalum-implanted surface is structurally and chemically similar to a titanium-implanted surface, electrochemically their behaviors are quite different, as shown in Fig. 2. In a study of electrochemical behavior of titanium-implanted AISI 52100 steel, Hubler et al. [4] showed that, although the passive film on the amorphous matrix was resistant to acid attack, it broke down at the carbide–matrix phase boundaries, rapidly undermining the implanted surface layer. The present result suggests that tantalum implantation beneficially modifies the phase boundaries to resist penetration (e.g. better coherence of passive film across the boundary). This possibility and the greater thermodynamic stability of tantalum in acids may account for the improvement in corrosion resistance shown in Fig. 2.

Figure 3 indicates that the corrosion resistance in pitting solutions increases with tantalum fluence. It should be noted that there is a large drop in the critical current density for passivation in Fig. 3 between doses of 0.35 × 10^{17} and 0.6 × 10^{17} Ta$^+$ ions cm^{-2} and little change in the critical current density between 0.6 × 10^{17} and 1.8 × 10^{17} Ta$^+$ ions cm^{-2}. The Auger profiles in Fig. 1 show that the tantalum and carbon peak concentrations and surface concentrations rise rapidly between 0.2 × 10^{17} and 0.6 × 10^{17} Ta$^+$ ions cm^{-2} and that the carbon concentration has saturated at the 0.6 × 10^{17} Ta$^+$ ions cm^{-2} dose. The tantalum concentration is approaching saturation at this dose and has saturated at the dose of 1.2 × 10^{17} Ta$^+$ ions cm^{-2}. Therefore the drop in critical current density directly correlates with the increase in concentration of tantalum and carbon. A recent study of tantalum-implanted AISI 52100 by Clayton et al. [13] showed that after polarization to 300 mV in the same solution as for the data in Fig. 3, the passive layer was amorphous hydrated Ta_2O_5. Apparently, during polarization the iron is selectively dissolved, leaving behind

127

the tantalum which forms the thermodynamically stable Ta_2O_5. Therefore, as the dose increases, less dissolution of iron is required to form a stable hydrated Ta_2O_5 film and the critical current density for passivation decreases as shown in Fig. 3. Ashworth *et al.* [14] suggested this mechanism in early work on tantalum-implanted pure iron, and our results confirm this suggestion.

The improved wear results for tantalum-implanted steels are not so easily explained. Using calculations by Hills and Ashelby [15] of the stresses produced under sliding contacts, Singer [16] has argued that much of the wear improvement can be rationalized by the reduced friction and the associated reduction in shear stresses transmitted to the surface. The present friction and wear behavior is strikingly similar to that reported for titanium-implanted AISI 52100 steel where the amorphous layer formation is thought to be responsible for improved mechanical properties [1-3]. It should be noted that Oliver *et al.* [17] have shown that the hardness of either titanium- or tantalum-implanted AISI 52100 steel is not increased and may even decrease. Therefore, wear reduction caused by a hard surface coating is not a viable explanation for the improved wear behavior observed here.

Rolling contact fatigue and scuffing are at present not well understood, and a detailed discussion of mechanisms is beyond the scope of this paper. However, a few general comments and speculations about possible mechanisms are in order. According to Scott [18], rolling contact fatigue is influenced by highly local conditions as well as general properties of the bulk. When conditions of contact geometry, materials and lubrication are satisfied, failure is by subsurface initiation of cracks which propagate to the surface as a result of cyclic loading. Surface failure is induced by sliding action, lubrication and environmental effects (*i.e.* corrosion), and subsurface failure is induced by microstructural changes and stress raisers.

For the rolling contact fatigue and Ryder gear tests, the loads and sliding speeds are sufficient to produce boundary lubrication and large local temperature rises during frequent metal-to-metal contacts. Lower temperatures would result from the reduced friction of any sliding component in the contact areas. Therefore, subsurface initiation

of cracks could be influenced by implantation indirectly by reducing bulk temperatures or flash temperatures which would reduce crack nucleation caused by microstructural transformations. Surface crack initiation and propagation induced by sliding action and corrosion could be directly influenced by tantalum implantation because (i) low friction reduces shear stresses transmitted to the surface and reduces surface operating temperatures, (ii) improved corrosion resistance inhibits corrosion-induced crack formation and (iii) compressive stresses produced by implantation inhibit crack growth [16].

Scuffing wear occurs at high loads and high sliding velocities, and as in rolling contact fatigue it is thought that high temperatures play a role. As the load is increased, the lubricant can no longer separate the asperities and metal-to-metal contact causes welding and severe plastic yielding of the surfaces. High flash temperatures can temper the surface, which reduces the yield strength and increases the plastic flow. The low friction surface on tantalum-implanted gears may reduce the flash temperatures during asperity contacts such that a higher load can be sustained before the deleterious tempering of the surface occurs. The friction power intensity is proportional to $\mu_k pv$ where p is the maximum hertzian pressure and v is the sliding velocity. Our measurements of the friction coefficient in dry sliding (which simulates the asperity contacts through the lubricating film) show that μ_k is reduced by 37%. According to the above expression, the pressure p can then increase by the same factor before reaching the friction power intensity in the unimplanted case. This is of the same order as the 24%–31% increase in load-carrying capacity measured for the tantalum-implanted Ryder gears and suggests that the friction reduction for contacting asperities may be partly responsible for the improved scuffing resistance.

5. CONCLUSIONS

Implantation of 150 keV tantalum ions to a dose of 1×10^{17} ions cm^{-2} into iron and steel produces a carburized surface. The carbon concentration saturates as a result of sputtering at a dose of 0.6×10^{17} Ta^+ ions cm^{-2} while the tantalum concentration saturates at a dose of 1.2×10^{17} Ta^+ ions cm^{-2}. The optimum

210

dose for improving surface properties is therefore about 10^{17} Ta$^+$ ions cm^{-2} or more. The tantalum implantation treatment is beneficial to several surface-sensitive properties of steels, namely (1) the corrosion resistance of AISI M50 steel in 1 M H_2SO_4 solutions and of AISI 52100 steel in 0.01 M NaCl pitting solutions is substantially improved, (2) the friction coefficient in dry sliding of AISI 52100 steel is decreased by 37% and the wear scar generation is eliminated, (3) the L_{10} lifetime in rolling contact fatigue of AISI M50 is increased by a factor of 3 whereas chromium or chromium plus molybdenum implantation of AISI M50 produces no change in rolling contact fatigue life and (4) the load-carrying capacity in Ryder gear scuffing tests on AISI 9310 steel is increased by 24%.

The selective dissolution of iron, which leaves a tantalum-enriched oxide film on the surface, is responsible for the improved corrosion resistance while reduced friction is at least partly responsible for the improved wear results. The tantalum implantation treatment has significant practical importance for steels because (a) a single ion implantation processing step improves corrosion resistance and low load and high load wear resistance of hardened steels and (b) the improvement in mechanical properties in established engineering tests indicates that tantalum implantation can significantly extend the lifetime of hardened steels in bearing and gear applications.

REFERENCES

1 C. A. Carosella, I. L. Singer, R. C. Bowers and C. R. Gossett, in C. M. Preece and J. K. Hirvonen (eds.), *Ion Implantation Metallurgy, Proc. Conf.*, Metallurgical Society of AIME, Warrendale, PA, 1980, p. 103.
2 I. L. Singer, C. A. Carosella and J. R. Reed, in R. E. Benenson, E. H. Kaufmann, G. L. Miller and W. W. Scholz (eds.), *Proc. 2nd Int. Conf. on Ion Beam Modification of Materials, Albany, NY, 1980*, in *Nucl. Instrum. Methods, 182-183* (1981) 923.
3 L. E. Pope, F. G. Yost, D. M. Follstaedt, J. A. Knapp and S. T. Picraux, *Wear of Metals*, American Society of Mechanical Engineers, New York, 1983, p. 280.
4 G. K. Hubler, P. Trzaskoma, E. McCafferty and I. L. Singer, in V. Ashworth, W. A. Grant and R. P. M. Procter (eds.), *Proc. Conf. on Ion Implantation into Metals, Manchester, 1981*. Pergamon, Oxford, 1982, p. 24.
5 I. L. Singer, *J. Vac. Sci. Technol. A, 1* (1983) 419.
6 L. E. Davis, N. C. MacDonald, P. W. Palmberg, G. E. Riach and R. E. Weber (eds.), *Handbook of Auger Electron Spectroscopy*, Physical Electronics Industries, Eden Prairie, MN, 1976.
7 *ASTM Stand. D 1947-73*, 1974.
8 I. L. Singer, *Appl. Surf. Sci.*, 18 (1984) 28.
9 Y. F. Wang, C. R. Clayton, G. K. Hubler, W. H. Lucke and J. K. Hirvonen, *Thin Solid Films*, 63 (1979) 11.
10 R. Valori, D. Popgoshev and G. K. Hubler, *J. Lubr. Technol.*, 105 (1983) 534.
11 N. E. W. Hartley and J. K. Hirvonen, in B. Biasse, G. Destefanis and J. P. Gaillard (eds.), *Proc. 3rd Int. Conf. on Ion Beam Modification of Materials, Grenoble, 1982*, in *Nucl. Instrum. Methods, 209-210* (1983) 933.
12 C. R. Clayton, W. K. Chan, J. K. Hirvonen, G. K. Hubler and J. A. Sprague, *J. Electrochem. Soc.*, to be published.
13 C. R. Clayton, W. K. Chan, J. K. Hirvonen, G. K. Hubler and J. R. Reed, in E. McCafferty, C. R. Clayton and J. Oudar (eds.), *Proc. Int. Symp. on Fundamental Aspects of Corrosion Protection by Surface Modification, Washington, DC, October 9-14, 1983*, in *Spec. Publ. 84-3*, 1984, p. 17 (Corrosion Division, Electrochemical Society, Pennington, NJ).
14 V. Ashworth, D. Baxter, W. A. Grant and R. P. M. Procter, *Corros. Sci.*, 17 (1977) 947.
15 D. A. Hills and D. W. Ashelby, *Wear*, 75 (1982) 221.
16 I. L. Singer, in G. K. Hubler, C. W. White, O. W. Holland and C. R. Clayton (eds.), *Ion Implantation and Ion Beam Processing of Materials, Materials Research Society Symp. Proc.*, Vol. 27, Elsevier, New York, 1984, p. 585.
17 W. C. Oliver, R. Hutchings, J. B. Pethica, I. L. Singer and G. K. Hubler, in G. K. Hubler, C. W. White, O. W. Holland and C. R. Clayton (eds.), *Ion Implantation and Ion Beam Processing of Materials, Materials Research Society Symp. Proc.*, Vol. 27, Elsevier, New York, 1984, p. 603.
18 D. Scott, *Treatise Mater. Sci. Technol.*, 13 (1979) 321.

Section II.D

WEAR BEHAVIOR OF FLAT AND GRADED PROFILE BORON - IMPLANTED BERYLLIUM

K. Kumar and H. Newborn[1]
R. Kant[2]

[1]The Charles Stark Draper Laboratory, Inc.
Cambridge, MA   02139

[2]Materials Modification & Analysis Branch
Condensed Matter & Radiation Sciences Division
Naval Research Laboratory

131

WEAR BEHAVIOR OF FLAT AND GRADED PROFILE BORON-IMPLANTED BERYLLIUM

K. KUMAR*, H. NEWBORN*, AND R. KANT**
*The Charles Stark Draper Laboratory, Inc., Cambridge, MA 02139
**Naval Research Laboratory, Washington, D.C. 20375

ABSTRACT

Pin-on-disk tests were performed for comparative friction and wear behavior on flat and graded profile boron implanted beryllium samples. Peak, intended boron concentrations of 10, 20, 30 and 40 atom percent were investigated. Auger Electron Spectroscopy was used to determine the boron concentration as a function of depth. Preliminary work was performed to study the effects of (1) a low temperature (450°C, 1-1/2 hours) heat treatment of the implanted specimens and (2) a change in the pin material. All of the boron implanted beryllium samples showed significant improvement versus unimplanted beryllium and an anodized beryllium surface. Graded samples showed comparable friction coefficients but inferior wear resistance with respect to the flat profile samples.

INTRODUCTION

The feasibility of implanting boron atoms into beryllium parts to significantly improve their surface hardness[1] and wear resistance [2] has been previously demonstrated. Variations in concentration of implanted boron as a function of depth are achieved through control of: (1) the boron ion flux, (2) the accelerating voltage, and (3) the duration for which the implantations are performed. Samples may be heat treated after implantation to form hard, beryllium borides and to change the boron concentration depth profile.

This paper reports upon the friction and wear behavior of implanted beryllium samples for intended peak boron concentrations of 10, 20, and 30 atom percent. In addition, the effect of pin material on friction and wear is discussed. In particular, a beryllium-titanium diboride composite[3] which is being examined as a potential gas bearing surface, was used as a pin. A comparison is, also, made between the wear resistance of the implanted beryllium with that of an anodized beryllium surface.

EXPERIMENTAL

Samples with intended peak boron concentrations of 10, 20, and 30 atom percent, denoted as samples 1, 2, and 3, respectively, were compared with previously discussed[2] 40 atom percent graded and flat profile samples, (identified here as 4 and 5), as well as with a lubricated anodized beryllium specimen. The energies used for this work were 25, 43, 67, 100, 140, and 192 keV and the fluences used for the 10 atom percent peak boron concentration sample corresponded to 7.1, 8.6, 8.8, 8.0, 6.3, and 3.8 x 10^{16} B/cm^2. The fluences used for the 20 and 30 atom percent samples, respectively, were two and three times these values.

The samples were analyzed by AES for concentration and depth profiles. Samples 1, 2, and 3 were additionally heat treated at 450°C for 1-1/2 hours and examined for wear behavior, designated 1HT, 2HT, and 3HT, respectively. Auger evaluation of the implanted materials was

650

performed on a Physical Electronics instrument operated at 5 kV with a 1μm-diameter spot size.

Wear testing was performed using the pin-on-disk technique with a flex pivot wear-tester[4]. The tests were performed at 100 rpm for 10 minutes duration. Pins used were a 3.2-mm sapphire ball installed in a steel cylinder and a beryllium-titanium diboride composite cylinder with its end ground to the same radius of curvature. The samples were wear-tested with progressively higher loads applied to the pin to give a relative measure of performance. Optical micrographs were taken of the wear tracks generated at the increased loads.

RESULTS

AES Studies

As with the earlier 40 atom percent samples,[2] the peak boron concentrations (Figure 1) were consistently higher than intended. The profile of sample 1 shows a peak boron content of about 20 atom percent (versus an expected value of 10 percent). Sample 3 shows a peak value exceeding about 45 atom percent (versus an expected value of 30 percent boron). Sample 2 likewise had a peak value of about 35% boron. Of these three samples, only sample 3 had a smooth graded composition profile (similar to the 40 atom percent graded sample in Reference 2). Samples 1 and 2 showed a fluctuating composition profile as indicated in Figure 1.
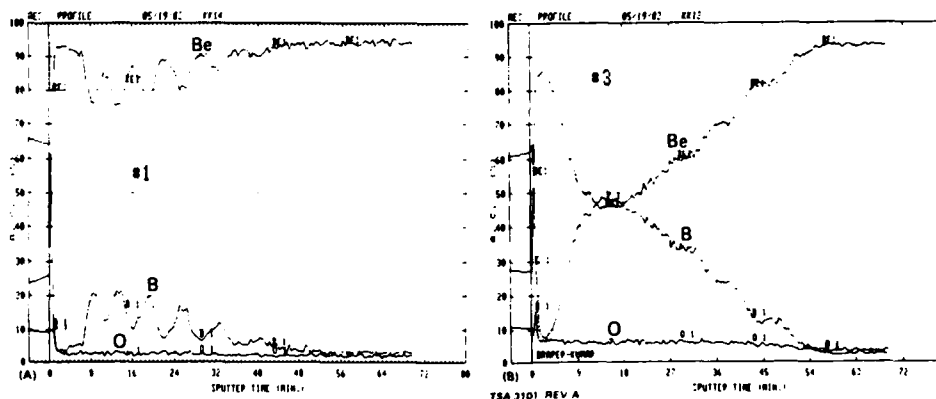
Figure 1.   Plots of atom concentration versus sputter time (depth) for (A) Sample No. 1, and (B) Sample No. 3.

Friction and Wear Studies

Table I summarizes the friction coefficient data obtained with a 20g applied load. The peak intended boron concentrations of the different samples are shown in parentheses in the second column of this table.

The most repeatable values for μ were obtained at loads below which no evidence of a wear track could be detected with a Dektak surface profilometer. In most instances, applied loads of about 20g showed little or no evidence of a wear track. The data using the sapphire pin, indicated that even at the lowest (10 percent) boron levels, the initial friction coefficient was significantly lower than

133

that measured for unimplanted beryllium,[6] <u>and</u> that this value was relatively constant for short duration (~0.1 sec). Figure 2 illustrates the observed effect of increasing the applied load on the coefficient of friction.

TABLE I. Measured values of the friction coefficients at different time for the several wear runs.

| Speci-men No. | Actual (Intended) Peak %B | μ (20 g load) | | Composite 1 Min | Load Causing Severe Damage in Wear Region |
| | | Sapphire | | | |
		.1 Min	1 Min		
1	20(10)	0.14(3)**	0.21(3)**	–	30g
2	35(20)	0.15(2)**	0.20(2)**	–	>40g
3	45(30)	0.14(3)**	0.26(3)**	–	30g
*4	55(40)	0.16(4)**	0.21(4)**	–	50g
*5	55(40)	0.15(6)**	0.15(6)**	0.46	60g with sapphire; up to 110g with composite
Be (anodized)	–		0.66	0.30	50g
1HT				0.53	30g
2HT				0.39	60g
3HT			0.22	0.63	60g

* The behavior of these samples was discussed in Reference 2. (Samples 4 and 5 had graded and flat profiles respectively.

**Number in parentheses indicates that the reported friction value was measured and averaged over that number of runs. Other data reported is based on a single run.

Figure 2. Schematic showing observed effect of increases in applied load on characteristics of friction trace of implanted beryllium.

$W_1 < W_2$.

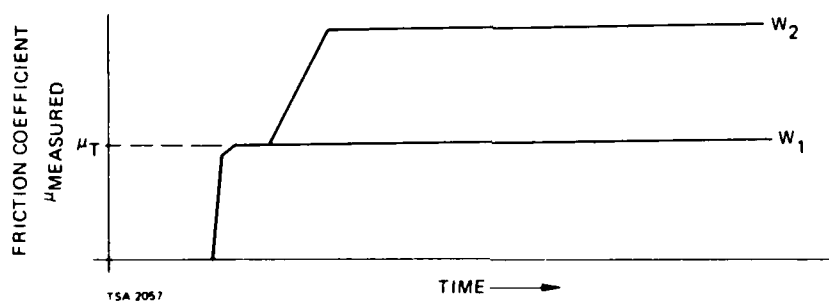$\mu_{measured} = \mu_T + \mu_W$, where μ_W is dependent on wear of surface, and

μ_T = true value of the friction coefficient.

652

This observed effect of the load on the friction traces was explained in
the following way. The boron depth profiles indicated that little or no
boron existed in the region near the surface of the implanted samples.
The initial low and constant μ (for all the compositions that were
investigated) were, therefore, possibly associated with increased wear
resistance imparted to the surface by radiation damage from the
penetrating boron ion flux. This reasonably boron-free beryllium
surface layer was destroyed with increase in time of test and/or
increased load, during which time the friction coefficient registered a
reasonably rapid increase. Additional wear was very gradual through the
boron rich layers. This latter effect appeared in the form of a very
slowly increasing value of the friction coefficient with time. Somewhat
surprisingly, this rapid stepped increase in μ was not noticed with the
composite pin tests. The higher friction coefficient values that were
measured were considered an indication that the microscopically rough
surface of the composite pin possibly removed the boron-free beryllium
surface quite rapidly to be sensed by the instrumentation.
Inconsistency in μ at the 0.1-minute interval with the composite pin
required tabulation at the 1-minute duration; the sapphire data obtained
at 1 minute is, therefore, also included for comparison.

Optical

Although the initial (0.1 second duration) μ values, for the
sapphire pin, were roughly the same for all of the specimens, the wear
resistance over full 10-minute intervals was quite different for various
implanted conditions. Figure 3 depicts the wear tracks observed on

(A) 30g LOAD   SAMPLE 1   (B) 30g LOAD   SAMPLE 2
                                                                   ⊢——— 40µm

(C) 30g LOAD   SAMPLE 3   (D) 50g LOAD   ANODIZED Be
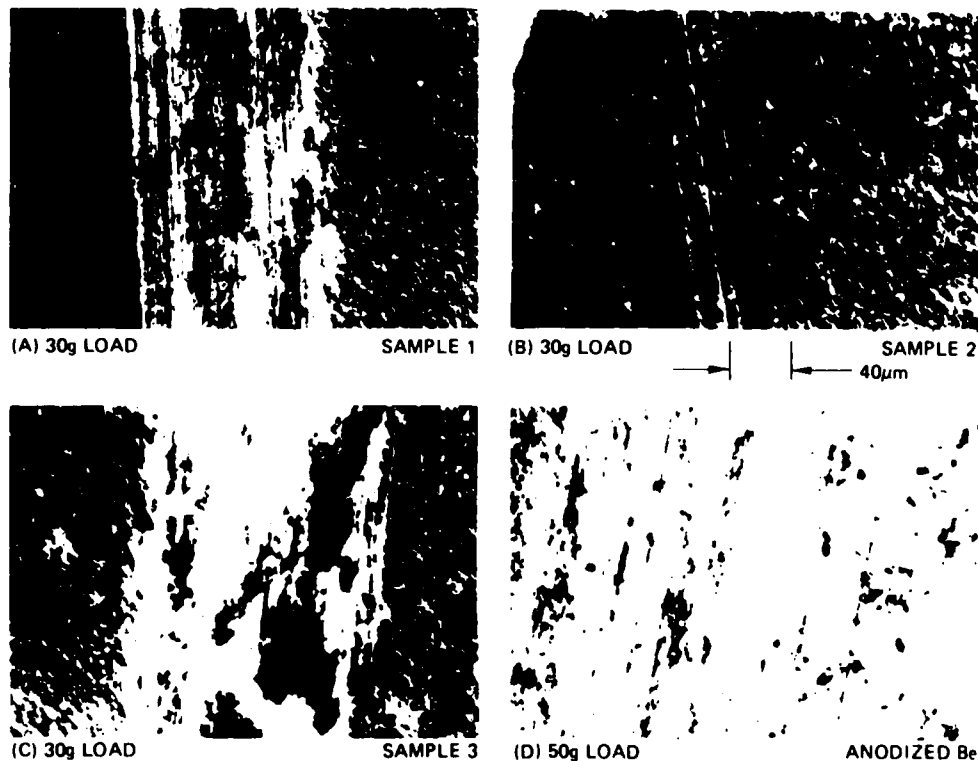
Figure 3.   Wear tracks observed at indicated loads. Samples 1,2,3 contacted
            a Sapphire Pin. The anodized Beryllium sample was run against a
            Be-TiB$_2$ composite pin.

135

samples 1, 2, and 3 after 10 minutes of test using a sapphire pin at 30-gram load. Severe wear (i.e. significant debris, rugged wear track) has been initiated in samples 1 and 3. However, even at 40 grams, sample 2 showed no such signs. The reasons for this anomalous behavior of sample 2 are not clear. As indicated in Table I, after heat treatment, sample 1HT showed severe wear at the same 30g level with the composite pin; samples 2 and 3 HT survived to the 60-gram load level. This is an improvement after heat treatment for sample 3. It is possible that the heat treatment flattened the highly graded profile of sample 3. It could be concluded, similar to earlier work[2], that flat profile samples show superior wear resistance to graded samples. This study also demonstrates that the composition of the layer, a given distance below the actual wearing surface, determines the resistance of that surface to further wear. Further study on 40 intended atom percent flat profile samples has shown inconsistent results as to resistance to severe wear. One sample showed absence of severe wear even after a 110-gram loading with the composite pin.

Experiments performed with the composite pin on an anodized beryllium surface exhibited signs of severe wear after a 50-gram loading (Figure 3D). A low μ value was measured for this sample. However, the surface was lubricated prior to the measurement. This is believed to be responsible for the low value.

Microhardness Measurements

The hardness of a surface is generally considered an indication of its wear resistance. Therefore, the higher the hardness, the greater would be the expected wear resistance. Microhardness values in Knoop Hardness Numbers, KHN (expressed in kg/mm^2) made on several of the samples are shown in Table II. It is difficult to measure the hardness of such thin surface regions accurately. At high applied indentation load the substrate contribution is excessive. At very low loads the surface contribution dominates but questions arise with respect to "the actual" as compared to "the intended" load. We have, therefore, devised a procedure whereby microhardness measurements are made in a range of applied loads. The variation of microhardness as a function of applied load gives a more reliable assessment of the hardness of the surface.[5] Conventional thinking notwithstanding, the data in Table II show that the wear behavior of these samples cannot be explained on the basis of the measured microhardness data.

TABLE II. Average microhardness readings KHN (Kg/mm^2) on several implanted samples.

Applied Load (g) \ Sample	1	2	3	4	5
50				341	356
25	372	381	390		
10	703	643	686	762	542
5	1123	1017	1184	1211	1153
2	1736	1682	1622	2233	1965

654

CONCLUSIONS

1. Boron concentrations as low as 10 atom percent result in a substantial lowering of the friction coefficient. Higher concentrations appear to be needed for high resistance to wear. The behavior of sample 2 was anomalous and could not be explained.

2. The beryllium subsurface composition (of the implanted layers) plays a strong role in determining the wear resistance of the surface.

3. Microhardness and initial pin-on-disk friction coefficients do not correlate with resistance to longer-term severe wear.

4. Friction traces obtained using sapphire and beryllium titanium diboride composite pins were significantly different. It was suspected that this difference was related to rapid removal of the relatively boron free beryllium surface layer versus the composite pin material.

ACKNOWLEDGMENT

REFERENCES

1. R.A. Kant, J.K. Hirvonen, A.R. Knudson, and J. Wollam, Thin Solid Films, 63, 27-30 (1979).
2. R.A. Kant, K. Kumar, A.R. Knudson, 1981 Annual MRS Meeting, Boston. Published in Proc of Symp E: Metastable Materials Formation by Ion Implantation; Eds: S.T. Picraux, W.T. Choyke, Elsevier Science Publ. Co. Inc., N.Y. 1982, p. 253.
3. K. Kumar, D. Das, Am. Ceram. Soc. Bull., 62, No. 2, 249-252, (1983).
4. K. Koehler, Technical Report C-5413, The Charles Stark Draper Laboratory, Inc., June 1981.
5. D.K. Das and K. Kumar, Thin Solid Films, 83, 53-60 (1981).
6. D. Das and K. Kumar, Thin Solid Films, 108, 181-188 (1983).

Section II.E

A STUDY OF THE MECHANISMS OF FATIGUE LIFE IMPROVEMENT IN AN ION IMPLANTED NICKEL-CHROMIUM ALLOY

R.G. Vardiman and J.E. Cox

Physical Metallurgy Branch
Materials Science and Technology Division
Naval Research Laboratory

A STUDY OF THE MECHANISMS OF FATIGUE LIFE IMPROVEMENT IN
AN ION IMPLANTED NICKEL-CHROMIUM ALLOY

R. G. Vardiman and J. E. Cox
Naval Research Laboratory
Washington, D.C. 20375-5000

ABSTRACT

Wires of the alloy Ni20Cr with and without carbon ion implantation have been tested in tension-tension fatigue. A 17% increase in endurance limit was found with implantation. The fatigued surface was examined by SEM, and the wire then nickel plated so that transverse sections could be made for TEM study. It was found that bulk slip was unaffected by implantation but slip in surface grains was unable to penetrate the implanted layer to a significant degree. Slip band cracking which was found in unimplanted specimens was replaced by grain boundary cracking in the implanted specimens.

INTRODUCTION

An increase in high cycle fatigue life by ion implantation has been demonstrated in a number of materials, including carbon steel (1, 2), copper (3), and titanium alloys (4, 5). The implanted ions have included interstitials such as nitrogen (1, 5), carbon (5) and boron (2) as well as substitutional atoms such as Al (3, 4) and Cr (3). Not all implants improved fatigue life, but for those which did the increase in endurance limit, when measured, was typically 10 to 20 percent.

Observations of surface slip markings have formed the basis of explanations of the underlying mechanisms of fatigue life improvement. Slip homogenization was frequently found (2, 3, 4), and a total supression of surface slip was reported in one case (6). The implanted layer is considered a barrier to normal surface slip processes due to compressive stress, solid

140

solution hardening, and in some cases precipitation. Thus the development of surface cracks which can lead to failure is suppressed. However, the same mechanism may not be applicable in every case. For example, the ease of cross slip leading to slip homogenization will differ. The occurrence of subsurface failure crack origination found in one study (5) indicates that a totally different mechanism may be involved.

The absence of any observation of the dislocation processes involved in the fatigue of ion implanted materials inhibits our ability to determine basic mechanisms. The present investigation is an attempt to shed some light on this aspect of the problem. A nickel-20 wt. pct. chromium alloy was chosen for study. A substantial increase in the fatigue life of carbon implanted wire specimens was found. By nickel plating the fatigued specimens, transverse sections could be prepared for transmission electron microscope (TEM) examination. Extensive observations of the area adjacent to the implanted layer, coupled with scanning electron microscope (SEM) observations of the surface, has led to several conclusions regarding high cycle fatigue life improvement by implantation.

EXPERIMENTAL TECHNIQUES

Material and preparation - The starting material was a nickel-20 wt. pct. chromium alloy in the form of annealed wire 1.14 mm in diameter. Sections were strained 10%, then cut and masked for electropolishing. First, a 12.7 mm gauge length was made by polishing in a solution of $60\%H_3PO_4-40\%H_2SO_4$ to reduce the diameter to approximately 0.84 mm uniformly over this length. Then the masking was removed and the full length given a final light polish in a solution of $37\%H_3PO_4-56\%glycerol-7\%H_2O$. This gave specimens 63.5 mm in length with a 12.7 mm section in the middle of roughly half the cross sectional area of the ends.

All specimens were then given a vacuum anneal at 800°C for one half hour. This resulted in a grain size of about 25 µm. Some thermal etching of the grain boundaries was visible on the wire surface. The annealed microstructure also contained scattered carbides of 1 to 6 µm size.

Implantation - Implanted wires were given a dose of 2×10^{17} ions/cm^2 of carbon at 125 keV. The theoretical distribution (7, 8) for these conditions on a flat surface is a maximum concentration of 15 at. pct. at a depth of 150 nm. Since the beam was wider than the wire diameter, part of the implant occurred at low incidence angle which would tend to skew the carbon distribution toward the surface, thus a maximum of 8-10% carbon may be expected. For implantation the ends of the wires were soldered into a large copper block in a widely spaced configuration. Despite this, temperatures approaching 300°C were observed by infra-red pyrometry during implantation.

Fatigue Tests - All fatigue tests were performed in a hydraulic testing machine at a frequencey of 20 Hz with R=+0.1. The specimens were soldered in copper cylinders at each end, and these placed in specially designed grips (see Fig. 1) which eliminated all possibility of stress prior to beginning the test. Most specimens were run to fracture, but some tests were stopped at a predetermined number of cycles. The same apparatus was used to do tensile tests on both implanted and unimplanted specimens.

Characterization - After fatigue testing, wires were examined in a scanning electron microscope (SEM). Both the wire sides and the fracture surfaces were studied.

For TEM examination, selected wires were electroplated to a diameter of 3.0 mm. Because of the small depth of the implanted layer, it was necessary to modify the usual plating preparation steps which involve material removal. The wire was solvent cleaned and rinsed, then placed in a nickel strike solu-

142

tion. It was found that plating adhesion was greatly improved by reversing the current (specimen anodic) for about five seconds, which removed at most a few hundred angstroms from the surface. The wire was then plated for ten minutes in the strike solution and transferred directly to a heated nickel sulfamate plating solultion. After a brief time at low current, a high plating rate could be used to complete the plating (9).

The plated specimen was then sliced perpendicular to the wire axis in a thin slicing machine, and TEM specimens were prepared by the usual process of mechanical polishing and electrolytic thinning. It was found that the thinning rate for the wire was slightly greater than for the nickel plating, so that a small step occurred at the wire-plating juncture. A perforation near this juncture then left little thinned area in the vicinity of the original wire surfce. Better results were obtained by electrolytically thinning to perforation nearer the center of the wire, and then ion milling until material at the wire-plating interface was electron transparent. To retain clarity of the dislocation structure, the final stage of milling was done at reduced voltage, usually about 2.5 kV.

One wire not subject to mechanical testing was plated, and a set of TEM discs partially thinned on one side only. These were then implanted to the same energy and dose as above, and then fully thinned from the unimplanted side. This allowed the implanted layer to be studied in parallel section.

RESULTS

The microstructure of the material prior to fatigue testing is shown in Fig. 2 for implanted and unimplanted conditions in transverse section TEM. Some stacking faults are visible in Fig. 2(a), but these were not common, indicating a relatively high stacking fault energy. A common feature of adherent platings was found to be a layer of epitaxial growth, as seen here.

143

In Fig. 2(b) the contrast is caused by the damage and strain in the implanted layer. The extent of the layer agrees with the theoretical depth (8) of 200-250 nm. There is no evidence of strain effects beyond this layer. The full width of the implanted layer was not always present due to the previously mentioned polarity reversal prior to plating, but a substantial portion of the layer was always visible.

TEM sections which were implanted separately in the foil plane revealed only a few second phase particles, of a size less than 10 nm, thus most of the implanted carbon apparently remains in solid solution.

Tensile tests of the wires gave a value for the yield stress at 0.1% offset of 103 ksi. No difference could be distinguished between the curves for implanted and unimplanted specimens.

The fatigue test results are shown in Fig. 3. The increase in endurance limit for the ion implanted case is approximately 17%. This stress differential holds approximately over the entire test range, so that the effect of implantation may be regarded as raising the stress required to produce a given fatigue life by this amount.

SEM observations - Two types of surface slip marking were found by SEM examination of fatigued wire sides. As shown in Fig. 4, both fine wavy slip lines and coarser straight slip lines could be seen, with the former occurring much more often. This agrees with the TEM observation that stacking faults are not common in this material, thus cross slip producing wavy slip markings should not be difficult. Slip lines were found on only a small percentage of the grains. Both kinds of slip markings were also found on implanted specimens, though these usually appeared faint, indicating a very shallow offset.

Secondary cracks are most useful for revealing the surface features associated with cracking. Secondary cracking was found only at the highest

144

stress levels, however, in specimens with lifetimes of about 10^5 cycles or less. In the unimplanted case, some crack origins could clearly be identified with slip bands, as shown in Fig. 5(a). Slip band cracking is suppressed by implantation, and all secondary cracks appear to originate on grain boundaries (Fig. 5(b)). Examination of the fracture surfaces showed that all failure cracks originated at or extremely close to the surface.

TEM observations - Fig. 6 shows some of the observations of slip made in the wire bulk, away from the surface. All are from specimens fatigued to failure. Some clear cut slip bands were found, as in Fig. 6(a), often showing a sharp contrast change across the band. Such bands are also found with few or no dislocations in them, as in Fig. 6(b). These may have lost their dislocations during the preparation process. Since much observation was done in {111} dark field, slip planes were often seen edge on, as in Fig. 6(c). Occasional irregular dislocation walls, as in Fig. 6(d) may be due to intersecting slip planes.

The extent of deformation increased with increasing maximum fatigue stress, but even at 115 ksi, only about 15% of the grains showed clear indications of the occurrence of slip, in agreement with SEM observations of surface slip markings mentioned above. To determine if any difference in bulk deformation between implanted and unimplanted specimens existed, a test at 100 ksi on an implanted specimen was stopped after 190,000 cycles, the point at which an unimplanted specimen had fractured. The type and extent of deformation in the two specimens were the same, showing that implantation does not affect slip processes in the bulk. It is therefore necessary to look for surface effects.

Because of the epitaxy effect in plating, the original surface line of unimplanted wires was not always clear in transverse TEM sections. In some

145

areas, however, it was possible to distinguish surface slip bulges, as in Fig. 7. This is the expected behavior, and if comparable surface slip steps were forming in implanted specimens, they should be more easily distinguished, due to distortion of the implanted layer. In fact such distortion has not been found, and typically one sees slip planes simply stopping at the implanted layer, with no offset or distortion of the layer distinguishable. An example of this is shown in Fig. 8. It should be noted that small offsets, of the order of tens of angstroms, might not be resolvable, especially as the full depth of the implanted layer is not always visible.

One situation where offset of the implanted layer was found involves apparent grain boundary slip, Fig. 9. This effect was observed in only a few instances. In one case the boundary was determined to be a twin boundary, and it is likely that other cases of boundary slip involve twin boundaries also.

DISCUSSION

Two important effects of implantation on the affected layer need to be considered in connection with fatigue interactions. First, the material is strengthened by the presence of the high concentration of carbon in solid solution. Second, the lattice will want to expand due to the presence of the interstitial carbon. While expansion can occur normal to the surface, the layer is constrained laterally, which will produce a compressive stress. A rough estimate of the magnitude of these effects may be obtained from other work. Based on work on pure nickel at low carbon concentrations (10), an extrapolation to the maximum carbon concentration present here would give $\sigma_y^I \simeq 1.3\sigma_y$, where σ_y^I is the maximum yield stress in the implanted layer, and σ_y is the yield stress in the bulk. The lattice expansion of nickel due to carbon was found to be (11) $\alpha_0 = 3.5238 + 0.0074C$, where C is the atomic percent of carbon. Using our stress-strain tests for this alloy, the strain pro-

146

duced by the maximum carbon content would require a lateral compressive stress
of 109 ksi, or 1.06 σ_y to contain it. This exceeds the bulk yield stress, but
is somewhat less than the value of σ_y^I. Other determinations (12, 13) of com-
pressive stress in high dose interstitial implanted metals have found compres-
sive stresses which equaled or exceeded the bulk yield stress.

If one now considers what is required to cause yielding in the implanted
layer, it can be seen that an axial stress on the wire, S_A, must first over-
come the compressive stress, S_C, then the enhanced yield stress:

$$S_A > S_C + \sigma_y^I \simeq 2.4 \sigma_y$$

that is, a stress level roughly two and one half times the bulk yield stress
is required. Maximum stresses used in these experiments exceeded the bulk
yield stress by only a small amount. Thus we may presume that all surface
dislocation sources would be inoperative, and that slip in surface grains that
has its origin below the implanted layer could penetrate the implanted layer
and reach the surface only when stress concentrations due to dislocation pile
up reached a sufficiently high level. This should severely limit the size of
surface slip steps, thus greatly delaying crack formation at slip bands.

In the absence of slip band crack formation, grain boundary crack nucle-
ation appears to come into play (Fig. 5). Grain boundary cracking has previ-
ously been associated with high strain low cycle fatigue (14, 15). In that
case, the high strain promotes the formation of dislocation cells rather than
persistent slip bands. In the present case, the implanted layer suppresses
surface step formation from slip bands. In both cases, slip band cracking
cannot occur. Grain boundaries, however, are an already present flaw passing
through the implanted layer. Only the compressive stress is an additional
hindrance to their movement. In order to maintain compatibility where slip
has occurred on different planes in adjoining grains, stress concentrations

147

develop at the boundary, which can lead to boundary slip (14, 15). Boundary slip has in fact been observed in some instances in this work (Fig. 9). Surface irregularities may be seen adjacent to the boundary crack shown in Fig. 5(b), and were present at numerous sites on the surface of that specimen. These surface offsets may eventually open up into a crack (15). A preference for twin boundary cracks has been found in some systems (16), as seems to be the case here. Grain boundary cracking thus appears to offer an alternate route to failure in this alloy, requiring an increased stress level of 17% above that needed for the inhibited slip band cracking failure mode. This alternate failure mode may occur in other systems, and account for the relatively modest 10-20% increase in endurance limit found with ion implantation in other investigations, as mentioned earlier.

CONCLUSIONS

1.   Carbon implantation in a Ni-20% Cr alloy increases the stress required for a given fatigue lifetime by approximately 17%.

2.   Bulk slip is unaffected by implantation, but slip bands appear unable to penetrate the implanted layer to a significant degree.

3.   Solid solution strengthening and high compressive stress produced by the implanted carbon are considered to be the principal factors in forming the surface slip barrier.

4.   Slip band cracking is found in unimplanted specimens, but is suppressed by implantation where grain boundary cracking becomes the failure mechanism.

ACKNOWLEDGEMENT
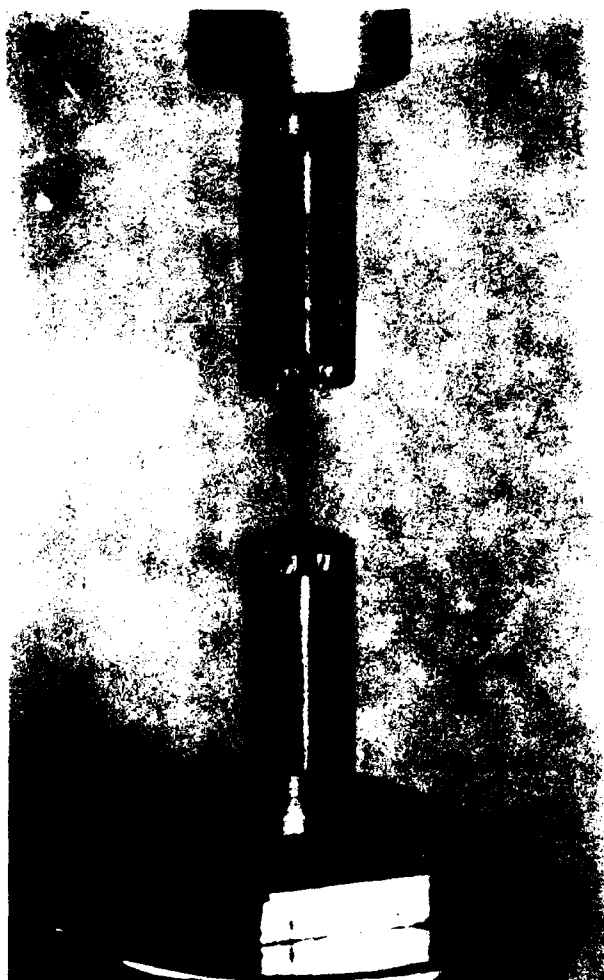
Fig. 1 — Fatigue specimen in holder, ready for fatigue test.
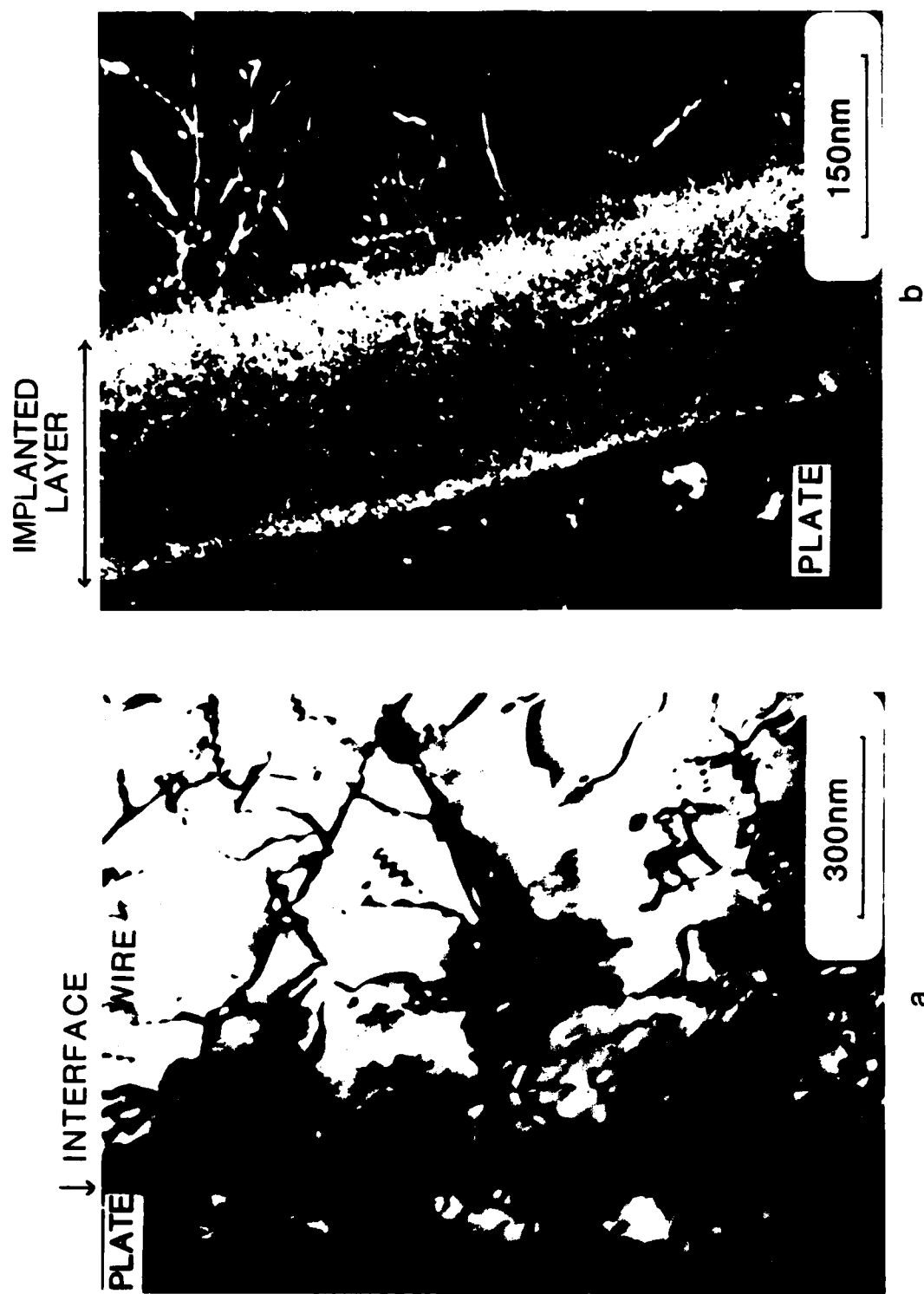
Fig. 2 — TEM micrographs of transverse sections of plated wires, unstrained; (unimplanted, dark field (g=(111)); (b) implanted, quasi-weak beam (g, g).
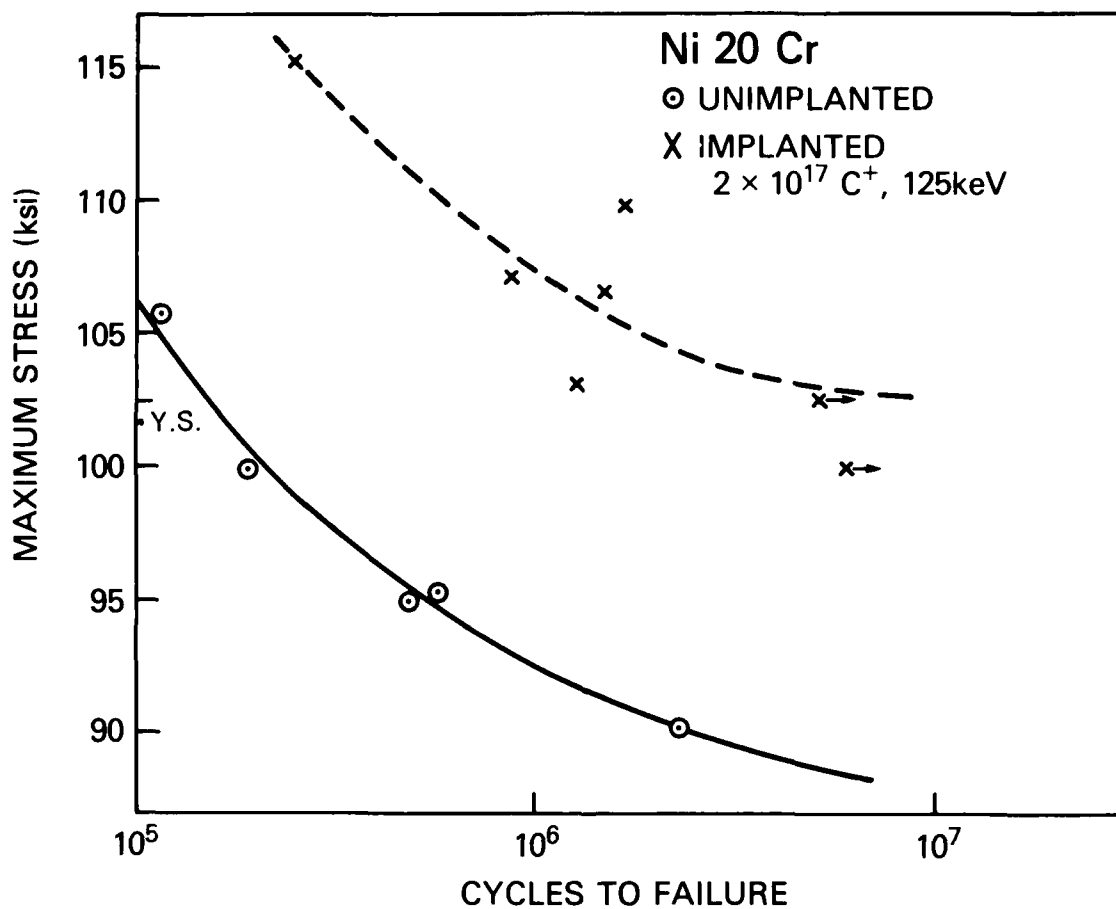
Fig. 3 — Maximum stress vs cycles of failure for implanted and unimplanted Ni20Cr. Arrows indicate no failure. YS shows the bulk yield stress of this material.
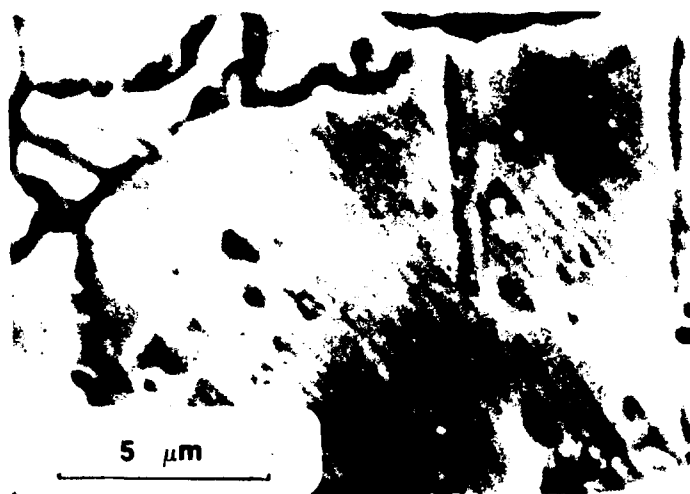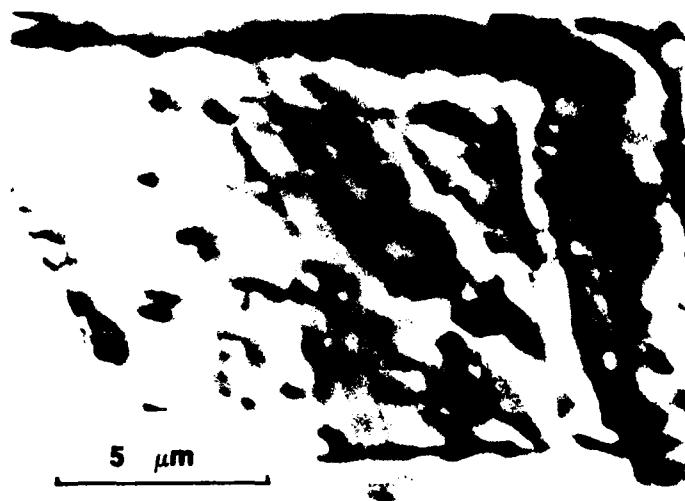
Fig. 4 — SEM micrographs of fatigued wire sides, showing types of slip traces.
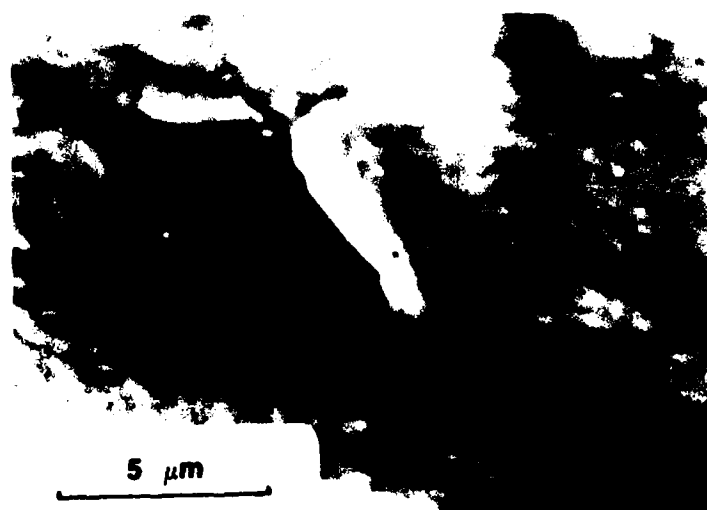
Fig. 5 — SEM micrographs of fatigued wire sides showing secondary cracking (a) unimplanted specimen with slip band cracks, (b) implanted specimen with a grain boundary crack.

Fig. 6 — TEM micrographs of bulk slip. All micrographs are dark field, $g = (111)$.

154

Fig. 7 — TEM micrograph of unimplanted specimen transverse section showing
slip extrusions on original wire surface.

Fig. 8 — TEM micrograph of implanted specimen transverse section showing
slip impinging on the implanted layer.
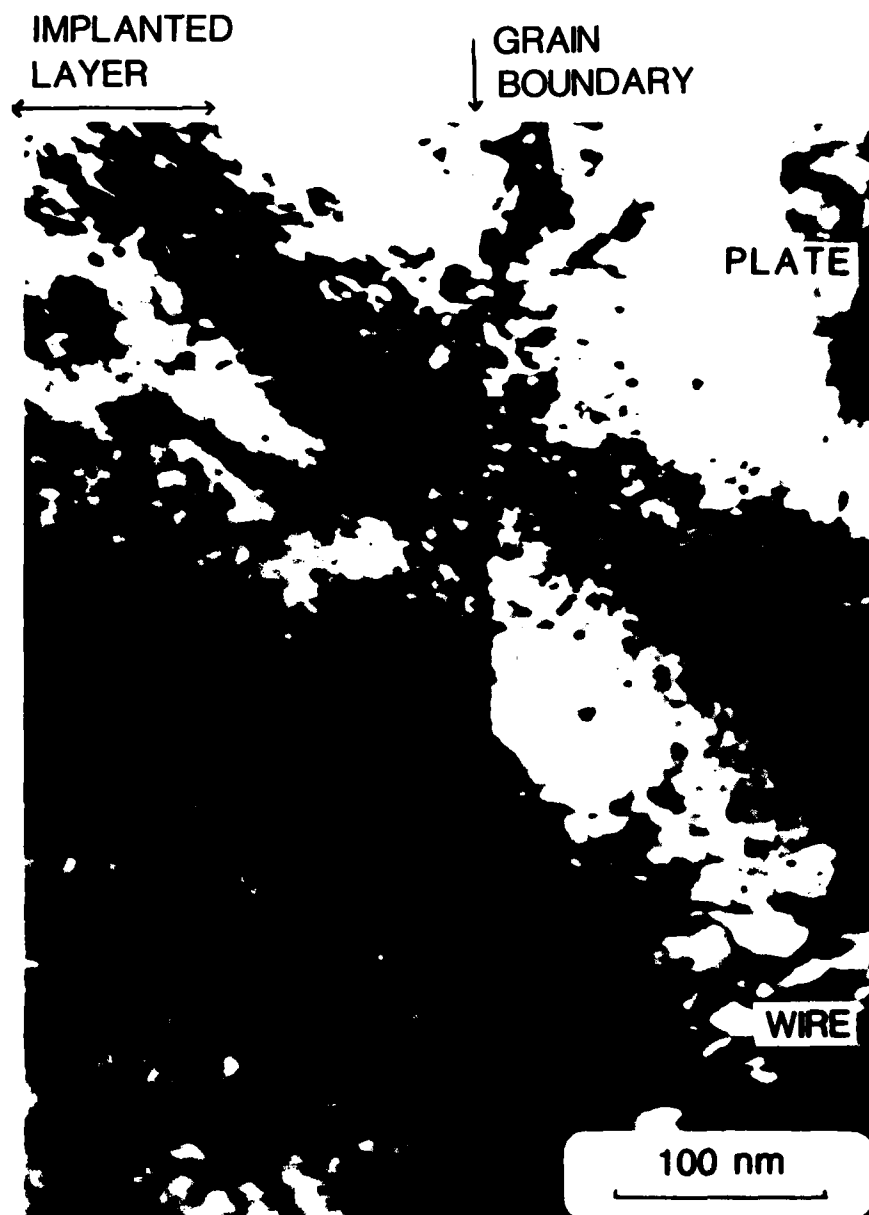
Fig. 9 — TEM micrograph of implanted specimen transverse section showing
grain boundary slip through the implanted layer.

REFERENCES

1. H. Herman, Nucl. Inst. and Meth. 182/183, 887 (1981).

2. P. W. Kao and J. G. Byrne, Fat. of Eng. Mat. and Struct. 3, 271 (1981).

3. A. Kujore, S. B. Chakrabortty, E. A. Starke and K. O. Legg, Nucl. Inst. and Meth. 182/183, 949 (1981).

4. K. V. Jata, J. Han, E. A. Starke, and K. O. Legg, Sc Met. 17, 479 (1983).

5. R G. Vardiman and R. A. Kant, Jour. Appl. Phys. 53, 690 (1982).

6. J. Mendez, P. Violan, and J. P. Villain, Ser. Met. 16, 179 (1982).

7. I. Manning and G. P. Mueller, Computer Phys. Comm. 7, 85 (1974).

8. F. Schultz and K. Witmaak, Rad. Eff. 29, 31, (1976).

9. J. B. Whitley, P. Wilkes, and G. L. Kulcinski, Trans. Am. Nucl. Soc. 23, 136 (1976).

10. Y. Nakada and A. S. Keh, Met. Trans. 2, 441 (1971).

11. L. Zwell, E. J. Fasiska, Y. Nakada, and A. S. Keh, Trans. TMS-AME 242, 765 (1968).

12. N. E. W. Hartley, J. Vac. Sci. Technicol 12, 485 (1975).

13. E. P. EerNisse and S. T. Picraux, Jour. Appl. Phys. 48, 9 (1977).

14. H. Margolin, Y. Mahajan, and Y. Saleh, Scr. Met. 10, 1115 (1976).

15. W. H. Kim and C. Laird, Acta Met. 26, 789 (1978).

16. R. C. Boettner, A. J. McEvily Jr., and Y. C. Liu, Phil. Mag. 10, 95 (1964).

Section III.A

RECENT ADVANCES IN THE APPLICATION OF ION IMPLANTATION TO CORROSION AND WEAR PROTECTION

F.A. Smidt

Materials Modification & Analysis Branch
Condensed Matter & Radiation Sciences Division
Naval Research Laboratory

159

RECENT ADVANCES IN THE APPLICATION OF ION IMPLANTATION TO CORROSION AND WEAR PROTECTION

F.A. SMIDT

Naval Research Laboratory, Washington, DC 20375, USA

Substantial progress has been made in the past few years in establishing viable approaches for the use of ion implantation for corrosion and wear protection. The major approaches, their theoretical basis and the engineering problems of scale-up to commercially acceptable rates of production and cost are examined in this paper.

1. Introduction

Ion implantation has many characteristics that recommend it for use in a wide range of applications dependent on surface sensitive properties. The ability to introduce almost any element in the periodic table into the surface region of a material independent of thermodynamic constraints, at low process temperatures, and in precisely controlled amounts provides an approach for surface modification with possibilities limited only by the imagination. The recognition of this potential in the mid-70's and the success of ion implantation in the microelectronics industry generated a tremendous surge of interest in ion implantation. Corrosion and wear control were among the first applications examined because of the large economic burden they impose on society. Early results were characterized by a large number of survey experiments with some successes, some failures, and some contradictory results. The most significant recent advances in applying ion implantation to corrosion and wear protection have been the advances in understanding of the mechanisms by which ion implantation modifies corrosion and wear behavior and a more realistic assessment of the constraints of ion implantation (thin layer, sputtering, interaction with chamber atmosphere). These results have helped formulate guidelines on how and where ion implantation can be usefully applied and defined design parameters for prototype production facilities. The paper will review various approaches to corrosion and wear protection using ion implantation and cite examples of recent work illustrative of the principles. The paper will conclude with some brief comments about processing parameters and a production facility under development in a manufacturing technology program of the US Navy.

2. Corrosion protection approaches

The basic framework for understanding corrosion phenomena is the mixed potential theory of corrosion [1]. Corrosion reactions in aqueous media are basically oxidation–reduction reactions in which the free energy change determines the feasibility of the reaction and the rate is controlled by electrode kinetics. These factors can be combined on electrode potential vs current density diagrams to describe corrosion reactions and their anodic and cathodic partial reactions. Passivity is an important corrosion phenomena in which an insoluble reaction product forms on the anode surface and reduces the rate at which anions dissolve in solution and hence the corrosion current. The use of ion implantation to control corrosion involves modification of the surface composition so as to manipulate either the anodic or cathodic reaction in a way which reduces the corrosion current.

The approaches to design of a corrosion protection surface alloy basically fall into three categories:
1) implantation of elements which promote passivity,
2) implantation of elements which alter the cathodic reaction kinetics to reduce the corrosion current, and
3) implantation of elements which produce amorphous surface alloys.

A possible fourth mechanism is the deposition and polymerization of hydrocarbons which originate from the residual gases in the implantation chamber and decomposition of these organic contaminants on the components being implanted. Such hydrocarbon films are often resistant to corrosion and may confuse the interpretation of implantation experiments, but they are usually considered an artifact.

The first approach, surface alloying to induce passivity, is applied in commercial alloys such as stainless steels where enough Cr is added to the alloy to form a passive film of hydrated $Cr(OH)_3$. An example is the implantation of Cr to provide protection for M50 and

52100 steel gas turbine engine bearings which develop pitting corrosion in chloride contaminated environments [2]. Ion implantation also offers the potential to use a variety of less conventional alloying elements. An example is the implantation of Ta into bearing steels to provide corrosion protection [3,4]. Pure tantalum forms a stable, dense, adherent oxide layer in oxidizing acids but its solubility in iron is too low (max. of 0.5%) to form a protective layer on iron by conventional alloying methods. Implantation of Ta into 52100 steel at 150 keV to a fluence of 1.0×10^{17} ions/cm^2 produced an amorphous surface alloy with a concentration of 10 at.% Ta at the surface and 20 at.% at 19 nm. depth. While the amorphous nature of the film also contributes to the corrosion protection, the passivity is due to the presence of Ta. Anodic polarization scans have been run in a 0.01M NaCl solution buffered to pH 6 to compare 52100 implants with Cr and Ta. Unimplanted 52100 shows little passivity in this solution while Cr and Ta show a passive region. Cr implantation produces little change in the open circuit potential, a shift of +600 mV in the breakdown potential and a minimum passive current density of 12 μA/cm^2. Ta implantation under identical conditions shifts the open circuit potential by +200 mV and increases the breakdown potential by +875 mV, although the passive current density is somewhat higher at 20 μA/cm^2. This represents the largest modification of corrosion behavior of 52100 by ion implantation observed to date.

The application of surface analytical techniques to the characterization of the passive films has provided a major advance in understanding the relationship between electrochemical measurements and the physical characteristics of the films that provide protection [3]. Passive films formed on the above specimens were examined by reflection high energy electron diffraction (RHEED) to determine the structure of the film, Auger electron spectroscopy (AES) with depth profiling to determine the thickness and composition of the films, and X-ray photoelectron spectroscopy (XPS) at two takeoff angles to determine the chemical state of cations and anions in the film. The passive film on the Cr implanted sample was found to be amorphous, 1.0 nm thick and primarily a highly hydrated Cr(OH)$_3$ film. It contained Cr ions in the +3 valence state, Fe in both +2 and +3 states with a ratio of Cr to Fe (total) of 1.9, and a few Cl ions. The passive film on the Ta implanted sample was also found to be amorphous and 1.5 nm thick. It was highly enriched in Ta^{+5} ions, devoid of Fe except at the metal interface and contained no Cl ions. The film appeared to be a highly hydrated form of Ta$_2$O$_5$. The protective nature of the passive film on the Ta implanted alloy is attributed to the chemical stability of the Ta$_2$O$_5$ film which forms in preference to iron oxides, the amorphous nature of the film which makes repair easy, and some unknown characteristic which

makes it impervious to Cl$^-$ penetration and increases the breakdown potential for pitting.

A second approach to modifying corrosion behavior is to change the cathodic reaction kinetics. The rate of the cathodic reaction, $2H^+ + 2e^- \rightarrow H_2$, is controlled by the rate at which hydrogen exchange (adsorption of H$^+$ ions on the surface, electron transfer and diffusion of H atoms to recombine as H$_2$ molecules) takes place on the metal surface. Metals such as Pt and Pd have a high exchange rate (10^{-3} A/cm^2 in 1N HCl) while metals such as Pb have a low exchange current (2×10^{-13} A/cm^2 in 1N HCl) [1]. If Pt is connected to a less noble metal, H$_2$ evolution will occur on the Pt at an accelerated rate and the overall corrosion rate will increase.

An example of the cathodic reaction control of corrosion is provided by Pd implantation of Ti studied by McCafferty and Hubler [5] and more recently by Munn and Wolf [6]. Titanium is passive in oxidizing acids but the film breaks down in strong non-oxidizing acids. Alloying with Pd or Pt accelerates the cathodic reaction and shifts the corrosion potential into the passive region. McCafferty and Hubler [5] implanted Ti with 1×10^{16} Pd ions/cm^2 at 90 keV. to produce an alloy with 0.1 at.% Pd at the surface and 5 at.% at a depth of 24 nm. The open circuit corrosion potential of the implanted alloy followed that of Ti for the first minute of exposure in a boiling H$_2$SO$_4$ solution, then shifted toward the more noble open circuit potential of Pd. Rutherford backscattering analysis of the sample after various times showed the Pd concentration at the surface increased as the Ti dissolved away until ultimately reaching a value of 20 at.% after 125 min. Anodic polarization curves showed current densities in the passive regime which were comparable to those of pure Ti. Wolf and co-workers [6] compared the properties of ion implanted and ion beam mixed surface alloys with those prepared by electrodeposition and vacuum evaporation. The implanted specimens had a concentration of 3.5 at.% Pd at 10 nm. The open circuit potential of the specimens was monitored as a function of time of exposure in 20% H$_2$SO$_4$ to determine how long they remained passive. Commercially pure Ti became active in this solution after 6 to 20 h while the specimen implanted with Pd remained passive for approximately 100 d. Ion beam mixing of a 50 nm electrodeposited layer using 200 keV and 400 keV Kr^{+2} ions resulted in protection for a year. Thus implantation of small quantities of Pd are effective in protecting Ti by stimulating the cathodic hydrogen evolution process and shifting the potential to a more noble passive protection region.

The third major approach to corrosion protection is the production of amorphous alloys. A combination of the amorphous structure with a composition which will form passive films obviously enhances the protection over either mechanism by itself. Compositions containing Fe Cr and a metalloid such a P, C, B, or Si have

V. ION IMPLANTATION...

shown remarkable corrosion properties in that they spontaneously passivate in hot concentrated HCl [7]. The behavior is attributed to the rapid formation of hydrated chromium oxy-hydroxide passive films on the surface of the amorphous alloy and the absence of fluctuations in composition that might promote film pitting.

Clayton, Hubler and co-workers have published a number of studies on enhancing corrosion resistance by ion implantation of metalloid ions such as P and B into 316 stainless steel to form amorphous surface alloys [8,9]. Phosphorous was implanted into 316 SS to a fluence of 1×10^{17} ions/cm^2 at 40 keV to produce a peak P concentration of 50 at.% at 24 nm with a surface concentration of 37 at.% and B was implanted to a fluence of 1×10^{17} ions/cm^2 at 25 keV to produce a peak B concentration of 20 at.% at 40 nm and a surface concentration of 5 at.%. RHEED analysis showed both surfaces were amorphous after implantation. Anodic polarization measurements in 0.5M H$_2$SO$_4$ and 0.5M H$_2$SO$_4$ + 0.5M NaCl solutions showed a complete elimination of the active region of 316 SS by the P implant, a reduction of the current density in the passive region by a factor of about 5, and for the B implant an increase in the breakdown potential in NaCl solution by 400 mV. RHEED, AES and XPS analyses were performed on passive films formed after 1 h in the 0.5M H$_2$SO$_4$ solution. The film on 316 SS was found to be crystalline, consisting of Cr(OH)$_3$ and Green Rust II, (4Fe(OH)$_2$ · 2Fe(OH)$_3$ · FeSO$_4$ · xH$_2$O) while the films on both the P and B implanted specimens were amorphous. The P implanted 316 passivated spontaneously by formation of insoluble Cr and Fe phosphates. The phosphate barrier film was attacked by Cl$^-$ ions however and pitted at a lower potential than 316 SS. The B implanted film contained Fe and Cr hydroxide and was similar to the film on 316 SS although more highly hydrated. The greater resistance to pitting in chloride solutions of the B implanted 316 SS was attributed to both the amorphous structure and higher bound water content of the passive film. These experiments thus confirm the feasibility of creating corrosion resistant amorphous surface layers by ion implantation.

Ion implantation also has some constraints which must be kept in mind when designing practical systems. The most important concern is the depth of the implanted layer which is typically 20–200 nm thick. While implantation may produce a system which forms passive films with a low current density there is always some dissolution of the metal. Thus a current density of 10 μA/cm^2 for stainless steel in the passive region corresponds roughly to the removal of 0.15 nm/min or protection for roughly 22 h for a 200 nm deep implanted layer. All coating methods are subject to galvanic coupling attack at scratches, cracks or pin holes in the protective layer where metals with different potentials

may be in contact. While ion implantation is not subject to damage from cracking or spalling of the coating it is thinner and thus more subject to abrasion damage. Heterogeneities in composition and electrochemical potential commonly occur in commercial alloys at the site of precipitates. Ion implantation can not uniformly change the composition of both matrix and precipitates so that pitting may still occur at precipitates as observed in 52100 [10], where attack at the carbides breached the implanted layer. Corrosion attack at carbide precipitates is a problem in more conventional approaches as well, where for example an electrodeposited coating may not adhere or deposit uniformly on carbides. Ion implantation can in some cases alleviate the problem by amorphizing the carbide as has been observed in Cr implantation of 52100 [3]. Future advances in corrosion protection could well come from a combination of thin film deposition with ion bombardment. This combination treatment overcomes the thickness constraint of ion implantation with the superior adherence of an ion bombarded film to offer unique possibilities [11].

In summary ion implantation offers three basic approaches to corrosion control, implantation of passive film forming elements, implantation to stimulate cathodic reactions and implantation to produce amorphous films which reduce both chemical and structural heterogeneities in the surface. Ion implantation produces only a thin surface layer which may be damaged by abrasion. It is best applied to precision components operating in relatively benign environments. Under these conditions it can extend the life of high cost components and should prove to be cost effective.

3. Wear resistance approaches

One of the major problems in defining the conditions under which ion implantation will improve the wear resistance of materials is the complexity of the wear process itself. Although conventional approaches to wear resistance such as surface hardening by diffusion and electrodeposition of coatings are firmly established in commercial practice our understanding of the mechanisms of wear have been inadequate until recently. Several conferences and reviews provide a good update on recent advances in the field of tribology [12–14]. Of particular importance for ion implantation is the recognition that many tribological properties are controlled by thin films adsorbed on the surface or at most only a few layers deep [15]. Another substantial advance in our understanding has come from the recognition that wear of ductile metals is basically a fatigue process and therefore subject to failure by progressive work hardening, crack nucleation and crack propagation [16,17]. This identification of the failure process with fatigue has served to blur some of the older distinc-

tions between mechanisms of adhesive and abrasive wear.

The wear process can generally be described by the following sequence of events: (a) initial contacts between the surfaces take place at asperities which plastically deform to redistribute the load, (b) after (a) the coefficient of friction is determined by adsorbed species and environmental reactions which take place at the surface, (c) stress from the load is coupled to the subsurface region across the surface with the magnitude and direction of the stress controlled by the coefficient of friction, the geometry and relative motion of the contact, and the applied load, (d) fatigue damage develops in the wear region with the rate of accumulation and failure mode dependent on the material properties (yield stress work hardening coefficient), stress level and the number of fatigue cycles (sliding velocity, distance). Temperature increase in the contact zone, which is influenced by the coefficient of friction, sliding velocity and applied load, can slow the rate of accumulation of fatigue damage, and accelerate metallurgical reactions in the surface and subsurface region. At high temperatures a transition to oxidation dominated wear may occur. (e) Final failure occurs when the surface delaminates or generates wear debris which destroys the integrity of the surface.

Three approaches have been used to improve the wear resistance of metals by ion implantation:

1) implantation to decrease the coefficient of friction,
2) implantation to increase the yield strength (or hardness), and
3) implantation to stabilize a wear resistant phase.

The first approach, implantation to lower the coefficient of friction, represents a significant advance in our understanding of how implantation can be used to modify wear behavior and in our understanding of the wear process itself. The principle involved is to reduce the stress coupled into the sub-surface region by reducing the coefficient of friction [16]. Singer [18] has applied this mechanism to explain how ion implantation can either reduce wear by reducing the rate of accumulation of fatigue damage at a given normal load or raise the Hertzian stress threshold at which severe wear begins.

Examples of this mechanism are provided by experiments conducted at NRL in which strong carbide forming elements (Ti, Ta, Nb) are implanted into fully hardened steels such as 52100, M50 or M-2. Auger analysis has shown that carbon bearing materials in the vacuum chamber chemisorb on the Ti exposed at the surface by sputtering, diffuse inward from the surface at a rate enhanced by the high defect concentrations produced by implantation and eventually form an amorphous Fe–Ti–C layer which is about 50 nm thick for implantation at 190 keV to a fluence of 5×10^{17} ions/cm^2 [19]. Recent in-situ surface analysis measure-

ments, described in the last section of this paper, have provided detailed information on the conditions necessary for incorporation of carbon into the surface and modelling experiments [20] have related it to physical processes. The coefficient of friction was found to be reduced from 0.6 to 0.3 by implantation with Ti under test conditions which applied an initial Hertzian contact stress of 830 MPa (120 ksi) with a sliding velocity of 0.1 mm/s (0.24 in/min) [19]. Ultra-microhardness tests of specimens implanted under similar conditions show no increase in surface hardness [21].

Wear tests of Ti implanted specimens have been conducted under a range of conditions of Hertzian stress, sliding velocity and lubrication. A recent example of one of the more definitive tests was a Faville-6 test conducted by Ramalingam in conjunction with NRL [22]. This test, developed by Begelinger and DeGee [23], uses a spherical slider loaded against a rotating thrust washer under lubricated conditions to map out scuffing wear transitions under a range of Hertzian stresses and sliding velocities. The tests were conducted on specimens of fully hardened M-2 steel implanted with 3.5×10^{17} Ti ions/cm^2 at 55 keV and with 7×10^{17} Ti ions/cm^2 at 190 keV and tested at sliding velocities of 10–100 mm/s (24–240 in/min) under mineral oil lubrication. Scuffing wear transitions, manifested as a change in coefficient of friction during the 2 h test, were observed at 815 MPa (118 ksi) in the unimplanted specimen, at 1625 MPa (236 ksi) in the 3.5×10^{17} ions/cm^2 at 55 keV implant, and at 1345 MPa (195 ksi) in the 7×10^{17} ions/cm^2 at 190 keV implant. The lower threshold in the latter specimen was attributed to surface relief of carbides due to sputtering. Other recent tests of Ta implanted 9310 under the simulated service conditions of the Ryder gear test have shown a 30% increase in load carrying capacity [4]. These tests demonstrate that substantial improvements in the wear performance of bearing and tool steels can be achieved by the friction reduction mechanism under Hertzian contact stresses and sliding velocities typical of practical applications. Even larger increases in wear improvement have been achieved by combining friction reduction with an increase in hardness in the sub-surface region as illustrated by the dual implantation of Ti and C performed by Sandia [24]. These experiments will be discussed in the next section.

The second approach, implantation to increase the yield stress, is based on the traditional approach to wear improvement represented by carburizing or nitriding of surfaces to increase the flow stress by solid solution hardening, dislocation pinning or dispersion hardening of precipitates. While the depth of the treated layer obtainable by ion implantation may be less than that of conventional diffusion treatments, there are advantages in treatment at low processing temperatures to avoid warpage, reheat-treatment or refinishing of parts and to conserve energy.

V. ION IMPLANTATION...

163

An example of wear improvement by hardening is the implantation of N into iron and low carbon steels which has been demonstrated by a number of investigators (see refs. [18,25] for a more complete review). For example, improvements in wear performance of 7–20 × have been reported by the Harwell group [26,27] for a variety of industrial forming and cutting tools. Recent activity on this approach has concentrated on the hardening mechanisms and the mobility of implanted nitrogen. LoRusso et al. [28] showed that radiation damage by itself does not contribute to hardening. Ar ion implantation into steel did not change the wear behavior although a dual implant with Ar and 5×10^{16} N ions did show some decrease in wear rate. In general implants of 2×10^{17} N ions/cm^2 or greater into low carbon steels produce the largest improvements while implants into fully hardened martensitic steels produce little benefit [25]. The primary hardening mechanism in steels, is dispersion hardening by the complex nitride precipitates which form at high fluences [29]. Lesser contributions from solution hardening and dislocation pinning occur at the lower fluences. Nitrogen implantation into steel [30] does not change the coefficient of friction.

The observation of the perserverance of wear resistance after the removal of material in the wear track to depths well beyond the ion range has led to considerable speculation as to the mobility of nitrogen under the stress or thermal gradients induced under wear conditions. Nitrogen redistribution during implantation and post-implant annealing does occur in Fe and low alloy steels although not in steel with strong nitride formers [30,31]. Post implant annealing at temperatures above 200°C results in a decrease in nitrogen content in the implanted profile [31], probably due to detrapping of N or dissolution of fine precipitates. A critical review of the evidence for nitrogen redistribution under wear conditions found no incontrovertible support for transport of nitrogen ahead of a wear region. Transfer of wear debris from the edge of the scar was suggested as a more plausible explanation of the observations [18].

Ion implantation under conditions where a dual implant produces both a hardened layer [21] and a low coefficient of friction provide substantial improvements in wear resistance of steels. Pope et al. [24] at Sandia National Laboratories have published a series of papers on this technique. Of particular interest to the present discussion are pin on disk wear tests of Ti + C implanted 440C and N implanted 440C. The Ti + C implants used a total fluence of 2×10^{17} Ti and C ions/cm^2 to produce an implanted layer 75 nm deep with 20 at.% Ti and 20 at.% C. Pin on disk tests conducted under unlubricated sliding conditions at a velocity of 17 mm/s (39 in/min) were run at increasing loads to monitor the coefficient of friction and wear track profile. The Ti + C implanted 440 C showed a decrease in coefficient of

friction from 0.65 in the unimplanted specimen to 0.3 up to loads of 600 g. The wear rate also remained constant up to 600 g thus indicating a wear threshold at 2800 MPa (408 ksi) compared to a wear rate at 1225 MPa (177 ksi) in the unimplanted specimen. Nitrogen implantation, by contrast, produced relatively minor changes in the wear behavior. These tests show the benefit of combining a low coefficient of friction with a hardened, somewhat deeper surface layer and the relative ineffectiveness of N implants in martensitic steels. Ion beam enhanced deposition, provides an approach to synthesize even thicker layers of refractory compounds with high adherence, high hardness and low coefficient of friction. Simultaneous deposition of Ti by physical vapor deposition and bombardment with N ions has been used to produce remarkably adherent films of TiN [11].

A third approach which has received less attention but which represents a different principle is illustrated by the implantation of N into 304 stainless steel. The surface of the steel is softened by the implantation but shows superior wear resistance compared to unimplanted control specimens [32]. The proposed mechanism is a stabilization of the austenite phase against strain induced transformation to martensite. The hard martensite tends to fracture and form abrasive wear debris while the austenite is more ductile [18].

In conclusion, ion implantation can improve the wear resistance of bearing and tool steels by lowering the coefficient of friction of the surface and by producing a thin hard layer on the surface. It should be recognized that the implanted region is 10 to 50 times less than the region affected by Hertzian stresses so hardening of a thin surface region is less effective in reducing wear than bulk hardening by alloying. Ion implantation hardening is therefore less effective at high loads than a coating laid down by some vapor deposition process although it can provide some benefit in delaying ploughing of the surface by asperity contact through an EHD or boundary layer film. Additional research is needed to determine the optimum trade-off between thickness and ductility in thin film, hard coats. Friction reduction, even in the absence of a hardened surface layer, appears to be effective in raising the threshold for scuffing wear under lubricated conditions by 30–100%. Within this range of stresses, one would expect to see beneficial increases in wear life. Additional research is required to investigate the higher velocity (< 100 mm/s) lubricated sliding wear conditions which are more typical of modern machinery operations to determine the applicability of ion implantation based wear protection schemes.

4. Advances in processing methods

The final area where substantial progress has been made in the past year is the analysis of ion beam processing problems and the design of a production facility capable of processing actual components for corrosion and wear protection. Space does not permit a full discussion of the pertinent issues but Smidt and Sartwell [33] have reported on the Navy Manufacturing Technology Program and Armini and Bunker [34] have described the facility design. The major design problem for a high throughput facility was identified as heat removal from the workpiece. Spire Corporation designed a facility in which a 10 mA beam can be spread to a 15" diameter using a quadrupole lens. Work piece handling fixtures for a variety of component geometries have been designed for batch mode operation. Throughput using the batch mode operation is found to be 5 to 10 times higher than a piece by piece implantation mode without beam spreading. Cost estimates for treatment range from 50 to 64 ¢/cm^2 for ball bearings to 11 to 14 ¢/cm^2 for flat specimens [33].

Substantial new insights on the dependence of retained dose on sputtering yield and angle of incidence of the beam have led to the decision to mask the samples to restrict the angle of incidence to $\pm 30°$ from normal [35]. Detailed analysis of the surface composition changes during implantation of steel with Ti under UHV and a 10^{-6} Torr atmosphere of CO [36] have shown that carbon monoxide adsorbs on the surface, the carbon forms carbide bonds to the Ti exposed by sputtering of the surface and the carbon diffuses inward at a rate somewhat enhanced over thermal diffusion processes. Oxygen is not transported across the surface–metal interface so recoil implantation appears to be a minor contribution to the transport process. Formation of an Fe–Ti–C amorphous layer at the surface reduces the sputtering yield of Ti and increases the retained dose. Thus, control of vacuum conditions is essential to assure reproducibility of properties influenced by implantation.

5. Conclusion

Substantial progress has been made in the past few years in determining what approaches are possible in applying ion implantation to corrosion and wear protection, and developing a sound theoretical basis for the approaches. This research provides sound guidelines for reducing these approaches to engineering practice.

References

[1] M.G. Fontana and N.D. Greene, Corrosion Engineering, ch. 2, 9, 10 (McGraw-Hill, New York, 1978).

[2] D. Popgoshev, R. Valori and G.K. Hubler, ASME J. Lub. Technol. 105 (1983) 534.

[3] C.R. Clayton, W.K. Chan, J.K. Hirvonen, G.K. Hubler and J.R. Reed, Proc. Symp. on Fundamental Aspects of Corrosion Protection by Surface Modification, eds., E. McCafferty, C.R. Clayton and J. Oudar (Electrochem. Soc., Pennington, NJ, 1984) Proc. vol. 84-3, p. 17.

[4] G.K. Hubler, I.L. Singer and C.R. Clayton, Int. Conf. on Surface Modification of Metals by Ion Beams, Heidelberg (1984) to be published.

[5] G.K. Hubler and E. McCafferty, Corros. Sci. 20 (1980) 1030.

[6] P. Munn and G.K. Wolf, Ion Beam Modification of Materials Conf., Cornell (1984) to be published.

[7] K. Hashimoto, in: Amorphous Metallic Alloys, ed., F.E. Luborsky (Butterworths, London, 1983) p. 471

[8] C.R. Clayton, Y-F Wang and G.K. Hubler, in: Passivity of Metals and Semiconductors, ed., M. Froment (Elsevier Science, Amsterdam, 1983) p. 305.

[9] C.R. Clayton, Y-F Wang and G.K. Hubler, on Fundamental Aspects of Corrosion Protection by Surface Modification, eds., E. McCafferty, C.R. Clayton and J. Oudar, Electrochemical Society (Pennington, NJ 1984) Proc. vol. 84-3, p. 32.

[10] G.K. Hubler, P. Trzaskoma, E. McCafferty and I.L. Singer, in: Ion Implantation into Metals, eds., V. Ashworth, W.A. Grant and R.P.M. Proctor (Pergamon, New York, 1982) p. 24.

[11] R.A. Kant and B.D. Sartwell, Conf. on Ion Beam Modification of Materials, Cornell (1984) to be published.

[12] P.B. Senholzi, Tribological Technology, vols. 1 and 2 (Martinus Nijhoff, The Hague, 1982).

[13] D.A. Rigney, Fundamentals of Friction and Wear of Materials (American Society for Metals, Metals Park, OH, 1981).

[14] K.C. Ludema, Wear of Materials 1983 (American Society of Mechanical Engineers, New York, NY, 1983).

[15] D.H. Buckley, in: Fundamentals of Tribology, eds., N.P. Suh and N. Saka (MIT Press, Cambridge, MA, 1980) p. 173.

[16] N.P. Suh, in: Tribological Technology, vol. 1, ed., P.B. Senholzi (Martinus Nijhoff, The Hague, 1982) p. 37.

[17] J.P. Hirth and D.A. Rigney, in: Dislocations in Solids, vol. 6, ed., F.R.N. Nabarro (North-Holland, Amsterdam, 1983) p. 1.

[18] I.L. Singer, in: Ion Implantation and Ion Beam Processing of Materials eds., G.K. Hubler, O.W. Holland, C.R. Clayton and C.W. White (North-Holland, New York, 1984) p. 585.

[19] I.L. Singer, C.A. Carosella and J.R. Reed, Nucl Instr. and Meth. 182/183 (1981) 923.

[20] D. Farkas, M. Rangaswamy and I.L. Singer, in: Ion Implantation and Ion Beam Processing of Materials, eds., G.K. Hubler, O.W. Holland, C.R. Clayton and C.W. White (North-Holland, New York, 1984) p. 609.

[21] W.C. Oliver, R. Hutchings, J.B. Pethica, I.L. Singer and G.K. Hubler, ibid., p. 603.

[22] S. Ramalingam, University of Minnesota, unpublished results (1984).

V ION IMPLANTATION

[23] A. Begelinger and A.W.J. DeGee, Wear 28 (1974) 103.

[24] L.E. Pope, F.G. Yost, D.M. Follstaedt, S.T. Picraux and J.A. Knapp, in: Ion Implantation and Ion Beam Processing of Materials, eds., G.K. Hubler, O.W. Holland, C.R. Clayton and C.W. White (North-Holland, New York, 1984) p. 661.

[25] G.K. Hubler and F.A. Smidt, Conf. on Ion Beam Modification of Materials, Cornell (1984) to be published.

[26] G. Dearnaley, in: Ion Implantation Metallurgy, eds., C.M. Preece and J.K. Hirvonen (TMS-AIME, Warrendale, PA, 1980) p. 1.

[27] N.E.W. Hartley, in: Ion Implantation, ed., J.K. Hirvonen (Academic Press, New York, 1980) p. 321.

[28] S. LoRusso, P. Mazzoldi, I. Scotoni and G.L. Zhang (1982), cited by J.K. Hirvonen and C.R. Clayton, in: Surface Modification by Alloying, eds., J.M. Poate, G. Foti and D.C. Jacobson (Plenum, New York, 1983) p. 323.

[29] I.L. Singer, Vacuum 84, York, England (1984) p. 853.

[30] I.L. Singer and R.A. Jeffries, in: Ion Implantation and Ion Beam Processing of materials, eds., G.K. Hubler, O.W. Holland, C.R. Clayton and C.W. White (North-Holland, New York, 1984) p. 667.

[31] N. Moncoffre, T. Barnavon, J. Tousset, S. Fayeuelle, P. Guiraldenq, T. Treheux and M. Robelet, NATO Advanced Study Institute on Surface Engineering, eds., R. Kossowsky and S.C. Singhal (Martinus Nijhoff, Dordrecht, 1984) p. 148.

[32] R.G. Vardiman and I.L. Singer, Materials Lett. 2 (1983) 150.

[33] F.A. Smidt and B.D. Sartwell, 5th Int. Conf. on Ion Implantation – Equipment and Techniques, Smugglers Notch, Vt. (1984) Nucl. Instr. and Meth. B6 (1985) 70.

[34] A.J. Armini and S.N. Bunker, ibid., p. 214.

[35] K.S. Grabowski, N.E.W. Hartley, C.R. Gossett and I. Manning, in: Ion Implantation and Ion Beam Processing of Materials, eds., G.K. Hubler, O.W. Holland, C.R. Clayton and C.W. White (North-Holland, New York, 1984) p. 615.

[36] D. Baldwin, B.D. Sartwell and I.L. Singer, Ion Beam Modification of Materials, Cornell (1984) to be published

Section III.B

EFFECT OF Cr^+ IMPLANTATION ON THE THERMAL OXIDATION OF Ta

K.S. Grabowski and C.R. Gossett

Materials Modification & Analysis Branch
Condensed Matter & Radiation Sciences Division
Naval Research Laboratory

167

EFFECT OF Cr$^+$ IMPLANTATION ON THE THERMAL OXIDATION OF Ta

K.S. GRABOWSKI AND C.R. GOSSETT
Naval Research Laboratory, Washington, D.C. 20375

ABSTRACT

Cr$^+$ implantation of Ta was undertaken in an attempt
to improve oxidation resistance at temperatures between
500 and 750°C, and for oxidation times up to 100h.
Samples were implanted with 1.5×10^{17} Cr$^+$/cm^2 at 150
keV, and compared to samples implanted with 1×10^{16} or
1×10^{17} Ta$^+$/cm^2 at 145 keV to evaluate the role of
physical effects from ion implantation. Following
oxidation, samples were examined using helium and proton
backscattering, electron and optical imaging techniques,
and auger electron spectroscopy. Improved resistance to
oxidation was observed in Cr$^+$-implanted samples oxidized
at 500°C for up to 100h, and at 600°C for about 1h.
However, some local breakdown occurred in these samples
and no protection at all was observed at 750°C. Reasons
for this breakdown are discussed and alternate approaches
for improving oxidation resistance using ion implantation
are proposed.

INTRODUCTION

Ta is one of the refractory metals which suffers from poor resistance
to thermal oxidation. Coatings and alloys have been developed to improve
its oxidation resistance, but these approaches degrade bulk mechanical
properties, are expensive, and provide poor resistance to thermal shock,
as reviews have discussed [1,2]. Recent work by Kaufmann et al. [3]
attempted to overcome these difficulties by implanting various ions into
Ta, thereby maintaining bulk mechanical properties while producing,
hopefully, protective well-integrated coatings. This approach was
unsuccessful for 1000°C oxidation, but Cr$^+$ implantation was shown to
improve the oxidation resistance of Ta at 500°C for 1h. Analysis
suggested that a thin Cr-rich oxide at the surface provided the
protection. This work expands that earlier investigation of Cr$^+$
implantation to longer times at 500°C and to the intermediate
temperatures of 600 and 750°C.

The oxidation of pure Ta between 500 and 750°C has been well
studied and reviewed and yet is not completely understood [1,2,4]. The
oxidation mechanisms are complex and time dependent. Sub-oxide platelet
formation and their incursion into the metal has been observed, and
considerable dissolution of O into the metal occurs. In the temperature
regime of interest, diffusion controlled oxide growth undergoes a
transition to a more rapid oxide growth process. It was hoped that Cr$^+$
implantation might prevent, or at least delay, this transition.

EXPERIMENTAL

Specimens were prepared from 99.9% pure Ta sheet material having a
grain size of 20 μm. Large coupons 375 μm thick were cleaned and
implanted in the central region with 1.5×10^{17} Cr$^+$/cm^2 at 150 keV,
or with 1×10^{16} or 1×10^{17} Ta$^+$/cm^2 at 145 keV. In each case a
current density of about 4 μA/cm^2 was used, and the target-chamber

pressure was about 1.5×10^{-4} Pa during the implantation. Twelve smaller coupons (6.4x12.7 mm) were cut from each of these larger sheets, producing samples that were each implanted over one-half of their surface area.

The smaller coupons were oxidized in a flowing (1 l/min) 80-20 mixture of research purity Ar and O_2 to represent pure dry air. Oxidations were conducted for 1 to 100h at 500°C, and for 1h at 600 and 750°C.

Helium backscattering at 2.0 MeV was used to investigate the kinetics of oxidation at 500°C. A scattering angle of 135° and a grazing exit angle of 20° were used. Proton backscattering of 1.5-MeV ions was used to investigate the thicker oxides formed at 600 and 750°C. A scattering angle of 135° and symmetric entrance and exit angles were used.

All samples were examined by optical microscopy. Selected samples were also investigated by scanning electron microscopy (SEM), auger electron spectroscopy (AES), or Read camera x-ray diffraction with Cu-$K\alpha$ radiation and a 10° glancing-incidence angle.

RESULTS AND DISCUSSION

Unimplanted, 500°C Oxidations

The development of oxide film on unimplanted Ta can be understood with the help of the Helium backscattering spectra shown in Fig. 1. These profiles effectively show the Ta concentration in a region close to the sample's surface, which appears at about 1.85 MeV. The lowest energy shown corresponds to a depth of 280 nm in Ta or 390 nm in Ta_2O_5 (equivalent to 160 nm of Ta completely oxidized to Ta_2O_5). The intensity decreases with increasing oxidation time because 0 diffuses into the sample and causes dilution of the Ta.
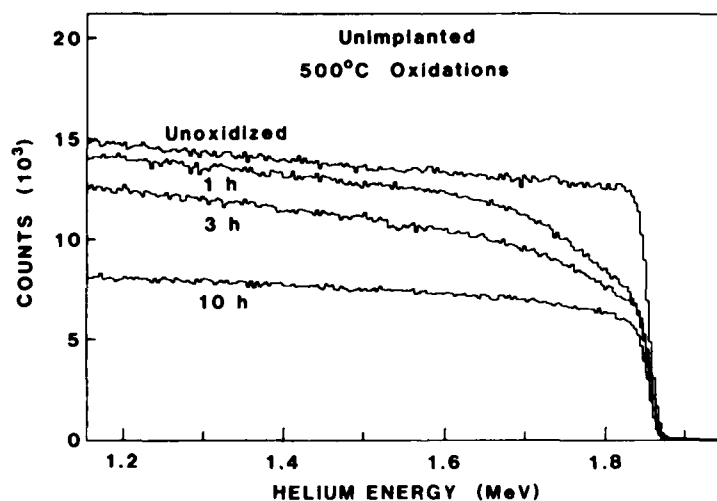

Fig. 1 Helium backscattering spectra for unimplanted Ta, oxidized for various times at 500°C.

For samples oxidized up to about 3h, the Ta concentration
increases with depth from about that of Ta_2O_5 on the surface to a
higher plateau level some 100 nm or so below the surface. This plateau
level of Ta corresponds to about 16 at.% O in the 1-h sample and about 37
at.% O in the 3-h sample, both well in excess of the 1 at.% solubility
limit for O in Ta at 500°C [5]. This large O concentration, and the
broad transition region from near Ta_2O_5 on the surface to the
plateau level beneath is probably caused by incursions of sub-oxide
platelets into the base metal. Such incursions along $\{100\}_{Ta}$ planes
have been reported for Ta oxidized at 500°C [6-8].

For oxidation times of 10h or more, only compositions near
Ta_2O_5 could be seen by the backscattering measurements. Read-camera
x-ray diffraction of a 30-h oxidized sample indicated that the oxide was
the low-temperature phase of Ta_2O_5. After 100h of oxidation, the
stresses generated were so large that a complete sheet of oxide film,
70 μm thick, separated from the sample.

These results are consistent with the theory that after an
incubation time of 150-250 min at 500°C, Ta_2O_5 nuclei form on the
surface and rapid oxidation commences [8].

Implanted, 500°C Oxidations

Cr-implanted samples showed a remarkable improvement in oxidation
resistance for oxidation times up to about 100h, as is indicated by
Fig. 2. After 100h of oxidation, regions of both thin and thick oxide
were present within the Cr-implanted portion of the sample. The spectrum
for the thin region is virtually the same as was found for samples
oxidized from 1 to 30h. This indicates that nearly all the oxidation of
Cr-implanted Ta occurs in the first 1h or so of oxidation, and that after
100h some type of localized breakdown occurs. Even without oxidation,
the Ta backscattering yield was somewhat decreased by an 18 at.% Cr
concentration present within the first 50 nm or so of the surface. This
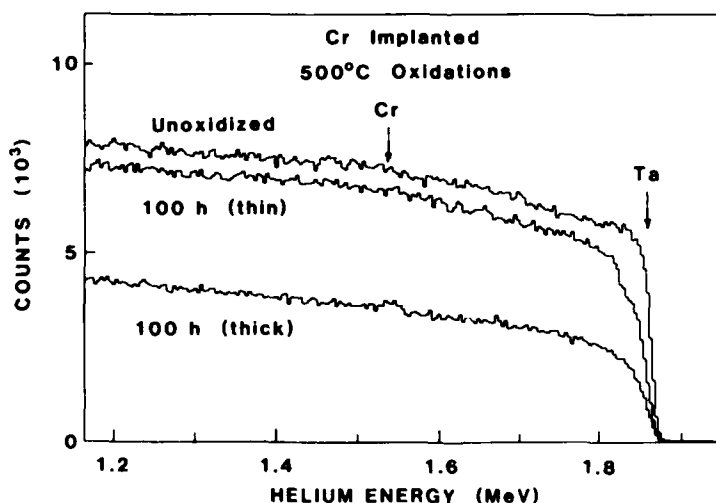dilution effect persisted in the oxidized samples as well.

Fig. 2 Helium backscattering spectra for Cr-implanted Ta, unoxidized and
oxidized 100h at 500°C. Different regions of the oxidized
sample are shown. Same analysis conditions as Fig. 1. Arrows
indicate energy for backscattering from the surface of Ta and Cr.

Considerable detail can be gleaned from the spectrum of the thin oxide region shown in Fig. 2. Within the first 1h of oxidation, oxide platelets apparently started to intrude into the base metal, as indicated by the plateau in Ta concentration, but their growth was then checked. The O concentration was lower near the surface compared to that in unimplanted samples oxidized for 1h (see Fig. 1), and the slight shift of the Ta edge to lower energies following oxidation indicates that a Cr-rich oxide layer formed on the surface, consistent with earlier work of Kaufmann et al. [3]. These results suggest that Cr implantation prevented Ta oxidation by forming a thin barrier layer on the surface which blocked the inward diffusion of O.

The consequence of physical effects from ion implantation (e.g., sputtering, radiation damage, vacuum carburization, etc.) were checked by performing Ta-ion implantations followed by oxidations for up to 27h. While the rate of incursion of oxide platelets was slowed slightly for oxidations beyond 1h, no significant long term benefits to oxidation resistance were provided.

The suggestion from helium backscattering that localized breakdown of the barrier layer was able to occur in the 100-h oxidized sample was confirmed using an SEM, as Fig. 3 shows. Sporadic eruptions about 20 μm tall were observed in the implanted region. They were arranged in groups located near the boundary of the implanted region, randomly within the implanted region, and along scratches in the surface. This should be compared to the 100 μm-thick oxide scale which formed on the unimplanted region.

Fig. 3 SEM image of sample oxidized 100h at 500°C. Cr-implanted
region is in foreground, unimplanted region (minus 70 μm of
scale) is in background. 25° angle of incidence.

Examination of an area adjacent to one of these large eruptions provided evidence that the eruptions nucleate over some type of extended defect in the surface, as shown by Fig. 4. Perhaps after a long enough oxidation period, Ta oxide nuclei form locally beneath the Cr-rich oxide layer, fracture the barrier layer, and cause rapid local oxidation to ensue.

Fig. 4 SEM image of area of
incipient breakdown
in Cr-implanted
sample oxidized 100h
at 500°C. 45°
angle of incidence.

Implanted, 1-h Oxidations

The durability of oxidation protection provided by Cr
implantation was further evaluated through 1 h oxidations conducted at
600 and 750°C. As Fig. 5 shows, while some protection was provided at
600°C, little was provided at 750°C. The lowest energy shown in
this figure corresponds to a depth of 4.4 µm in Ta and 6.2 µm in Ta_2O_5
(equivalent to 2.5 µm of Ta). Virtually no difference was observed
between spectra from unoxidized and 500°C 1 h oxidized samples.
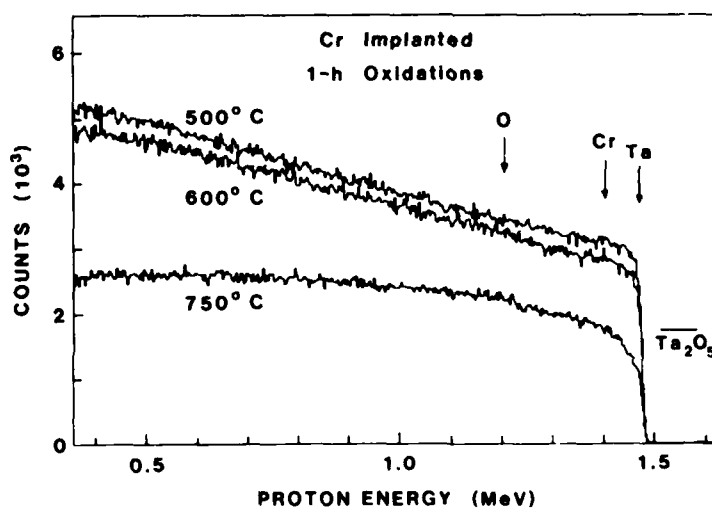

Fig. 5 Proton backscattering spectra for Cr-implanted Ta, oxidized for
1h at 500, 600 or 750°C. The yield for Ta_2O_5 at the
surface is shown, as is the energy for backscattering from the
surface of O, Cr, and Ta.

746

The 600°C sample showed evidence that incipient breakdown was occurring. Different regions of the same sample produced different levels of Ta concentration in the plateau region of the spectra. Furthermore, optical microscopy indicated that small eruptions were present on some regions of the surface. AES analysis indicated that, as in 500°C 1h oxidations, a resevoir of Cr was still present in the metal beneath the oxide film. By comparison, the unimplanted area of this sample entirely lost its oxide when the sample was cooled to room temperature. The oxide literally exploded from the surface in small flakes.

Since no reduction in oxide thickness from Cr implantation was observed in the 750°C sample (by either proton backscattering or optical microscopy), an additional oxidation sequence was performed. To ensure sufficient time for a Cr-rich oxide barrier film to form, a sample was first oxidized at 500°C for 1h before further oxidation at 750°C for 1h. The same result as shown in Fig. 5 was obtained. Apparently, at 750°C the barrier layer can no longer sufficiently slow O inward diffusion, or it is no longer stable.

CONCLUSIONS

While Cr implantation has been shown to provide significant improvement to the oxidation resistance of Ta under relatively mild conditions (500°C, t<100h), this protection cannot endure longer times or higher temperatures of oxidation. Improved protection may be possible with a thicker Cr-rich barrier layer, although the AES results indicate that excess Cr was already present in the metal beneath the oxide film. Ultimately such protection will probably fail since Cr_2O_3 is thermodynamically less stable than Ta_2O_5. Ta_2O_5 should nucleate beneath the barrier layer, grow, produce stress, and cause breakdown or dissolution of the protective film. Formation of a more stable diffusion barrier might be able to provide more durable protection. Candidate elements for such protection include Al, Si, and Zr, and further implantation work with these elements is continuing.

ACKNOWLEDGEMENTS

The authors gratefully acknowledge the assistance of Jim Sprague for the SEM work and Dave Baldwin for the AES analysis.

REFERENCES

1.   F.E. Bacon and P.M. Moanfeldt in: Columbium and Tantalum, F.T. Sisco and E. Epremian, eds. (Wiley, New York 1963) ch. 9, p. 347.
2.   J. Stringer, Reviews on High-Temperature Materials 1, No. 3, 256 (1973).
3.   E.N. Kaufmann, R.G. Musket, J.J. Truhan, K.S. Grabowski, C.R. Gossett, and I.L. Singer, Nucl. Instrum. Methods 209/210, 953 (1983).
4.   P. Kofstad, High-Temperature Oxidation of Metals (Wiley, New York 1966) pp. 190-227.
5.   G. Horz, Acta Metall. 27, 1893 (1979).
6.   J. Stringer, J. Less-Common Met. 12, 301 (1967).
7.   J.V. Cathcart, R. Bakish, and D.R. Norton, J. Electrochem. Soc. 107, 668 (1960).
8.   P. Kofstad and O.J. Krudtaa, J. Less-Common Met. 5, 477 (1963).

Section III.C

MODIFICATION OF THE OXIDATION AND HOT CORROSION BEHAVIOR OF CoCrAl ALLOYS BY ION IMPLANTATION

F.A. Smidt[1]
G.R. Johnston[2]
J.A. Sprague and V. Provenzano[3]
S.Y. Hwang, G.H. Meier and F.S. Pettit[4]

[1]Materials Modification & Analysis Branch
Condensed Matter & Radiation Sciences Division
Naval Research Laboratory

[2]Visiting Scientist
Materials Research Laboratory
Melbourne, Australia

[3]Thermostructural Materials Branch
Materials Science & Technology Division
Naval Research Laboratory

[4]Metallurgical and Materials Engineering Department
University of Pittsburgh
Pittsburgh, PA

MODIFICATION OF THE OXIDATION AND HOT CORROSION BEHAVIOR OF CoCrAl ALLOYS BY ION IMPLANTATION

F.A. Smidt[1], G.R. Johnston[1], J.A. Sprague[1],
V. Provenzano[1], S.Y. Hwang[2], G.H. Meier[2], and F.S. Pettit[2]

[1]U.S. Naval Research Laboratory, Washington, D.C.
[2]University of Pittsburgh, Pittsburgh, PA.

ABSTRACT

The early stages of oxidation and hot corrosion at 700°C were studied in Co–22Cr–11Al and Co–22Cr–11Al–0.5Y alloys in the cast and heat–treated form. Ion implantation was used to study the effect of Y on oxidation and hot corrosion mechanisms. Analytical transmission electron microscopy, Auger electron spectroscopy, Rutherford backscattering spectroscopy and scanning electron microscopy with energy dispersive x–ray analysis were used to characterize mcirostructure, oxide growth rate and oxide film composition. Implantation of 2×10^{16} Y ion/cm^2 was found to increase the oxidation rate by a factor of 2, increase the hot corrosion rate and suppress void formation at the oxide–metal interface. Possible mechanisms for these observations are discussed.

1. INTRODUCTION

Overlay coatings of the MCrAlY type, where M is Co, Ni, Fe or combinations thereof have been successfully used to provide protection against oxidation in gas turbine engines operating at temperatures up to 1000–1200°C.[1] More recently, gas turbine engines operating in the marine environment have also been found to suffer from deposit–modified high temperature corrosion which is most severe in the 700°C regime.[2]. Protection against both oxidation and hot corrosion attack relies on the formation of a stable, dense, adherent reaction product such as Al$_2$O$_3$, to provide protection in the service environment. Active elements such as Y, Ce, and Hf are frequently added to MCrAl coatings to improve the oxidation performance. Whittle and Stringer have recently reviewed the

176

published literature on the effect[3] and it is clear that the major effect of active elements is to improve scale adherence but no one mechanism clearly explains the effect. Although several mechanisms of hot corrosion attack have been proposed[4] little work has been done on the early stages of attack and the role of active elements in hot corrosion attack is poorly characterized.

Ion implantation provides an excellent tool for the study of high temperature oxidation and hot corrosion mechanisms because of the ability to selectively introduce known concentrations of elements into the surface region of the alloy to be studied. When combined with modern surface analytical techniques ion implantation can provide new insights into these complex processes. Numerous papers and reviews[5,6] by the Harwell group testify to the fruitfulness of this approach. The work reported in this paper is a summary of current progress in a cooperative study of mechanisms of hot corrosion attack of CoCrAlY alloys involving the U.S. Naval Research Laboratory, University of Pittsburgh and Materials Research Laboratory of Australia. Previous publications describing the work are listed in references 7-11.

2. EXPERIMENTAL PROCEDURES AND RESULTS.

2.1 Alloy Processing and Characterization

The alloys studied in this investigation were prepared by arc-melting in a purified argon atmosphere and drop-casting into a copper chill mold. Two compositions were prepared, a Co-22Cr-11Al alloy and a Co-22Cr-11Al-0.5Y alloy. All compositions are given in weight percent. The CoCrAlY alloy was annealed for 4h at 1080°C, followed by 17h at 700°C while the CoCrAl alloy was annealed for 100h at 1100°C and furnace cooled to room temperature. Both heat treatments produced a microstructure consisting of a matrix of β-CoAl (ordered cubic) with α-Co solid solution precipitates. The size and distribution of the phases varied with heat treatment. The 4h at 1080°C + 17h at 700°C heat treatment produced a bimodal size distribution of α-phase precipitates with the larger ones which formed during the 1080°C anneal being approximately 2 x 0.7 μm in size and the smaller ones which formed during the 700°C anneal being approximately 500 x 30 nm in size. Figure 1 shows, a transmission electron microscopy (TEM) micrograph of the structure. The 100h at 1100°C heat treatment produced larger α-phase precipitates, approximately 10μm across, and they formed a network separating the β-phase grains. Thin film energy dispersive X-ray spectroscopy (EDS) showed the composition of the α-phase was Co-28Cr-7Al and that of the

β-phase was Co–14Cr–25Al. A widely dispersed yttride phase, approximately 2 μm in diameter, was also found in the CoCrAlY alloy. The yttride phase had an average composition of Co–16Cr–11Y–2Al. Specimens were prepared from the heat treated ingots in the form of TEM disks, 3mm in diameter by 125 μm thick and in the form of coupons 10mm x 10mm x 2mm. One face of each specimen was polished to a metallographic finish.

2.2 Ion Implantation

The initial studies of ion implantation used Y to study the role of active elements in oxidation and hot corrosion and Co to serve as a control to evaluate the role of lattice defects introduced by the ion implantation. All implantations were performed in the high-current ion implantation facility at the Naval Research Laboratory. The specimens were bonded to the target ladder with a heat conducting paint to minimize specimen heating. A 1cm x 2cm beam was scanned across the sample area to produce a uniform coverage. A Ta mask was placed across each of the specimens during implantation to allow a direct in-situ comparison of the effects of ion implantation on oxidation and hot corrosion. Ion implantation conditions for Y were

Fig 1. Microstructure of Co–22Cr–11Al–0.5Y alloy after 4h anneal at 1080°C and 17h anneal at 700°C which produces a bimodal distribution of α-Co precipitates in a β-CoAl matrix.

178

2×10^{16} ions/cm^2 at 150 keV and for Co were 5×10^{16} ions/cm^2 at 150 keV. The mean range of the Y ions was 29 nm which gave an average Y concentration of 2 wt.% in the implanted region. The mean range of Co ions was 42 nm. The higher dose of Co ions was used so that the two implantations produced approximately the same amount of displacement damage in the near surface region of the specimens.

2.3 Oxidation Experiments

Oxidation experiments were performed in either dry air or an Ar-20% O_2 mixture with the samples rapidly inserted into and withdrawn from a pre-heated horizontal tube furnace so as tominimize heat-up and cool-down times. Most of the oxidation experiments were performed at 700°C to provide a comparison with the hot corrosion experiments but a few were also run at 850°C and 1000°C. Oxidation times at 700°C ranged from 10m to 96h.

The initial study of oxide structure and morphology was conducted on the cast CoCrAlY alloy oxidized in air at 700°C[7]. The specimens were jet-electrolytically thinned from one side leaving intact an electron transparent oxide film supported by the metal specimen. TEM observations of the film showed the oxide to be thicker over the α-Co solid solution phase. The oxides over both phases were very fine grained with diameters of 10-100 nm. Electron diffraction patterns of the oxide over the β-phase showed it to be predominately γ-Al$_2$O$_3$ while that over the α-phase was a mixture of cubic Spinels, most likely Co$_2$CrO$_4$ and CoCr$_2$O$_4$. Composition of the metallic elements, sampled in a 20 nm diameter area by EDS, showed wide variations in composition across both oxide regions. The average through thickness composition of Al in the thin oxide over the β-CoAl phase showed up to 85 at.% Al while that of the thick oxide over the α-Co phase was as low as 10 at.% Al. No Y was detected in the oxide films although yttrium rich pegs extending into the metal were observed to form on pre-existing yttride precipitates.

CoCrAl alloys oxidized under similar conditions in a subsequent experiment[8] showed the same features except for the pegs. The oxide regions in the CoCrAl were easier to characterize because the primary α-phase precipitates were larger and had no fine scale α precipitates from the low temperature aging treatment. The Y implanted CoCrAl sample did show different behavior in that EDS showed the Y to be uniformly distributed in the oxides formed over both phases and electron diffraction showed the presence of Y$_2$O$_3$ in the oxide films.

179

One of the most striking features observed in these oxidation experiments was the formation of voids at the metal-oxide interface. TEM and SEM observations of the metal-oxide surface back thinned from the metal side and TEM observations of stripped films showed the voids to be located in the metal at the oxide-metal interface and extending into the metal. The voids were also readily visible when imaged with secondary electrons through thin oxide films on the specimen surface. This latter method also provided information on the distribution of the voids with respect to the alloy phases as illustrated in Fig 2b. Void size in the CoCrAl alloy was a strong function of time and temperature as can be seen in table 1.

TABLE 1 - AVERAGE VOID SIZE IN CoCrAlY
AFTER VARIOUS OXIDATION TREATMENTS

TIME	TEMPERATURE		
	700°C	850°C	1000°C
30m	100nm	600nm	1200nm
19h	500nm	----	----

The void distribution was also strongly influenced by the microstructure of the alloy, as can be seen in Fig 2b for the CoCrAl alloy. Void formation and growth occurs predominantly in the β-CoAl matrix and is particularly prominent along α-β interfaces with some precipitates completely outlined by voids. Yttrium implantation at a fluence of 2×10^{16} Y/cm^2 (~2 wt.%Y) had a profound effect on void nucleation as can be seen in Figure 2a where the left half of the figure was implanted with Y and the right half was masked from the beam. Void formation in the β-phase was completely suppressed although a few voids were still found along α-β boundaries as can be seen in Figure 2c. Suppression of void formation by Y implantation has been observed at times up to 96h at 700°C. Cobalt implantation to a fluence of 5×10^{16} ions/cm^2 was also performed to evaluate the influence of the defects produced by ion damage on the nucleation of voids. The results are shown in Figure 2d after 1h oxidation at 700°C. Void formation in the β-phase is not suppressed but the voids nucleate on a finer scale and are more numerous. This can be rationalized on the basis of the defects introduced by implantation assisting nucleation of the interfacial voids. A more surprising observation is that void formation at the α-β interface is suppressed in the Co implanted alloy.

180

Quantitative measurements of oxide growth rate were made on the CoCrAl alloy using Auger electron spectroscopy (AES) with profiling and Rutherford backscattering spectroscopy (RBS). The AES results in Table 2 provide a relative measure of oxide thickness in terms of the time required to sputter through the oxide to the metal surface. Thickness ratios calculated from the data in Table 2 were as follows: $\beta + Y^+/\beta = 2.27$ for 10m and 1.96 after 60m, $\alpha + Y^+/\alpha = 2.17$ after 60m. The α/β ratio is not considered to be reliable because of the differences in the sputtering rate of the two oxides. Preliminary measurements using electron energy loss measurements in the oxide film indicate the α/β ratio may be as large as 2. Absolute measurements of the oxide film thickness over the β phase were made using RBS measurements. The concentration of oxygen atoms in the oxide layer was determined from the magnitude of the energy shift in the Co edge of the RBS spectrum using the assumption that the β-phase oxide was as thin as or thinner than
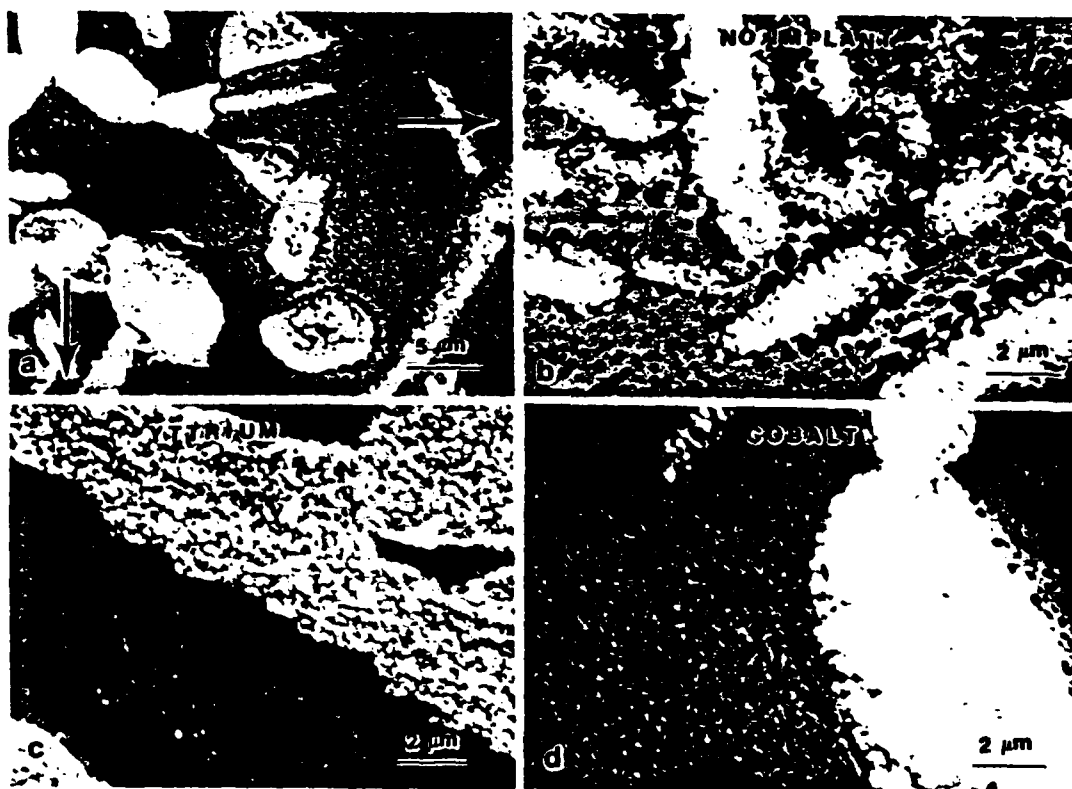

Fig. 2. Void formation produced by 1h oxidation of Co–22Cr–11Al alloys at 700°C: a) boundary region between non-implanted (right) and Y implanted (left) b) non-implanted c) implanted with 2×10^{16} Y/cm^2 d) implanted with 5×10^{16} Co/cm^2.

181

the α-phase oxide and that its density was that of α-Al_2O_3. The results are summarized in Table 3 for oxidation at 700°C for times from 10 m to 96 h. Thickness ratios were as follows: $\beta + Y^+/\beta$ = 2.1 for 10m, 2.0 for 1h, 2.2 for 8.5h, and 1.6 for 96h; $\beta + Co^+/\beta$ = 1.1 for 1h and also for 96h. The RBS and AES results show good agreement for the β-phase ratios.

Composition profiles in the oxide and near-surface substrate regions were obtained from changes in Auger line intensity as the surface region was profiled by sputtering. Profiles were measured on the α and β-phase oxides of the CoCrAlY alloy after 1h oxidation at 700°C using a Physical Electronics Inc. PHI 600 and on α and β-phase oxides of CoCrAl and Y implanted CoCrAl oxidized for 10m at 700°C using a JEOL JAMP-10. The CoCrAlY profiles are presented in the form of at.% concentrations vs. sputtering time while the CoCrAl profiles are presented as relative intensity curves for each element, normalized so that the maximum oxygen intensity was 1.0 and the other elements further scaled by the factors designated on the plots.

TABLE 2 - RELATIVE OXIDE THICKNESS AFTER 700°C OXIDATION OF CO-22Cr-11Al AS DETERMINED BY AUGER PROFILING

OXIDATION TIME(m)	SUBSTRATE MATERIAL	SPUTTERING TIME(m)
10	β	11
10	$\beta+Y$	25
60	β	14.3
60	$\beta+Y$	28
60	α	18
60	$\alpha+Y$	39

TABLE 3 - OXYGEN ATOM CONCENTRATION (N_o x10^{17} ATOMS/CM²) ON β-PHASE AS DETERMINED FROM RUTHERFORD BACK-SCATTERING SPECTRA

MATERIAL	TIME AT 700°C			
	10m	1h	8.5h	96h
CoCrAlY	1.7	--	3.8	--
CoCrAl	$\begin{cases} 2.1 \\ 1.5 \\ 1.6 \end{cases}$	3.0	3.6	7.2
CoCrAl +Y	$\begin{cases} 3.8 \\ 3.3 \end{cases}$	6.0	8.0	11.4
CoCrAl +Co	--	3.4	--	8.0

The profiles for CoCrAlY after 1h at 700°C are shown in Figure 3 a, b and c. The oxygen profiles in Figure 3a show that in the region selected for sampling the oxides were nearly identical in thickness, assuming the sputtering rate was equal for the two oxides, although other measurements have shown the α-phase oxide to be 1.5 to 2.0 times thicker. A comparison of Figure 3b and 3c shows some significant differences in the elemental distribution of all 3 metallic elements. Al is most prominent in the β-phase oxide in agreement with its identification as γ-Al_2O_3. The mixed oxides over the α-phase show non-uniform profiles with Co slightly enriched at the surface, Cr peaked in the center of the oxide and Al relatively constant. Co and Cr are enriched below the metal surface of the β-phase while Al is depleted in the sub-surface region.
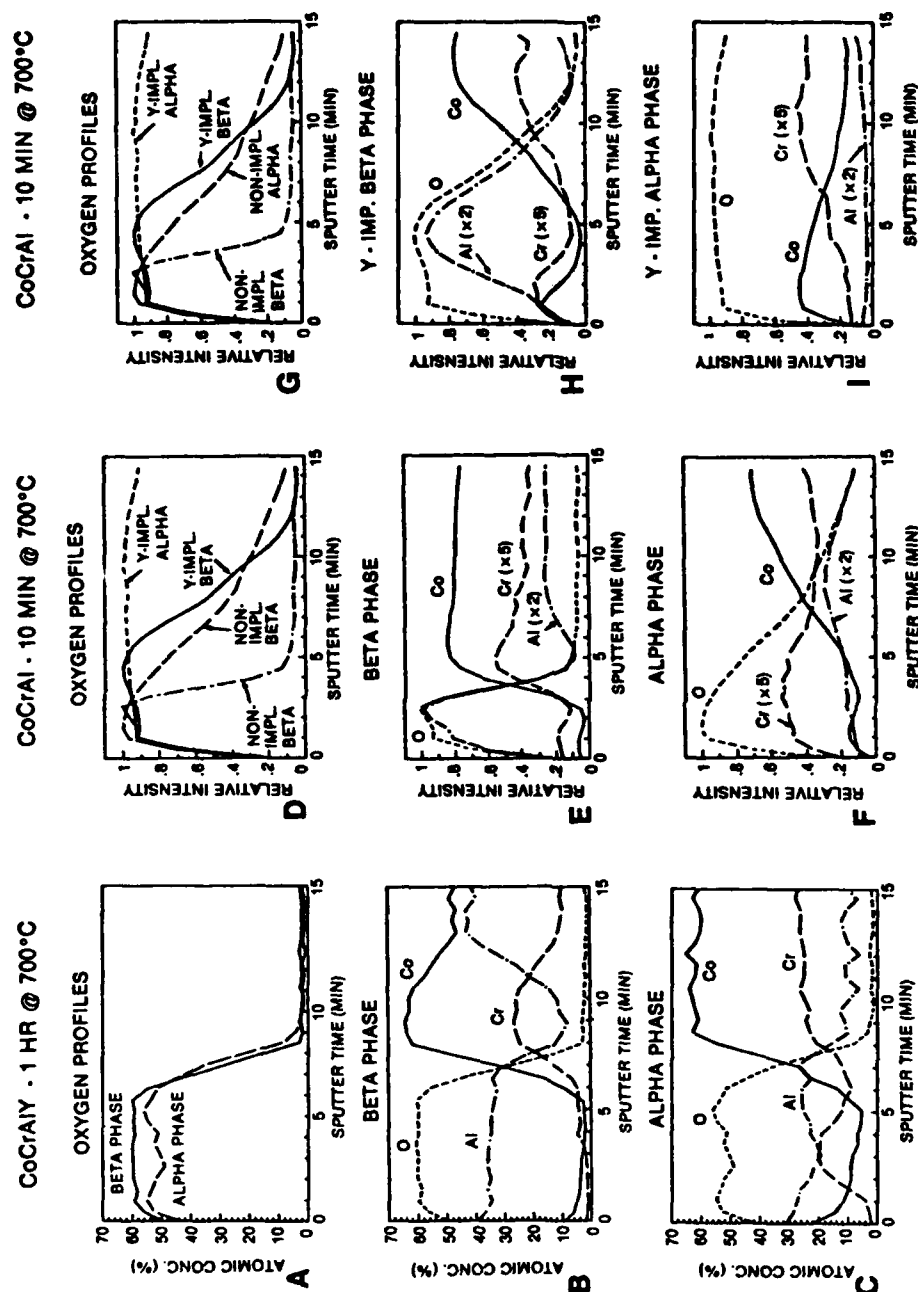
182

Fig. 3. Composition profiles determined by change in Auger line intensity while sputtering through the oxide and surface region of alloys.

The oxygen profiles for the four CoCrAl conditions after 10m at 700°C are shown in Figure 3d. In this case the difference in the α and β oxide thicknesses are readily apparent and the influence of the Y implant in doubling the oxide growth rate is also clearly illustrated. Figure 3e and 3f compare the metallic element profiles. The β-phase profile is similar to that for CoCrAlY with predominately Al in the oxide phase, Co and Cr enrichment in the sub-surface region and Al depletion in the same region. The α-phase profile shows a less sharply defined oxygen-metal interface than the β-phase (or the signal may be intergrated over oxide grains of varying thickness). Co shows a slight enrichment at the exterior surface and generally follows the inverse of the oxygen profile, while Al shows an increase in interface and subsurface regions.

The Y implanted specimens exhibit oxide growth rates double the rate of the unimplanted specimens. Figures 3h and 3i show the metallic element profiles. The Y implantation further accentuates the trends observed in the β-phase CoCrAl with Co and Cr enrichment at the metal-oxide interface and a marked depletion of the Al concentration at the interface. The Co is also noticeably enriched at the exterior surface. The oxide over the α-phase in the Y implanted sample was so thick that the interface region was not sampled during the sputtering. Co was found to be greatly enriched in the exterior half of the oxide coating with relatively low uniform concentrations of Cr and Al. The Cr and Al concentrations were increasing deeper in the oxide but the interface region was not reached. Complimentary measurements of composition profile by RBS confirmed the enrichment of Co in the outer surfaces of the Y implanted specimens but the area exposed to the beam was too large to provide separate information about the α and β-phase composition profiles. Analytical electron microscopy measurements of composition averaged through the oxide film thickness were consistent with the compositions measured by AES. In addition the analytical microscopy measurements showed that all the Y in the implanted specimen was contained in the oxide film.

2.4 Hot Corrosion Experiments

The hot corrosion exposures were performed at the University of Pittsburgh on the 10 mm x 2 mm coupons which were oxidized for one hour in air at 700°C, sprayed with a solution of Na_2SO_4 at 120°C and dried to a deposit of $1mg/cm^2$ Na_2SO_4. The specimens were then exposed to an atmosphere of O_2 and 100 ppm SO_2. The gases were passed over a platinum catalyst to establish the equilibrium SO_2/SO_3 partial pressures of $7x10^{-5}$ atm SO_3 and $3x10^{-5}$ atm SO_2 at 700°C. Metallographic preparation of the specimens prior to

exposure consisted of a polish through 0.05 μm alumina (U. of Pittsburgh) or 0.25 μm diamond polishing compound (NRL).

The specimens were examined by optical and SEM following the hot corrosion exposures to determine the morphology of the deposit. The samples were then immersed in boiling water to remove the deposits and the surfaces were again examined by the same techniques to determine the te of attack. Selected specimens were also cross-sectioned through the specimen and salt deposit and mounted for examination. These specimens were polished with boron carbide abrasive to avoid contamination with alumina and without lubrication to avoid dissolution of the salt deposit. Conventional SEM and EDS were used to identify the major constituents in the salt deposit.

One of the more obvious features of the hot corrosion attack of the CoCrAlY was the non-uniform distribution of the salt deposit over the α-Co phase precipitates as illustrated in Fig. 4 after a 30m exposure (9). The voids in the β-matrix and at the α-β interface were also readily visible. Another obvious feature of the observations is that the salt deposit over both the α and β-phases was molten at the exposure temperature of 700°C. Since the melting point of Na_2SO_4 is 884°C the presence of a liquid requires formation of a low melting eutectic with Co_2SO_4 or $Al_2(SO_4)_3$. Immersion of the specimens in boiling water removed the water soluble sulfates and revealed areas where the protective oxide film had been breached and attack of the substrate had begun. Fig. 5 shows several areas of attack where the film had been penetrated at pin holes and then undercut by lateral attack under the film. The severity of attack increased with time. The distribution of pin holes and their size after initial penetration was very similar to the distribution of yttride precipitates. The absence of yttride precipitates after hot corrosion attack strongly suggests this as the point of attack in CoCrAlY alloys. Analysis of the salt deposits on CoCrAlY specimens using EDS showed the deposits over the α-Co phase oxide contained Co, Cr and substantial amounts of Y while those over the β-phase contained much smaller amounts of Co.

The general features of the deposit morphology on the CoCrAl specimens were similar to the CoCrAlY results in that the deposit over the α-Co phase was thicker than that over the β-CoAl phase(9,11). Hot corrosion attack of the CoCrAl alloy had occurred after 15m exposure but the site of attack appeared to have shifted from the yttride precipitates to the larger voids along the α-β interface. Yttrium implanted CoCrAl was found to have a more accelerated form of hot corrosion attack as exhibited by the thicker deposits of salt over the α-phase, the extent of residue remaining after removal of the water soluble

sulfates and the severity of the attack. X-ray element maps of a metallographic section through the deposit and a region of hot corrosion attack showed the characteristic features of hot corrosion attack with Co leached from the metal surface and redistributed to the outer surface of the deposit, Cr and S enrichment in the corrosion pit, and Al fairly uniformly distributed through the deposit. Metallographic sections in the Y implanted region and the unimplanted region of the CoCrAl specimen are compared in Fig. 6 to show the severity of the attack in the two regions. The a and c panels show secondary electron images of the specimen and deposit with the corrosion sites labeled. The depth of penetration is substantially greater in the Y implanted sample. Panels b and d show the same areas of the specimen imaged with backscattered electrons to provide a better differentiation of phases. The β-CoAl phase is found to be the phase attacked most severely in both cases. The Co implanted CoCrAl specimen was subjected to the same series of examinations and found to have a slightly more accelerated attack than unimplanted CoCrAl. The α-phase oxide had larger salt deposits than the β-phase oxide but as noted previously the corrosion sites were at points where the film was penetrated over the β-phase and the β-phase showed the more severe attack.
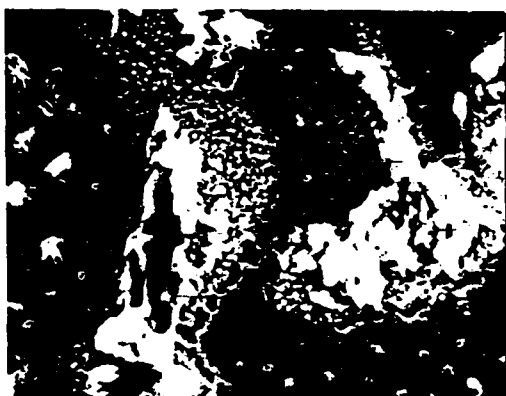

Fig. 4. Surface of CoCrAlY specimen after 30m exposure to hot corrosion conditions at 700°C showing build up of deposits over α-Co phase

Fig. 5. Surface of CoCrAlY specimen shown in Fig. 4 after washing in boiling water to remove soluble sulfates. Note holes where oxide film has been penetrated

3. DISCUSSION

The use of ion implantation to selectively introduce Y and Co into the surface region of CoCrAl alloys and the utilization of high resolution surface analytical techniques to characterize the surface has provided valuable insights into the early stages

186

Fig. 6. Cross-section through area under hot corrosion attack on CoCrA alloy. Panels a and b are non-implanted, c and d are Y-implanted specimen. Panels a and c imaged with secondary electrons, panels b and d are imaged with backscattered electrons. Note attack of β-CoAl phase.

of oxidation and hot corrosion of these overlay coating alloys. A general understanding of the processes occurring at 700°C has emerged from the study but a few crucial pieces of evidence needed to fully describe the mechanisms are still missing.

The oxide film formation observed on the various materials was found to be consistent with the theory of selective oxidation of alloys. The γ-Al_2O_3 film was the most stable oxide over the aluminum-rich β-phase in CoCrAl alloys at 700°C, so it formed at an early stage and suppressed formation of the other oxides. The lower Al concentration of the α-phase allowed other oxides to nucleate and initially grow more rapidlythan Al_2O_3. The concentration profile for Al in the α-phase oxide on the CoCrAl and CoCrAlY alloys indicates an increase in Al near the metal-oxide interface which would be consistent with a lateral spreading of Al_2O_3 on the surface. The Y implanted specimens showed changes in oxide growth rate and hot corrosion attack which suggest a modification of the oxide scale. Analytical electron microscopy evidence showed Y to be incorporated into the oxide and electron diffraction patterns showed it to be present as Y_2O_3. However crucial Y concentration profiles through the oxide layer are not available at this time and the grain structure of the oxide was too fine to resolve the distribution of Y_2O_3 grains in the oxide film with TEM. These results do show however that the distribution of Y is very important in oxidation and hot corrosion behavior.The cast CoCrAlY alloy had the bulk of the Y in the form of yttride precipitates which were widely spaced in grain boundaries, had little effect on oxidation, had no obvious effect on void formation and served as points at which the oxide film was breached in hot corrosion. The Y implanted specimens had a thin uniform layer of Y, either as isolated atoms or as small precipitates, which doubled the oxide growth rate, suppressed void formation and accelerated hot corrosion attack. Thus heat treatment and processing conditions are important parameters in assessing the role of active elements on oxidation and hot corrosion. Future experiments will examine PVD and plasma spray coatings.

Void formation at the metal-oxide interface is another phenomenon of considerable interest and importance to scale adherence that has been addressed in this study. The dependence of void size on time and temperature supports a diffusional process as the origin of the effect. The composition profiles through the β-phase oxides of CoCrAlY and CoCrAl show a depletion of Al in the sub-surface region which provides a source of vacancies from the Kirkendall effect. Nucleation of the voids would then occur at the lowest energy site, the metal-oxide interface and in particular the α-β phase boundary —

188

oxide intersection. The composition profiles through the α-phase, where very little void formation was observed, show little or no depletion of metallic elements in the surface region. The effectiveness of Y in suppressing void formation in the implanted CoCrAl alloy is readily apparent but the mechanism of the action is still in question. Yttrium concentration profiles unfortunately could not be obtained as part of the experiments reported here. Evidence from analytical electron microscopy of the foils indicates the Y was incorporated in the oxide but the exact distribution is unknown. The Al concentration profiles of the Y implanted β-phase showed a broader depletion trough but this might simply reflect a greater variation in thickness of the oxide grains in the region being profiled. The Co implant showed that radiation damage per se did not suppress void formation although the number of sites at which nucleation occurred was increased. Whittle and Stringer (3) suggest that the mechanism by which active elements influence void nucleation is either as individual atoms or as dispersed internal oxides that serve as nucleation sites for voids, thus increasing the number of sites and moving the sites from the metal-oxide interface. The present results are not inconsistent with this hypothesis.

The suppression of void formation by the Y implantation clearly has important implications for improving oxide scale adherence. The increase in growth rate of the β-phase oxide film after Y implantation may also be related to the absence ofvoids. If oxide growth rate is controlled by transfer of Al atoms across the metal-oxide interface, then the presence of voids at the interface will reduce the diffusional flux in proportion to the cross-sectional area of the voids. The elimination of voids would thus increase the growth rate of the oxide over the β-phase although it does not explain the increased growth rate over the α-phase.

The model of hot corrosion operative on CoCrAl and CoCrAlY alloys(4) involves a reaction of the Na_2SO_4 solid deposit with $CoSO_4$ to form a low melting point eutectic liquid. The protective oxides are then dissolved in the melt by basic or acidic fluxing reactions depending on the SO_3 partial pressure at the oxide-melt interface. The observation that the salt is preferentially distributed over the α-phase is consistent with the higher Co content in the α-phase oxide since Co dissolves and readily forms $CoSO_4$ in the SO_3 partial pressures used in this experiment. Once the preformed oxide scale is breached, the underlying alloy is attacked rapidly as pits deepen and spread laterally under the scale. In this propagation stage the O_2 and SO_3 partial pressures change as a function of the depth in the deposit. Thus fluxing reactions dissolve Co oxides in particular and transport them to the surface of the melt

189

where they then oxidize again and form the Co rich, water insoluble deposits observed over the α-phase.

The experiments did provide new insight into the events leading to the transition from initiation stage to propagation stage and the role of Y in hot corrosion attack. The observation that penetration of the oxide film on CoCrAlY occurred at pin holes left by the dissolution of yttride protrusions (or the oxidized surface layer on the yttride protrusions) is significant. These observations are consistent with recent results by Jones[12] which showed that Y_2O_3 readily forms a sulfate under SO_3 partial pressures as low as 5×10^{-5} atm and that it forms a eutectic with Na_2SO_4 at about 25% $Y_2(SO_4)_3$ which melts between 750 and 800°C. Ternary mixtures with Na_2SO_4 and $CoSO_4$ with melting points below 700°C probably exist. Deanhardt and Stern[13] have shown the solubility minimum for Y_2O_3 in Na_2SO_4 at 927°C is at Na_2O activity of 10^{-10} ($P_{SO_3} \sim 10^{-6}$) with greater solubility at the pressures of this experiment. The rapid attack of the Y implanted CoCrAl can also be rationalized if Y was present in the oxide films as Y_2O_3. An alternative mechanism for the accelerated hot corrosion attack of the Y implanted CoCrAl is that the enrichment of Co in the exterior surface of both the α and β-phase oxides, which was seen in the composition profiles, increases the rate and extent of eutectic formation. The mechanism of Co enrichment on the exterior surface of the oxide is unknown. Further work will be required to establish which of these mechanisms is dominant.

Finally the more severe attack of the β-phase in the propagation stage is consistent with previous observations of alloy compositional effects. The high Al and low Cr content of the β-CoAl phase make it more susceptible to attack under the conditions of this experiment. Stroud and Rapp have shown that Al_2O_3 has a solubility minimum at $P_{SO_3} \sim 10^{-8}$ atm while Cr_2O_3 has a minimum at $P_{SO_3} \sim 10^{-3}$ atm[14].
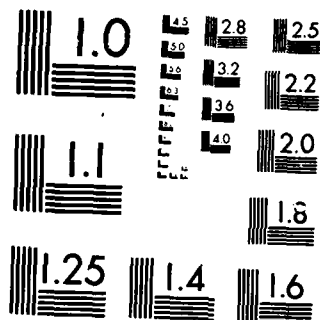
MICROCOPY RESOLUTION TEST CHART

NATIONAL BUREAU OF STANDARDS 1963 A

REFERENCES

(1) Pettit, F.S., "Design of Structural Alloys With High Temperature Corrosion Resistance" in, Fundamental Aspects of Structural Alloy Design by R.I. Jaffee and B.A. Wilcox, Plenum, NY (1977) p. 597

(2) Proceedings of 1974 Gas Turbine Materials in the Marine Environment Conference, MCIC Report MCIC 75-27 (1975).

(3) Whittle, D.P. and Stringer, J. "Improvements in High Temperature Oxidation Resistance by Additions of Reactive Elements or Oxide Dispersions," Phil. Trans. R. Soc. London, A295, pp. 309-329, 1980.

(4) Giggins, C.S. and Pettit, F.S. "Corrosion of Metals and Alloys in Mixed Gas Environments at Elevated Temperatures," Oxidation of Metals 14, pp. 363-413, 1980.

(5) Dearnaley, G., "Thermal Oxidation" in Treatise on Materials Science and Technology: Vol. 18, Ion Implantation ed. by J.K. Hirvonen, Academic Press, NY (1980), pp. 257-320.

(6) Bennett, M.J., "The Role of Ion-Implantation in High Temperature Oxidation Studies," paper presented at NACE Int. Conf. on High Temperature Corrosion, San Diego, CA March 1981, also available as AERE-R10082, UKAEA, Harwell Feb. 1981.

(7) Sprague. J.A., Provenzano, V., and Smidt, Jr., F.A., "Initial Stages of Oxide Formation on a CoCrAlY Alloy at 700°C," Thin Solid Films, 95, pp 57-64, 1982.

(8) Sprague, J A., Johnston, G.R., Smidt, Jr., F.A., Hwang, S.Y., Meier, G.H., Pettit, F.S., "Oxidation of CoCrAlY and Y-Implanted CoCrAl Alloys,"in High Temperature Protective Coatings ed. by S.C. Singhal, Metallurgical Soc. of AIME, Warrendale, PA (1982), pp. 93-103.

(9) Hwang, S.Y., Meier, G.H., Pettit, F.S., Johnston, G.R., Provenzano, V., and Smidt, Jr., F.A., "The Initial Stages of Hot Corrosion Attack of CoCrAlY Alloys at 700°C," in High Temperature Protective Coatings ed by S.C. Singhal, Metallurgical Soc. of AIME, Warrendale, PA (1982), pp. 121-134.

(10) Johnston, G.R., Sprague, J.A., Singer, I.L. and Gossett, C.R., "The Characterization of Complex Oxide Scales on CoCrAlY and Ion-Implanted CoCrAl Alloys," presented at 5th Australian Conf. on X-ray Analysis with Sessions on Surface Analysis, Melbourne, 15-20 May 1983, to be published.

191

(11) Provenzano, V., Johnston, G.R. and Sprague, J.A., The Effects of Ion Implantation on the Initial Stages of Hot Corrosion Attack of a Cast Co22Cr11Al at 700°C," presented at 1983 Metallurgical Coatings Conference, SanDiego, CA, to be published.

(12) Jones, R.L., private communication 1983.

(13) Deanhardt, M.L. and Stern, K.H., J. Electrochem. Soc. $\underline{129}$, pp. 2228-2232, 1982.

(14) Stroud, W.P and Rapp, R.A., "The Solubilities of Cr_2O_3 and $\alpha-Al_2O_3$ in Fused Na_2SO_4 at 1200°K," $\underline{Proc.}$ $\underline{Symp.\ on\ High\ Temperature\ Metal\ Halide\ Chemistry}$, ed. by D.L. Hildenbrand and D.D. Cubicciotti, Electrochem Soc. (1978) p. 574.

192

Section IV.A

INFRARED PROPERTIES OF HEAVILY IMPLANTED SILICON, GERMANIUM AND GALLIUM ARSENIDE

W.G. Spitzer, L. Liou, K-W. Wang and C.N. Waddell[1]
G.K. Hubler[2]
S.I. Kwun[3]

[1]Departments of Materials Science and Physics
University of Southern California
Los Angeles, CA 90089-0241

[2]Materials Modification & Analysis Branch
Condensed Matter & Radiation Sciences Division
Naval Research Laboratory

[3]Department of Physics
Seoul National University
Seoul 151, Korea

Infrared properties of heavily implanted silicon, germanium and gallium arsenide

William G. Spitzer, Lihyeh Liou, Kou-Wei Wang and Charles N. Waddell

Departments of Materials Science and Physics, University of Southern California
Vivian Hall of Engineering 602, Los Angeles, CA 90089-0241

Graham Hubler

Naval Research Laboratory
Washington, DC 20375

and

Sook-Il Kwun

Department of Physics, Seoul National University
Seoul 151, Korea

Abstract

A review of the techniques developed for using infrared reflection spectroscopy to study properties of heavily implanted semiconductors is presented. Several structural models are considered and calculations based on them are applied to measurements of implanted Si, Ge and GaAs. These comparisons of model calculations and measured spectra show how a number of important physical parameters can be obtained as well as new information concerning implantation-induced amorphous material.

Introduction

There have been many studies of the properties of amorphous semiconductors produced by high fluence ion implantation. Most of these studies have emphasized the use of experimental techniques such as ion channeling, backscattering, electron microscopy, electron paramagnetic resonance, electrical transport measurements (particularly for material being recrystallized), etc. The study of amorphous material produced by the ion implantation of single crystal samples is attractive because, if done under proper conditions, the amorphous layer is essentially free of macroscopic voids, the amorphous-crystalline interface is expected to be relatively free of contaminants, and the influence of specific impurities can be investigated by using different ions for the implantation. These advantages have been exploited in a number of important experiments on amorphous materials by several groups of investigators such as those of J. Mayer[*], M. Nicolet, and co-workers[1] (California Institute of Technology), J. F. Gibbons and co-workers[2] (Stanford University) and D. K. Sadana, J. Washburn and co-workers[3] (UC Berkeley), as well as others. In recent years several experiments have indicated that measurements of the infrared dielectric properties can also make a significant contribution to the knowledge and understanding of amorphous semiconductors.[4-13] For example, it has been found that previously unknown metastable states[11] can be demonstrated by the infrared work and, when coupled with the other types of measurements mentioned previously, one can develop an improved appreciation of the processes involved in the annealing-induced changes of the amorphous material.[14,15] Much of this infrared work is still in process and it is the primary purpose of this paper to review the progress of the infrared research. Most of the work reviewed here is that of the present authors and some additional colleagues. This is not because we believe that our work is in some manner superior, but rather it is a reflection of the fact that there are very few investigators involved in these types of studies.

General concepts and models

It has been known for some time that, when samples of Si, GaAs, GaP, etc. are implanted under conditions such as to produce a heavily damaged or amorphous surface layer, the infrared reflection (transmission) as a function of frequency has interference fringes.[4-6] The fringes in the reflection arise from the presence of two reflecting boundaries (the back surface of the sample is heavily ground so as to be a diffuse scatterer), i.e. the front air-amorphous interface and the amorphous-crystalline interface. In the simplest case, that of a macroscopically homogeneous and non-absorbing amorphous layer of uniform thickness and with a sharp interface between the amorphous and crystalline materials (interface width << wavelength of the radiation in the material), the fringe pattern is of simple

[*]now at Cornell University

194

character, i.e. fringes of essentially constant amplitude and uniform frequency spacing. If the amorphous layer does not extend to the front surface but is buried under a damaged but crystalline surface layer or if there is an essentially uniform heavily damaged layer between the amorphous layer and crystalline substrate, then the fringes become more complicated with "beat-like" and "carrier wave-like" patterns.

In the simplest case mentioned above the infrared refractive indices of the semiconductors are generally between 3 and 4 while the change $\frac{\Delta n}{n}$ between the undamaged crystalline and amorphous states is generally between 10 and 15% with the amorphous value being larger. Therefore the reflected amplitude at the air-amorphous interface, $(1-n_a)/(1+n_a)$, is much larger in magnitude than the reflected amplitude at the amorphous-crystalline interface, $(n_a-n_c)/(n_a+n_c)$, which results in fringes having small amplitudes in the reflection intensity. Because of the difficulty of making sufficiently accurate reflection measurements to permit quantitative analysis, most of the early work simply measured the mean frequency interval, $\Delta\nu$, between adjacent fringe oscillations and used the standard expression, $t = 1/[2n_a(\Delta\nu)]$, where ν is wave number, to determine the layer thickness, t. If one measures the reflection to an accuracy of about 0.2% reflection, e.g. R = 0.340+0.002, then the refractive indices can be deduced to an accuracy of approximately two in the third significant figure, e.g. n = 3.80+0.02. Because the refractive index is a function of the damage state of the material, it will be shown such measurements can yield considerable information concerning the macrostructure of the amorphous layer and changes in the properties of amorphous material produced by the thermal annealing.

We first show some computer generated curves for several different geometries which illustrate the predicted behavior of samples having amorphous layers. In these examples optical parameters essentially appropriate to Si are employed to insure the illustrations are realistic and to facilitate comparisons to measurements. The details of the computer calculations have been described elsewhere[10,12], and therefore, we will make the present discussion brief. For a given model of the depth dependence of the dielectric constant, the calculation employs the thin-film equations of Heavens[16]. A computer code calculates the reflection for an arbitrary number of uniform layers of specified refractive index (n), extinction coefficient (k), and thickness. At each frequency these quantities are calculated from Sellmeir-type equations for the refractive indices, and where appropriate, the plasma (carrier) contribution to the dielectric constant is also included.[16] For the frequency range covered here, the measured extinction coefficient is sometimes found to have only a small effect on the fringes and can be taken to be zero, i.e. Si and GaAs, while in another case it has a significant role in damping of the fringe amplitude, i.e. Ge. In regions where the refractive index is changing rapidly with depth, e.g. the transition layers or where the carrier density is changing, the region is divided into a number of layers, each layer having uniform properties. The layer thicknesses in such a case are typically $\sigma/10$, where σ is the standard deviation of the Gaussian approximating the change. A detailed account of procedure, including the sensitivity of the calculated reflection to variations in each of the model parameters, is available in a previously published work.[16]

The simple model of a homogeneously damaged layer on a substrate is illustrated in Fig. 1. The term substrate refers to the portion of the sample beyond the region damaged by the implantation. The figure shows the n and k values at a given frequency. The frequency dependence of each of the refractive index portions, D for the damaged region and s for the substrate, is given by a dispersion equation

$$n_{D,s}^2 = A_{D,s} + \frac{B_{D,s}}{\Omega_{D,s}^2 - \nu^2} \, ,$$

while the frequency dependence of k is obtained directly from transmission measurements. The two uniform regions are connected smoothly by a half-Gaussian of standard deviation σ_D which represents the transition region. Figure 2 shows the calculated reflection for the dispersion parameters indicated and for the assumptions $k_D(\nu) = 0$ and $\sigma_D = 0$. Several points of interest are illustrated by this figure. As expected the small change in n at the damage-substrate interface relative to $n_D - 1$ means the fringes are small in amplitude. The smooth curve joining the fringe minima is the reflection curve one would have if there were no damaged layer,[17] i.e. $R_s(\nu) = \{[n_s(\nu) - 1]/[n_s(\nu) + 1]\}^2$, where n_s is the refractive index for the substrate. At frequencies other than at the minima the reflection is larger than $R_s(\nu)$ because $n_D > n_s$ and the mean or average reflection curve is given by $R = \{[n_s(\nu) - 1]/[n_s(\nu) + 1]\}^2$. As will be shown there are cases in which this simple interference spectrum is indeed observed, and in such cases the values of R_D, n_D and n_s are obtained directly. If the model is correct, n_s should equal n_c, the refractive index of undamaged crystalline material. One expects R_D to be related to R_p, the projected range of the implanted ions. If one has previously established the value of n_a, the refractive index of as-implanted, amorphous material (assuming a unique value exists), then the value of n_D obtained will indicate whether a continuous amorphous layer has been formed.

The simple model used for the calculation of Fig. 2 can now be altered in several ways. Elimination of the assumption $\sigma_D = 0$ is illustrated in Fig. 3 for three different σ_D values. To simplify the result, dispersion has been omitted in this calculation, i.e. n_D and n_s are assumed to be frequency independent. Changes in the layer thickness, R_D, will alter the spacing, $\Delta\nu$, but will not influence the attenuation of the amplitude in these cases. Two other models are illustrated in Fig. 4 along with the calculated reflection curves. The second case, called (b), is of special interest as the assumed curve for $n_D(\nu)$ approximates the nuclear scattering energy deposition per ions per unit depth curve for ions (2.7 MeV ions of P^+) incident on a Si sample.[6] In both examples the reflection drops well below the value of R_s given by the dashed curves. The remaining case for a single layer with absorption on a non-absorbing substrate will be discussed in the sections on Si and Ge.

It is also instructive to consider the case for two layers on a substrate. Examples requiring this type of model would be ion-implanted samples in which (a) there is a buried amorphous layer covered by a damaged but crystalline layer or (b) an amorphous surface layer followed by an essentially uniform, heavily damaged layer and then the substrate. Sample cases are calculated and shown in Fig. 5, where the thicknesses of the two layers are very different and the parameters used are given in the caption. The two cases differ in the sequence of the thick and thin layers. They give very different spectra and are easily distinguished from one another.

The last case to be considered in this generalized section is the one in which free carriers are produced as a result of annealing the ion-implanted samples, such as is observed in P^+-implanted Si and Be^+-implanted GaAs. In such cases the complex dielectric constant must be modified to include a plasma term, and the calculation becomes more complicated – again the details have been given previously.[10] The effect is illustrated in Fig. 6. The model assumes an amorphous or damaged layer of total thickness R_T and a Gaussian transition interface between n_D and n_s. The lower figures show the sample in three different anneal stages. In each case it is assumed that some of the damaged (amorphous) material has recrystallized epitaxially, and the carriers are generated only in the recrystallized region. It is further assumed that the lattice contribution to the dielectric constant may not completely recover to give $\epsilon = n_s^2$ in the recrystallized region. This remaining difference is due to the presence of residual damage, and thus, for the recrystallized material, we use $n_R = f_R n_s$, where $f_R > 1.0$ is an adjustable fitting parameter. Another possible complication introduced is that the implanted ion distribution and hence the generated carrier distribution may not have a simple Gaussian shape for its depth dependence. Two half-Gaussians having different σ values are joined at their peaks as shown by the N curve in the figure.[18] The calculated reflection for each case is given by the solid curves. The points are the measured reflection data for a 2.7 MeV, P^+ implanted, <111> Si sample, where the P^+ ion fluence is 1.7×10^{16} cm^{-2} and the anneal stages are as indicated in the figure caption. All of the assumptions mentioned above were necessary in order to obtain the fit to the data as shown in Fig. 6.

Experimental results and discussion

Silicon

The data points and fitted reflection curves for two implanted Si samples are shown in Figs. 7(a) and 7(b). The 7(a) sample was implanted at room temperature with 1.0×10^{16} P^+ ions/cm^2 with an incident energy of 300 keV/ion. Only a portion of the measured data points are shown for 7(b) in order to avoid confusion in the figure. This sample was also P^+ ion-implanted but at 200 K with 1.7×10^{16} ions/cm^2 of 2.7 MeV/ion incident energy. Several characteristics are immediately apparent by inspection and comparison of the data for these two samples: (i) The primary difference in the data sets is in the frequency spacings of the fringes--not the amplitudes nor the absolute reflection values; (ii) The mean reflection values are essentially the same indicating the $n_D(\nu)$ for the damaged (amorphous) layers are the same; (iii) The minima for both sets at the lower frequencies lie close to the reflectivity curve expected for crystalline Si: (iv) Both data sets show similar attenuation of the fringe amplitudes at the higher frequencies. The similarities noted are in spite of a substantial difference in fluence, almost an order of magnitude difference in incident ion energy and a $\Delta T \sim 100K$ in the sample implantation temperature. In both cases the dashed curves are calculated by using the simple single layer model with $\sigma_D + k_D \approx 0$. The solid curves of Fig. 7 are for $\sigma_D = 0$ and k_D given by measurements reported for sputtered layers[1] of amorphous Si (a-Si). Later measurements of k_D for a-Si layers formed by implantation[6,15] gave $k_D \sim 4 \times 10^{-14} \nu^3$ which is very similar to the curve for the sputtered material. The essential point in the solid curve calculations is that the amorphous layer of 7(b) is about 5 times the thickness of that for 7(a)-- 2.52 µm vs. 0.5 µm, respectively as deduced from fitting the data--with the result that a $k_D(\nu)$ curve required to produce the observed damping of 7(b) would be completely inadequate for the data of 7(a). A good fit to the data for both samples is obtained if one assumes $k_D(\nu) = 0$ and $\sigma_D = 0.044$ µm (for 7(a)) and 0.041 µm (for 7(b)).

The refractive indices used to obtain the good fits for these and a number of other
implanted samples are shown in Fig. 8, where the $n_D(\nu)$ is the average obtained of best fits
for several samples. The error bars indicate the standard deviation. The $n_{crystalline}(\nu)$
curve is used as a given parameter in the fitting process and this curve is obtained by an
independent fit of the Sellmeier equation to the prism data of Salzburg and Villa[16,17]. The
Sellmeier parameters for both $n_D(\nu)$ and $n_{crystalline}(\nu)$ are given in the figure caption.
Additional measurements have been reported recently which indicate that the $n_D(\nu)$ curve
applies for all implantation-produced amorphous layers, independent of the implanted ion
species[15] (same for ^{12}C, [29]Si, [120]Sn), the fluence (for an order of magnitude change for
both [29]Si and ^{31}P), the incident ion energy (200 keV to 2.7 MeV) and implantation tempera-
ture (77K to 300K). We therefore conclude that this amorphous material is in a defineable
thermodynamic state referred to hereafter as a-Si-I. This conclusion is supported by recent
measurements[18,15] which indicate that the density change for C-Si → a-Si-I, the EPR measured
"dangling bond" spin densities and the absorption edges are independent of the implantation
parameters in those cases where comparisons are made.

An interesting effect is observed when the as-implanted a-Si-I is thermally (furnace)
annealed. It is generally known from channeling measurements of ion implanted samples that
the amorphous Si usually recrystallizes by epitaxial regrowth from the substrate, if the
implantation produced amorphous material up to the top sample surface. However, it was not
appreciated that the a-Si-I undergoes a change with annealing to a new state, called a-Si-II,
prior to recrystallization. This change is illustrated in Fig. 9 for a [29]Si-implanted Si
sample (380 keV/ion and fluence = 0.5 x 10^{16} ions/cm^2). The initial measurements of sample
A, prior to annealing, are shown by the data points and comparison with Fig. 7 indicates
that a $n_D(\nu)$ curve like that given in Fig. 8 will produce a good fit. The data points for
the measurements after annealing for 2 h and 12 h at 500°C are not shown but rather repre-
sented by smooth curves drawn through them. Several of the characteristics of the anneal-
ing-induced changes are apparent in this figure and are as follows: (i) Annealing at 500°C
results in a substantial decrease in the refractive index of the a-Si-I layer. (ii) There
is no change in the value of the index as a result of extending the annealing time from 2 h
to 12 h. (iii) Annealing removed the high frequency attenuation of the fringes. (iv) A sim-
ple single layer on a substrate is the appropriate model for both annealing measurements.
(v) Regrowth is apparent in the 500°C-12 h annealing curve. The refractive index in the
anneal-stabilized state, a-Si-II, is shown in Fig. 8 by the $n_D'(\nu)$ curve. For comparison,
the crosses in Fig. 8 give the values of the refractive index of a-Si produced by pyrolytic
decomposition of silane onto quartz substrates[19] at T = 590°C. The values compare very well
with those for a-Si-II. Also it is noted from Fig. 8 that $[n_D'(\nu)]/[n_D(\nu)] = 0.96$ for all ν
and that $n_c(\nu)/n_D(\nu) = 0.89$. Further measurements have shown that the 0.96 value is also
independent of all implantation parameters, i.e. fluence, ion mass, ion energy, temperature
of implantation, and sample orientation. Moreover, the same value is obtained[15] for anneal-
ing temperatures between 400 and 600°C. It is also observed that the decrease of "dangling
bond" spin density (approximately a factor of 2) for a-Si-I → a-Si-II is largely independent
of ion mass.[15]

All of the above information suggests that there are two definable states for a-Si. The
transition from a-Si-I to a-Si-II results in a 4% decrease in refractive index and a signi-
ficant decrease in dangling bond density. The measured mass density charge resulting from
the transition is found to be too small for measurement[18,15] i.e. $\Delta\rho/\rho$ for c-Si → a-Si-I is
~ 0.02 and the change in $\Delta\rho/\rho$ for a-Si-I → a-Si-II is <0.005. It appears that there is a
network reorganization produced by annealing the a-Si which causes significant changes in
some of the physical properties.

Germanium

Although Ge has not been investigated as extensively as Si, the results obtained for
heavily [29]Si-implanted Ge samples are very similar to those just reviewed for Si samples.
Figure 10 shows measurements of a 380 keV/ion implanted sample, where the fluence was
1.0 x 10^{16} ions/cm^2 and implantation was done at 77K. The drop in refractive index for
a-Ge-I → a-Ge-II upon annealing at 250°C is apparent as is the reduction in layer thickness
via epitaxial regrowth with annealing at higher temperatures. From absorption studies it is
found that some of the attenuation in the fringe amplitude at higher frequencies in the as-
implanted case is due to the absorption in the a-Ge-I layer even for the thin layers dis-
cussed here. As in Si samples, isothermal measurements show that there is no evidence for a
change in $n_D'(\nu)$ with prolonged annealing once one reaches the a-Ge-II state, in this case at
300°C. Thus one again finds two metastable states, a-Ge-I and a-Ge-II. The refractive
index data for a series of samples is shown in Fig. 11 and the general similarity to the
Si case is apparent. Regrowth rates and their temperature dependencies as well as residual
plasma effects in the recrystallized material will be discussed in a future work.[20]

Gallium Arsenide

Gallium arsenide presents an interesting contrast to the discussions for Si and Ge given
above. Most of the infrared work done thus far has been for Be$^+$-ion implantations.

197

The $^9Be^+$ is a lighter ion than any used in the Si studies and it is generally observed that high fluence implantations at room temperature will not amorphize the implanted material. This effect is attributed to the much smaller nuclear scattering energy loss term for light ions. At low temperatures however, amorphous material is produced indicating that annealing effects are also involved at room temperature. This difference is seen very clearly in Fig. 12 which shows measurement results for two samples which had almost indentical implantation conditions except for the temperature, the upper data are for -100°C and the lower for room temperature. These two implantation temperatures lead to very different results and from our previous analyses, we can qualitatively anticipate the results of computer fitting. For the lower implantation temperature we clearly have a double layer on a substrate, where the structure consists of a thick, high refractive index layer on a thin, lower index layer and then the substrate which has the lowest index value (see Fig. 5). A different ordering of thicknesses or indices would produce a different interference pattern. Therefore, the likely physical structure is a thick amorphous layer covering a thin, probably heavily damaged, crystalline layer on the undamaged substrate. This view is supported by preliminary results of annealing experiments,[21] where it is observed that the top layer regrows, largely epitaxially, until the entire implanted region is of the heavily damaged type, and that this damaged region anneals back to the pre-implantation condition non-epitaxially but only at substantially higher annealing temperatures.

The lower curve of Fig. 12, which is for a room temperature implantation, is close to that for a single layer on a substrate but with a very large σ_D, i.e. a wide transition region. The refractive index of the top layer is very close to that found for the thin damaged but crystalline layer in the -100°C implanted sample. Thus, the results appear to be in qualitative agreement with our expectations.

Figure 13 shows the results of annealing a room temperature, Be^+-implanted sample. In this case the annealing for 2h at each temperature produces a non-epitaxial removal of the damage with essentially complete recovery to the pre-implantation reflectivity after annealing for 2h at 400°C. The behavior is similar to that described above for the -100°C implanted sample after the epitaxial regrowth of the amorphous region. It is of interest to note that there is no evidence of a plasma effect even though Be is an acceptor in conventionally grown GaAs. The plasma effect is observed only after prolonged annealing at 400°C or after annealing at higher temperatures as shown in Fig. 14. These results for GaAs suggest that removal of damage which produces changes in the dielectric properties and generation of carriers from the Be^+ ions may be different processes.[13]

Summary

The review of some of the infrared work done on ion-implanted samples of Si, Ge and GaAs indicate that these measurements can provide useful information which, in many cases, can be modeled directly into physical parameters of interest. Quantities such as layer thicknesses, widths of transition layers, carrier density profiles, regrowth rates, etc. are readily measurable non-destructively. The values of quantities deduced from the infrared measurements compare favorably with those deduced from other measurements.[6,9,10,12] The infrared measurements have also been instrumental in the recognition of the existence of two well-defined amorphous states for both Si and Ge.

References

1. See for example: J. W. Mayer, L. Erikson, and John A. Davis, Ion Implantation in Semiconductors (Academic Press, New York, 1970); L. Csepregi, J. W. Mayer, and T. W. Sigmon, Phys. Lett. A54, 157 (1975); M. G. Grimaldi, B. M. Paine, M. Mäenpää, M. A. Nicolet, and D. K. Sadana, Appl. Phys. Lett. 39, 70 (1981); and numerous other papers.
2. See for example: J. F. Gibbons, Handbook on Semiconductors (North-Holland Publishing Co., Edited by T. S. Moss, Vol. 3, edited by S. P. Keller, 1980) Chapter 10; W. S. Johnson and J. F. Gibbons, Projected Range Statistics in Semiconductors, 1970 (Stanford U. P., Stanford, California, 1970).
3. See for example: D. K. Sadana, M. Stratham, J. Washburn, C. W. Magee, M. Mäenpää, and G. R. Booker, Appl. Phys. Lett. 37, 615 (1980); D. K. Sadana, M. Stratham, J. Washburn, and G. R. Booker, J. Appl. Phys. 51, 5718 (1980); D. K. Sadana, J. Washburn, and G. R. Booker, Phil. Mag B, 611 (1982).
4. M. H. Brodsky, R. S. Title, K. Weiser, and G. D. Pettit, Phys. Rev. B1, 2632 (1970).
5. T. E. Seidel, G. A. Pasteur, and J.C.C. Tsai, Appl. Phys. Lett. 29, 648 (1976).
6. G. K. Hubler, C. N. Waddell, W. G. Spitzer, J. E. Fredrickson, S. Prussin and R. G. Wilson, J. Appl. Phys. 50, 3294 (1979).

7. W. G. Spitzer, J. S. Ko, C. N. Waddell, G. K. Hubler, and J. E. Fredrickson, J. Appl. Phys. $\underline{50}$, 3775 (1979).

8. Sook-Il Kwun, W. G. Spitzer, C. L. Anderson, H. L. Dunlap, and K. V. Vaidyanathan, J. Appl. Phys. $\underline{50}$, 6873 (1979).

9. W. Wesch and G. Gotz, Radiat. Eff. $\underline{49}$, 137 (1980).

10. G. K. Hubler, P. R. Malmberg, C. N. Waddell, W. G. Spitzer, J. E. Fredrickson, Radiat. Eff. $\underline{60}$, 35 (1982).

11. J. E. Fredrickson, C. N. Waddell, W. G. Spitzer, and G. K. Hubler, Appl. Phys. Lett. $\underline{40}$, 172 (1982).

12. C. N. Waddell, W. G. Spitzer, G. K. Hubler, and J. E. Fredrickson, J. Appl. Phys. $\underline{53}$, 5851 (1982).

13. Sook-Il Kwun, C.-H. Hong and W. G. Spitzer, J. Appl. Phys. $\underline{54}$, 3125 (1983).

14. W. G. Spitzer, G. K. Hubler, and T. A. Kennedy, Nucl. Inst. and Meth. $\underline{209/210}$, 309 (1983).

15. C. N. Waddell, W. G. Spitzer, J. E. Fredrickson, G. K. Hubler, and T. A. Kennedy (to be published).

16. O. S. Heavens, Optical Properties of Thin Solid Films, (Academic Press, New York, 1955).

17. C. D. Salzberg and J. J. Villa, J. Opt. Soc. $\underline{47}$, 244 (1957).

18. J. F. Gibbons and S. Mylroie, Appl. Phys. Lett. $\underline{22}$, 568 (1973).

19. M Janai, D. D. Allred, D. C. Booth, and B. O. Seraphin, Solar Energy Mat. $\underline{1}$, 11 (1979).

20. Kou-Wei Wang and W. G. Spitzer, unpublished work.

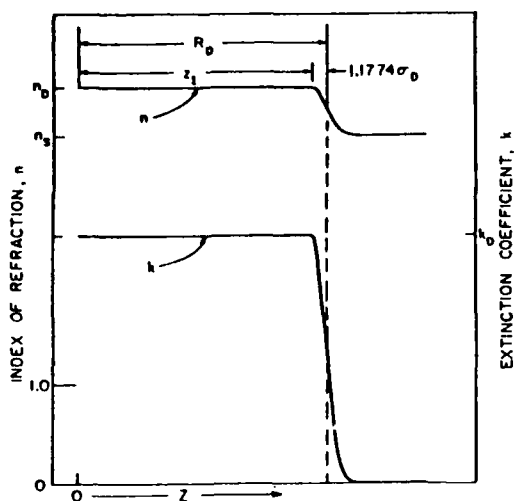21. L. Liou, Sook-Il Kwun and W. G. Spitzer, unpublished work.

Fig. 1 The refractive index and extinction coefficient vs depth for a homogeneously damaged implanted sample.
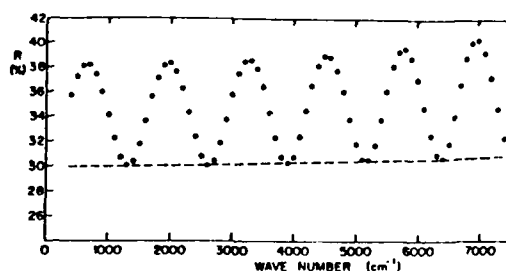

Fig. 2. Points are calculated reflection vs. frequency (cm^{-1}) for a single layer on a Si substrate as given in Fig. 1 with σ_D = 0 and $k(\nu)$ = 0. The R_D = 1.0 µm and the dispersion parameters are as follows: for amorphous Si, A_D = 7.03, B_D = 2.64 x 10^9 cm^{-2} and Ω_D = 18,860 cm^{-1}; for crystalline Si, A_S = 4.1476; B_S = 5.8876 x 10^9 cm^{-2} and Ω_S = 27,973 cm^{-1}. The smooth dashed curve is the reflectivity for crystalline Si.
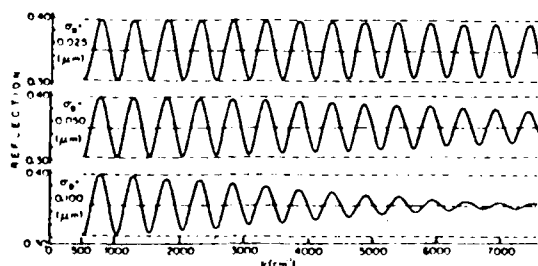

Fig. 3. Calculated reflection vs. frequency for three different values of σ_D as shown. Values of n_S = 3.45, n_D = 3.90 (both frequency independent) and a R_D = 2.5 µm were used.
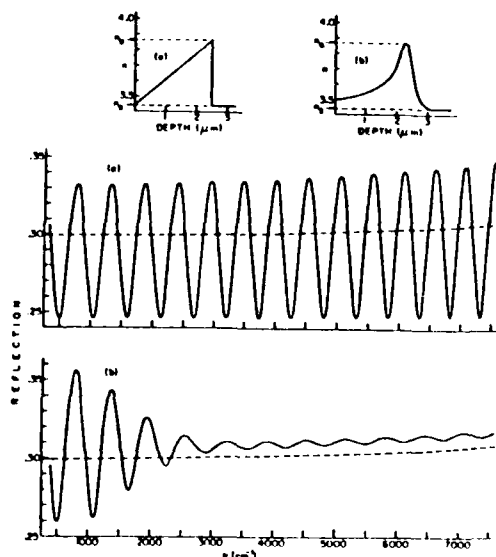

Fig. 4. Calculated reflection curves for two assumed refractive index profiles. The dashed curves are the reflectivity for crystalline Si.
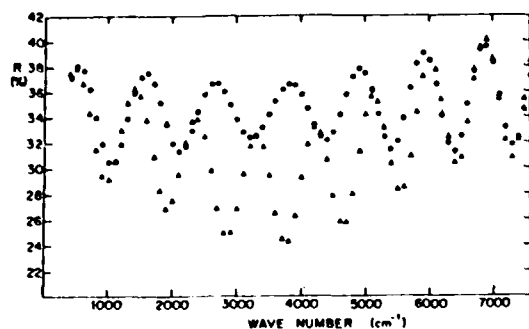
200

Fig. 5. Calculated reflections for two layers on a Si substrate. The · is for the thick layer (R_{D1} = 1.2 μm, σ_1 = 0, k_1 = 0; A_D, B_D, Ω_D as in Fig. 2) followed by the thin layer (R_{D2} - R_{D1} = 0.2 μm, σ_2 = 0, k_2 = 0, n/n_s = 1.03) and then the substrate with n_s = n (crystalline Si)--see Fig. 2. The Δ is for the same layers but with the sequence of the thick and thin layers reversed.
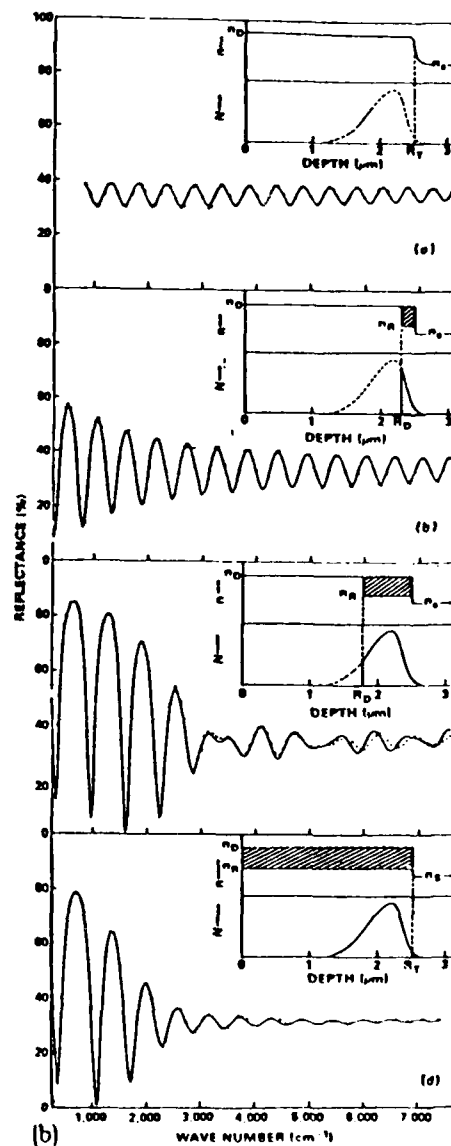

(b)

Fig. 6. Calculated curves for the case where a plasma is formed in the recrystallized material. The data points are measurements of a Si sample implanted with 2.7 MeV ions of P+, fluence = 1.74 x 10^{16}/cm^2. (a) no anneal, (b) 500°C for 30h, (c) 500°C for 70h and (d) 500°C for 750h.
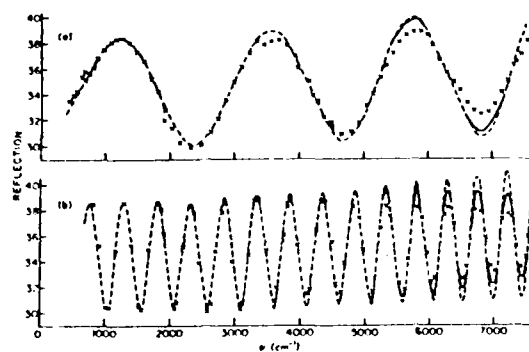
Fig. 7. Reflection measurements for two implanted Si samples are given by the data point (x). The curves are calculated as described in the text.
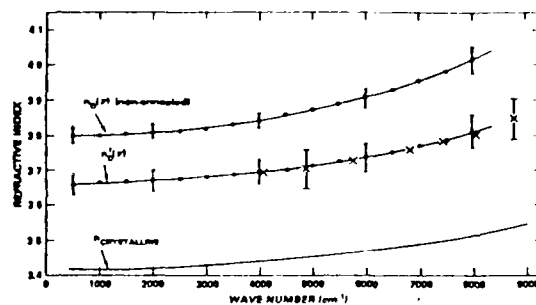
Fig. 8. Refractive index vs. frequency (cm^{-1}) for (i) as-implanted amorphous Si, $n_D(\nu)$, (ii) anneal-stabilized amorphous Si, $n_D'(\nu)$, and (iii) crystalline Si.

Fig. 9. Reflection measurements of a ^{29}Si-implanted Si sample. The conditions of implantation are given in the text.
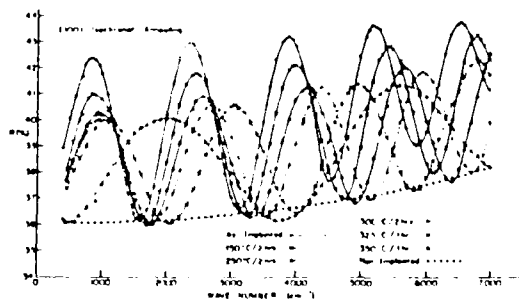
Fig. 10. Reflection of a ^{29}Si-implanted Ge sample which was annealed for a sequence of temperatures and times as indicated. Also shown is the reflectivity of non-implanted Ge.

202
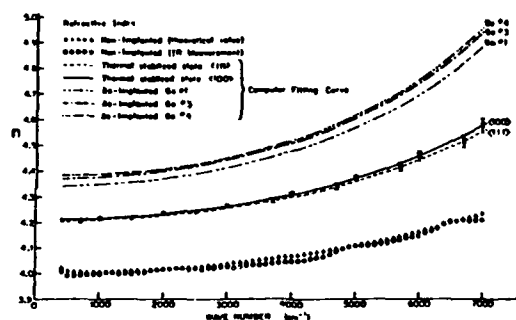
Fig. 11. Refractive index curves for $n_D(\nu)$, $n'(\nu)$, and n_s which are a-Ge-I (top curves), a-Ge-II (middle curves), and crystalline Ge (lower curves), respectively.
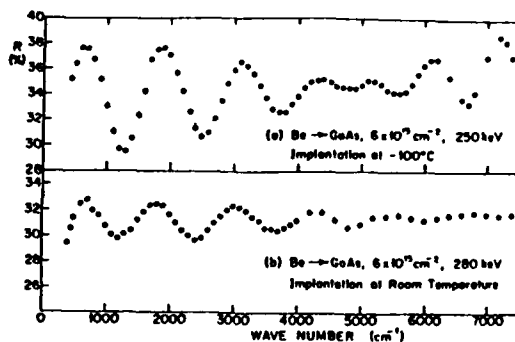
Fig. 12. Measured reflection data for two $^9Be^+$ ion implanted GaAs samples.
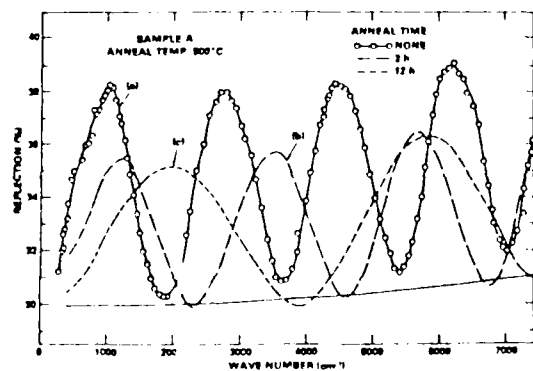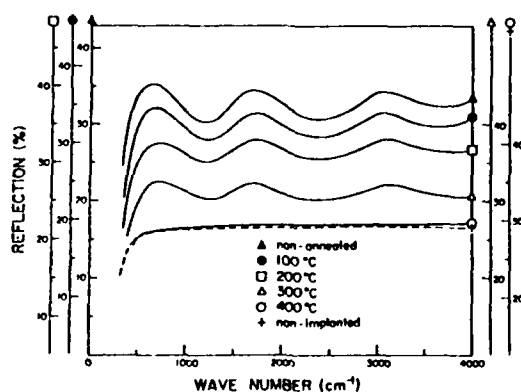
Fig. 13. Reflection of Be-implanted GaAs for different annealing temperatures. The implantation was at room temperature, ion fluence = 6 x 10^{15}/cm^2 at 280 keV. The dashed curve is the reflectivity of non-implanted GaAs.
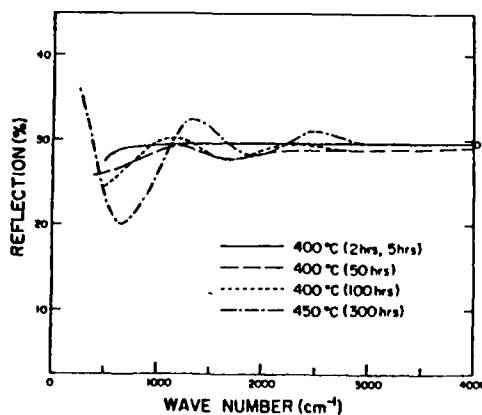
Fig. 14. Reflection of a GaAs sample implanted similarly to the one in Fig. 13. Effect of isothermal annealing at 400°C is shown with a curve for a sample annealed at 450°C.

Section IV.B

AMORPHOUS SILICON PRODUCED BY ION IMPLANTATION: EFFECTS OF ION MASS AND THERMAL ANNEALING

C.N. Waddell and W.G. Spitzer[1]
J.E. Frederickson[2]
G.K. Hubler[3]
T.A. Kennedy[4]

[1]Departments of Physics and Materials Science
University of Southern California
Los Angeles, CA 90089

[2]Department of Physics-Astronomy
California State University
Long Beach, CA 90840

[3]Materials Modification & Analysis Branch
Condensed Matter & Radiation Science Division
Naval Research Laboratory

[4]Semiconductors Branch
Electronics Division
Naval Research Laboratory

Amorphous silicon produced by ion implantation: Effects of ion mass and thermal annealing

C. N. Waddell and W. G. Spitzer
Physics and Materials Science Departments, University of Southern California, Los Angeles, California 90089

J. E. Fredrickson
Physics-Astronomy Department, California State University, Long Beach, California 90840

G. K. Hubler and T. A. Kennedy
Naval Research Laboratory, Washington, D.C. 20375

Characterization of the two optical states of amorphous Si produced by ion implantation is extended to include electron paramagnetic resonance, fundamental absorption edge, and density measurements in addition to infrared reflection. It is found that the properties of the two a-Si states are not dependent upon the mass of the incident ion (^{12}C, ^{29}Si, ^{11}P, ^{120}Sn) or upon the anneal temperature for $400\,°\leqslant T_A \leqslant 600\,°$C. The dangling-bond density drops about a factor of 2 when the a-Si makes a transition between the two states. The absorption coefficient also drops by more than a factor of 5, but the density of the a-Si does not change when the transition occurs. The transition between states was not completed at $T_A = 300\,°$C, so the annealing mechanism may be temperature dependent.

I. INTRODUCTION

One of the more attractive methods of producing amorphous Si, a-Si, for the purpose of characterizing some of its properties is by ion implantation of high purity, single crystal Si samples. Previous indications are that the a-Si layer formed by a high fluence implantation is essentially void-free, the amorphous-crystalline interface is expected to be relatively clean and the influence of specific impurities can be investigated by using different ions for the implantation. In the present work we report measurements of the infrared refractive index, the fundamental absorption edge, the electron spin resonance and the density of a-Si formed by the implantation of ^{12}C, ^{29}Si, or ^{120}Sn into single crystal Si samples. The effects of thermal annealing on these properties were investigated.

II. BACKGROUND

In previous studies, measurements were presented which demonstrated that a-Si produced by ion implantation can exist in two distinguishable states which we shall refer to as a-Si-I and a-Si-II. In one study[1] a number of Si samples were heavily implanted at either 200 K or room temperature with Si or P ions which had incident energies between 200 keV and 2.7 MeV and fluences between 1.0 and 10.0×10^{16} ions/cm^2. In all cases the a-Si produced by the implantation process had an infrared refractive index [called $n_I(\bar{v})$—see curve in Fig. 1] which was independent of the fluence and whether Si or P was the implanted ion. The change in index of refraction is about 12%. At $\bar{v} = 4000$ cm^{-1} the value of $n_c/n_I = 0.89$, where n_c is the crystalline value of 3.44.

In subsequent studies[2,3] it was found that annealing the implanted samples for about 2 h at 500 °C or for 1/2 h at 550 °C caused the index of refraction to decrease to a new value, $n_{II}(\bar{v})$ also shown in Fig. 1. The ratio $n_{II}/n_I = 0.96$ at $\bar{v} = 4000$ cm^{-1} indicates that annealing causes the refractive

index to drop about 1/3 of its original implantation induced increase from $n_c(\bar{v})$. The values of $n_{II}(\bar{v})$ are also independent of the implantation parameters and do not change with further annealing at 500 or 550 °C until epitaxial recrystallization occurs. These two optical states were identified as (I), the defect saturated (as-implanted), and (II), the thermally-stabilized (annealed) states of a-Si.[4]

In a recent study[5] the infrared refractive indices, the strength of the electron paramagnetic resonance (EPR) dangling-bond signal, and the changes in density of the a-Si were measured as a function of annealing time at $T_A = 500$ °C for ^{29}Si-implanted samples of Si. These measurements indicated that the dangling bond density behaved in a manner similar to that of the refractive index, i.e., a large drop in the early stages (first two hours) of the 500 °C anneal, and only slight
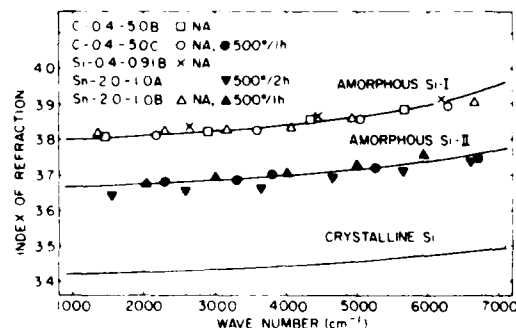

FIG. 1. Indices of refraction of crystalline Si [$n_c(\bar{v})$] and of amorphous Si in the two metastable states—$n_I(\bar{v})$ (as-implanted) and $n_{II}(\bar{v})$ (thermally stabilized). The curves are from previously reported work (Refs. 1, 2) and the data points are measurements of C, Si, and Sn implanted samples in the as-implanted state (NA) and after annealing at 500 °C

further changes resulting from prolonged anneal times. However, there was no corresponding change in density. These results were interpreted as supportive of the existence of two metastable states for a-Si produced by ion implantation and suggested that the two states differ because of annealing induced network reorganization which leads to a reduction in dangling bond concentration.

The results presented here extend those of Ref. 5 in two ways: (i) measurements were made for implantations of Group IV ions having widely different masses (^{12}C, ^{29}Si, ^{120}Sn), and (ii) a series of different isothermal annealing temperatures T_A were used within the range $300 < T_A < 600$ °C.

It is well known that the structural characteristics of the damaged regions produced during the amorphization process are quite different for implantations of light or heavy ions.[6–9] Previous measurements, such as particle channeling, have indicated that the a-Si produced by light or heavy ions are indistinguishable, and this is normally considered to be the case.[6,8] However, there are experiments in which the changes in the index of refraction of a-Si near the absorption edge have been found to vary with the mass of the implanted ions.[7,10] These variations are not monotonic in mass and Baranova et al. suggest that they are due to dispersion over the 1–2 μm region studied.[7] There is a possibility that the different defect production history during the approach to amorphization could lead to different nonequilibrium structures in a-Si-I. If there are different structures they could affect the complex dielectric constant of a-Si-I, the annealing behavior of the transition from a-Si-I to a-Si-II, and even the properties of a-Si-II. Because the present techniques have been used to study the properties of a-Si-I and a-Si-II in

detail only for implantations of medium weight ions ($A = 29,31$), it is important to determine if these properties are dependent upon the mass of the amorphizing ion. Group IV ions were chosen to avoid complications from the free carrier plasma in the epitaxially recrystallized regions.[11]

Similarly, since the transition between the two states has only been studied for two annealing temperatures, 500 and 550 °C, it is important to study the annealing process over a wider temperature range to determine whether the properties of the thermally stabilized state (a-Si-II) are dependent upon the anneal temperature employed. If the several properties of a-Si-II are independent of all implantation parameters and of the annealing temperatures employed, then the results would suggest that a definable and unique thermodynamic state has been produced.

III. EXPERIMENTAL PROCEDURES

The techniques used are essentially the same as those used previously[1–3,5] and therefore they will be reviewed here only briefly.

A. Implantations

The samples and implantation conditions employed are listed in Table I. The sample designation is by implanted ion, incident ion energy in MeV, fluence in units of 10^{16} ions/cm^2, and if there is more than one sample, by A, B, etc. Thus, C-0.4-5-A is a C ion-implanted Si sample, where the C ion energy is 400 keV, the fluence is 5×10^{16}/cm^2, and "A" indicates that this is the first such implanted sample. In all cases the starting material was single crystal Si having an initial

TABLE I. Samples and implantation conditions.[a]

Orientation	Sample no.[b]	Ion implanted	Ion energy (keV)	Fluence (10^{16} ions/cm^2)
⟨111⟩	C-0.4-5-A, B, C	^{12}C	25	0.30
	and		60	0.62
			120	0.87
⟨100⟩	C-0.4-5-D, E	^{12}C	200	1.20
			300	0.52
			400	1.49
			Total =	5.00
⟨111⟩	Si-0.3-0.3-A, B, C	^{29}Si	300	0.30
⟨111⟩	Si-0.4-0.57-A, B, C	^{29}Si	400	0.57
⟨100⟩	Si-0.4-0.91-A, B, C, D, E	^{29}Si	50	0.023
			100	0.045
			150	0.056
			200	0.113
			250	0.225
			325	0.225
			400	0.225
			Total =	0.912
⟨100⟩	Si-0.38-0.5-B, D	^{29}Si	380	0.50
⟨100⟩	Sn-2.0-1.0-A, B	^{120}Sn	2000	1.00
⟨111⟩	Sn-2.0-1.0-C, D	^{120}Sn	2000	1.00

[a] All samples were implanted at 200 K and a bombardment angle of 8°
[b] Sample designation is as follows: Implanted ion-ion energy (MeV) - fluence (10^{16} cm^{-2}).

207

resistivity $> 10 \, \Omega$ cm. Multiple energy implantations were used in some cases to achieve more uniform ion and damage density profiles within the implanted layer. The sample temperature was maintained near 200 K during implantation and, to reduce channeling, the incident ion beam direction was approximately 8° off of the high symmetry directions indicated in Table I.

B. Infrared reflection

Room temperature, near-normal incidence, reflection measurements were made over the wave number range $400 < \bar{v} < 7000$ cm^{-1}. The reflected intensity varies strongly with $\bar{v}$ because of the interference between the reflections at the air-amorphous and amorphous-crystalline interfaces. The back surfaces of the samples are roughened to eliminate reflections from the final crystalline-air interface. Computer analysis of the reflection spectra yields (i) the refractive-indices of the a-Si and the recrystallized region, (ii) the depth of the amorphous layer, and (iii) the width of the transition between the a-Si and c-Si regions.[11]

C. Density

During the implantations a mask covered a small portion of the surface of each sample. The swelling of the implanted region produces a sharp step in surface height at the edge of the mask. Because the thickness of the implanted region is very small compared to the lateral dimensions of the implanted region, only the thickness of the sample is significantly affected by the radiation damage.[12] Using this model the change in density $\Delta\rho$ is given by

$$\Delta\rho = \rho_c \left(\frac{\text{Step height}}{a\text{-Si Thickness}} \right).$$

The thickness of the a-Si region was determined from the infrared reflection measurements, and a Sloan Dektak profilometer was used to determine the step height to an accuracy of ~ 25 Å per measurement. Because the latter measurements contributed most of the inaccuracy in the determination of $\Delta\rho$, they were repeated and each value reported is the average of 10–20 measurements of step height.

D. Electron paramagnetic resonance

The EPR measurements were made at room temperature with a Varian E3 spectrometer at 9 GHz. The signal from a-Si, which has an isotropic $g = 2.0055$, has been attributed to dangling bonds.[11] Since this signal was found to be negligible both prior to implantation and after the a-Si had recrystallized, it was concluded that the signal strengths obtained for the implanted samples were due to the a-Si layer. To obtain relative spin density values, the EPR signal strength is divided by the a-Si volume which is obtained by using the sample surface area and the layer thickness determined from the infrared reflection measurements.

E. Infrared band edge absorption

These measurements were made at 77 K by directly comparing the infrared transmission of the implanted sample with that of an identical, non-implanted sample. After averaging out the interference fringes in the transmission spectrum of the implanted sample, the frequency-dependent absorption α_a of the a-Si was determined by using the approximate expression

$$T = \frac{I}{I_0} \approx \frac{(1 - \bar{R})^2 e^{-(\alpha_c x_c + \alpha_a x_a)}}{1 - \bar{R}^2 e^{-2(\alpha_c x_c + \alpha_a x_a)}},$$

where T is the fraction of the incident energy transmitted by the implanted sample; $\bar{R}$ is the average reflection of a-Si and c-Si determined from the reflection measurements; $\alpha_c x_c$ is the product of the absorption coefficient and thickness of the crystalline region and it is determined from the transmission measurements of the nonimplanted reference sample; and x_a is the thickness of the a-Si layer which is determined from the reflection measurements of part (B). In all cases, $x_a \ll x_c$. The extinction coefficient is $k_a = \alpha_a / 4\pi\bar{v}$, where both α_a and $\bar{v}$ have units of cm^{-1}.

IV. RESULTS
A. Refractive indices, absorption edge, and dangling-bond densities

The curves in Fig. 1 show the refractive indices $n_1(\bar{v})$ of as-implanted a-Si, $n_{11}(\bar{v})$ of thermally stabilized a-Si, and $n_c(\bar{v})$ for crystalline Si, all as previously reported.[2] The $n_1(\bar{v})$ and $n_{11}(\bar{v})$ curves are averages of values obtained from computer fits to the reflection spectra from a number of Si- and P-implanted samples where the anneal temperature used to produce $n_{11}(\bar{v})$ was $T_A = 500$ °C. The data points presented in Fig. 1 are the refractive indices obtained for several of the samples of Table I, which were implanted with ^{12}C, ^{29}Si, or ^{120}Sn ions. Both the as-implanted and the 500 °C anneal refractive indices for all samples are in excellent agreement with our previously published results.[1-3] Thus, there is no discernible dependence upon the mass of the incident ion (^{12}C→^{120}Sn).

In an earlier communication[1] we reported results of absorption edge measurements for a nonannealed, heavily ^{31}P-implanted Si sample. The measured absorption coefficient was $\alpha_1 \sim 5 \times 10^{-13} \bar{v}^4$ cm^{-1} corresponding to $k_1 \sim 4 \times 10^{-14} \bar{v}^3$.[14] In order to determine if there is a change in absorption with implanted ion species or when the a-Si makes a transition from the defect-saturated to the thermally stable state, transmission measurements were made for ^{12}C, ^{29}Si, and ^{120}Sn implanted samples. In all cases the measured absorption for nonannealed samples in the region of the absorption edge was close to $\alpha_1 \sim 5 \times 10^{-13} \bar{v}^4$ in agreement with the previous results for P-implanted Si. As in the case for the refractive index there is no detectable dependence upon which ion is used for the implantation.

The implanted samples were annealed for 2 h at 500 °C to produce the change from $n_1(\bar{v})$ to $n_{11}(\bar{v})$ and the absorption edge was remeasured. In these cases it was not possible to detect a difference between the absorption of the annealed implanted samples and the crystalline reference samples. Because of the small thickness of the amorphous layer compared to the thickness of the crystalline substrate, we were unable to obtain meaningful values for α_{11}, the absorption coefficient for the thermally stabilized state. We estimate that $\alpha_{11}(\bar{v})$ is less than $\alpha_1(\bar{v})/5$ for all cases. It is clear that

there is a large change in the absorption in the region of the absorption edge when the amorphous Si changes between the two states.

EPR measurements were made for some of the ^{12}C, ^{29}Si, and ^{120}Sn implanted samples of Table I. The results of these measurements are presented in Table II as the dangling bond signal strengths divided by the volumes of the a-Si layers. The values for ^{29}Si are the same as those given previously,[5] and it was indicated there that the as-implanted value corresponds to a dangling bond density of $\sim 2 \times 10^{19}$ cm^{-3}. When the samples are annealed (500 °C/2 h) the spin density drops about a factor of 2 with, possibly, a small further reduction with continued annealing at 500 °C.[5] There are variations in the values measured for both as-implanted and annealed samples, but no trend due to ion mass is discernible. Therefore, the decrease in the spin density is also attributed to the transition between the two states of the a-Si.

B. Annealing temperature dependence

In the preceding section physical changes accompanying the 500 °C annealing-induced transition between the two states of a-Si were discussed, and it was found that the experimental results are consistent with the interpretation that the two states are essentially unique and that their properties are independent of the masses of the implanted ions. In this section we seek to determine whether the properties of the annealed state are dependent upon the anneal temperature.

The changes in index of refraction and density were measured over the anneal temperature range $300 < T_A < 600$ °C for samples implanted with ^{12}C, ^{29}Si, and ^{120}Sn ions. To characterize the changes in the indices of refraction we define a single parameter f_D by

$$f_D = \frac{n(\bar{v})}{n_1(\bar{v})}.$$

The value of this parameter was determined at $\bar{v} = 4000$ cm^{-1}, the average frequency of the infrared measurements.

The results of annealing ^{12}C, ^{29}Si, and ^{120}Sn implanted samples of Table I at 500 °C are shown in Fig. 2. The f_D measurements in Fig. 2(a) clearly show the change in the index of refraction that occurs when the a-Si makes a transition between the two states. There is no discernible difference due to the implanted ion specie or the duration of the annealing time. The average value of $f_D = 0.966 \pm 0.004$ is in good agreement with the previously determined f_D

TABLE II. Relative dangling-bond densities.[a]

Anneal/Ion	^{12}C	^{29}Si	^{120}Sn	Average
as-implanted	299	353[b] 325 320	252	310 ± 38
500 °C/2 h	150	136	148	
500 °C/8 h	163	~100		140 ± 22
			Ratio	0.45 ± 0.10

[a] (The isotropic g = 2.0055 EPR signal)/(a-Si volume).
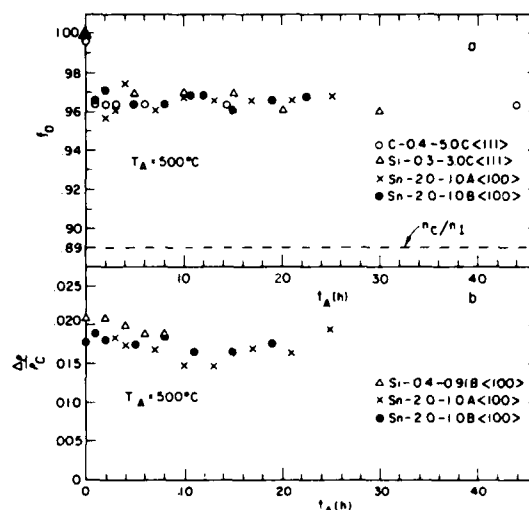[b] This value corresponds to a spin density of ~2·10^{19} cm^{-3}.

FIG. 2. Comparison of the change in index of refraction to the change in mass density for C, Si, and Sn implanted samples annealed at 500 °C. The change in index is characterized by the parameter $f_D = n(\bar{v})/n_1(\bar{v})$ where $n_1(\bar{v})$ is shown in Fig. 1 and f_D is evaluated at $\bar{v} = 4000$ cm^{-1}. The density change is shown as the fractional change $\Delta\rho/\rho$.

$\approx 0.961 \pm 0.004$ for Si implants and $f_D = 0.963 \pm 0.009$ for P implants.[5]

The density measurements shown in Fig. 2(b) indicate that there is no change in the density of the a-Si layer when the transition in states occurs for an anneal time of about 1 h. Note that for an anneal time of one hour, large changes are observed for f_D and the EPR spin density. There is also no observed density effect due to the implanted ion specie. It should be noted that there is a factor of 2 difference in the depths of the a-Si layers studied for the different implantations and that the relative accuracy of the step height measurement decreases as the thickness decreases. Thus the relative errors in the measurements increase with annealing time due to epitaxial regrowth.

Similar measurements for annealing at $T_A = 400$ °C are shown in Fig. 3. The results agree with those found at 500 °C—independence of ion specie, the decrease in f_D, and no change in density. The only difference for the two temperatures is that it takes a longer time for the transition to take place at 400 °C, but this observation is in agreement with previous results showing that the transition time decreases at higher temperatures.[2]

Figure 4 shows the results obtained when ^{29}Si implanted samples are isothermally annealed at temperatures between 300 and 600 °C. Again the f_D values indicate similar values of index of refraction $n_{II}(\bar{v})$ for the annealed state for $T_A = 400$, 500, and 600 °C. However, at $T_A = 300$ °C the transition rate is much slower, and the index of refraction did not change during the anneal period from 7 to 118 h. The value $f_D = 0.974$ is significantly greater than the value $f_D = 0.965 \pm 0.005$ obtained at the higher temperatures. This sample was subsequently annealed for 24 h at 500 °C and the final value of $f_D = 0.971$ still appears to be slightly high. These results are not conclusive but suggest that the
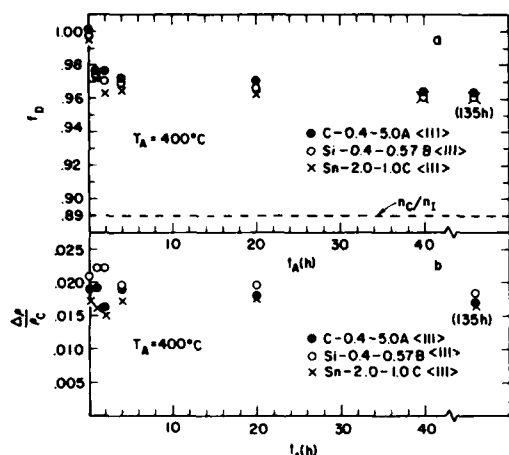
FIG. 3. Comparison of the change in index of refraction to the change in mass density for C, Si, and Sn implanted samples annealed at 400 °C. The change in index is characterized by the parameter $f_D = n(\bar{v})/n_1(\bar{v})$ where $n_1(\bar{v})$ is shown in Fig. 1 and f_D is evaluated at $\bar{v} = 4000 \text{ cm}^{-1}$. The density change is shown as the fractional change $\Delta\rho/\rho_c$.

annealing mechanism responsible for the transition between states may be different at the lowest anneal temperature. Further study appears warranted.

V. DISCUSSION

The experimental results presented above support the view that the physical properties being measured are intrinsic to two distinct states of a-Si. The results are most readily
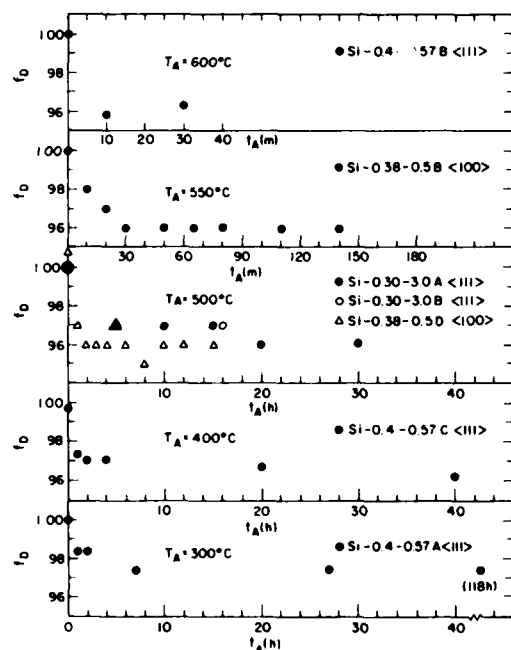

FIG. 4. Comparison of the changes in index of refraction for anneal temperatures $T_A = 300, 400, 500, 550,$ and 600 °C.

interpreted in terms of a network reorganization during the early stages of annealing which produces a reduction in the dangling bond density. Moreover, the states described by $n_1(\bar{v})$ and $n_{II}(\bar{v})$ appear to be unique for $400 < T_A < 600$ °C. For 300 °C annealing the final $n_{II}(\bar{v})$ state is not quite achieved and this may indicate that some complexes are formed which prevent reaching the value $n_{II}(\bar{v})$ even after further annealing at 500 °C.

The measured spin density of $\sim 2 \times 10^{19} \text{ cm}^{-3}$ for a-Si-I is comparable to the $\sim 6 \times 10^{19} \text{ cm}^{-3}$ obtained by Thomas et al.[13] for very pure evaporated samples deposited on a room temperature substrate under high vacuum conditions. They found that the effect of isochronal annealing or of increasing the substrate temperature during deposition is to decrease the spin density by, at most, a factor of 3 before the onset of crystallization. In our case we find a decrease of about a factor of 2 in spin density from the transition of a-Si-I to a-Si-II.

Following a suggestion by Wales et al.[15] that the increase in index of refraction of amorphous Ge could be attributed to the increase in polarizability of the dangling bonds, Schwidefsky[16] has calculated the polarizability of a dangling bond in a-Si by using both the Lorentz–Lorentz equation and the classical harmonic-oscillator model to fit their measured change in index and spin density for evaporated Si films. For the measured spin density of $\sim 8 \times 10^{20} \text{ cm}^{-3}$ Schwidefsky calculated that the polarizability of the dangling bond would be about 25 times greater than that of a crystalline homopolar bond if only the dangling bonds were responsible for the increase in the index of refraction. If we follow the same suggestion and attribute the initial radiation damage induced change in refractive index, $n_c(\bar{v}) \rightarrow n_1(\bar{v})$, to the introduction of $\sim 2 \times 10^{19} \text{ cm}^{-3}$ dangling bonds and to the decrease in dipole moment/volume due to the observed 2% decrease in mass density, then an increase by a factor of 2500 for the dangling bond polarizability is required. This result is physically unreasonable and indicates that the dangling bonds are not responsible for the change in indices of refraction.

By using either the Drude or the Lorentz–Lorentz equations for dielectrics, one finds that there is an increase of $\sim 28\%$ in the average bond polarizability for the change from c-Si to a-Si-I, and a decrease of $\sim 8\%$ for the change from a-Si-I to a-Si-II.

The observed decrease in the near band edge absorption or the "blue shift" in the edge when a-Si-I $\rightarrow$ a-Si-II appears to be consistent with the proposal of a network reorganization in which there is a reduction in disorder. The absorption in this region is often associated with the fluctuations in the atomic configuration[17] which cause shifts in electronic states and give rise to band tails. The reduction in disorder thus appears to be the cause for both the reduction in absorption and the $\sim 8\%$ decrease in average bond polarizability.

ACKNOWLEDGMENT

4365   J. Appl. Phys., Vol. 55, No. 12, 15 June 1984   Waddell et al.   4365

210

Note Added in Proof. For our implantation conditions we estimate that 5–11 Å of Si was removed by sputtering for ^{29}Si implants, 18 Å for C implants, and 38 Å for Sn implants. Since step heights for the as-implanted samples were usually between 100 and 160 Å, the correction to the density would be negligible for Si, 10% for C, and about 20% for Sn. Since the step height measurements themselves are accurate only to about 20%, and the sputtering coefficient estimates are accurate only to 50%, we have not applied the correction. It should be noted, however, that the correction would bring the density measurements for the different ions into closer agreement.

[1]G. K. Hubler, C. N. Waddell, W. G. Spitzer, J. E. Fredrickson, S. Prussin, and R. G. Wilson, J. Appl. Phys. **50**, 3294 (1979).

[2]J. E. Fredrickson, C. N. Waddell, W. G. Spitzer, and G. K. Hubler, Appl. Phys. Lett **40**, 172 (1982).

[3]C. N. Waddell, W. G. Spitzer, G. K. Hubler, and J. E. Fredrickson, J. Appl. Phys **53**, 5851 (1982).

[4]M. Janai, D. D. Allred, D. C. Booth, and B. O. Seraphin, Solar Energy Mater. **1**, 11 (1979).

[5]W. G. Spitzer, G. K. Hubler and T. A. Kennedy, Nucl. Instrum. Methods **209/210**, 309 (1983).

[6]J. F. Gibbons, Proc. IEEE **60**, 1062 (1972).

[7]E. C. Baranova, V. M. Gusev, Yu. V. Martyenko, C. V. Starnin, and I. B. Haibullin, Radiat. Eff. **18**, 21 (1973).

[8]J. Buorgoin, "Defect Production in Semiconductors," in *Ion Implantation in Semiconductors*, edited by S. Namba (Plenum, New York 1976).

[9]J. R. Dennis and E. B. Hale, J. Appl. Phys. **49**, 1119 (1978).

[10]W. Wesch and G. Gotz, Radiat. Eff. **49**, 137 (1980).

[11]G. K. Hubler, P. R. Malmberg, C. N. Waddell, W. G. Spitzer, and J. E. Fredrickson, Radiat. Eff **60**, 35 (1982).

[12]R. E Whan and G. W Arnold, Appl. Phys. Lett. **17**, 378 (1970); K. N. Tu, P. Chaudhari, K. Lai, B. L. Crowder, and S. I. Tan, J. Appl. Phys. **43**, 4262 (1972).

[13]P. A. Thomas M. H. Brodsky, D. Kaplan, and D. Lepine, Phys. Rev. B **18**, 3059 (1978). See this reference for earlier studies.

[14]In Ref. 1, $k_D = 5.939 \times 10^{-18} \bar{v}^4$ is quoted for sputtered Si. This expression is in error and should have read $\alpha_D = 5.939 \times 10^{-13} \bar{v}^4$. This corresponds to $k_D = 4.73 \times 10^{-14} \bar{v}^3$ for sputtered Si.

[15]J. Wales, G. J. Lovitt, and R. A. Hill, Thin Solid Films **1**, 137 (1967).

[16]F. Schwidefsky, Thin Solid Films **18**, 45 (1973); **30**, 233 (1975).

[17]G. A. N. Connell, "Optical Properties of Amorphous Semiconductors," in *Amorphous Semiconductors*, edited by M. H. Brodsky (Springer, Berlin, 1979).

Section IV.C

THERMAL ANNEALING BEHAVIOR OF HYDROGEN-FREE AMORPHOUS SILICON AND GERMANIUM

[1]G.K. Hubler and E.P. Donovan
[2]K-W Wang and W.G. Spitzer

[1]Materials Modification & Analysis Branch
Condensed Matter & Radiation Sciences Division
Naval Research Laboratory

[2]Department of Materials Science & Physics
University of Southern California
Los Angeles, CA 90089-0241

Thermal Annealing Behavior of Hydrogen-Free
Amorphous Silicon and Germanium

Graham K. Hubler and Edward P. Donovan
Naval Research Laboratory, Washington, D.C. 20375

and

Kou-Wei Wang and William G. Spitzer
Department of Materials Science and Physics, University
of Southern California, Los Angeles, CA 90089-0241

Abstract

Recent work has demonstrated that the infrared properties (refractive index and absorption) of amorphous silicon and germanium prepared by ion implantation depend upon the low temperature thermal annealing history ($150^\circ C < T < 600^\circ C$). This thermal relaxation phenomenon is the subject of this review. The data suggest the change in refractive index is caused by a structural reorganization of a continuous random network but that changes in absorption and spin density are chiefly caused by the annealing of defects within the amorphous structure.

Introduction

The isothermal annealing behavior of amorphous semiconductors prepared by ion implantation has not until recently been extensively investigated for annealing temperatures less than about $600^\circ C$, the temperature characteristically used as the first step in furnace annealing for device fabrication.[1] This situation came about because the focus of early annealing studies (circa 1968) was upon the optimization of electrical properties, and it was determined that much higher temperatures (e.g., > $900^\circ C$ for B in Si)[2] were required for good electrical activation of the implanted dopants. Among the first studies to utilize low temperature isothermal annealing of amorphous semiconductors were a now classic set of experiments by Cspregi et al.[3-5] They measured the epitaxial crystallization rates for various orientations of the substrates silicon and germanium and the effects of impurities on these rates. Numerous other investigators expanded these studies for different impurities and temperature regimes.[6] One problem with the standard device fabrication process steps of furnace annealing at $600^\circ C$ for 30 min then at $1100^\circ C$ for 20 min is that of dopant redistribution by diffusion.[1] The concentration profile following annealing at temperature T varies as a function of the square root of the diffusivity D times the time t, or $(Dt)^{1/2}$. Much work is currently underway to solve the problem with rapid transient thermal annealing techniques to reduce the time at high temperature in the solid state. Formation of a fully amorphous layer prior to implantation followed by rapid thermal annealing was found to help reduce the diffusion problem by Siedel et al.[7] A second approach to solve the problem is through longer time anneals at $T < 600^\circ C$; possibly of fully amorphous layers. It therefore has become desirable to understand low temperature isothermal annealing in amorphous semiconductors.

The focus of many studies of low temperature (e.g., $T < 600^\circ C$) thermal annealing has been upon amorphous silicon alloyed with hydrogen which is incorporated during the deposition process; the hydrogen neutralizes dangling bonds in the amorphous structure and facilitates chemical doping of the amorphous material. Infrared spectroscopy has proved to be a useful characterization probe for such materials, because the observed index of refraction, band edge absorption and Si-H localized vibrational mode absorption depend strongly on hydrogen concentration and thermal history.[8-10]

Recent investigations by the authors have demonstrated that infrared dielectric property measurements can also make a significant contribution to the understanding of the behavior of non-hydrogenated amorphous semiconductors during long term isothermal anneals for an anneal temperature $T_A < 600^\circ C$.[11-21] For example, the processes of implantation damage removal and carrier activation at low temperature were simultaneously and nondestructively characterized with infrared analysis for dopants implanted into silicon [11-13] and gallium arsenide.[16,20] This allowed the determination that the removal of damage and electrical activation are seperate processes in Be-implanted GaAs.[20] Again for example, the index of refraction of non-hydrogenated amorphous Si and Ge produced by ion implantation changed in magnitude during thermal annealing;[14,17-19,21] both elements were shown to have two reproducible optical states of the amorphous material, i.e., as-implanted and well-annealed. Two optical states of amorphous Si have also been reported by Heidemann.[22]

In this paper we review the progress in an on-going project to characterize these amorphous states of Si and Ge. The infrared analysis method is introduced and used to demonstrate the existence of different optical states. These results are then compared with measurements from other techniques, such as ion channeling, electron paramagnetic resonance and electron diffraction, as well as measurements in the literature using the techniques of EXAFS, ellipsometry and differential scanning calorimetry. The results suggest that the relaxation observed is structural rather than electronic in nature.

214

Infrared Measurement and Analysis

Infrared characterization begins with the measurement of the intensity of light, reflected from or transmitted through an implanted sample, versus wave number, typically in the range 250 cm^{-1} to 7500 cm^{-1} (wavelength 40 μm to 1.3 μm). Semiconductor samples whose front surfaces have been polished and rear surfaces have been coarsely lapped prior to implantation are normally measured in the reflection geometry. This geometry is chosen because the sensitivity to refractive index changes in the implanted region is approximately double that of transmission; in addition, certain simplifications can then be made in the multilayer interference code used to model the experiment and analyze the data.[13] The variation of index with depth into the implanted semiconductor, which is caused by radiation damage and/or amorphization, causes modulation of the measured intensity vs wavenumber by means of thin film interference effects. Models of the refractive index distribution vs depth and the multilayer interference code are used to fit the data by means of a non-linear least squares fitting routine. Accurate refractive index profiles of the implanted region can be obtained with surprisingly simple models. A detailed description of the models and computational procedures has been reviewed by Spitzer et al.[20] The method will be briefly described here with the aid of Figures 1-3.

Figure 1 shows the infrared reflection spectrum for <111> silicon implanted with 2.7 MeV phosphorus to a dose of $1.7x10^{16}$ ions/cm^2 and for a substrate temperature during implantation of 200K.[11,13] The crosses are the data and the solid curve is the result of a fit in which three parameters were varied. The parameters are, along with their fitted values: R_D = 2.50 μm, the depth of the amorphous layer; σ_D = 0.035 μm, the standard deviation of the half-gaussian used to connect the amorphous refractive index with the crystalline value n_C; and n_D, the refractive index of the amorphous material. The refractive index profile is schematically shown in the insert. The slight rise in the average value of refectance with increasing wave number is caused by dispersion and was accounted for by the model. Also shown are the data (circles) for an unimplanted sample and a model calculation (line) using the crystalline refractive index.

Figure 1. Infrared reflectance results and the calculated best fit curves are shown for unimplanted and as-implanted silicon.
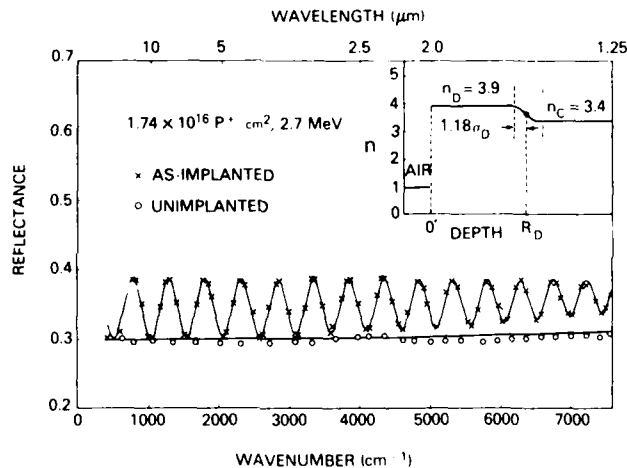
The absorption k is modelled with the same depth dependence as for n shown in the insert, and the damping of the fringes in Figure 1 at high wave numbers contains a small contribution attributed to absorption.[11] However, after annealing Si, or for layers less than 1 μm in thickness, the effect of absorption on the reflection curves is negligible away from the band edge. For Ge, the absorption is larger and cannot be neglected even for thin amorphous layers.[21] It should be noted that this simple model represents the data extremely well and that R_D, n_D and σ_D are simply related to features in the data; namely, R_D is inversly proportional to the fringe spacing, n_D-n_C is proportional to the fringe amplitude, n_D is proportional to the average value of the reflectance, and the damping of the fringes at high wave numbers is proportional to σ_D.

The refractive index profile (@ 7000 cm^{-1}) derived from the fit to the data for the sample in Figure 1 is shown in Figure 2 for the as-implanted and well-annealed cases. The conditions during implantation were such that the dose of ions was sufficient to produce an amorphous layer from the surface to the amorphous-crystalline phase boundary. The experimentally measured projected range R_p of the phosphorus ions[15] is indicated in Figure 2, as well as the depths from the surface R_p + (1,2) ΔR_p where ΔR_p is the standard deviation of the projected range. The amorphous-crystalline phase boundary is approximately at the depth R_p + $2\Delta R_p$ in the as-implanted index profile. After thermal annealing for 2 h at 500°C, the surface layer, has a uniformly lower refractive index n'_D and the phase boundary has sharpened.[15] For longer annealing times at 500°C, the index remains n'_D while the phase boundary moves toward the

215

surface by means of solid phase epitaxy.[15,17]

Very similar behavior is reported for amorphous Ge layers on Ge substrates produced by ion implantation.[20,21] Figure 3 shows infrared reflection data and computer fits for an as-implanted sample of Ge, and for two annealing conditions.[21] This sample was implanted at a temperature of 100K with [29]Si ions to a dose of 10^{16} ions/cm^2 at an energy of 370 keV. When the as-implanted infrared data in Figures 1 and 3 are compared, it is clear that the fringe spacing is much smaller and the average reflection is larger for the Ge data. These differences are to be expected, since, as noted earlier, the fringe spacing is inversely proportional to R_p, the range of 370 keV Si in Ge is much smaller than the range of 2.7 MeV P in Si, and the crystalline index of refraction of Ge is 18% larger than that of Si. For the first anneal at $T_A = 300°C$, the fringe amplitude in Figure 3 decreases. After a second anneal at a higher temperature of 375°C, the fringe amplitude stays constant which indicates that the well-annealed state had been reached during the first anneal. The increase in fringe spacing following the second anneal indicated epitaxial growth of the substrate into the amorphous layer. Values of R_D, σ_D and n_D derived from the three fits are given in Table 1.
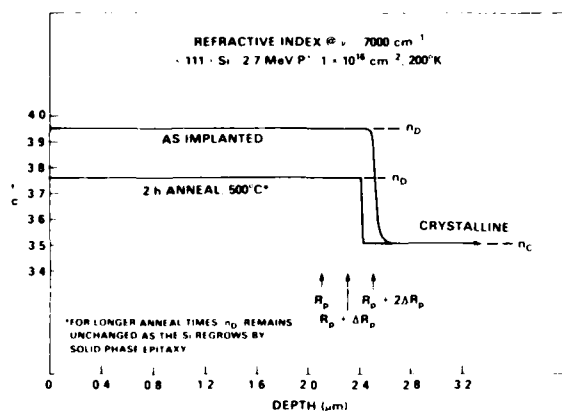

Figure 2. Refractive index vs depth derived by fitting curves like that of Figure 1 for the as-implanted and well-annealed conditions.
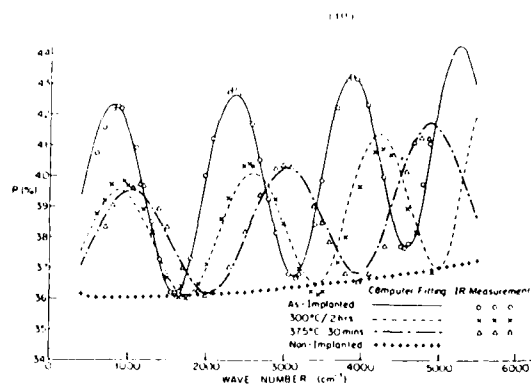
Figure 3. Infrared reflection results and the calculated best fit curves are shown for as-implanted, well annealed and partially regrown layers on Si-implanted Ge. The fitting parameters are given in Table 1.

The data presented in Figures 1-3 serve to demonstrate the utility and simplicity of the infrared technique. One can nondestructively measure the depth of amorphous layers,[11] the width of the transition region,[11] and rates of solid phase epitaxial growth.[15] Unique information concerning the relaxation of amorphous semiconductors can also be obtained.[14,17] Although examples have not been presented, infrared spectra from substrates with buried amorphous layers can be modeled and refractive index profiles measured with equal precision as for single layers.[20,23]

Table 1. Parameter values for the curves fitted in Figure 3

Anneal Condition	R_D (µm)	σ_D $(10^{-2}$µm)	n/n_C (@ 3000 cm^{-1})
as-implanted	0.72	5.3	1.092
$T_A = 300°C$, 2h	0.68	1.0	1.054
$T_A = 375°C$, 0.5h	0.58	4.2	1.054

Experimental Results

Several <100> Si substrates were implanted with a dose of 0.5×10^{16} cm^{-2} 380 keV silicon ions with the substrate temperature held at 200K. The thickness of crystallized material versus time during solid phase epitaxial growth at 500°C was measured by infrared analysis and is shown in Fig. 4.[15] Samples were quenched between anneals for the infrared measurement. All three samples show an initial period of rapid growth followed by a period of uniform growth rate. The velocity of epitaxial growth is found from the average of the slopes in the latter region to be 3.7 Å/min.

Several <100> Ge samples were implanted under the same conditions as the Si in Figure 3 and Table 1. The thickness measured of the amorphous layer versus time during epitaxial growth at 300°C is shown in Figure 5, along with data from subsequent isochronal anneals at the indicated temperatures.[23] The amorphous thickness decreases linearly with annealing time as expected, following an initial transient period. From these and similar data from <111> substrates of germanium the activation energy for epitaxial growth (i.e., Q for $V = V_0 \exp(-Q/k_BT)$ where k_B is the Boltzmann constant) was derived to be Q = 2.0 eV for both <100> and <111> orientations. A summary of growth rates for Si and Ge measured by the infrared method is given in Table 2. The crystal growth rates agree with values in the literature measured by other techniques to within a factor of two.[6,24]
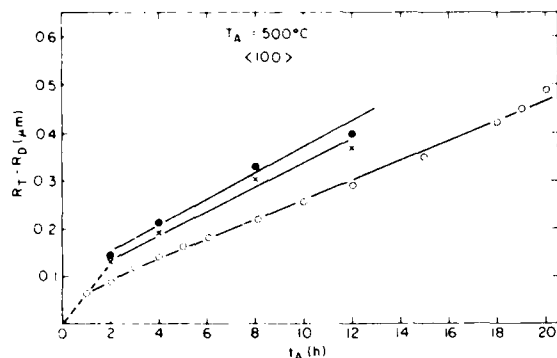

Figure 4. The width of the crystallized layer R_T-R_D, as a function of annealing time for three <100> Si-implanted Si samples annealed at 500°C. R_T is the as-implanted amorphous layer depth.
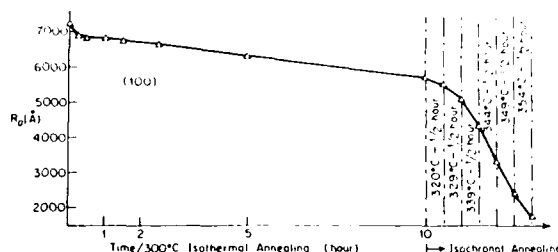
Figure 5. The computer fitting results for R_D vs annealing for <100> Si-implanted Ge is shown.

Table 2. Epitaxial growth rates of Ge and Si measured by the infrared method

Orientation	Velocities (Å/min)		
	Ge/300°C	Si/500°C	Si/550°C
<100>	46	3.7	34
<111>	4.0	0.23	--

Table 3 shows the depth of the amorphous layer for as-implanted Ge samples measured by infrared analysis and by ion channeling on the same samples.[23] The independent techniques yield the same results within errors (±3% for infrared; ±10% for ion channeling). The good agreement between measurements from the well accepted ion channeling technique for growth rate and layer thickness and the infrared measurements presented in Tables 2 and 3 establishes infrared analysis as a reliable and quantative characterization tool.

Table 3. Comparison of amorphous layer depths on Ge measured by infrared and channeling techniques for the as-implanted condition

Implanted Ion (implant temp)	Ion Energy (keV)	Dose ($10^{16}/cm^2$)	R_D (um) ion channeling	infrared
^{29}Si (110K)	370	1.0	0.78	0.72
^{20}Ne (80K)	1500	0.3	----	----
	2250	0.3	----	----
	3000	0.3	2.78	2.82

Evidence has already been presented for the existence of two well defined optical states of amorphous Si (a-Si) and amorphous Ge (a-Ge). The high refractive index as-implanted condition we call state I and the well annealed condition having an intermediate refractive index value we call state II.[18] The two

217

stable optical states for a-Si have been extensively studied by infrared and are found to be independent of implantation temperature (77K to 300K), ion dose (5x10^{15}ions/cm^{2} to 10[17]ions/cm^{2} at 300K), and ion mass (B to Sn).[11,14,15,18] Furthermore, a-Si-II is independent of the annealing temperature between T_A = 350°C and 600°C.[18] For T_A between 150°C and 350°C the kinetics of the transition between the states is very slow so that states of intermediate index of refraction may be achieved.[23] Implanted samples not annealed and held at room temperature for one year have shown no change in the index of refraction.[23] Germanium has been less extensively studied (only one ion mass) but the trends are similar to those of Si samples.[20,21]

In order to elucidate the nature of the difference in the two states, several additional characterization techniques were employed. Results of these studies for a-Si and a-Ge are summarized in Table 4.

Table 4. Summary of properties of a-Si and a-Ge

Property	a-Si-I	a-Si-II	a-Ge-I	a-Ge-II
$n/n_{Crystal}$(@3000cm^{-1})	1.12	1.08	1.09	1.05
band edge absorption ($k/k_{crystal}$)	5	1	100	30
density ($\rho/\rho_{crystal}$)	0.98	0.98	0.98	0.98
epr spin density	2x10^{19}/cm^{3}	1x10^{19}/cm^{3}	--	--
etch rate in boiling 50% H-F	100Å/min (non-uniform attack, spalling)	50Å/min (uniform attack)	--	--

The values of the index of refraction have already been discussed. A large increase in band edge absorption over the crystalline value for both Si and Ge is almost completely removed by annealing to state II for Si,[15] but only partially removed for Ge.[21] These relative numbers for absorption are approximate because they depend upon the wavelength of the measurement near the band edge and are given here to show the general trend. The mass density of states I and II are the same for both Si and Ge and are 2% less than the crystalline values.[17,21] For amorphous silicon samples, the dangling bond density measured by electron paramagnetic resonance drops by a factor of two between state I and state II[18] and the chemical etch rate of state II is slower and much more laterally uniform than for state I.[25]

Electron diffraction of states I and II for Si show only amorphous ring patterns which indicates that the transition to state II is not caused by polycrystalline grain nucleation.[26,17] This measurement does not eliminate the possibility of microcrystallinity in these samples, however.

Discussion

It has been suggested that the optical transition from state I to state II is caused by the reorganization of a continuous random network which reduces the average polarizability per bond.[14,17,19] This picture is supported by several recent measurements in the literature which are reviewed here. Vasquez et al.[27] performed spectroscopic ellipsometry measurements on a-Si-I and a-Si-II produced by Si ion implantation. Figure 6 shows the imaginary part of the dielectric function ϵ_2 for as-implanted and well-annealed a-Si states after correction for 18Å of native oxide. For comparison, the corresponding behavior of crystalline silicon (c-Si) is also shown. There are small but significant differences in ϵ_2 between the two amorphous states, and the character of state II clearly remains amorphous.

Vasquez et al.[27] applied two different physical models to the data utilizing the Bruggeman effective medium approximation in order to understand the differences in the dielectric functions of states I and II. The effect of a density increase caused by the collapse of voids upon annealing was considered in the first model. None of a wide range of void concentrations gave a reasonable fit. This is consistent with the lack of any density change between state I and state II as indicated in Table 4; also an increase in density would cause the refractive index to increase rather than to decrease as is observed. The second model applied allowed for partial crystallization within the film. Again a reasonable fit was not obtained indicating that nucleation of microcrystals is not the mechanism. This is consistent with the previously mentioned electron diffraction data. Also, the refractive index of state II becomes constant in time for annealing temperatures greater than 400°C; if crystalline grain growth were responsible, the refractive index of the mixture a-Si-I and c-Si would decrease with time as the polycrystalline grains grew in size.

Further support for the network reorganization between state I and state II was recently obtained in a study of thermally stabilized a-Ge films prepared by sputter deposition.[28] The films were characterized by Raman spectroscopy and extended x-ray absorption fine structure (EXAFS). In that study, a bond angle distortion $\Delta\theta$ was used to characterize the degree of transformation of different states. The value of $\Delta\theta$

was determined by comparison of the EXAFS data of the sample with the models of amorphous material generated by adding bond angle distortion to the crystalline data. A $\Delta\theta = 9.7^o$ was reported for as-deposited a-Ge, and $\Delta\theta = 7^o \pm 1^o$ was found for a sample with 1 h annealing at $T_A = 400^oC$. In the latter case, the volume fraction of crystalline material was $\leq 10^{-3}$ from the Raman result. In a second study by the same group,[29] the average bond angle distortions were measured by means of Raman spectroscopy, by comparing the broadening of the TO-phonon linewidth in amorphous samples with the broadening generated by stress in crystalline samples. Germanium films were sputter deposited and the silicon films were prepared by molecular beam deposition under very pure conditions. Differences in the bond angle distortions were obtained for different annealing conditions of the samples. Table 5 summarizes the results for both EXAFS and Raman measurements for samples that should correspond reasonably well to our a-I and a-II states. These results suggest that the distortion of bond angle is related to the disorder of the amorphous germanium and silicon and that the transition of a-I to a-II is possibly a re-ordering in which the change in the bond angle is correlated with the change of the optical constant in the infrared reflection studies.
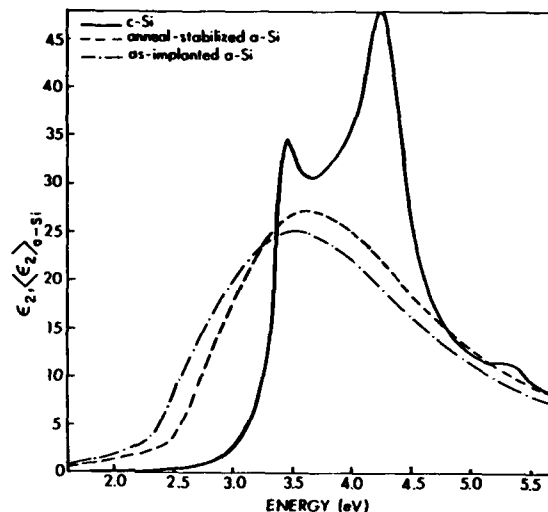

Figure 6. Imaginary part of the dielectric functions of as-implanted and anneal-stabilized a-Si obtained after correcting for the presence of an 18Å thick native oxide. For comparison, shown also is the corresponding behavior of c-Si. The data is taken by ellipsometry of plasma cleaned samples (from Vasquez et al., ref.[27]).

Table 5. Average bond angle distortions for a-Si and a-Ge (from refs. 28,29)

	a-I	a-II	Measurement method	Deposition method
Si	11.2°	8.3°	Raman	(MBD)
Ge	9.7°	7.0°	EXAFS	(Sputter
	8.8°	6.3°	Raman	deposited)

Evidence of thermally-induced structure relaxation was recently observed in differential scanning calorimetry measurements of ion-implanted Ge by Donovan et al.[24] In that study, the heat released during heating (40K/min) of thick amorphous layers on Ge was measured. It was observed that of the total heat released, 2/3 was attributed to the heat of crystallization and 1/3 resulted from relaxation in the a-Ge layer prior to crystallization. The experimental conditions of Donovan et al. were quite different from those employed here, making direct comparison of annealing temperature difficult. However, the data do not preclude the possibility that the heat release and drop in refractive index are directly correlated.

As mentioned in the introduction, the presence of hydrogen can produce large changes in the optical properties of a-Si. Although we have not measured the hydrogen content of our samples directly, we consider the possibility that hydrogen is causing the changes as highly unlikely for four reasons. First, hydrogen incorporation decreases the refractive index of a-Si[8] and both state I and state II have a refractive index above the crystalline value. Second, the decrease in polarizability between states I and II would require that hydrogen enter the sample at temperatures between 350°C and 600°C. However, hydrogen rapidly diffuses to the surface and desorbs at temperatures above 350°C.[9] Third, we do not observe localized vibrational modes associated with Si-H bonding.[9,10] Fourth, H effusion from Si above 350°C causes the spin density to increase[9] and the spin density decreases for our implanted samples (see Table 4).

219

The approach to amorphization can directly provide information about the relationship between damage and polarizability. Wesch and Gotz[30] measured the absorption coefficient and refractive index of Si versus ion dose for B and Ar ion implantation. They suggested that the increase in absorption was predominately governed by the concentration of point defects and defect clusters because more than half of *the total increase in absorption occured at low doses before any increase in n was measured for B implants at 77K.* The increase in n did correlate with the formation and overlap of amorphous zones as determined by comparing the infrared refractive index measurements with their ion channeling measurements.[30] The data of Wesch and Gotz support the arguments that the change in polarizabi'ity from state I to state II in Si occurs primarily by means of an average relaxation of the entire amorphous structure,[14,17] and that the decrease in epr spin density and band edge absorption (Table 4) occur primarily through the removal of defects within the amorphous material.[19]

In an extensive study on the dose dependence of the optical constants of Si during amorphization with Ge ions, Heidemann[22] reached a similar conclusion and added the observation that the changes in n and k during the transitions a-Si-I to a-Si-II and from a-Si-II to c-Si do not follow the same path as that taken during amorphization from c-Si to a-Si-I. He concludes that, during the transition a-Si-I to a-Si-II, not only is the quantity of defects reduced, but a qualitative change in the defect structure must occur as well.

It is apparent from the previous discussion that partial crystallization, shrinkage of voids, hydrogen ingress or egress and electronic effects associated with defect concentrations do not cause the change in refractive index between states I and II. The most likely explanation is the relaxation of average bond angle and bond length distortions in a random network model of the type measured by EXAFS for sputtered a-Ge films that was described above. Because the optical properties of a-Si-II are independent of all implantation parameters and of the annealing temperatures employed, the results strongly suggest that a-Si-II is in a definable and unique metastable thermodynamic state[18] which is achieved only under *special conditions for deposited amorphous films.*[31,14] *The a-Si-I state is also independent of all implantation parameters employed.* However, the evidence is insufficient to assign a unique thermodynamic state to a-Si-I. We consider a-Si-I a defect saturated and highly reproducible state of a-Si which may be unique because of the demonstrated stability of the state at room temperature.

Summary

A review of infrared studies on amorphous Si and Ge prepared by ion implantation indicated that these measurements provide quantitative information regarding the structure and regrowth rates of the amorphous layers. The values of amorphous layer depths and regrowth rates compare favorably with values obtained by ion channeling. It was also demonstrated that the infrared properties of refractive index and absorption strongly depend upon the thermal annealing history in the temperature regime $150^\circ C < T < 600^\circ C$. Evidence for the existence of two well defined optical states of a-Si and a-Ge was reviewed and compared with other measurements in the literature. The information reviewed suggests that the optical transition between the two states is correlated with a structural ordering within the amorphous material.

Acknowledgements

References

1. J.F. Gibbons, D.M. Dobkin, M.E. Greiner, J.L. Hoyt and W.G. Opyd, Mat. Res. Symp. Proc. Vol. 23 (North Holland, New York, 1984) p. 37.

2. J.C. North and W.M. Gibson, in Ion Implantation, eds. F.K. Eisen and L.T. Chadderton (Gordon and Breach, New York, 1971) p. 143.

3. L. Csepregi and J.W. Mayer, Phys. Lett. 54A, 157 (1975).

4. L. Csepregi, E.F. Kennedy, S.S. Lau, J.W. Mayer and T.W. Sigmon, Appl. Phys. Lett. 29, 645 (1976).

5. L. Csepregi, R.P. Kullen, J.W. Mayer and T.W. Sigmon, Solid State Comm. 21, 1019 (1977).

6. A recent review of this sizable body of work is given by J.M. Poate and J.S. Williams, in Ion Implantation and Ion Beam Processing, eds. J.S. Williams and J.M. Poate (Academic Press, Sydney, 1984) p. 14.

7. T.E. Seidel, IEEE Elec. Dev. Lett. EDL-4, 10, Oct. (1983).

8. E.C. Freeman and W. Paul, Phys. Rev. B20, 716 (1979).

9. C.C. Tsai and H. Fritzsche, Solar Energy Mat. 1, 29 (1979).

10. P.J. Zanzucchi, C.R. Wronski and D.E. Carlson, J. Appl. Phys. **48**, 5227 (1977).

11. G.K. Hubler, C.N. Waddell, W.G. Spitzer, J.E. Fredrickson, S. Prussin and R.G. Wilson, J. Appl. Phys. **50**, 3294 (1979).

12. W.G. Spitzer, J.S. Ko, C.N. Waddell, G.K. Hubler, and J.E. Fredrickson, J. Appl. Phys. **50**, 3775 (1979).

13. G.K. Hubler, P.R. Malmberg, C.N. Waddell, W.G. Spitzer and J.E. Fredrickson, Radiat. Eff. **60**, 35 (1982).

14. J.E. Fredrickson, C.N. Waddell, W.G. Spitzer and G.K. Hubler, Appl. Phys. Lett. **40**, 172 (1982).

15. C.N. Waddell, W.G. Spitzer, G.K. Hubler and J.E. Fredrickson, J. Appl. Phys. **53**, 5851 (1982).

16. Sook-Il Kwun, C.-H. Hong and W.G. Spitzer, J. Appl. Phys. **54**, 3125 (1983).

17. W.G. Spitzer, G.K. Hubler and T.A. Kennedy, Nucl. Inst. and Meth. **209/210**, 309 (1983).

18. C.N. Waddell, W.G. Spitzer, J.E. Fredrickson, G.K. Hubler and T.A. Kennedy, J. Appl. Phys. **55**, 4361 (1984).

19. G.K. Hubler, C.N. Waddell, W.G. Spitzer, J.E. Fredrickson and T.A. Kennedy, Mat. Res. Symp. Proc. Vol. **27** (North Holland, New York, 1984) p. 217.

20. W.G. Spitzer, L. Liou, K-W Wang, C.N. Waddell, G.K. Hubler and S.-I. Kwun, Advanced Semiconductor Processing and Characterization of Electronic and Optical Materials, Proc. of SPIE, Vol. **463**, Los Angeles, eds. D.K. Sadana and C.M. Lampert (SPIE, Bellingham, 1984) p. 546.

21. Kou-Wei Wang, W.G. Spitzer, E.P. Donovan and G.K. Hubler, J. Appl. Phys., in press.

22. K.F. Heidemann, Phil. Mag. **B44**, 465 (1981).

23. Kou-Wei Wang, W.G. Spitzer and G.K. Hubler, unpublished data.

24. E.P. Donovan, Thesis of Harvard Univ. (1982); E.P. Donovan, F. Spaepen, D. Turnbull, J.M. Poate and D.C. Jacobson, J. Appl. Phys., in press.

25. L. Liou, W.G. Spitzer and S. Prussin, J. Electrochem. Soc. **131**, 672 (1984).

26. R.A. Kant and G.K. Hubler, unpublished data.

27. R.P. Vasquez, A. Madhukar and A.R. Tanguay, Jr., unpublished data.

28. M.A. Paesler, D.E. Sayers, Raphael Tsu and J.G. Hernandez, Phys. Rev. **B28**, 4550 (1983).

29. R. Tsu, J.G. Hernandez and F.H. Pollack, J. Non-Cryst. Solids, **66**, 109 (1984); and J.G. Hernandez, S.S. Chau, D. Martin and R. Tsu, these proceedings.

30. W. Wesch and G. Gotz, Radiat. Eff. **49**, 137 (1980).

31. M. Janai, D.D. Allred, D.C. Booth and B.O. Seraphin, Solar Energy Mat. **1**, 11 (1979).

BIBLIOGRAPHY

1. E. A. Wolicki, C. R. Gossett, K. W. Marlow, and M. E. Toms, "Capabilities for Nonnuclear Applications with Nuclear Facilities at NRL," NRL Report 6599, 17 October 1967. (AD660658)

2. I. Manning and D. Padgett, "Transport Theory of Penetration by Heavy Ions," NRL Memorandum Report 2631, August 1973. (AD765315)

3. I. Manning and G. P. Mueller, "Depth Distribution of Energy Deposition by Ion Bombardment," Comp. Phys. Comm. 7, 85 (1974).

4. G. P. Mueller, "Total Cross-Section Corresponding to the Differential Cross-Section of Lindhard, Nielsen and Scharff," Radiat. Eff. 21, 253 (1974).

5. J. W. Butler, "Ion Implantation and Wear," Extended Abstracts [ONR-NRL] Tribology Workshop, Washington, DC, 14-16 October 1975 p. 90.

6. H. W. Kugel, L. Eytel, G. K. Hubler, and D. E. Murnick, "The Temperature Dependence of Hyperfine Fields at Rare-Earth Nuclei in Iron and Nickel," Phys. Rev. B13, 3697 (1976).

7. J. W. Butler, "Ion Implantation and Wear," Reports, Memoranda and Technical Notes of the Materials Research Council Summer Conference, La Jolla, CA (University of Michigan Document 005020, 1976) p. 255.

8. Irwin Manning, Mervine Rosen, and J. E. Westmoreland, "Adaptation of a Program for Depth Distribution of Energy Deposition by Ion Bombardment: Calculation of Ion Lateral Ranges," Comp. Phys. Comm. 12, 335 (1976).

9. I. Manning, M. Rosen, and J. E. Westmoreland, "Computer Code for the Calculation of Lateral Range of a PKA," NRL Memorandum Report 3358, September 1976. (ADA030633)

10. J. M. Poate, J. A. Borders, A. G. Cullis, and J. K. Hirvonen, "Ion Implantation as an Ultrafast Quenching Technique for Metastable Alloy Production: The Ag-Cu System," Appl. Phys. Letters 30, 365 (1977).

11. G. P. Mueller and Mervine Rosen, "A Boltzmann Transport Code for Ion Penetration in Matter," NRL Memorandum Report 3556, July 1977. (ADA043502)

12. S. P. Singhal, H. Herman, and J. K. Hirvonen, "Spinodal Decomposition in Amorphous Au-Implanted Pt," Appl. Phys. Letters 32, 25 (1978).

13. A. G. Cullis, J. A. Borders, J. K. Hirvonen, and J. M. Poate, "Metastable Alloy Layers Produced by Implantation of Ag^+ and Ta^+ Ions into Cu Crystals," Phil. Mag. B37, 615 (1978).

14. J. K. Hirvonen, "Ion Implantation in Tribology and Corrosion Science," J. Vac. Sci. Technol. 15, 1662 (1978).

15. Wen-Wei Hu, C. R. Clayton, H. Herman, and J. K. Hirvonen, "Fatigue-Life Enhancement by Ion Implantation," Scr. Met. 12, 697 (1978).

16. E. McCafferty and G. K. Hubler, "Electrochemical Behavior of Palladium-Implanted Titanium," J. Electrochem. Soc. 125, 1892 (1978).

17. J. W. Butler, "Some Effects of Ion Implantation on Fluid-Solid Surface Interactions," Proceedings of the Fourth Symposium on Fluid Solid Surface Interactions, sponsored by the U.S. Department of the Navy and the West German Federal Ministry of Defense, 18-20 October 1978, National Bureau of Standards, Gaithersburg, MD, p. 267.

18. J. K. Hirvonen, C. A. Carosella, R. A. Kant, I. L. Singer, R. Vardiman, and B. B. Rath, "Improvement of Metal Properties by Ion Implantation," Thin Solid Films 63, 5 (1979).

19. G. K. Hubler, P. R. Malmberg, and T. P. Smith, III, "Refractive Index Profiles and Range Distributions of Silicon Implanted with High-Energy Nitrogen," J. Appl. Phys. 50, 7147 (1979).

20. G. K. Hubler, C. N. Waddell, W. G. Spitzer, J. E. Fredrickson, S. Prussin, and R. G. Wilson, "High-Fluence Implantations of Silicon: Layer Thickness and Refractive Indices," J. Appl. Phys. 50, 3294 (1979).

21. R. A. Kant, J. K. Hirvonen, A. R. Knudson, J. S. Wollam, "Surface Hardening of Beryllium by Ion Implantation," Thin Solid Films 63, 27 (1979).

22. E. G. Spitzer, J. S. Ko, C. N. Waddell, J. E. Fredrickson, and G. K. Hubler, "Plasma Region in High-Fluence Implants of Phosphorus in Amorphized Silicon," J. Appl. Phys. 50, 3775 (1979).

23. Y. F. Wang, C. R. Clayton, G. K. Hubler, W. H. Lucke, and J. K. Hirvonen, "Applications of Ion Implantation for the Improvement of Localized Corrosion Resistance of M50 Bearing Steel," Thin Solid Films 63, 11 (1979).

24. J. K. Hirvonen, "Implantation Into Metals - Mechanical Property Changes," Proceedings of the 1st Conference on Ion Beam Modification of Materials, eds., J. Gyulai, T. Lohner, and E. Pasztor, Central Research Institute for Physics, H-1525, Budapest 114 POB 49, Hungary, Vol. III, p. 1753 (1979).

25. J. K. Hirvonen and J. W. Butler, "Improved Corrosion and Mechanical Behavior of Alloys by Ion Implantation," 1978 Science and Engineering Symposium Proceedings (Joint Air Force and Navy), Vol. IV (Basic Research), Navy Material Command and Air Force Systems Command, p. 981 (1979).

26. J. K. Hirvonen, J. W. Butler, T. P. Smith, III, R. A. Kant, and V. C. Westcott, "Sliding-Wear Reduction by Ion Implantation," Proceedings of the 1st Conference on Ion Beam Modification of Materials, eds., J. Gyulai, T. Lohner, and E. Pasztor, Central Research Institute for Physics, H-1525, Budapest 114, POB 49, Hungary, Vol. III, p. 1973 (1979).

27. J. K. Hirvonen, J. M. Poate, Z. L. Liau, and J. W. Mayer, "Sputtering Limitations for High-Dose Implantations," Proceedings of the 1st Conference on Ion Beam Modification of Materials, eds., J. Gyulai, T. Lohner, and E. Pasztor, Central Research Institute for Physics, H-1525, Budapest 114, POB 49, Hungary, Vol. III, p. 1519 (1979).

28. G. K. Hubler, P. R. Malmberg, C. A. Carosella, T. P. Smith, III, W. G. Spitzer, C. N. Waddell, and C. N. Phillippi, "Optical Effects Resulting from Deep Implants of Silicon with Nitrogen and Phosphorus," Proceedings of the 1st Conference on Ion Beam Modification of Materials, eds., J. Gyulai, T. Lohner, and E. Pasztor, Central Research Institute for Physics, H-1525, Budapest 114, POB 49, Hungary, Vol. II, p. 1323 (1979).

29. W. W. Hu, C. R. Clayton, H. Herman, J. K. Hirvonen, and R. A. Kant, "Fatigue-Life Enhancement of Steel by Nitrogen Implantation," Proceedings of the 1st Conference on Ion Beam Modification of Materials, eds., J. Gyulai, T. Lohner, and E. Pasztor, Central Research Institute for Physics, H-1525, Budapest 114, POB 49, Hungary, Vol. III, p. 1977 (1979).

30. D. J. Land, D. G. Simons, J. G. Brennan, M. D. Brown, and J. K. Hirvonen, "Range Distribution for 25-100 keV $^{14}N^+$ Ions," Proceedings of the 1st Conference on Ion Beam Modification of Materials, eds., J. Gyulai, T. Lohner, and E. Pasztor, Central Research Institute for Physics, H-1525, Budapest 114, POB 49, Hungary, Vol. I, p. 93 (1979).

31. E. McCafferty, G. K. Hubler, and J. K. Hirvonen, "Corrosion Control by Ion-Implantation," Proceedings of the 1978 Tri-Service Conference on Corrosion, ed. by M. Levy and J. Brown, Materials and Ceramics Information Center, Battelle, OH, p. 435, May 1979. (ADA073054)

32. R. G. Vardiman, R. A. Kant, and T. W. Crooker, "The Effect of Ion Implantation on Fatigue Behavior of Ti/6Al/4V Alloy," Report of NRL Progress, p. 4, May 1979.

33. I. Manning, "Use of Range Distributions to Approximate Energy Distributions," F. A. Smidt and L. A. Beach, Coordinators, Cooperative Radiation Effects Simulation Program (Annual Progress Report) NRL Memorandum Report 4080 (October 1979), p. 2. (ADA075608)

34. I. Manning, "Approximation for Energy Deposition in Ion Beam Bombardment," F. A. Smidt and L. A. Beach, Coordinators, Cooperative Radiation Effects Simulation Program (Annual Progress Report) NRL Memorandum Report 4080 (October 1979), p. 8. (ADA075608)

35. M. Zamanzadeh, A. Allan, H. W. Pickering, and G. K. Hubler, "Effect of Helium-, Iron-, and Platinum-Ion Implantation on Permeation of Hydrogen Through Ion Membranes," ONR Technical Report No. 10 (Contract No. N00-14-75-C-0264), July 1979. (ADA071595)

36. G. K. Hubler and E. McCafferty, "The Corrosion Behaviour and Rutherford Backscattering Analysis of Palladium-Implanted Titanium," Corros. Sci. 20, 103 (1980).

37. R. N. Bolster and L. L. Singer, "Surface Hardness and Abrasive Wear Resistance of Nitrogen-Implanted Steels," Appl. Phys. Letters 36, 208 (1980).

38. I. L. Singer and J. S. Murday, "The Chemical State of Ion-Implanted Nitrogen in Fe$_{18}$Cr$_8$Ni Steel," J. Vac. Sci. Technol. 17, 327 (1980).

39. G. P. Mueller, "New Analytical Calculation of Displacement Damage," Nucl. Instr. and Methods 170, 389 (1980).

40. G. P. Mueller, "Differential Cross Section and Related Integrals for the Moliere Potential," Radiat. Eff. Letters 50, 87 (1979-1980)

41. W. N. Allen, P. Brant, C. A. Carosella, J. J. DeCorpo, C. T. Ewing, F. E. Saalfeld, and D. C. Weber, "Ion Implantation Studies of (BN)$_x$ and (CH)$_x$," Synthetic Metals 1, 151 (1979/80).

42. L. Buene, J. M. Poate, D. C. Jacobson, C. W. Draper, and J. K. Hirvonen, "Laser Irradiation of Nickel Single Crystals," Appl. Phys. Lett. 37, 385 (1980).

43. J. K. Hirvonen, J. M. Poate, A. Greenwald, R. Little, "Pulsed Electron Beam Irradiation of Ion-Implanted Copper Single Crystals," Appl. Phys. Lett. 36, 564 (1980).

44. G. K. Hubler, P. R. Malmberg, C. A. Carosella, T. P. Smith, III, W. G. Spitzer, C. N. Waddell, and C. N. Phillippi, "Optical Effects Resulting fom Deep Implants of Silicon with Nitrogen and Phosphorus," Radiat. Eff. 48, 81 (1980).

45. G. K. Hubler and E. McCafferty, "The Corrosion Behaviour and Rutherford Backscattering Analysis of Palladium-Implanted Titanium," Corrosion Science 20, 103 (1980).

46. M. Zamanzadeh, A. Allam, H. W. Pickering, and G. K. Hubler, "Effect of Helium, Iron, and Platinum Implantation on the Absorption of Hydrogen by Iron," J. Electrochem. Soc. 127, 1688 (1980).

47. C. A. Carosella, I. L. Singer, R. C. Bowers, and C. R. Gossett, "Friction and Wear Reduction of Bearing Steel via Ion Implantation," Ion Implantation Metallurgy, eds. C. M. Preece and J. K. Hirvonen, (The Metallurgical Society of AIME, 1980), p. 103.

48. C. R. Clayton, K. G. K. Doss, H. Herman, S. Prasad, Y-F. Wang, J. K. Hirvonen, and G. K. Hubler, "Modification of the Corrosion Behavior of 304 Stainless Steel by Phosphorus Implantation," Ion Implantation Metallurgy, eds. C. M. Preece and J. K. Hirvonen, (The Metallurgical Society of AIME, 1980), p. 65.

49. J. K. Hirvonen, "Introduction," Ion Implantation, Treatise on Materials Science and Technology 18, 1-16, Academic Press (1980).

50. J. K. Hirvonen, ed., Ion Implantation, Treatise on Materials Science and Technology 18, Academic Press (1980).

51. J. W. Mayer, S. S. Lau, B-Y Tsaur, J. M. Poate, and J. K. Hirvonen, "High-Dose Implantation and Ion-Beam-Mixing," Ion Implantation Metallurgy, eds., C. M. Preece and J. K. Hirvonen, (The Metallurgical Society of AIME, 1980), p.37.

52. W. W. Hu, H. Herman, C. R. Clayton, J. Kozubowski, R. A. Kant, J. K. Hirvonen, and R. K. MacCrone, "Surface-Related Mechanical Properties of Nitrogen-Implanted 1018 Steel," Ion Implantation Metallurgy, eds. C. M. Preece and J. K. Hirvonen, (The Metallurgical Society of AIME 1980), p.92.

53. C. M. Preece and J. K. Hirvonen, Editors, Ion Implantation Metallurgy, (The Metallurgical Society of the AIME, 1980).

54. I. L. Singer, R. N. Bolster, and C. A. Carosella, "Abrasive Wear Resistance of Titanium and Nitrogen Implanted 52100 Steel Surfaces," Thin Solid Films 73, p. 283 (1980).

55. G. K. Hubler, J. K. Hirvonen, I. L. Singer, R. C. Bowers, C. R. Gossett, M. R. Weller, C. R. Clayton, and Y. A. Wang, " Application of Ion Implantation for the Improvement of Localized Corrosion Resistance of M50 Steel Bearings," NRL Memorandum Report 4481, Mar 1980. (ADA097230)

56. I. L. Singer, J. S. Murday, H. Ravner, J. K. Hirvonen, and N. L. Jarvis, "New Opportunities in Tribology," Naval Research Reviews 32, #4 p. 4 (1980).

57. I. L. Singer and R. N. Bolster, "Surface Hardness and Abrasive Wear Resistance of Nitrogen-Implanted Steels," Ion Implantation Metallurgy, eds. C. M. Preece and J. K. Hirvonen, The Metallurgical Society of AIME, p. 116 (1980).

58. J. H. Harding and R. H. Bassel, "A Theoretical Study of the Defect Structure of Praseodymium Chromite," TP.862, Theoretical Physics Division, AERE Harwell, Oxfordshire, United Kingdom, July 1980.

59. F. A. Smidt, "The Use of Ion Implantation for Materials Processing," Semi-annual Progress Report for Period 1 Oct. 1979 - 31 Mar. 1980, NRL Memorandum Report 4341, Oct. 6, 1980. (ADA090714)

60. L. Buene, D. C. Jacobson, S. Nakahara, J. M. Poate, C. W. Draper, and J. K. Hirvonen, "Laser Irradiation of Nickel: Defect Structures and Surface Alloying," pp. 583-590 in Laser and Electron-Beam Solid Interactions and Materials Processing, eds. Gibbons, Hess, Sigmon, Elsevier North Holland, Inc., 1981.

61. G. K. Hubler, "Use of Ion Beam Analysis in Metal Modification By Means of Ion Implantation," Nucl. Instrum. Methods 191, p. 107 (1981).

62. F. A. Smidt, "The Use of Ion Implantation for Materials Processing," Semi-annual Progress Report for the Period 1 Apr. 1980 - 30 Sept. 1980, NRL Memorandum Report 4527, June 24, 1981. (ADA102154)

63. F. A. Smidt, J. K. Hirvonen, and S. Ramalingam, "Preliminary Evaluation of Ion Implantation as a Surface Treatment to Reduce Wear of Tool Bits," NRL Memorandum Report 4616, Naval Research Laboratory, 25 Sep 1981. (ADA105-053)

64. M. Rosen and G. P. Mueller, "Calculation of Self Sputtering of High Energy Copper Ions," 1981 NRL Review. pp. 152-154.

65. I. L. Singer, C. A. Carosella, and J. R. Reed, "Friction Behavior of 52100 Steel Modified by Ion Implanted Ti," Nuclear Instruments and Methods 182/183, pp. 923-932 (1981).

66. I. L. Singer, "Surface Morphologies Produced by Ion Milling on Ion-Implanted 18Cr8Ni Steels," J. Vac. Sci. Technol. 18 (2), p. 175 (1981).

67. R. N. Bolster, I. L. Singer, W.A. Glaeser, and D.A. Rigney, "Surface Hardness and Abrasive Wear Resistance of Ion-Implanted Steels," ASLE Trans. 24, p. 526 (1981).

68. R. G. Allas, A. R. Knudson, J. M. Lambert, P. A. Treado, and G. W. Reynolds, "Self-Ion Sputtering Yields for Copper, Nickel, and Aluminum," Nucl. Instrum. Methods 194, p. 615 (1982).

69. G. K. Hubler, P. Trzaskoma, E. McCafferty, and I. L. Singer, "Electrochemical Behavior of an Amorphous Fe-Ti-C Surface in Titanium-Implanted Steel," Ion Implantation Into Metals, eds., V. Ashworth, W. A. Grant, and R. P. M. Procter, Pergamon Press, NY, pp. 24-34 (1982).

70. R. G. Vardiman, D. Creighton, G. Saliver, A. Effatian, and B. B. Rath, " The Effect of Ion Implantation on Fretting Fatigue in Ti-6A1-4V," in STP 780 Symposium on Materials Evaluation Under Fretting Conditions, Ed. S. R. Brown, American Soc. for Testing and Materials, Philadelphia, Pa., p. 138 (1982).

71. J. E. Fredrickson, C. N. Waddell, W. G. Spitzer, and G. K. Hubler, "Effects of Thermal Annealing on the Refractive Index of Amorphous Silicon Produced by Ion Implantation," Appl. Phys. Lett. 40, 172 (1982).

72. G. K. Hubler, P. R. Malmberg, C. N. Waddell, W. G. Spitzer, and J. E. Fredrickson, "Electrical and Structural Characterization of Implantation Doped Silicon by Infrared Reflection," Radiat. Eff. 60, 35 (1982).

73. R. G. Vardiman, R. N. Bolster, and I. L. Singer, "The Effect of Nitrogen Implantation on Martensite in 304 Stainless Steel," in Metastable Materials Formation by Ion Implantation, Eds. S. T. Picraux and W. J. Choyke, Elsevier Science Publishing Co., NY, p. 269 (1982).

74. R. G. Vardiman and R. A. Kant, "The Improvement of Fatigue Life in Ti-6A1-4V by Ion Implantation," J. Appl. Physics 53, pp. 690-694 (1982).

75. C. N. Waddell, W. G. Spitzer, G. K. Hubler, and J. E. Fredrickson, "Infrared Studies of Isothermal Annealing of Ion Implanted Silicon: Refractive Indices, Regrowth Rates, and Carrier Profiles," J. Appl. Phys. 53, pp. 5851-5862 (1982).

76. C. R. Clayton, K. G. K. Doss, Y-F Wang, J. B. Warren, and G. K. Hubler, "RHEED, AES, and XPS Studies of the Passive Films Formed on Ion-Implanted Stainless Steel," Ion Implantation into Metals, eds., V. Ashworth, W. A. Grant, and R. P. M. Procter, Pergamon Press, NY, pp. 67-76 (1982).

77. C. R. Gossett, "Near Surface Analysis with Energetic Ion Beams," in ACS Symposium Series, No. 199, Industrial Applications of Surface Analysis, eds. L. A. Casper and C. J. Powell, American Chemical Society, Washington, DC, pp. 49-68 (1982).

78. K. S. Grabowski and L. E. Rehn, "Ion Implantation Effects on the Thermal Oxidation of Metals," in Corrosion of Metals Processed by Directed Energy Beams, eds. C. R. Clayton and C. M. Preece, The Metallurgical Society of AIME, p. 23 (1982).

79. G. K. Hubler, "DOD Applications of Implantation-Modified Materials," in Metastable Materials Formation by Ion Implantation, eds., S. T. Picraux and W. J. Choyke, Elsevier Science Publishing Co., NY, pp. 341-354 (1982).

80. F. A. Smidt, "The Use of Ion Implantation for Materials Processing," Annual Progress Report for the Period 1 Oct. 1980 - 30 Sept. 1981, NRL Memorandum Report 4821, 2 July 1982. (ADA119719)

81. R. A. Kant, A. R. Knudson, and K. Kumar, "Mechanical and Microstructural Properties of Boron Implanted Beryllium," in Metastable Materials Formation by Ion Implantation, eds., S. T. Picraux and W. J. Choyke, Elsevier Science Publishing Co., NY, pp. 253-259 (1982).

82. E. McCafferty, P. G. Moore, J. D. Ayers, and G. K. Hubler, "Effect of Laser Processing and Ion Implantation on Aqueous Corrosion Behavior," in Corrosion of Metals Processed by Directed Energy Beams, eds., C. R. Clayton and C. M. Preece, AIME, pp. 1-21 (1982).

83. G. W. Reynolds, F. R. Vozzo, R. G. Allas, A. R. Knudson, and J. M. Lambert, "The Surface Behavior of a Binary Alloy by Ion Implantation," in Metastable Materials Formation by Ion Implantation, eds., S. T. Picraux and W. J. Choyke, Elsevier Science Publishing Co., NY, pp. 51-57 (1982).

84. W. K. Chan, C. R. Clayton, R. G. Allas, C. R. Gossett, and J. K. Hirvonen, "Electrochemical and A. E. S. Studies of Fe-Cr Surface Alloys Formed on AISI 52100 Steel by Ion Beam Mixing," Nucl. Instr. Methods 209-210, pp. 857-865 (1983).

85. E. N. Kaufmann, R. G. Musket, J. J. Truhan, K. S. Grabowski, C. R. Gossett, and I. L. Singer, "High-Temperature Oxidation of Ion Implanted Tantalum," Nucl. Instr. Methods, 209/210, pp. 953-961 (1982).

86. M. Rosen, G. P. Mueller and W. A. Fraser, "Computer Study of Self-Sputtering of Cu and Ni at 90 KeV," Nucl. Inst. Methods, 209/210, p. 63 (1983).

87. K. S. Grabowski and R. A. Kant, "Methods to Control Target Heating During Ion Implantation," Ion Implantation: Equipment and Techniques, eds. H. Ryssel and H. Glawisehnig, Springer Series in Electrophysics Vol. XI, Springer-Verlag, New York, p. 364 (1983).

88. R. Valori, D. Popgoshev, and G. K. Hubler, "Ion Implantation of Bearing Surfaces for Corrosion Resistance," ASME, J. Lub. Technology 105, pp. 534-541 (1983).

89. J. M. Lambert, P. A. Treado, D. Trbojevic, R. G. Allas, A. R. Knudson, G. W. Reynolds, and F. R. Vozzo, "Sputtering Analysis with PIXE," IEEE Trans. Nucl. Sci. NS-30, pp. 1285-1290 (1983).

90. G. W. Reynolds, R. G. Allas, J. M. Lambert, and P. A. Treado, "Sputtering from Binary Alloys - A Technique for Evaluating Change in Surface Binding Energy," IEEE Trans. Nucl. Sci. NS-30, pp. 1749-1751 (1983).

91. N. E. W. Hartley and J. K. Hirvonen, "Wear Testing Under High Load Conditions," Nucl. Instr. Methods 209/210, pp. 933-940 (1983).

92. W. G. Spitzer, G. K. Hubler, and T. A. Kennedy, "Properties of Amorphous Silicon Produced by Ion Implantation: Thermal Annealing," Nucl. Instr. Methods 209/210, p. 309 (1983).

93. C. R. Clayton, Y-F Wang, and G. K. Hubler, "An Electrochemical Study of Amorphous Ion Implanted Stainless Steels," Passivity of Metals and Semiconductors ed. by M. Froment, Elsevier, Science Publishers, Amsterdam, Netherlands, pp. 305-310 (1983).

94. R. G. Vardiman and I. L. Singer, "Transformation of Stress-Induced Martensite in 304 Stainless Steel by Ion Implantation," Materials Letters 2, pp. 150-154 (1983).

95. J. K. Hirvonen and C. R. Clayton, "Materials Modification by Ion Implantation" Ch. 12 in Surface Modification and Alloying ed. by J. M. Poate, G. Foti and D. C. Jacobson, Plenum Press, N.Y., pp. 323-384 (1983).

96. I. L. Singer and R. A. Jeffries, "Surface Chemistry and Friction Behavior of Ti-implanted 52100 Steel," J. Vac. Sci. Technol. A1, p. 317-321 (1983).

97. I. L. Singer, "Carburization of Steel Surfaces During Implantation of Ti Ions At High Fluences," J. Vac. Sci. Technol. A1, p. 419-422 (1983).

98. I. L. Singer and T. M. Barlak, "Absorption of Carbon from Residual Gases During Ti-Implantation of Alloys," Appl. Phys. Letts. 43, pp. 457-459 (1983).

99. I. L. Singer, Discussion of "Tribological Properties of Ion-Implanted 52100 Steel," by T. E. Fischer, et al. ASLE Trans. 26, pp. 473-474 (1983).

100. I. L. Singer and R. A. Jeffries, "Effects of Implantation Energy and Carbon Concentration on the Friction and Wear of Titanium-Implanted Steel," Appl. Phys. Letts. 43, pp. 925-927 (1983).

101. S. A. Dillich and I. L. Singer, "Effect of Titanium Implantation on the Friction and Surface Chemistry of A Co-Cr-W-C Alloy," Thin Solid Films 108, pp. 219-227 (1983).

102. B. D. Sartwell, G. K. Hubler and E. McCafferty, "High Dose Ion Implantation and the Corrosion Behavior of Ferrous Metals", Proceedings of the Workshop on Ion Mixing, Sandia Report SAND 83-1230, pp. 136-149 (1983). (ADP001663)

103. K. S. Grabowski, R. J. Colton, W. K. Chan and C. R. Clayton, "Ion Mixing of Cr Layers on Steel: Effect of Impurities During Ion Mixing," Proc. Workshop on Ion Mixing and Surface Layer Alloying, SAND 83-1230, p. 117 (1983). (ADP001661)

104. N. C. Koon, P. Pehrsson, D. Weber and A. I. Schindler, "Magnetic Properties of Iron-Implanted Graphite," J. Appl. Phys. 55, pp. 2497-2499 (1984).

105. F. A. Smidt., "The Use of Ion Implantation for Materials Processing Annual Progress Report for the Period 1 Oct. 1981-30 Sept. 1982," NRL Memorandum Report 5177, Sept. 28, 1983. (ADA134457)

106. R. N. Bolster and I. L. Singer, "Polishing Wear Studies of Coating Materials," in Mechanical Properties, Performance and Failure Modes of Coatings, ed by T.R. Shines and M.B. Peterson, Cambridge Univ. Press, Cambridge, U.K. pp. 200-207 (1984).

107. S. A. Dillich, R. N. Bolster and I. L. Singer, "Effects of Ion-Implantation on the Tribological Behavior of a Cobalt-Based Alloy," in Surface Engineering ed. by R. Kossowsky and S.C. Singhal, M. Nijhoff Publishers, Dordrecht. Neth. p. 197-207 (1984).

108. P. R. Malmberg, R. G. Allas, J. M. Lambert, P. A. Treado, and G. W. Reynolds, "Effects of Non-Normal Incidence on the Implantation of Copper with Gold and Tantalum," Nucl. Insts. and Meth. in Phys. Res. B2 p. 679-683 (1984).

109. G. W. Reynolds, F. R. Vozzo, R. G. Allas, P. A. Treado and J. M. Lambert, "A Model of the Surface Binding Energy For A Ternary Alloy Produced by Ion Implantation," Nucl. Inst. and Meth. in Phys. Res. B2 p. 804-808 (1984).

110. M. Rosen and R. H. Bassel, "Binary Collision Cascade Calculation of Sputtering from Cu-Ni Alloys by 90 keV Cu and Ni Ions", Nucl. Insts. and Meth. in Phys. Res. B2, p. 592-595 (1984).

111. C. R. Clayton, Y-F Wang, G. K. Hubler, "Modification of Passivity of 316 Stainless Steel by B and P Implantation, "Fundamental Aspects of Corrosion Protection by Surface Modification, eds., E. McCafferty, C.R. Clayton and J. Oudar, The Electrochem. Soc., Pennington, N.J., p. 32-41 (1984).

112. C. R. Clayton, W. K. Chan, J. K. Hirvonen, G. K. Hubler and J. R. Reed, "Modification of the Localized Corrosion Behavior of AISI 52100 Steel by Ion Implantation, "Fundamental Aspects of Corrosion Protection by Surface Modification, eds., E. McCafferty, C.R. Clayton and J. Oudar, The Electrochem. Soc., Pennington, N.J. p. 17-31 (1984).

113. C. N. Waddell, W. G. Spitzer, J. E. Fredrickson, G. K. Hubler and T. A. Kennedy, "Amorphous Silicon Produced by Ion-Implantation: Effects of Ion Mass and Thermal Annealing", J. Appl. Phys. 55, 4361-4366 (1984).

114. G. K. Hubler, C. N. Waddell, W. G. Spitzer, T. P. Smith and J. E. Frederickson, "Physical Propties of Two Metastable States of Amorphous Silicon," Ion Implantation and Ion Beam Processing of Materials, eds. G. K. Hubler, O. W. Holland, C. R. Clayton and C. W. White, p. 217-222 (1984).

115. I. Manning, "Boltzmann Approach to Cascade Mixing," Ion Implantation and Ion Beam Processing of Materials, eds. G. K. Hubler, O. W. Holland, C. R. Clayton and C. W. White, pp. 91-96 (1984).

116. N. C. Koon, D. C. Weber, P. E. Pehrsson, and A. I. Schindler, "Magnetic Properties of Ion Implanted Materials," Ion Implantation and Ion Beam Processing of Materials, eds. G. K. Hubler, O. W. Holland, C. R. Clayton and C. W. White, pp. 445-448 (1984).

117. R. A. Kant and B. D. Sartwell, "Surface Modification by Ion Beam Enhanced Deposition," Ion Implantation and Ion Beam Processing of Materials, eds. G. K. Hubler, O. W. Holland, C. R. Clayton and C. W. White, p. 525-530 (1984).

118. D. Farkas, M. Rangaswamy and I. L. Singer, "Computer Modeling of High Fluence Ti Implantation and Vacuum Carburization in Steel," Ion Implantation and Ion Beam Processing of Materials, eds. G. K. Hubler, O. W. Holland, C. R. Clayton and C. W. White, p. 609-614 (1984).

119. K. S. Grabowski, N. E. W. Hartley, C. R. Gossett and I. Manning, "Retention of Ions Implanted At Non-Normal Incidence," Ion Implantation and Ion Beam Processing of Materials, eds. G.K. Hubler, O. W. Holland, C. R. Clayton and C. W. White, p. 615-620 (1984).

120. I. L. Singer and R. A. Jeffries, "Processing Steels for Tribological Applications by Titanium Implantation," Ion Implantation and Ion Beam Processing of Materials, eds. G. K. Hubler, O. W. Holland, C. R. Clayton and C. W. White, p. 673-678 (1984).

121. R. G. Vardiman, "Wear Improvement in Ti-6Al-4V by Ion Implantation," Ion Implantation and Ion Beam Processing of Materials, eds. G. K. Hubler, O. W. Holland, C. R. Clayton and C. W. White, p. 699-704 (1984).

122. K. Kumar, H. Newborn and R. A. Kant, "Wear Behavior of Flat and Graded Profile Boron Implanted Beryllium," Ion Implantation and Ion Beam Processing of Materials, eds. G. K. Hubler, O. W. Holland, C. R. Clayton and C. W. White, p. 649-654 (1984).

123. S. Dillich, R. N. Bolster, and I. L. Singer, "Friction and Wear Behavior of Hardface Materials Implanted with Ti or N," Ion Implantation and Ion Beam Processing of Materials, eds. G. K. Hubler, O. W. Holland, C. R. Clayton and C. W. White, p. 637-642 (1984).

124. I. L. Singer, "Tribomechanical Properties of Ion Implanted Alloys: Approaches, Present Knowledge and Future Directions," Ion Implantation and Ion Beam Processing of Materials, eds. G. K. Hubler, O. W. Holland, C. R. Clayton and C. W. White, p. 585-596 (1984).

125. W. C. Oliver, R. Hutchings, J. B. Pethica, I. L. Singer and G. K. Hubler, "Hardness as a Measure of Wear Resistance," Ion Implantation and Ion Beam Processing of Materials, eds. G. K. Hubler, O. W. Holland, C. R. Clayton and C. W. White, p. 603-608 (1984).

126. I. L. Singer and R. A. Jeffries, "Friction, Wear and Deformation of Soft Steels Implanted with Ti and N," Ion Implantation and Ion Beam Processing of Materials, eds. G. K. Hubler, O. W. Holland, C. R. Clayton and C. W. White, p. 667-672 (1984).

127. K. S. Grabowski and C. R. Gossett, "Effect of Cr^+ Implantation on the Thermal Oxidation of Ta," Ion Implantation and Ion Beam Processing of Materials, eds. G. K. Hubler, O. W. Holland, C. R. Clayton and C. W. White, p. 741-746 (1984).

128. F. A. Smidt, G. R. Johnston, J. A. Sprague, V. Provenzano, S. Y. Hwang, G. H. Meier, and F. S. Pettit, "Modification of the Oxidation and Hot Corrosion Behavior of CoCrAl Alloys by Ion Implantation", in Surface Engineering, ed. by R. Kossowsky and S. C. Singhal, Martinus Nijhoff Publishers, Dordrecht, Neth. p. 507-523 (1984).

129. J. A. Sprague, I. L. Singer and C. R. Gossett, "Characterization of Oxide Scales on Complex Alloys Using Multiple Microanalytical Techniques," in Proceedings of the 42nd Annual Meeting of the Electron Microscopy Society of America, ed. by G. W. Bailey, San Francisco Press, San Francisco, CA pp. 600-603 (1984).

130. I. L. Singer and R. A. Jeffries, "Processing Steels for Tribological Applications by Titanium Implantation", ASLE Trans. 28, p. 134-138 (1984).

131. I. L. Singer, "Surface Analysis, Ion Implantation and Tribological Processes Affecting Steels", Applications of Surface Science 18, p. 28-62 (1984).

132. W. M. Bone, R. J. Colton, I. L. Singer and C. R. Gossett, "SIMS, Auger and Nuclear Reaction Analysis of N-Implanted Fe Alloys", J. Vac. Sci. Technol. A2, p. 788-789 (1984).

133. I. L. Singer "Composition of Metals Implanted to Very High Fluences," Vacuum 34, p. 853-859 (1984).

134. G. K. Hubler, T. A. Kennedy, C. N. Waddell, W. G. Spitzer and J. E. Fredrickson, "Physical Properties of Two Metastable States of Amorphous Silicon", in Ion Implantation and Ion Beam Processing of Materials, eds. G. K. Hubler, O. W. Holland, C. R. Clayton and C. W. White, Elsevier, New York, p. 217 (1984).

135. W. G. Spitzer, L. Liou, K-W Wang, C. N. Waddell, G. K. Hubler and S-I Kwun, "Infrared Properties of Heavily Implanted Silicon, Germanium and Gallium Arsenide", in Advanced Semiconductor Processing and Characterization of Electronic and Optical Materials, SPIE, Vol 463, eds., D. K. Sadana and C. M. Lampert, SPIE, Bellingham, WA, p. 46-55 (1984).

136. R. A. Neiser, K. S. Grabowski and C. R. Houska, "A Nondestructive Near Surface X-ray Diffraction Probe", in Nondestructive Evaluation: Application to Materials Processing, eds. O. Buck and S. M. Wolf, American Society for Metals, Metals Park, OH, p. 207-214 (1984).

137. F. A. Smidt and B. D. Sartwell, "Manufacturing Technology Program to Develop a Production Ion Implantation Facility for Procssing Bearings and Tools", Nucl. Instr. Methods in Physics Research B6, pp. 70-77 (1985).

138. R. A. Kant, B. D. Sartwell, I. L. Singer, and R. G. Vardiman, "Adherent TiN Films Produced by Ion Beam Enhanced Deposition at Room Temperature", Nucl. Instr. Methods in Physics Research B7/8, pp. 915-919 (1985).

139. D. A. Baldwin, B. D. Sartwell, and I. L. Singer, "In Situ Auger Analysis of Surface Composition During High Fluence Ion Implantation", Nucl. Instr. Methods in Physics Research B7/8, pp. 49-53 (1985).

140. B. D. Sartwell and D. A. Baldwin, "In Situ Proton-Induced X-ray Emission and Auger Electron Spectroscopy Study of Titanium and Niobium Implantation of Iron Films", Materials Sci. and Engr. 69, pp. 539-547 (1985).

141. R. H. Bassel, K. S. Grabowski, M. Rosen, M.L. Roush and F. Davarya, "Carburization During Cr Self Implantation in a ^{13}CO Atmosphere," Nucl. Insts. and Meth. in Physics Research B9 p. 30-32 (1985).

142. D. Farkas, I. L. Singer, and M. Rangeswamy "Modeling of High Fluence Ti Ion-Implantation and Vacuum Carburization in Steel", J. Applied Physics 57, pp. 1114-1120 (1985).

143. G. K. Hubler, I. L. Singer and C. R. Clayton, "Mechanical and Chemical-Properties of Tantalum-Implanted Steels", Material Sci. and Engr. 69, pp. 203-210 (1985).

144. F. A. Smidt "Recent Advances in the Application of Ion-Implantation to Corrosion and Wear Protection", Nucl. Instr. and Meth. in Phys. Res. B10, p. 532-538 (1985).

145. G. K. Hubler, E. P. Donovan, K-W. Wang and W.G. Spitzer, "Thermal Annealing Behavior of Hudrogen-Free Amorphous Silicon and Germanium", Advanced Applications of Ion Implantation, SPIE Vol. 530, eds., M.I. Current, D. K. Sadana, SPIE, Bellingham, WA, p. 222-229 (1985).

146. R. B. Benson, Jr., L. S. Stephenson, J. Bentley, G. K. Hubler and P. A. Parrish, "The Microstructures in Aluminum Annealed After Implantation With Selected Concentrations of Molybdenum", Fifth International Conference on Ion and Plasma Assisted Techniques, ed. H. Oechsmer, C.E.P. Consultants, Edinburgh, U.K., p. 169 (1985).

147. K-W. Wang, W. G. Spitzer, G. K. Hubler and E. P. Donovan, "Effect of Annealing on the Optical-Properties of Ion-Implanted Ge", J. Appl. Phys. 57, 2739-2751 (1985).

148. G. K. Hubler and F. A. Smidt "Application of Ion-Implantation to Wear Protection of Materials", Nucl. Instrum. & Meth. in Phys. Res. B7/8, 151-157 (1985).

149. K. S. Grabowski, F. D. Correll and F. R. Vozzo "Sputtering and Migration During Ta Implantation of Fe", Nucl. Instrum. and Meth. in Phys. Res. B7/8, p. 798-802 (1985).

150. K. S. Grabowski, G. K. Hubler, E. R. Hodge, R. A. Jeffries, C. R. Clayton, Y. F. Wang and G. Kuhlman, "Ion Beam Processing of Bearing Steels for Corrosion and Wear Resistance", NRL Memorandum Report 5592, Naval Research Laboratory, Washington, DC, June 27, 1985. (ADB093105)

151. R. G. Vardiman and J. E. Cox, "A Study of the Mechanisms of Fatigue Life Improvement in an Ion Implanted Nickel-Chromium Alloy", Acta Metallurgica, in press.

152. R. G. Vardiman, The Modification of Fatigue Properties of Ion Implantation", ASM Conference on the Applications of Ion Plating and Implantation to Materials, to be published (1985).

153. K-W. Wang, W. G. Spitzer, G. K. Hubler and D. K. Sadana, "Ion Implantation of Si by ^{12}C, ^{29}Si and ^{120}Sn: Amorphization and Annealing Effects", in press.

235

END

FILMED

4-86

DTIC